PRINCIPLES GUIDING IM30-MEDIATED MEMBRANE REMODELING

Dissertation

zur Erlangung des Grades

„Doktor der Naturwissenschaften“

im Promotionsfach Chemie

am Fachbereich Chemie, Pharmazie, Geographie und Geowissenschaften

der Johannes Gutenberg-Universität Mainz

Carmen Siebenaller

geb. in Donauwörth

Mainz, 2021

D77

Dekanin: [redacted]

1. Berichterstatter: [redacted]

2. Berichterstatter: [redacted]

Die vorliegende Arbeit wurde in der Zeit von 2017 bis 2021 am Department für Chemie der Johannes Gutenberg-Universität Mainz unter Betreuung von [redacted] angefertigt. Ich versichere, dass ich diese Arbeit selbständig verfasst habe und keine anderen als die angegebenen Quellen und Hilfsmittel benutzt habe.

Table of contents

I. Summary

The *inner membrane-associated protein of 30 kDa* (IM30) is critically involved in the biogenesis and dynamics of thylakoid membranes (TMs). However, its exact physiological function is unclear so far. IM30 appears to be involved in both the stabilization as well as the continuous reorganization of the TM network. Membrane remodeling could involve the membrane-fusogenic activity of IM30 which is observed when Mg^{2+} is present. Since membrane fusion requires at least partial destabilization of the lipid bilayer, the two main functions of IM30 appear to be contradictory. Consequently, it is essential to clearly regulate these two functions *in vivo*. Since regulation of the IM30 activity is essentially not understood thus far, my research has focused on the impact of various factors on the *in vitro* structure and membrane interactions of IM30 of the cyanobacterium *Synechocystis* sp. PCC 6803.

My observations indicate that binding of nucleotides to IM30 and their hydrolysis do not affect oligomerization of the IM30 monomers. The results further suggest that the IM30 NTPase activity has no decisive impact on membrane interactions of IM30. Consequently, the relevance of nucleotide hydrolysis by IM30 remains to be shown. In contrast, mildly acidic pH (~ 5) had considerable effects on the IM30 structure, accompanied by an enhanced membrane binding propensity and membrane fusion. Since low pH likely occurs at defective TM regions where protons leak out of the TM lumen, IM30 is suggested to sense and seal proton leaks of damaged TM regions. Further observations indicate that IM30 rings disassemble on a membrane in absence of Mg^{2+}, and that smaller IM30 oligomers have an increased membrane binding affinity. In contrast, increased binding of IM30 to both native and model membranes was observed in the presence of Mg^{2+}, accompanied by IM30-induced membrane defects. Thus, Mg^{2+} might be a switch regulating the dual function of IM30. Another regulatory mechanism could be the phosphorylation of specific amino acids, since phosphomimetic mutations were shown to result in a decreased membrane fusion activity of IM30. Similar consequences were observed when the conserved Trp71 was mutated. Furthermore, a relevance of the TM-specific lipid MGDG for the IM30-mediated membrane fusion was revealed, since MGDG-containing membranes are considerably more resistant at high Mg^{2+}-concentrations against induced membrane fusion.

In summary, the results of this thesis provide insights into the potential *in vivo* regulation of IM30 and suggest a structural basis of the dual IM30 function.

II. Zusammenfassung

Das *inner membran-associated protein of 30 kDa* (IM30) ist entscheidend an der Biogenese und Dynamik von Thylakoidmembranen (TM) beteiligt. Die genaue physiologische Funktion dieses Proteins ist jedoch bisher ungeklärt. IM30 scheint sowohl an der Stabilisierung als auch an der kontinuierlichen Reorganisation des TM-Netzwerks beteiligt zu sein. Die Membranreorganisation wird dabei vermutlich durch die in Gegenwart von Mg^{2+} beobachtete fusogene Aktivität von IM30 vermittelt. Da die Membranfusion zumindest eine partielle Destabilisierung der Membran erfordert, scheinen die beiden Hauptfunktionen von IM30 widersprüchlich zu sein. Folglich ist eine klare Regulierung dieser beiden Funktionen *in vivo* essentiell. Da die Regulation der IM30-Aktivität bisher weitgehend unbekannt ist, wurde im Rahmen dieser Arbeit der Einfluss verschiedener Faktoren auf die *in vitro* Struktur und Membraninteraktionen von IM30 aus dem Cyanobakterium *Synechocystis* sp. PCC 6803 untersucht.

Die Ergebnisse dieser Arbeit zeigten, dass die Nukleotidbindung und -hydrolyse durch IM30 die Oligomerisierung der IM30-Monomere zu Ringstrukturen nicht beeinflusst. Die Ergebnisse zeigen weiterhin, dass die NTPase-Aktivität keinen entscheidenden Einfluss auf die Membraninteraktionen von IM30 hat. Folglich ist Relevanz der Nukleotidbindung bisher unklar. Im Gegensatz dazu hatte ein leicht saurer pH-Wert (~ 5) bemerkenswerte Auswirkungen auf die IM30-Struktur und resultierte in erhöhter Membranbindung und Fusion. Da ein niedriger pH-Wert vermutlich in der Nähe von TM-Defekten auftritt, könnte IM30 *in vivo* Protonenleckagen aus beschädigten TM-Regionen erkennen und versiegeln. Weitere Ergebnisse dieser Arbeit zeigen, dass der IM30-Ring in Abwesenheit von Mg^{2+} auf der Membran dissoziiert und dass kleinere IM30-Oligomere eine erhöhte Membranbindungsaffinität aufweisen. Im Gegensatz dazu induziert IM30 in Gegenwart von Mg^{2+} Membrandefekte, wobei eine erhöhte Bindung von IM30 sowohl an native als auch an Modellmembranen festgestellt wurde. Somit könnte Mg^{2+} ein molekularer Schalter sein, der die Doppelfunktion von IM30 reguliert. Außerdem könnte die IM30 Funktion auch durch Phosphorylierung reguliert sein, da gezeigt wurde, dass phospomimetische Mutationen zu einer verringerten Membranfusionsaktivität von IM30 führen. Ähnliches wurde nach Mutation des konservierten Tryptophans 71 beobachtet. Darüber hinaus wurde in dieser Arbeit eine Relevanz des TM-spezifischen Lipids MGDG für die IM30-vermittelte Membranfusion gezeigt, da MGDG-haltige Membranen bei induzierter Membranfusion wesentlich stabiler sind.

Zusammenfassend geben die Ergebnisse dieser Dissertation einen ersten Einblick in die potentielle *in vivo*-Regulation von IM30 und definieren erstmals eine strukturelle Grundlage der dualen IM30 Funktion.

III. Publications

The below listed publications or already prepared manuscript drafts were generated in the course of this thesis. The already published articles are summarized in chapters 4.1 – 4.4 and the original articles are added in chapters VIII.1 – VIII.5. The manuscript draft and additional data are implemented into this thesis as individual chapters 4.5-4.8.

Published articles ([#]equal contribution)

- Siebenaller C.[#], Junglas B.[#] and Schneider D. (2019) Functional implications of multiple IM30 oligomeric states, Front. Plant Sci. 10, 1500 [*review article*]
- Junglas B.[#], Siebenaller C.[#], Schlösser L., Hellmann N. and Schneider, D. (2020) GTP hydrolysis by *Synechocystis* IM30 does not decisively affect its membrane remodeling activity, Sci. Rep. 10, 9793
- Siebenaller C.[#], Junglas B.[#]; Lehmann A., Hellmann N. and Schneider D. (2020) Proton Leakage Is Sensed by IM30 and Activates IM30-Triggered Membrane Fusion, Int. J. Mol. Sci. 21(12), 4530
- Junglas B., Orru R., Axt A., Siebenaller C., Steinchen W., Heidrich J., Hellmich U.A., Hellmann N., Wolf E., Weber S. and Schneider D. (2020) IM30 IDPs form a membrane protective carpet upon supercomplex disassembly, Nature Comm. Biol. 3, 595
- Siebenaller C., Schlösser, L., Junglas B., Schmidt-Dengler M., Jacob D., Hellmann N., Sachse C., Helm M. and Schneider D. (2021) Binding and/or hydrolysis of purine-based nucleotides is not required for IM30 ring formation, FEBS Letters, 595(14), 1876-1885

Manuscript prepared for submission

- Junglas B.[#], Axt A.[#], Siebenaller C.[#], Sonel H., Hellmann N., Weber S. and Schneider D. (2020) Mg^{2+}-binding to the *Synechocystis* IM30 (Vipp1) protein results in membrane destabilization and pore formation, *in preparation*.

1. Introduction

1.1. (Bacterial) Membrane Remodeling

Lipid bilayers are crucial for the survival of all living organisms as they act as physical barriers. In the case of simple unicellular organisms, they separate the outside from the inside of a cell. Furthermore, the formation of internal membrane systems is the basis for compartmentalization and specialization of eukaryotic cells (Bohuszewicz et al., 2016). The separation of different environments e.g. allows to build up a proton gradient, which is the driving force for ATP synthesis in the thylakoid membranes (TMs) of chloroplasts and cyanobacteria or the inner mitochondrial membrane of eukaryotes (Junge and Nelson, 2015).

Lipid bilayers have to be sufficiently rigid to maintain the membrane integrity, yet they still have to be flexible enough to enable continuous remodeling of the membrane (Bohuszewicz et al., 2016). This allows the membrane to shape to exert different biological functions. The dynamic rearrangement of the membrane is vital for all organisms, since essential steps in the development of any cell involve reorganization of the cell membranes. E.g., extensive membrane remodeling is required for cell division, endo-/exocytosis or intracellular trafficking in eukaryotes (Vega-Cabrera and Pardo-López, 2017). Although bacteria clearly exhibit lower membrane complexity as eukaryotic cells, membrane reorganization has been observed for example during cytokinesis (Lutkenhaus et al., 2012), outer-membrane vesicle formation (Zhou et al., 1998) or spore morphogenesis (McKenney et al., 2012). Recently it has been shown that the thus far solely in eukaryotes identified *endosomal sorting complex required for transport* (ESCRT) protein family also has prokaryotic superfamily members (Gupta et al., 2021; Junglas et al., 2021; Liu et al., 2021).

Membrane remodeling is often triggered by integral or peripheral membrane proteins, which tune the bilayer curvature by either actively inducing membrane curvature or passive remodeling e.g. via protein crowding (Bohuszewicz et al., 2016). Typical examples in eukaryotes are SNARE proteins, dynamins and BAR-domain containing proteins (Praefcke and McMahon, 2004; Jahn and Scheller, 2006; Mim and Unger, 2012). In bacteria, dynamin-like proteins or the protein complex consisting of FtsZ, FtsA and ZipA are well-studied membrane remodeling machineries (Bramkamp, 2012; Lutkenhaus et al., 2012). In cyanobacteria and chloroplasts, the peripheral membrane protein IM30 clearly is involved in TM remodeling (Hennig et al., 2015) as described later on.

1.2. IM30: an essential protein in oxygenic photosynthetic organisms

1.2.1. Cyanobacteria

Cyanobacteria are oxygenic, photoautotrophic prokaryotes. Together with plants and algae, they are responsible for the production of all oxygen that is consumed by aerobic organisms, and thus they stabilize the oxygen content in the atmosphere (Knoll, 2008). Cyanobacterial species are versatile and resilient microorganisms that are present in various habitats, such as marine or freshwater, but also in extreme environments, such as volcanic ash (Gaysina et al., 2019).

The ancestors of today's cyanobacteria have emerged around 3.5 billion years ago and are therefore among the oldest autotrophic organisms. The release of oxygen by cyanobacteria had a tremendous impact on the atmosphere, since the increasing population of cyanobacteria led to an enrichment of oxygen in the previously reducing atmosphere (Knoll, 2008). This enabled the development of organisms with an aerobic metabolism, which is significantly more effective than an anaerobic metabolism (Jiang et al., 2012). Chloroplasts presumably evolved via endocytosis of an ancient cyanobacterium by a eukaryotic host cell (Gray, 1999).

Because of the common evolutionary origin of cyanobacteria and chloroplasts, cyanobacteria are often used as model organisms to study photosynthesis, since the cultivation of cyanobacteria often is far more easier than the cultivation of plants (Vermass et al., 1988). Furthermore, the use of cyanobacteria for light-driven biotechnology or sustainable agriculture is promising for the development of ecological production systems (Pathak et al., 2018; Hitchcock et al., 2020). Still, the use of cyanobacteria is limited, since the photosynthetic efficiency is insufficient for large-scale productions so far (Luan et al., 2020). Further potential applications of cyanobacteria are their use as nutritional supplements (Khan et al., 2005), food-colorants (Galetovic et al., 2020) or biofertilizers (Song et al., 2005).

In this work, the protein IM30 of the cyanobacterium *Synechocystis* sp. PCC 6803 (hereafter: *Synechocystis*) was examined. *Synechocystis* is a cyanobacterial model to study the principles of photosynthesis, plus it was the first phototrophic organism with a completely sequenced genome (Kaneko et al., 1996; Ikeuchi and Tabata, 2001).

1.2.2. The Thylakoid Membrane

1.2.2.1. Photosynthesis

TMs form an extra internal membrane system in cyanobacteria and chloroplasts. The TM system harbors the protein complexes of the photosynthetic light reaction, as shown in Fig. 1.2.1 (Lea-Smith et al., 2016).

During the photosynthetic light reaction, sunlight is converted into chemical energy via producing the reduction equivalent nicotinamide adenine dinucleotide phosphate (NADPH) and by the phosphorylation of adenosine diphosphate (ADP) to adenosine triphosphate (ATP). In the following reactions, glucose is synthesized via the reduction of CO_2 in the Calvin-Benson cycle. In cyanobacteria, the light energy collected by phycobilisomes is passed on to photosystem II (PS II). Upon charge separation in the PS II reaction center, which is coupled with oxygen release, electrons are transferred to plastoquinone and subsequently to the cytochrome b_6f-complex, plastocyanin or cytochrome c_6, photosystem I (PS I) and to ferredoxin. Finally, the electrons are transferred from ferredoxin to $NADP^+$. During this electron transport, a proton gradient (ΔpH) is built up across the TM, which is used by the ATP synthase to catalyze phosphorylation of ADP and formation of ATP (Lea-Smith et al., 2016).

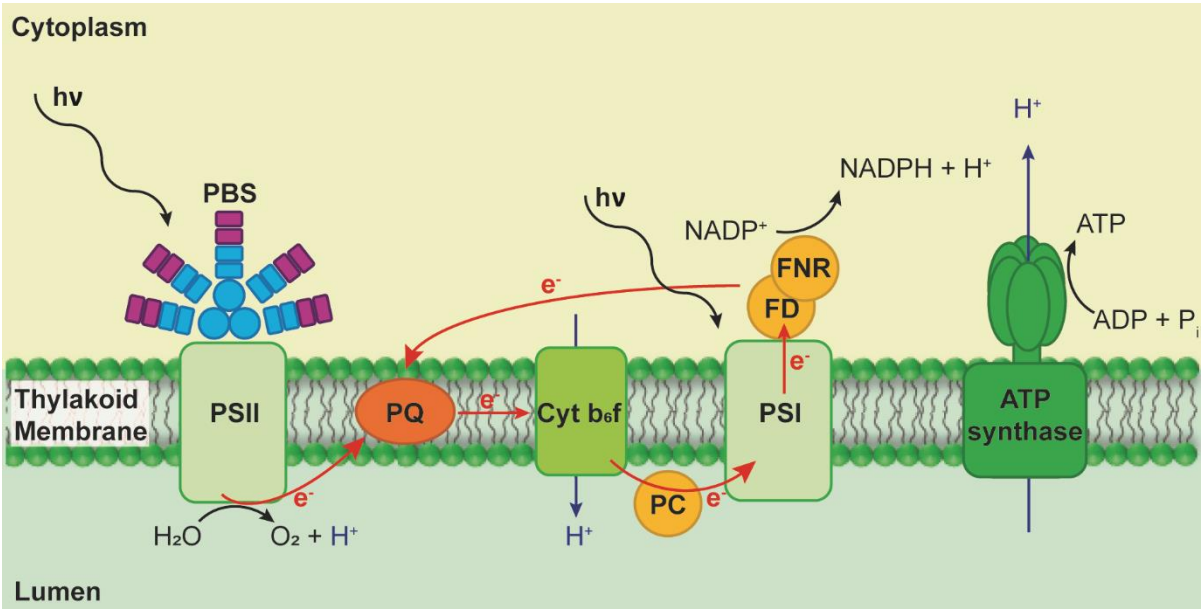

Figure 1.2.1: Schematic representation of the photosynthetic light reaction in cyanobacteria.

The thylakoid membrane harbors the protein complexes of the photosynthetic light reaction. The light energy is collected by the phycobilisomes (PBS) and transferred to photosystem II (PS II), in which electrons are generated by water splitting. The electrons are transferred via plastoquinone (PQ), the cytochrome b_6f complex (Cyt b_6f), plastocyanin (PC) and photosystem I (PS I) to ferredoxin (FD). The ferredoxin $NADP^+$ reductase (FNR) finally generates NADPH. During electron transport within the electron transfer chain, a proton gradient (H^+) is built up across the thylakoid membrane, which is used for the synthesis of ATP by the ATP synthase.

In addition, the cyanobacterial TM contains components of the respiratory chain, resulting in photosynthetic and respiratory electron transfer reactions simultaneously in one compartment (Peschek, 1999). Consequently, the electrons of the plastoquinone pool can originate from photosynthesis (PS II) or cellular respiration (Mullineaux, 2014).

1.2.2.2. Structure

The TMs form an internal membrane system in cyanobacteria and chloroplasts, which encloses the thylakoid lumen. In pea chloroplasts, about 40 % of the total mass can be referred to lipids, while about 60 % are mainly attributed to the photosynthetic complexes and further pigments (Chapman et al., 1983).

The structure of the TM network differs in chloroplasts and cyanobacteria. While the TMs of chloroplasts are organized as thylakoid stacks (grana thylakoids) with high amounts of PS II and connecting unstacked stroma thylakoids with high amounts of PS I and ATP synthase, the structure of cyanobacterial TMs is organized less complex. Yet, a spatial order of the photosystems has been observed in *Synechocystis* and *Synechococcus elongatus* sp. PCC 7952 (Mullineaux, 1999; Lea-Smith et al., 2016; Liu, 2016; Huokko et al., 2021). The architecture of the TM network varies between different cyanobacterial species. As an example, the *Synechocystis* structure is shown in Fig. 1.2.2. While the TMs of *Synechocystis* are mainly parallel and finally converge close to the cytoplasmic membrane, TMs from *Synechococcus* strains do not form these highly curved membrane regions (Rast et al., 2015). *Gloeobacter violaceus* is a special cyanobacterium, as it does not even have an internal TM network. In this organism, the photosynthetic complexes are inserted in the cytoplasmic membrane (Rippka et al., 1974). Still, it is discussed that photosynthetically active microdomains exist within the plasma membrane, which might be a starting point for the evolutionary TM development (Rexroth et al., 2011). Despite the quite remarkable difference in the TM organization and architecture, the function of the TM network is conserved in all species.

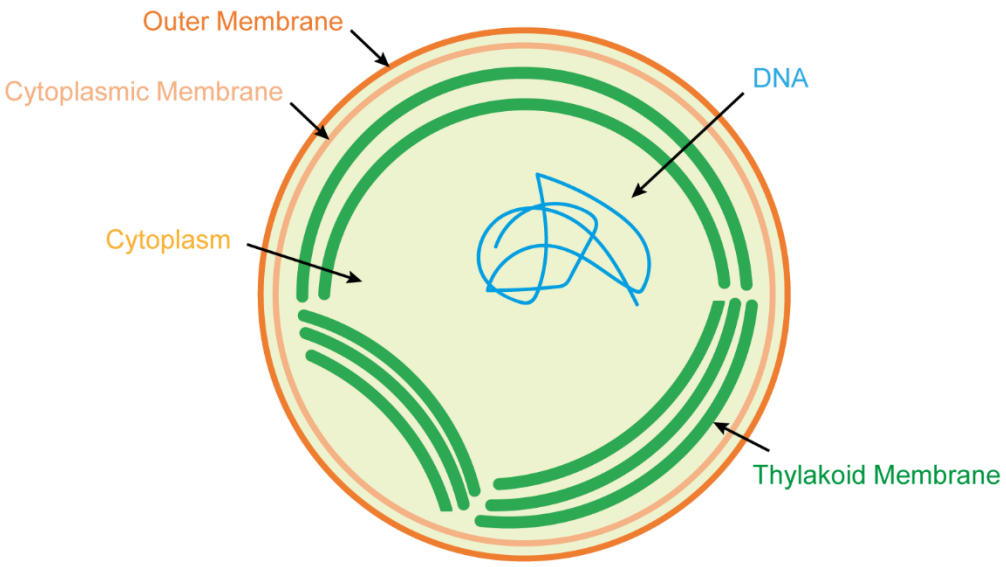

Figure 1.2.2: Schematic representation of a *Synechocystis* cell.

The *Synechocystis* cell is surrounded by the outer membrane and the inner cytoplasmic membrane (orange). The bacterium contains the thylakoid membranes as an internal membrane system (green), which encloses the thylakoid lumen. The DNA is located within the cytoplasm.

1.2.2.3. TM lipid composition

The lipid composition of the TM is unique compared to other biological membranes. The TMs contain a large amount of the galactolipids monogalactosyldiacylglycerol (MGDG), digalactosyldiacylglycerol (DGDG) and sulfoquinovosyldiacylglycerol (SQDG). Furthermore, it contains the negatively charged phospholipid phosphatidylglycerol (PG). In *Synechocystis*, the neutral charged lipids MGDG and DGDG represent 54% and 18% of all membrane lipids, respectively. Furthermore, the negatively charged lipids SQDG and PG make up 15% and 13%, respectively (Wada and Murata, 1989). An overview of the *Synechoystis* TM lipids is shown in Fig. 1.2.3.

A constant negative charge of the TM seems to be highly relevant for its function, since a lower SQDG content is always compensated by increased PG production and *vice versa* (Benning et al., 1993; Sato et al., 1995; Essigmann et al., 1998; Aoki et al., 2004). Interestingly, the most abundant lipid of the TM is the non-bilayer forming lipid MGDG. The typically highly unsaturated fatty acid chains result in a relatively broad volume of the fatty acid chains compared to the lipid headgroup and consequently a conically shaped lipid. In absence of further lipids or proteins, MGDG preferentially forms inverse hexagonal lipid structures (HII phase) (Simidjiev et al., 2000). In contrast, the lipids PG, SQDG and DGDG have a cylindrical shape and thus form classical lipid bilayers. In chloroplasts, MGDG has been found in higher concentrations in highly curved membrane regions of the TM (Gounaris et al., 1983).

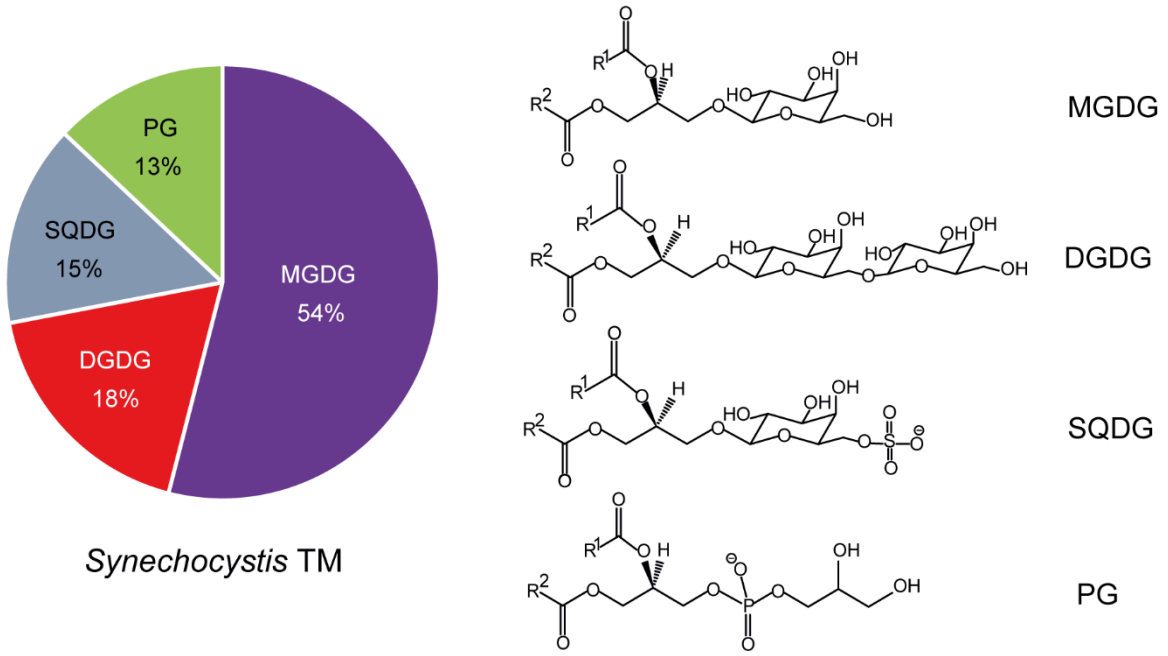

Figure 1.2.3: Lipid composition of the *Synechocystis* TM.

The TM of *Synechocystis* consists of 54% MGDG, 18%DGDG, 15% SQDG and 13% PG, respectively (Wada and Murata', 1989). MGDG, DGDG and SQDG are galactolipids. In contrast, PG is a phospholipid. SQDG and PG have negatively charged headgroups.

1.2.2.4. Biogenesis and dynamics of the TM

Despite the importance of the TM system, the biogenesis of the TMs remains elusive. In chloroplasts, thylakoid formation is initiated when undifferentiated proplastids are exposed to light (Rast et al., 2015). In cyanobacteria, the TMs likely develop as parallel stacks close to the cytoplasmic membrane (Barthel et al., 2013).

The biogenesis of the thylakoids requires a coordinated assembly of the individual membrane constituents. Thus far, it is not clear whether the TMs are completely assembled *de novo*, or whether lipids, proteins or pigments are transported from the cytoplasmic membrane (CM) of cyanobacteria or the inner envelope (IE) of chloroplasts to a preexisting TM structure. The transport might be enabled by either a vesicle transport system or by direct connections of the TM with the IE or the CM, respectively (Nickelsen et al., 2011). In cyanobacteria, a direct connection is controversially discussed, since fluorescence-based studies rather hint at a vesicular transport system (Schneider et al., 2007; Nickelsen et al., 2011; Rast et al., 2015). In chloroplasts, vesicles have been observed close to the IE and in the stroma (Kenneth Hoober et al., 1991; Westphal et al., 2001b; Lindquist et al., 2016). Despite the unclear mechanism of TM biogenesis, membranes remodeling is definitely necessary for TM biogenesis, since the TM biogenesis is a major structural (re)organization of lipid bilayers.

In general, the TM structure appears to be highly dynamic and extensive membrane remodeling is observed, as the TM structure constantly adapts e.g. to changing light conditions (Kirchhoff, 2014). Besides other proteins, the *inner membrane-associated protein of 30 kDa* (IM30) (Li *et al.* 1994) has been suggested to play a major role in the TM biogenesis/dynamics by catalyzing TM remodeling (Hennig et al., 2015).

1.2.3. The inner-membrane associated protein of 30 kDa

1.2.3.1. Origin of IM30

The IM30 protein was first discovered in chloroplasts of *Pisum sativum* (Li et al., 1994). Due to its location at both the thylakoid membrane and the chloroplast inner membrane, and due to its size of around 30 kDa, it was referred to as the *inner membrane-associated protein of 30 kDa* (IM30). Because of the apparent deficiency in vesicle formation of an IM30-depleted *Arabidopsis thaliana* (*Arabidopsis*) strain, the protein is also known as *vesicle inducing proteins in plastids* 1 (Vipp1) (Kroll et al., 2001). Still, this proposed function has never been proven by any additional data. In general, IM30 has been found to be essential for the formation and dynamics of TMs (summarized in Heidrich et al., 2017).

Early studies revealed that the *im30* gene is conserved in almost all plants and cyanobacteria (Li et al., 1994; Kroll et al., 2001; Westphal et al., 2001a; Fuhrmann et al., 2009b; Zhang et al., 2012). According to phylogenetic studies, IM30 probably evolved via duplication of the gene coding for the phage shock protein A (PspA) (Vothknecht et al., 2012). While both PspA and IM30 are encoded in cyanobacteria, in chloroplasts exclusively IM30 is encoded (Kroll et al., 2001; Westphal et al., 2001a; Vothknecht et al., 2012).

PspA is part of the phage shock proteins system (Psp system), which is a bacterial stress response system (Brissette et al., 1990; Brissette et al., 1991). This system helps to maintain the integrity of internal membranes, e.g. upon heat or osmotic stress, phage infections or organic solvents, which cause a dissipation of the proton motive force (Weiner et al., 1991; Kobayashi et al., 2007). The Psp-system contains seven proteins (PspA-G), from which PspA is the key effector protein (Darwin, 2005; Joly et al., 2010). PspA binds to the inner membranes of bacteria, and can this way e.g. prevent proton leakage of damaged membranes (Kobayashi et al., 2007). A further homologous protein of the IM30/PspA family is LiaH, which is e.g. found in *Bacillus* species (Wolf et al., 2010; Thurotte et al., 2017).

Very recently, it was shown that IM30 and PspA are members of the evolutionary conserved ESCRT-family (Gupta et al., 2021; Junglas et al., 2021; Liu et al., 2021). The endosomal sorting complex required for transport (ESCRT) was thus far only described being involved in diverse eukaryotic membrane remodeling processes, such as cytokinesis or multivesicular body biogenesis (Schmidt and Teis, 2012). During the process of membrane remodeling by the ESCRT machinery, the remodeled membrane is bent away from the cytosol. The ESCRT machinery consists of five distinct ESCRT complexes (ESCRT-0, -I, -II, -III and Vps4), from which the ESCRT-III complex seems to be most important, as it is part of all ESCRT-mediated remodeling processes (Schmidt and Teis, 2012). The ESCRT-III complex consists of the four core subunits Vps20/CHMP6, Snf7/CHMP4(A-C), Vps24/CHMP3 and Vps2/CHMP2(A, B), and furthermore of the 3 accessory proteins Did2/CHMP1(A, B), Vps60/CHMP5 and Ist1. The core subunits of ESCRT-III have a conserved oligomeric structure, which is similar to the IM30/PspA structure (Gupta et al., 2021; Junglas et al., 2021; Liu et al., 2021).

1.2.3.2. The structure of IM30

Proteins of the PspA/IM30 family have a high sequence and structural similarity. Until recently, solely the crystal structure of a PspA fragment (amino acid 1-144) was available (Osadnik et al., 2015) as well as low-resolution negative stain electron microscopy (EM) structures (Brissette et al., 1990; Hankamer et al., 2004; Bultema et al., 2010; Otters et al., 2013; Saur et al., 2017). Thus, most analyses were based on structural predictions. The *in vitro* formation of large homo-oligomeric ring or rod complexes (> 1.5 MDa) was shown to be a characteristic feature of the protein family (Aseeva et al., 2004; Hankamer et al., 2004; Liu et al., 2005; Liu et al., 2007; Fuhrmann et al., 2009a; Wolf et al., 2010; Gao et al., 2015; Heidrich et al., 2016; Saur et al., 2017). Very recent single-particle cryo-EM analyses of purified IM30 and PspA now resulted in high-resolution structures of IM30 (3.8 Å) and PspA (3.6 Å) (Gupta et al., 2021; Junglas et al., 2021; Liu et al., 2021). Since the results of this thesis have been generated before the high-resolution structure was available, also the IM30 structure model derived from earlier EM analysis (Saur et al., 2017) is introduced here.

IM30 from *Synechocystis* consists of 267 amino acids. The N-terminal part of the protein (~220 amino acids) is annotated as the PspA-domain, as it appears to be part of PspA as well as of IM30 proteins. Based on secondary structure predictions, the PspA domain was suggested to consist of 6 helices connected by short linker regions (Fuhrmann et al., 2009a; Gao et al., 2015). The recent analyses now reveal that the formerly termed helices 5 and 6 actually form only one continuous helix (Fig. 1.2.4 A). To maintain consistency in the nomenclature, this helix is called helix 5/6 in the following. The major structural difference from PspA and IM30 is the additional C-terminal helix of

IM30. Note that this helix was not resolved in the cryo-EM structure of IM30, most likely due to the intrinsically disordered nature of the extended linker and the high flexibility of this helix (see results, chapter 4.4). Most likely, helix 7 faces outwards the ring structure.

The previous model and the recent cryo-EM structure of the IM30 monomer is shown in Fig. 1.2.4 B. The exact monomeric structure depends on the layer, since the formed ring is not completely symmetrical (Fig. 1.2.5). Nevertheless, all structures contain a large coiled-coil structure formed by helices 2 and 3, as observed before in the crystal structure of the PspA fragment (Osadnik et al., 2015). In contrast to the earlier structural model, the residual helices 4-6 do not interact within the monomer, and also the helixes 1 and 2 likely do not interact within the monomer. The difference in the monomer structure within the layers is mainly caused by a helix-to-coil transition at the end of helix 4. The monomer structure also differs to some extent based on the ring size. Here, the angle of the flexible region between helix 3 and 4 was mainly responsible for the formation of increased ring diameters (Figure 1.2.5).

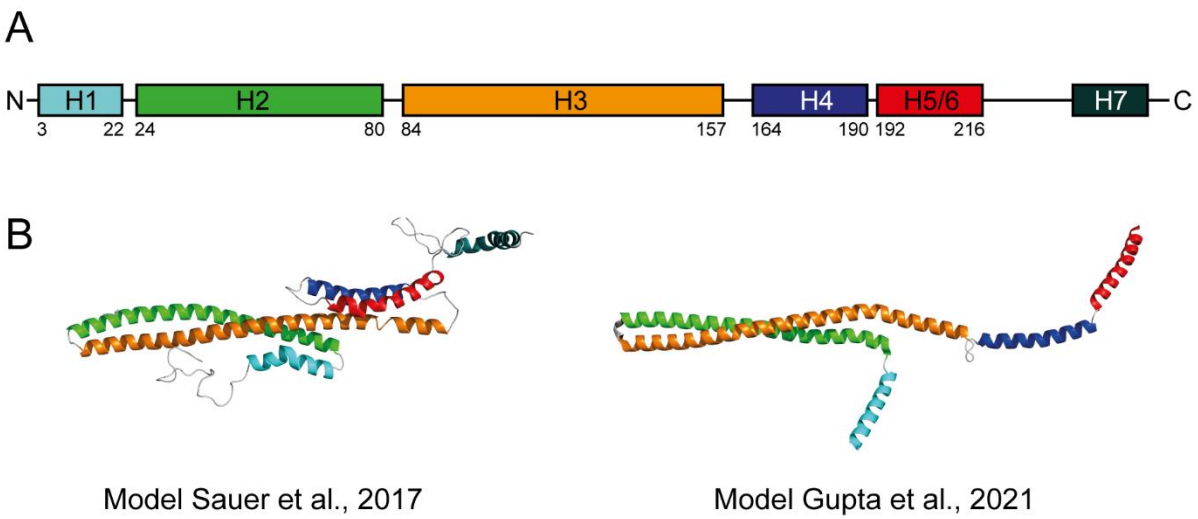

Figure 1.2.4: Structure of an IM30 monomer.

A: The localization of the helices within the IM30 sequence is displayed based on the available IM30 structure (C16-symmetry, layer 6, PDB 7O3Y). **B:** The IM30 monomer structures based on negative stain studies and predictions (Saur et al., 2017) and based on cryo-EM studies (Gupta et al., 2021) (C16-symmetry, layer 6) are shown. Note that helix 7 is not resolved in the cryo-EM structure.

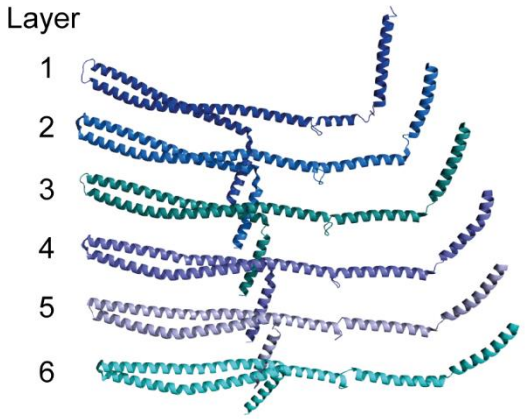

Figure 1.2.5: The IM30 monomer structure slightly differs in the individual ring layers.

The IM30 monomer structure differs depending on the ring layer. (C16-symmetry, PDB: 7O3Y)

IM30 forms rings with different rotational symmetries (at least 7-22fold) and a pronounced spike structure. The diameters were determined as 24-40 nm with a constant height of ~ 20 nm (Fuhrmann et al., 2009a; Saur et al., 2017; Gupta et al., 2021). Interestingly, also rod-like structures with similar diameters and rotational symmetries have been observed in the past (Liu et al., 2005; Liu et al., 2007; Fuhrmann et al., 2009a; Saur et al., 2017; Theis et al., 2019). In case of PspA, these rod-like structures even appear to dominate. While the rods were initially thought to consist of stacked rings, the now available high-resolution structure of PspA shows that rods have a helical structure (Junglas et al., 2021).

The orientation of the IM30 monomers within the ring was initially believed to be vertical, parallel to the ring axis (Saur et al., 2017). The new structures now show that the monomers are actually arranged horizontally in the ring (Gupta et al., 2021). The monomers form an interwoven layer structure, which further oligomerizes to a ring structure. Each ring consists of 6 (C14-C16) or 7 individual layers (C17-C18). The structure of the top (1) and the bottom layer (6 or 7) differ to some extent, leading to smaller diameters at both ends of the ring. From the now available high-resolution structures of IM30 rings, the ring with C16-symmetry had the best resolution (3.8 Å). Note that even at this resolution, the generation of the model required molecular dynamics (MD) simulations, and thus the orientation of the amino acid side chains does not necessarily reflect the "real" structure. In Fig. 1.2.6, the structure of an IM30 ring with C16 symmetry is shown in detail.

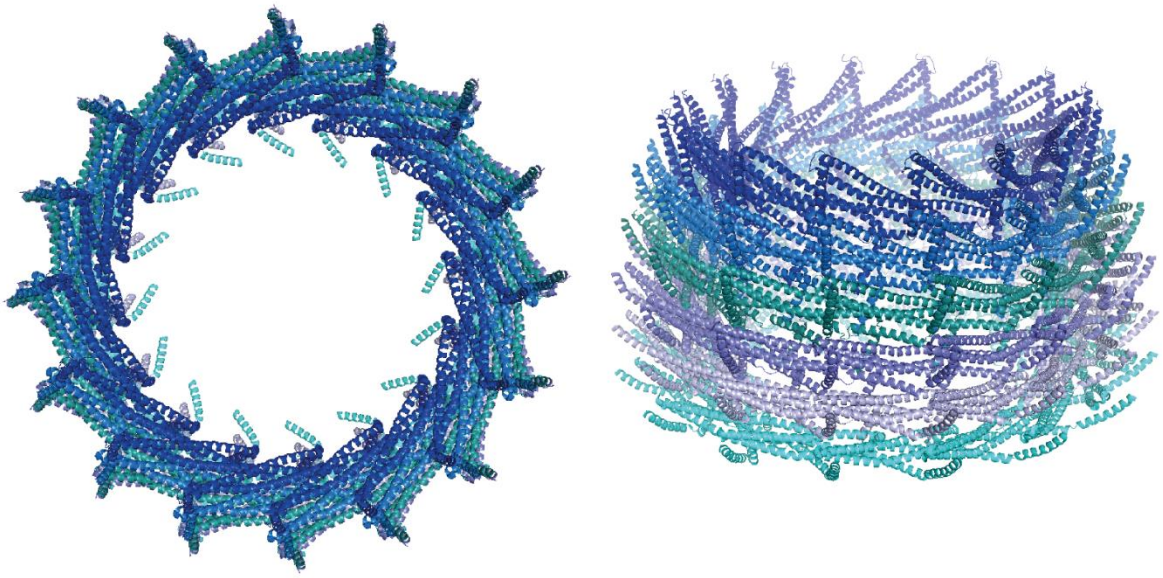

Figure 1.2.6: IM30 ring structure.

The oligomeric ring structure of IM30 based on cryo-EM studies (Gupta et al., 2021) (C16-symmetry, layer 6, PDB 7O3Y) is shown as top view (left) and side view (right). Note that helix 7 is not resolved in the Cryo-EM structure.

Oligomerization of the monomers into individual layers finally forming a C16-ring is shown in Fig. 1.2.7. While helix 1 faces the inside of the ring, the turn of the coiled-coil structure and helices 4-7 protrude out of the ring. In the assembled ring structure (Fig. 1.2.6) it is evident that the monomers clearly interact not only within the individual layers, but also with adjacent monomers from the upper and lower layers. Indeed, one IM30 monomer was shown to potentially interact with up to 16 monomers from three different layers (Gupta et al., 2021).

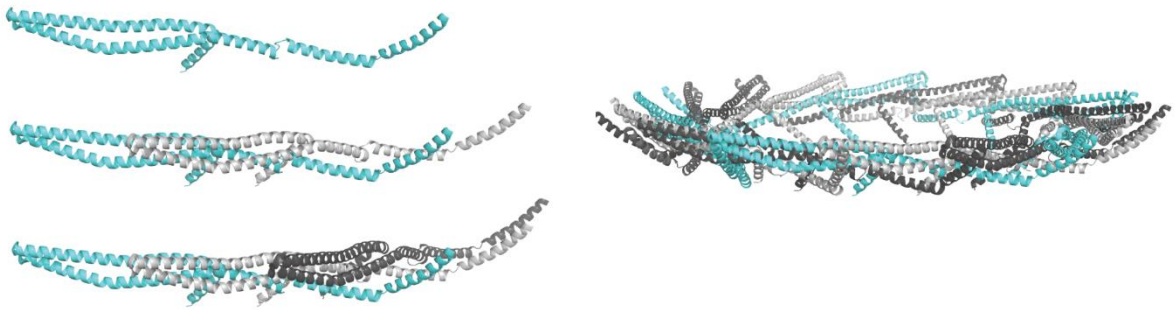

Figure 1.2.7: IM30 oligomerization into a ring layer.

IM30 monomers assemble into one layer of the ring structure (C16-symmetry, layer 6, PDB: 7O3Y).

1.2.3.3. The function of IM30

The exact physiological function of IM30 still is unclear. In the last years, many functions of IM30 have been proposed and controversially discussed (Li et al., 1994; Kroll et al., 2001; Benning et al., 2006; Benning, 2008; Fuhrmann et al., 2009b; Lo and Theg, 2012; Nordhues et al., 2012; Vothknecht et al., 2012; Zhang et al., 2012; Zhang et al., 2014; Hennig et al., 2015; McDonald et al., 2015; Zhang and Sakamoto, 2015; McDonald et al., 2017; Thurotte et al., 2017). Yet, it has become increasingly clear that IM30 is a membrane-active protein linked to TM biogenesis, dynamics and/or remodeling (reviewed in Heidrich et al., 2017). It is likely that IM30 has at least two major functions, i.e. a PspA-related membrane protecting activity as well as a TM-specific membrane remodeling function (reviewed in Siebenaller et al., 2019). Further suggested functions include lipid transport (Li et al., 1994; Benning et al., 2006), protein membrane insertion (Gohre et al., 2006; Walter et al., 2015), the formation of cytoskeleton-like elements (Anderson et al., 1973; Van De Meene et al., 2006) or GTP hydrolysis (Ohnishi et al., 2018). Yet, the relevance of these functions for TM biogenesis/dynamics remains completely unknown thus far.

The *in vivo* function of IM30 has been mainly studied using IM30 depleted or deleted cyanobacteria, algae, or plants. The studies were primarily performed in the cyanobacterium *Synechocystis*, the green alga *Chlamydomonas reinhardtii* or the higher plant *Arabidopsis thaliana*. Yet, the results of these studies were not entirely conclusive. The consequence of an IM30 depletion in *Arabidopsis* was a strongly disturbed TM structure and an overall low amount of TMs (Kroll et al., 2001; Aseeva et al., 2004; Vothknecht et al., 2012). In line with this, depletion of IM30 in the cyanobacteria *Synechocystis* and *Synechococcus* did also result in reduced TM networks (Westphal et al., 2001a; Fuhrmann et al., 2009b; Vothknecht et al., 2012; Zhang et al., 2014). In *Chlamydomonas*, IM30 is present as two paralogs. When only one paralog was depleted, the TM structure of *Chlamydomonas* was not affected, albeit the photosynthetic activity was reduced (Nordhues et al., 2012). In *Chlamydomonas* and in cyanobacteria, the reduction of IM30 did also lead to a reduced photosynthetic activity caused by an impaired PS II in *Chlamydomonas* and impaired PS I in cyanobacteria (Fuhrmann et al., 2009b; Nordhues et al., 2012; Vothknecht et al., 2012). Noteworthy, *Gloeobacter violaceus*, which does not contain TMs, does not express IM30 (Rippka et al., 1974), emphasizing the important role of IM30 in TM biogenesis.

A main function of IM30 is the remodeling of the TM via membrane fusion (Hennig et al., 2015). This way, components of the TM could be either transported by a vesicle-traffic system, or by the formation of TM contacts with the IE or CM. Consequently, it might be essential to adapt the size and structure of the TM system during TM development and in response to changing light conditions

(Chuartzman et al., 2008; Nagy et al., 2011; Liberton et al., 2013b). *In vitro*, IM30 has been shown to specifically bind to membranes containing negatively charged lipids in a curvature-dependent manner, which changes the order and polarity in the headgroup region (Hennig et al., 2015; McDonald et al., 2015; Heidrich et al., 2016). The membrane fusion activity was shown to be strictly dependent on Mg^{2+}, which was suggested to be a regulator of the IM30 function, since the interaction of IM30 with Mg^{2+} induces a rearrangement of the IM30 structure (Heidrich et al., 2018). Clearly, further control of the potential fusion activity is necessary *in vivo*. Yet, further regulators are unknown thus far.

Controversial to the proposed membrane-fusion activity, IM30 has also been suggested being involved in membrane protection, which appears to be a conserved function of all IM30/PspA family members. Indeed, IM30 can replace PspA in *E. coli* (DeLisa et al., 2004). PspA is known to maintain the cytoplasmic membrane integrity and proton motive force (PMF) in many Gram-negative bacteria (Kleerebezem et al., 1996; Kobayashi et al., 2007; Joly et al., 2010). PspA is assumed to stabilize membranes against proton leakage via forming membrane-protecting assemblies (Mehta et al., 2015). In cyanobacteria and chloroplasts, GFP-labeled IM30 also forms large assemblies located at highly curved TM regions (Bryan et al., 2014; Zhang et al., 2016; Gutu et al., 2018). The protection and maintenance of the TM system are necessary to prevent energy dissipation and to maintain a proton gradient across the TM, a membrane system highly vulnerable to membrane damage (Kirchhoff, 2014). Nevertheless, the mechanism for this membrane protecting activity by PspA/IM30 remains largely unknown.

1.2.3.4. Regulation of the IM30 activity

The regulation of the IM30 protein *in vivo* appears to be highly relevant, since the proposed dual function of IM30 requires strict separation of membrane fusion vs. membrane protection.

The first regulation level of any protein is its availability within the cell, which depends on the expression of the gene and potentially the production of an antisense-RNA. For instance, an *im30* antisense-RNA of was shown to be produced in high concentrations in the initial phase of resuscitation of chlorotic *Synechocystis* cells (Klotz et al., 2016). It was discussed that during this initial phase, IM30 production is suppressed to prevent too early biogenesis of TMs (Klotz et al., 2016). Furthermore, increased levels of IM30 have been observed locally at highly curved membranes under high-light stress, but not low-light conditions in *Synechocystis* and *Arabidopsis* (Bryan et al., 2014; Gutu et al., 2018). Noteworthy, the IM30 clusters observed on the membranes

likely do not consist of IM30 rings, but rather smaller oligomers (Junglas and Schneider, 2018). Such smaller oligomers have a higher membrane binding affinity (Heidrich et al., 2016). Consequently, the formation of the IM30 assemblies on a membrane is discussed to be relevant for the membrane-protective function under stress conditions. Still, also a regulation of the protective function is clearly vital, as the membrane rigidity increases upon IM30 binding (Heidrich et al., 2016), which is counterproductive for a functional TM system (Murata, 1989). A potential regulation of the IM30´s membrane-protective function is the interaction of IM30 with chaperones (Siebenaller et al., 2019). The interaction with e.g. the heat shock protein 70 (Hsp70) in *Chlamydomonas* or the heat shock protein 90C (HSP 90C) in *Arabidopsis* had large impact on the assembly as well as the disassembly of the IM30 supercomplexes (Liu et al., 2007; Gao et al., 2015). Also in *Synechocystis*, the interaction of IM30 with the HSP 70/40 homologous chaperones DnaK2 and 3 was observed (Bryan et al., 2014). The chaperones were suggested to prevent IM30-mediated membrane fusion via triggering ring disassembly, but also to remove membrane-bound IM30, e.g. after dissociation of rings on a membrane surface (Siebenaller et al., 2019). Still, the exact physiological impact of the interaction with chaperones is still unclear. Furthermore, the activity of IM30 is regulated via Mg^{2+}-binding, which triggers a rearrangement of the IM30 structure (Heidrich et al., 2018). This is supposed to be crucial for IM30 mediating membrane fusion Interestingly, the availability of Mg^{2+} in cyanobacteria and chloroplasts differs depending on the light conditions. Upon light exposure, Mg^{2+} is released from the thylakoid lumen to counterbalance a light-induced proton gradient (Pohland and Schneider, 2019). E.g. in the chloroplast stroma, the Mg^{2+} concentration increases by 1- 5 mM in the light (Shaul, 2002). Since thylakoid membranes develop upon illumination, the IM30-induced membrane fusion likely is relevant for TM biogenesis. Another putative regulator of the IM30 function is the phosphorylation of specific amino acid side chains. During resuscitation from chlorosis, defined amino acid side chains were found to be phosphorylated during the initial phase (Spät et al., 2018). Yet, the effect of phosphorylation on the IM30 structure and function is currently enigmatic.

2. Objectives of this thesis

The *inner membrane-associated protein of 30 kDa* (IM30/Vipp1) is vital in almost all oxygenic photosynthetic organisms. However, its exact physiological function, as well as the regulation of the IM30´s activity, is still unknown. Membrane interaction of IM30 is discussed to be crucial for stabilization, as well as in the continuous rearrangement of the TM network, which is indispensable for the photosynthetic energy production. Understanding the still enigmatic physiological function of IM30 will further enlarge our knowledge about these special organisms that are unequivocally vital for life on earth.

In my project, membrane interactions of IM30 from the cyanobacterium *Synechocystis* was analyzed *in vitro* with special focus on the regulation of the IM30 activity. In particular, the following topics were studied:

1. **The influence of nucleotides on the structure and membrane interaction of IM30**

   Recently, IM30 of *Arabidopsis thaliana* chloroplasts was reported to have a GTPase activity *in vitro,* and this function was suggested to influence the membrane interaction of IM30 (Ohnishi et al., 2018). Since IM30 does not exhibit features of classical GTPases, multiple assays were performed to analyze the GTP hydrolyzing activity of IM30 of *Synechocystis*. Additionally, the potential impact of GTP binding/hydrolysis on IM30 membrane binding and the IM30 membrane fusion activity was investigated. Also the relevance of nucleotide binding for the oligomeric structure of IM30 was studied e.g. by electron microscopy and LC-MS studies.

2. **The influence of acidic pH on the structure and membrane interaction of IM30**

   TMs are prone to oxidative damage, e.g. under high-light conditions, which bears the risk of proton leaks (Foyer, 2018; Junglas and Schneider, 2018). Thus, the consequence of acidic pH on the structure and function of IM30 was analyzed *in vitro*. In this context, the membrane binding affinity and the membrane-fusion activity were investigated at acidic conditions.

3. **The structure of IM30 on membranes**

   Since IM30 is a membrane-active protein (Hennig et al., 2015; McDonald et al., 2015; Heidrich et al., 2016; McDonald et al., 2017), the membrane-bound structure of IM30 is of special interest. As support for detailed atomic force microscopy studies (AFM) on solid-supported lipid bilayers, the structure of IM30 was analyzed by tryptic digestion in absence and presence of PG liposomes. As small oligomers seem to represent a potential intermediate structure in the membrane binding process, the structure of a dimeric IM30 mutant was analyzed by small-

angle X-ray scattering (SAXS). To analyze the membrane binding characteristics of this mutant, its binding to model membranes was kinetically analyzed.

4. The influence of Mg^{2+} on membrane interaction of IM30

While IM30 has been shown to trigger membrane fusion in presence of Mg^{2+} (Hennig et al., 2015), it remains unclear so far what impact the interaction of Mg^{2+} with IM30 and/or the membrane actually has on IM30 membrane binding. Therefore, in addition to AFM analysis on the membrane-bound structure of IM30, the influence of Mg^{2+} on membrane binding was studied via sucrose density gradient centrifugation and fluorescence microscopy using giant unilamellar vesicles (GUVs).

5. The influence of W71 on the structure and membrane interactions of IM30

Defined amino acids are conserved in homologous proteins from various species due to a crucial impact on the structure and/or function of the protein. In a sequence alignment of the IM30 coiled-coil region (helices 2–3), Trp71 has been identified to be highly conserved in IM30 proteins. IM30 variants carrying the mutations W71A, R74A and R93A, respectively, were analyzed and the impact of the mutations on the structure and membrane interactions of IM30 was studied.

6. The influence of the TM lipids on membrane interaction of IM30

The TM of cyanobacteria and chloroplasts has a unique lipid composition and architecture (Wada and Murata', 1989). *In vitro*, the interaction of IM30 with membranes has been shown to depend on the lipid composition of the model membrane (Hennig et al., 2015). Furthermore, membrane curvature appears to affect IM30 membrane binding (McDonald et al., 2015). Consequently, IM30-membrane interactions were analyzed using model membranes with different lipid compositions and curvatures.

7. The influence of phosphorylation on the structure and membrane interaction of IM30

The IM30 protein was shown to be phosphorylated during resuscitation of chlorotic cyanobacteria (Spät et al., 2015; Spät et al., 2018). To investigate the potential impact of phosphorylation on the IM30 structure and function, IM30 variants with phosphomimetic mutations were analyzed *in vitro*.

3. Materials and Methods

3.1. Materials

3.1.1. Chemicals, Buffers and Solutions

Chemicals were purchased from Merck (Darmstadt, GER), Roth (Karlsruhe, GER), Sigma-Aldrich (Munich, GER) AppliChem (Darmstadt), Fisher Scientific (Hampton, NH, USA) and VWR (Darmstadt, GER). Lipids were bought from Avanti Polar Lipids (Alabaster, ALA, USA). Enzymes were purchased from New England Bio Labs (Frankfurt, GER).

All buffer and solutions were prepared with deionized water and filtered, if necessary. The composition of the buffers and solutions is listed in Table 3.1.1.

Table 3.1.1: Composition of buffers and solutions.

Notation	Composition
Protein expression	
Ampicillin	10 % Ampicillin (w/v) 50 % Ethanol (v/v)
SDS-PAGE	
Stacking gel buffer	1.5 M TRIS, pH 6.8 0.4 % SDS (w/v)
Separation gel buffer	0 .5 M TRIS, pH 8.8 0.4 % SDS (w/v)
10x SDS running buffer	0.25 M TRIS, pH 8.3 1.92 M Glycine 1 % SDS (w/v)
5x SDS sample buffer	0.25 M TRIS, pH 6.8 10 % SDS (w/v) 0.2 % Bromphenol blue 50 % Glycerol (v/v) 0.5 M DTT
Coomassie staining solution	0.125 % Coomassie Brilliant Blue G-250 (w/v) 40 % Ethanol (v/v) 2 % Phosphoric acid (v/v)
Coomassie destaining solution	30 % Ethanol (v/v) 2 % Phosphoric acid (v/v)
Immunoblot detection	
TBST buffer	0.25 M TRIS, pH 7.8 0.125 M NaCl 0.05 % Tween 20 (v/v)

Transfer buffer	0.25 M TRIS, pH 7.6 0.192 M Glycerol 30 % Methanol (v/v)
Blocking buffer	5 % Milk powder in TBST
Protein purification	
Lysis buffer	50 mM Sodium phosphate, pH 7.6 300 mM NaCl 20 mM imidazole 0.1 % sigma-protease inhibitor (P8849) (v/v)
Washing buffer	50 mM Sodium phosphate, pH 7.6 300 mM NaCl 20-100 mM imidazole
Elution buffer	50 mM Sodium phosphate, pH 7.6 300 mM NaCl 500 mM imidazole
Protein storage	
HEPES buffer	20 mM HEPES, pH 7.6

3.1.2. Bacteria

The used bacteria strains are listed in Table 3.1.2. The bacteria were cultivated in LB-Medium (Table 3.1.3).

Table 3.1.2: Bacterial strains.

Bacteria strain	Genotype	Origin
E. coli BL21(DE3)	*F-ompT hsdS*(rB-mB-)*gal dcm* λ(DE3)	Novagen (Darmstadt, GER)
E. coli XL1-blue	*rec*A1 *end*A1 *gyr*A96 *thi*-1 *hsd*R17 *sup*E44 *rel*A1 *lac*	Novagen (Darmstadt, GER)

Table 3.1.3: Media.

Notation	Composition
LB medium	1 % Tryptone (w/v) 5 % Yeast extract (w/v) 1 % NaCl (w/v)
LB agar	1.5 % Agar (w/v) in LB medium

3.1.3. Oligonucleotides

The oligonucleotides were obtained from Eurofins genomics (Ebersberg, GER).

Table 3.1.4: Oligonucleotides used for site-directed mutagenesis.

Mutation	Sequence
IM30 W71A	Forward: CCAGGAAGCCAAGAAAGCGGAAGACCGGAGC Reverse: GCTCCGGTCTTCCGCTTTCTTGGCTTCCTGG
IM30 R74A	Forward: GAAATGGGAAGACGCGGCAAAATTAGCCCTCACC Reverse: GGTGAGGGCTAATTTTGCCGCGTCTTCCCATTTC
IM30 R93A	Forward: GGGAA GCCCTGGCCGCCAAAAAAAGTCTGACAG Reverse: CTGTCAGACTTTTTTTGGCGGCCAGGGCTTCCC
IM30 S96A	Forward: CTGGCCCGCAAAAAAGCTCTGACAGATACGGCG Reverse: CGCCGTATCTGTCAGAGCTTTTTTGCGGGCCAG
IM30 S96D	Forward: CCTGGCCCGCAAAAAAGATCTGACAGATACGGCG Reverse: CGCCGTATCTGTCAGATCTTTTTTGCGGGCCAGG
IM30 T155A	Forward: GAACTGCAGCAAGCCCTCGGGGGC Reverse: GCCCCCGAGGGCTTGCTGCAGTTC
IM30 T155D	Forward: GCTGAACTGCAGCAAGACCTCGGGGGCTTAGGT Reverse: ACCTAAGCCCCCGAGGTCTTGCTGCAGTTCAGC

3.1.4. Plasmids

Table 3.1.5: Plasmids.

Plasmid	Origin
pRSET IM30 wt	AG Schneider
pRSET IM30 H23	AG Schneider
pRSET IM30 W71A	AG Schneider
pRSET IM30 R74A	Siebenaller, 2016
pRSET IM30 R93A	Siebenaller, 2016
pRSET IM30 H23 W71A	this work
pRSET IM30 H23 R74A	this work
pRSET IM30 H23 R93A	this work
pRSET IM30 S96A	this work
pRSET IM30 S96D	this work
pRSET IM30 T155A	this work
pRSET IM30 T155D	this work

3.1.5. Kits

Table 3.1.6: Kits.

Kit	Notation	Manufacturer
Immunostaining	ECL Prime Western Blotting Detection Reagent	GE Healthcare (Munich, GER)
Plasmid preparation	Presto Mini Plasmid Kit NucleoSpin Plasmid Kit	Geneaid Biotech (Taipei, TW) Macherey Nagel (Düren, GER)
SEC marker	Molecular Weight Marker Kit	Sigma Aldrich (Munich, GER)

3.1.6. Instruments

Table 3.1.7: Instruments.

Instrument	Notation	Manufacturer
Atomic force microscope	Multimode 8, Nanoscope V controller Nanowizard IV	Bruker (Billerica, MA, USA) JPK, Bruker (Billerica, MA, USA)
Cell Homogenizer	SpeedMill PLUS	Analytik Jena (Jena, GER)
Centrifuges	Allegra X-15R Avanti J-26XP Centrifuge 5424	Beckmann Coulter (Krefeld, GER) Beckmann Coulter (Krefeld, GER) Eppendorf (Hamburg, GER)
CD spectrometer	J-815 with MTPC-490-515	Jasco (Pfungstadt, GER)
Chemoluminescene detection system	Stella	Raytest (Straubenhardt, GER)
Dynamic light scattering system	Zetasizer Nano S-Size	Malvern Instruments (Malvern, GB)
Electron microscope	FEI Tecnai 12 FEI Talos L120C	FEI Thermo Scientific (Darmstadt, GER)
Electrophoresis chamber	Mini-Protean 3 Cell	Bio-Rad (Munich, GER)
Electrophoresis power supply	PowerPac Basic	Bio-Rad (Munich, GER)
Extruder	Mini-Extruder	Avanti Polar Lipids (Alabaster, AL, USA)
FPLC	ÄKTA basic	GE Healthcare (Munich, GER)
Fluorescence microscope	Axio Observer.Z1	Carl Zeiss Microscopy (Jena, GER)
Fluorescence spectrometer	FluoroMax-4	Horiba Scientific (Kyoto, JPN)
Gel documentation	Quantum-ST4 1100/26MX	PeqLab (Erlangen, GER)
Gel scanner	ViewPix 700	Biostep (Burkhardtsdorf, GER)

Gradient system	Gradient master station	BioComp (Fredericton, CA)
Heating block	Thermomixer comfort	Eppendorf (Hamburg, GER)
Horizontal shaker	Duomax 1030	Heidolph (Schwabach, GER)
Incubator	Multitron HT	Infors (Bottmingen, CH)
Overhead shaker	CMV-ROM	Fröbel (Lindau, GER)
pH-Meter	pH211 Microprocessor	HANNA Instruments (Vöhringen, GER)
Photometer	Novaspec Plus	Amersham Biosciences (Little Chalfont, UK)
	Nanodrop 2000C	Thermo Scientific (Darmstadt, GER)
	Lambda 35	Perkin Elmer (Rodgau, GER)
Plasma Cleaner	Yocto	Diener electronics (Ebhausen, GER)
Plate Reader	FLUOstar Omega	BMG Labtech (Ortenberg, GER)
QCM system	qCell T Series	3T Analytik (Tuttlingen, GER)
Rotors	JA 25.50	Beckmann Coluter (Krefeld, GER)
	JLA-8.1	Beckmann Coluter (Krefeld, GER)
Sonifier	Branson Sonifier 250	Heinemann Labortechnik, (Duderstadt, GER)
Thermocycler	Thermocycler Primus 25	PeqLab (Erlangen, GER)
Western Blot system	Trans-Blot Turbo Transfer System	Bio-Rad (Munich, GER)

3.1.7. Software

Table 3.1.8: Software.

Application	Software
AFM analysis	Gwyddion 2.56
Chemical structures	PyMOL 2.3.4
	ChemDraw
Data analysis	Microsoft Excel (Office 365) Origin 2019b
Figure editing	Adobe Illustrator 2020
	Adobe Photoshop 2020
	ImageJ 1.47
Literature management	Mendeley 1.19.8
Sequence analysis	Clustal X2
Text editing	Microsoft Word (Office 365)

3.2. Methods

This section describes the general methodology of the performed experiments. Deviations from that are mentioned in the respective chapters.

3.2.1. Molecular Biological Methods

3.2.1.1. Site-specific mutagenesis

IM30 variants were generated by site-directed mutagenesis of the IM30 expression plasmid (Liu and Naismith, 2008). The mutations W71A, R74A, R93A, S96A, S96D, T155A and T155D were introduced into the plasmids pRSET IM30 wt (Fuhrmann et al., 2009a) or pRSET IM30 H23 (Thurotte and Schneider, 2019), respectively.

Therefore, a *polymerase chain reaction* (PCR) was performed using the primers listed in Table 3.1.4. The PCR compounds and the temperature program of the PCR are listed in Table 3.2.1 and 3.2.2. The DNA was incubated with *Dpn*I for 1 h at 37 °C to digest the parental DNA. The reaction mixture was transformed into *E. coli XL1 blue* cells as described below. After inoculation of 3 mL LB-medium (100 µg/mL amp) with a single colony, the bacteria were incubated for 16 h at 37 °C and 200 rpm (Multitron, Infors, Bottminger, CH). The bacteria were harvested at 16 000 g for 1 min at 4 °C. After plasmid preparation, the DNA mutagenesis was verified by sequencing of the plasmids.

Table 3.2.1: PCR reaction used for site-directed mutagenesis.

Application	Concentration	Volume
H_2O (sterile)		27 µL
Phusion GC-buffer	5x	10 µL
$MgCl_2$	50 mM	1 µL
DMSO		3 µL
Plasmid	100 ng/µL	1 µL
Primer (forward)	100 pmol/µL	1 µL
Primer (reverse)	100 pmol/µL	1 µL
dNTPs	2 mM	5 µL
Phusion Polymerase	2.5 U	1 µL

Table 3.2.2: PCR program used for site-directed mutagenesis of pRSET IM30.

	Temperature	Time	
Initial Denaturation	98 °C	30 s	
Denaturation	98 °C	20 s	17 x
Hybridization	55 °C	30 s	
Elongation	72 °C	3 min	
Final Elongation	72 °C	10 min	

3.2.1.2. Plasmid preparation

The plasmids were prepared using the Presto Mini Plasmid Kit (Geneaid, New Taipei City, TW) or NucleoSpin Plasmid Kit (Macherey Nagel, Düren, GER) following the manufacturer's instructions. The concentration of the DNA was determined by the absorption at 260 nm.

3.2.2. Microbiological Methods

3.2.2.1. Transformation competent bacteria

E. coli BL21 (DE3) cells were made transformation competent following the method described by Chung-Miller, using ice-cold TSB-medium (Chung et al., 1989).

Therefore, 3 ml of LB medium were inoculated with a colony of the corresponding *E. coli* strain and incubated for 16 h at 37 °C and 200 rpm (Multitron, Infors, Bottminger, CH). A culture of 50 mL LB medium was inoculated with this preculture and was incubated up to an OD600 of approx. 0.8 at 37 ° C. and 200 rpm (Multitron, Infors, Bottminger, CH). The cell suspension was then centrifuged at 4 °C at 4600 rpm for 10 min (Allegra X-15R). The cell pellet was resuspended in 5 mL ice-cold TSB medium. Aliquots of 150 µL were frozen in liquid nitrogen and stored at -80 ° C.

3.2.2.2. Plasmid transformation

The uptake of plasmid DNA by bacteria is known as plasmid transformation. The plasmid transformation is used for the expression of proteins or the replication of plasmids in bacteria (Richter, 2003).

For the plasmid transformation, 150 µL competent bacteria were gently mixed with 2 µL of the respective plasmid solution (~100 nmol/µL) and were treated with a heat shock at 42 °C for 1 min at 900 rpm (Thermomixer comfort, Eppendorf, Hamburg, GER). After addition of 500 µL LB-

medium, the bacteria were incubated at 37 °C for 1 h at 900 rpm (Thermomixer comfort, Eppendorf, Hamburg, GER) and plated on LB agar plates.

3.2.2.3. Heterologous expression of IM30 proteins

Bacteria of the *E. coli* BL21(DE3) strain were used for the heterologous expression of IM30. The bacteria were grown on a LB-agar plate (100 µg/mL ampicillin) for 16 h. For the protein expression, precultures of 50 ml LB-medium (100 µg/mL ampicillin) were inoculated by a single colony and incubated at 37 °C and 200 rpm (Multitron, Infors, Bottminger, CH) for 16 h. Afterwards, 2 L of LB-medium (100 µg/mL ampicillin) were inoculated by addition of the pre-cultures. The optical density at 600 nm (OD_{600}) was used to determine the *E. coli* cell density. The protein expression was inducted via addition of 0.5 mM isopropyl-ß-*D*-thiogalactopyranoside (IPTG) at OD_{600} of 0.6-0.8 to activate the *lac* promoter, which controls the gene coding for the T7-polymerase (which transcribes the *im30* gene). After 4 h, the bacteria were harvested by centrifugation at 2500 rpm for 10 min (Beckmann Avanti J-26 XP, rotor JLA 8.100). The bacteria were flash-frozen in liquid nitrogen and stored at - 20 °C until use.

3.2.3. Biochemical Methods

3.2.3.1. Purification of IM30 via IMAC

The His-tagged IM30 protein was purified via immobilized metal affinity chromatography (IMAC) using nickel-nitrilotriacetic acid (Ni-NTA)-agarose. After protein expression, the bacteria from 4 L expression culture were resuspended in 200 mL lysis buffer. The bacteria were sonicated on ice with a branson sonifier 250 at a duty cycle of 50% and an output control of 6. Cell debris was removed by centrifugation at 10000 rpm (Beckman Avanti J-26 XP, rotor JA 25.50) for 10 min at 4 °C. The supernatant was incubated with 8 mL Ni-NTA-agarose (Macherey-Nagel, Düren, GER) for 2 h with gentle agitation on a rotational shaker. Afterwards, the beads were transformed to 4 disposable columns (5 mL polypropylene columns, Thermo Fisher Scientific, Rockford, IL, USA) and were washed with each 200 mL of washing containing 20 mM, 50 mM or 100 mM imidazole, respectively. The protein was eluted with 5 x 1 mL elution buffer. Subsequently, the buffer was changed to 20 mM HEPES (pH 7.6) by dialysis or gelfiltration (Sephadex G25).

3.2.3.2. Dialysis

Dialysis is used to remove low molecular weight components from solutions through a semipermeable membrane. The membrane is characterized by the Molecular Weight Cut-Off (MWCO), which refers to the size of a molecule that is retained by the membrane to ~ 90% (Doonan, 1996). In this work, a cellulose membrane (MWCO of 14-18 kDa) was used to exchange the buffer after purification of IM30. Therefore, the protein solutions were dialyzed twice for 1 hour and once overnight against 1.5 L 20 mM HEPES (pH 7.6) each.

3.2.3.3. Size Exclusion Chromatography

Size Exclusion Chromatography (SEC), also known as gel filtration, is a technique to separate molecules of different sizes (Richter, 2003). In this work, SEC was used to analyze the oligomeric state of IM30. The size of IM30 oligomers was analyzed using an ÄKTA basic system (GE Healthcare, Munich, GER) with a Superose12 10/300 GL column (GE Healthcare, Munich, GER) equilibrated with 20 mM HEPES (pH 7.6) at 8 °C. Protein elution was followed via monitoring the absorbance at 280 nm. The column was calibrated using standards of known size (blue dextran >2000 kDa, ferritin (440 kDa), β-amylase (200 kDa), aldolase (158 kDa), conalbumin (75 kDa), ovalbumin (44 kDa), carbonic anhydrase (29 kDa) and cytochrome c oxidase (16.4 kDa).

3.2.3.4. Bradford Assay

The protein concentration of IM30 was determined with a Bradford assay (Bradford, 1976). The assay is based on a shift of the absorption maximum of the Coomassie brilliant blue G-250 dye upon binding to cationic and non-polar side chains of amino acid.

50 µL of the protein solution were incubated with 50 µL formic acid for 10 min at room temperature (RT). After addition of 900 µL Bradford-reagent (Bio-Rad, Munich, GER), the mixture was further incubated for 20 minutes at RT. Afterwards, the absorption of the Coomassie-dye at 595 nm was determined. The protein concentration was calculated by linear regression from a BSA standard curve.

3.2.3.5. Sucrose density gradient centrifugation

Sucrose density (SD) gradient centrifugation is a method to separate particles of a solution or suspension according to their density (Richter, 2003).

To analyze the binding of IM30 to DOPG liposomes at different Mg^{2+} concentrations, sucrose density gradient (SD) centrifugations were performed. All SD gradients were produced and fractionated using the Gradient Master Station (BioComp, Fredericton, CA). 160 µg DOPG liposomes (0.1 % NBD-DOPE) were incubated with 12 µg IM30 for 60 min at RT in 120 µL 20 mM HEPES, pH 7.6. The samples were loaded onto linear sucrose density gradients (5-50%) in 20 mM HEPES buffer (pH 7.6) containing 0, 2.5, 5, 7.5 or 10 mM $MgCl_2$ and centrifuged at 40000 rpm for 6 h at 25 °C followed by immediate fractionation. The individual fractions were analyzed by SDS-PAGE with subsequent immunoblot analysis to determine the protein distribution. The immunoblots were analyzed quantitatively by using the densitometric analysis of the program ImageJ (Rueden et al., 2017). The liposome distribution was analyzed via fluorescence spectroscopy detecting the lipid-coupled NBD fluorophore.

Binding of IM30 to *Synechocystis* membranes was analyzed at varying Mg^{2+} concentrations via SD centrifugation of *Synechocystis* cell lysates. Cells were grown under standard conditions (Fuhrmann et al., 2009b; Hennig et al., 2015). The cells were harvested in the midlog growth phase by centrifugation (5000 g, 10 min, 4 °C). The cells were resuspended in buffer (20 mM HEPES, pH 7.6, 150 mM NaCl, 5 mM $MgCl_2$, 5 mM $CaCl_2$) and disrupted in a homogenizer (SpeedMill PLUS, Analytik Jena, Jena, GER) using 0.5 mm glass beads. Cell debris and glass beads were removed by centrifugation (5000 g, 5 min, 4 °C). The cell lysate of 1 L culture (OD_{750} ~ 2) was split into multiple fractions. To detect the localization of endogenous IM30, the fractions of the lysate were mixed with Mg^{2+}-containing HEPES buffer to achieve final concentrations of up to 20 mM Mg^{2+}. As a control, HEPES buffer containing 20 mM EDTA was added to remove endogenous Mg^{2+}. The membrane fractions of the samples were isolated by ultracentrifugation (40000 rpm, 30 min, 4 °C). The supernatant was discarded, and the pellets were resuspended with buffer containing the respective amounts of Mg^{2+} and incubated for 30 min. Finally, the pellets were resuspended to a final concentration of 1 mg/mL chlorophyll and 68 % sucrose. The chlorophyll concentration was determined as described in (Porra et al., 1989) using methanol as a solvent. Membrane fractions containing 200 µg chlorophyll were loaded at the bottom of a linear 34 – 68 % sucrose gradient. Cell fractions were separated by centrifugation at 40000 rpm for 6 h at 4 °C, and the gradients were immediately fractioned afterward. The TM fraction was identified by measuring the chlorophyll concentration of all gradient fractions. The TM fractions were analyzed by SDS-PAGE and

immunoblotting using an anti-IM30 antiserum (Fuhrmann et al., 2009a). To compare the amounts of detected protein, the blots were subjected to densitometric analysis using ImageJ (Rueden et al., 2017).

3.2.3.6. SDS-PAGE

Sodium dodecyl sulfate–polyacrylamide gel electrophoresis (SDS-PAGE) is a method to separate proteins according to their molecular weight (Richter, 2003). In this work, the SDS-PAGE was used to analyze the purity of the IM30 protein solutions. The composition of the used discontinuous gels is listed in Table 3.2.3.

Table 3.2.3: Composition of two separation and stacking gels

	Separation Gel (12 %)	Stacking Gel (6 %)
Water	4.5 mL	3 mL
Acrylamide (40%)	3.0 mL	0.75 mL
Specific Buffer	2.5 mL	1.25 mL
APS (10%)	50 µL	25 µL
TEMED	20 µL	10 µL

8 µL of the sample were mixed with 2 µL of 5x SDS sample buffer and heated for 5 min at 95 ° C. The electrophoresis was performed for 45 min at 200 V in 1x SDS running buffer. To fix and stain the proteins, the gel was incubated on a horizontal shaker for 60 min in coomassie staining solution and afterwards for at least 60 min in coomassie destaining solution.

3.2.3.7. Western Blot

Western Blot is a method to identify proteins after transfer from an SDS-PAGE gel to a nitrocellulose membrane. The identification is based on the immunodetection by specific antibodies (Richter, 2003).

An SDS-PAGE was performed as described in 3.2.3.6. After this, the proteins were transferred to a nitrocellulose membrane by applying an electric field perpendicular to the gel using the Trans-Blot Turbo Transfer System (Bio-Rad, Munich, GER) for 30 min at 25 V. After incubation of the membrane with blocking buffer for 1 h, the membrane was washed with TBST-buffer for 5 min. The membrane was incubated with the primary antibody for 1h. After washing of the membrane (five times with

TBST-buffer for 5 min), the membrane was incubated with the secondary antibody for at least 1 h. After washing of the membrane, the blot was stained with ECL Prime Western Blotting Detection Reagent (GE Healthcare, Munich, GER) according to the manufacturer's instructions. The luminescence was detected using the detection system Stella (Raytest, Straubenhardt, GER).

The IM30 protein was specifically detected using an anti-IM30 antiserum as a primary antibody (dilution 1:1000 in TBST) (Fuhrmann et al., 2009a) and a horseradish peroxidase (HRP)-coupled anti-rabbit antibody (dilution 1:160000 in TBST, IgG HRP, Sigma Aldrich).

3.2.3.8. Liposome preparation

Liposomes were used as *in vitro* model membranes to study the interaction of IM30 with the TM. Depending on the application, the liposomes contained various TM lipids and lipid-coupled fluorophores as listed in Table 3.2.4.

Table 3.2.4: Lipids.

Notation	
PG	1,2-Dipalmytoyl-sn-glycero-3-phosphoglycerol
PC	1,2-Dipalmytoyl-sn-glycero-3-phosphocholin
PE	1,2-Dipalmytoyl-sn-glycero-3-phosphoethanolamine
MGDG	Monogalactosyldiacylglycerol
DGDG	Digalactosyldiacylglycerol
SQDG	Sulfoquinovosyldiacylglycerol
LissRhod-PE	1,2-Dioleoyl-sn-glycero-3-phosphoethanolamine-N-(lissamine rhodamine B sulfonyl)
NBD-PE	1,2-Dioleoyl-sn-glycero-3-phosphoethanolamine-N-(7-nitro-2-1,3-benzoxadiazol-4-yl)

Preparation of small unilamellar vesicles

Small unilamellar vesicles (SUVs) were used for SD gradient centrifugations, quartz crystal microbalance and fluorescence spectroscopy. First, the respective lipids were dissolved in chloroform. The organic solvent was evaporated under a gentle stream of nitrogen gas followed by overnight vacuum desiccation to remove any traces of solvent. Unilamellar liposomes were prepared by rehydration of the dried lipid film with the corresponding buffer and five cycles of freeze-thawing.

For the liposome fusion assay, the liposomes were instead extruded 15 times through a 100-nm filter, using an extruder from Avanti Polar Lipids, Inc. (Alabaster, AL, USA).

Preparation of giant unilamellar vesicles (GUVs)

Giant unilamellar vesicles (GUVs) were used to analyze binding of IM30 to membranes in presence and absence of Mg^{2+}. The GUVs were generated by gel-assisted swelling of a lipid film on a dried PVA-film (*polyvinylalcohol*, MW 145000 Da; Merck Millipore, Darmstadt, GER). 30 µl of a 1 % PVA-solution was heated to about 90 °C on a glass coverslip for 30 min. After cooling to RT, 3 µL of a 3 mM lipid solution (20 % DOPG, 80 % DOPC + 1:1000 Atto-633-DOPE, dissolved in chloroform) were spread on the PVA film and dried under a gentle stream of nitrogen. GUVs were formed by the addition of 200 µL of the corresponding swelling buffer. To analyze binding of IM30 to the GUVs, 20 mM HEPES buffer (pH 7.6) ± 5 mM $MgCl_2$ were used as swelling buffers. After 45 min, the GUVs were transferred to a new observation well, and 1 µM IM30-CFP was added carefully. GUVs were observed with a 20x objective using a Zeiss Axio Observer Z.1 fluorescence microscope with the Colibri 7 illumination module. The GUVs containing the Atto-633 fluorophore and the IM30-CFP proteins were detected using appropriate filters. The Zeiss ZEN software was used for image processing.

3.2.4. Biophysical Methods

3.2.4.1. Quartz Crystal Microbalance

Quartz Crystal Microbalance (QCM) is a technique to analyze binding of material to a coated quartz crystal by monitoring the change of frequency and damping of the quartz crystal resonator (Johannsmann et al., 2021).

For QCM measurements, only degassed buffers were used. QCM chips were cleaned with 30 mM EDTA, 2% SDS followed by 1 M NaOH. Then, the chip was rinsed with water and dried with nitrogen. Prior to the measurement, the chip was treated with an ozone plasma cleaner for 20 s to remove any organic contaminations. 50 µL of a liposome suspension (1 mM lipid, 80 % DOPC, 20 % DOPG (w/w)) was mixed with 450 µL 20 mM HEPES + 5 mM $CaCl_2$. A SiO_2-coated QCM chip (3T Analytik, Tuttlingen, GER) was calibrated with the QCM device (3T Analytik, Tuttlingen, GER). To produce an SLB on the SiO_2 surface, the chip was washed with HEPES buffer. Next, 150 µL of the liposome suspension was pumped on the chip (60 µL/min). After completion of the liposome spreading (*i.e.* when the frequency shift reached a constant level of about 90 Hz and negligible damping), the chip was washed again with HEPES buffer or HEPES buffer + 10 mM Mg^{2+}

(150+300 µL; 60 µL/min). To start the measurement, 150 µL IM30 wt (4.5 µM in HEPES buffer or in HEPES buffer + 10 mM Mg^{2+}) was pumped on the SLB (60 µL/min) and binding of the protein was monitored over ~3500 s.

3.2.4.2. Atomic Force Microscopy

Atomic Force Microscopy (AFM) is a non-optical imaging technique. The sample is scanned by an AFM tip attached to a cantilever in a raster pattern. By monitoring the deflection of the cantilever, a three-dimensional topographic image of the sample surface is generated (Pleshakova et al., 2018). In this work, AFM was used to visualize binding of IM30 to mica or to a solid supported bilayer (SSB).

All buffers and solutions were freshly prepared and filter sterilized (0.2 µm filter) before use. To visualize IM30-binding to lipid bilayers, freshly cleaved muscovite mica (12 mm diameter; Ted Pella Inc. grade V1) was mounted on a teflon disc (16 mm) and washed with 2x50 µL of adsorption buffer (20 mM HEPES pH 7.6, 20 mM Mg^{2+}) to remove soluble ions from the mica surface. Afterward, the buffer was incubated for 5 min at RT on the mica disc. Thereafter, 50 µL liposome suspension (5 mg/mL DOPG) was added to the adsorption buffer. The mixture was incubated for 20 to 30 min at RT. Care was taken to let the substrate surface never run dry. The mica surface was washed carefully with 1 mL imaging buffer (20 mM HEPES w/o 10 mM Mg^{2+}). A drop of 100 µL of imaging buffer was left on the mica. Then the sample was mounted under the AFM head. AFM measurements were carried out using a Nanowizard IV (JPK) in the QI mode (Quantitative imaging). An uncoated AC240TS probe (OMCL-AC240TS: L=240 µm, W=40 µm, k=2 N/m; f=70kHz, Olympus) with a 7 nm tip was used for scanning. The formation of a lipid bilayer was checked by force curve measurements and indicated by the typical break-through shape of the force curve (Loi et al., 2002). A total concentration of ~1.5 µM IM30 was achieved by adding small volumes (30 – 50 µL) directly on the lipid-coated mica surface mounted in the AFM. The sample was incubated at RT until the drift in the deflection signal decreased. Scanning was started with a minimal setpoint. Images were scanned with 256x256 or 512x512 px.

The resulting images were analyzed with GWYDDION version 2.56 (Nečas and Klapetek, 2012). The measured height-signal images were leveled by removing a polynomial background, and scan rows were aligned using the median height. The images were cropped to the area of interest, where necessary and the offset was removed. Particle dimensions were analyzed by marking them by a threshold, excluded membrane defects, particles spanning only one pixel, and subsequently the

particle parameters were exported via the analysis tool provided by GWYDDION. Statistical analysis was performed with the Mann-Whitney Rank Sum Test employing SigmaPlot (Systat Software Inc.).

To visualize IM30-binding to mica surfaces, 50 µL adsorption buffer (10 mM TRIS, 150 mM KCl, 25 mM $MgCl_2$, pH 7.6) was incubated on freshly cleaved muscovite mica (12 mm diameter; Ted Pella Inc. grade V1) for 5 min at RT. The mica substrate was washed two times with 50 µL of adsorption buffer. Then, 5 µL protein was added to a final concentration of ~0.5 µM. The protein was incubated on the substrate for 10 min at RT. Thereafter, the substrate was washed with ~1 mL imaging buffer (10 mM TRIS, 150 mM KCl, pH 7.6). The samples were imaged with a Multimode 8 AFM (Bruker) using uncoated silicon cantilevers. Measurements were carried out in PeakForce tapping mode in imaging buffer at ~25 °C. The force setpoint was set as low as possible, typically < 300 pN. Images were scanned with 512 × 512 px and 2 ms pixel time. The resulting images were analyzed with GWYDDION. The measured height-images were leveled by removing a polynomial background, and scan rows were aligned by fitting a second-degree polynomial and aligning the offsets of the substrate surface. The images were cropped to the area of interest.

3.2.4.3. Electron Microscopy

Electron microscopy (EM) can visualize biological structures at atomic resolution. The illumination source is a beam of accelerated electrons (Richter, 2003). In this work, the oligomeric structure of the IM30 protein was analyzed by a transmission electron microscope (TEM).

The samples were prepared by Dr. Wolfgang Gebauer. 5 uL of a sample (0.2 mg/mL protein solution) were pipetted onto a glow-discharged continuous carbon grid (30 s at 25 mA in an Emitech K100X glow discharge system (Quorum Technologies, Lewes, GB)). After one minute, the samples were washed with 3 × 20 µL H_2O, blotted on the edge of the grid with a filter paper, contrasted for 45 s with 5 µl of 2 % uranyl acetate staining solution, and then blotted dry on the edge of the grid with filter paper. The pictures were taken with an FEI Tecnai 12 electron microscope (acceleration voltage: 120 kV, CS = 6.3 mm; nominal magnification: 71,540×; nominal underfocus: 0.5–1.5 µm) on a TVIPS TemCam-F416 4 K CCD camera.

In a different cooperation, the negatively stained samples were prepared by Benedikt Junglas. 3 µL sample (0.2 mg/mL protein solution) was applied to a glow-discharged (PELCO easiGlow Glow Discharger, Ted Pella Inc, Redding, CA, USA) continuous carbon grid (CF-300 Cu, Electron Microscopy Sciences). The sample was incubated on the grid for 1 min. Then the grid was side-blotted on filter paper, washed with 3 µL water, stained with 3 µL 2 % uranyl acetate for 30 s and-

air dried. The grids were imaged with an FEI Talos L120C electron microscope (acceleration voltage: 120 kV) equipped with a CETA camera at a pixel size of 4.06 Å/pix at an underfocus of 1 to 2.5 µm.

3.2.4.4. Dynamic Light Scattering

Dynamic Light Scattering (DLS) is a method to analyze the size distribution profile of a particle solution/suspension (Falke and Betzel, 2019). At this technique, a laser beam is passed through a sample and the light scattering is monitored. Due to the brownian motion, the distance and orientation of the particles change over time. The natural diffusion leads to a fluctuation in the intensity of the light scattering, which occurs faster with small particles than with large particles. Mathematical methods such as autocorrelation or fourier transformation are used to calculate the diffusion coefficient from the particle velocity. Afterwards, the radius of the particles is calculated using the Stoke-Einstein relationship (1) (Falke and Betzel, 2019).

$$D = k_B \cdot T \cdot 6\pi \cdot \eta \cdot r \quad (1)$$

Here, D refers to the diffusion coefficient, k_B to the Boltzmann constant, T to the temperature, η to the viscosity of the solution and r to the particle radius.

In this work, DLS was used to analyze the size of different IM30 variants. The mean particle diameter of IM30 was determined in 20 mM HEPES buffer, pH 7.6. 100 µL samples, containing 0.1 mg/ml protein were incubated for 30 min at RT and measured at 25 °C at a scattering angle of 173° (Zetasizer ZS, Malvern, UK). Three individual samples were each measured three times for 10 s and analyzed using the manufacturer's software.

3.2.4.5. Circular dichroism spectroscopy

Circular dichroism (CD) is the differential absorption of circularly polarized light by optically active molecules. By measuring the absorption difference at different wavelengths, a CD spectrum is obtained that provides information about the stereochemistry of the chiral substances such as amino acids (Richter, 2003)

In the case of proteins, the individual spectra of the amino acids overlap to an overall spectrum. The secondary structure of proteins can be analyzed by CD spectroscopy, since the secondary structure elements such as α-helices or β-sheets are characterized by typical CD spectra (Kelly et al., 2005).

The molar CD value Δε is defined as (2).

$$\Delta\varepsilon(\lambda) = \frac{\Delta A(\lambda)}{l \cdot c} \quad (2)$$

ΔA refers to the difference of absorption, l to the optical path length and c to the sample concentration.

The CD value is often described as ellipticity θ.

$$\theta(\lambda) = 3298.2 \cdot \Delta\varepsilon(\lambda) \quad (3)$$

In this work, CD was used to determine the secondary structure of IM30. CD spectra were recorded with a JASCO- 815 CD spectrometer (JASCO Corporation, Tokyo, JPN) using 0.1 mg/mL IM30 in 10 mM HEPES buffer (pH 7.6). The spectra were recorded from 200 nm to 250 nm at 20 °C with a scan rate of 100 nm/min, 1 nm steps and 1 s data integration time using quartz crystal suprasil cuvettes (1 mm; Hellma Analytics, Jena, GER). For each sample, three spectra were averaged and smoothed by the JASCO software package (Savitzky-Golay filter), if necessary.

Thermal stability of IM30 (0.1 mg/mL) was determined via CD spectroscopy (JASCO-815 CD spectrometer with an MPTC-490S temperature-controlled cell holder) with an overall heating rate of 0.27 °C/min (Heidrich et al., 2018). The thermal transition was determined via monitoring the ellipticity at 222 nm (θ). To analyze protein folding, the melting curve was fitted with an adapted Boltzmann-Fit that allows a linear slope in the first plateau region of the curve (4).

$$\theta_{meas}(T) = \frac{\left(T \cdot m_N + \theta_N\right) - \theta_D}{1 + e^{\frac{T-T_m}{dT}}} + \theta_D \quad (4)$$

Here, θ_N and θ_D refer to the molar ellipticity of the native or denatured state at 222 nm. m_N refers to the slope of the initial plateau. T_m refers to the transition point of the denaturation curve.

3.2.4.6. Laurdan fluorescence spectroscopy

Fluorescence is the emission of light after the excitation of chromophoric molecule. Due to relaxation processes, the emitted light is red-shifted compared to the excitation light (Richter, 2003).

Here, the dipolar relaxation/stokes shift of Laurdan (6-dodecanoyl-*N*,*N*-dimethyl-2-naphthylamine) was used to analyze binding of IM30 to membranes. Laurdan is a fluorescent dye that incorporates into lipid bilayers. Its fluorescence is sensitive to changes of the polarity of the environment and is therefore used to report changes of the membrane fluidity. Since polar solvent molecules as H_2O

decrease the excited state of Laurdan by antiparallel alignment of their dipole moment, the emitted light is red-shifted in environments with high polarity (Parasassi et al., 1990).

In order to quantify the spectral changes, the Generalized Polarization (GP) value defined by Parasassi was calculated for each spectrum.

$$GP = \frac{I_{440} - I_{490}}{I_{440} + I_{490}} \quad (5)$$

Here, I_{440} and I_{490} are the fluorescence emission intensities at 440 and 490 nm, respectively.

Laurdan (Sigma, Taufkirchen, GER) was added to the dissolved lipids in a molar ratio of 1:500. Unilamellar liposomes were prepared as described in 3.2.3.8. To analyze the binding of IM30 to the liposomes, 0 - 6 µM IM30 and 0.1 mM liposomes in 20 mM HEPES were mixed and incubated for 30 min in the dark at 25 °C. The fluorescence emission spectra were recorded using a Fluoromax-4 spectrometer (Horiba Scientific, Kyoto, JPN) from 400 to 550 nm with excitation at 350 nm at 25 °C. Quartz crystal suprasil cuvettes (3 mm; Hellma Analytics, Jena, GER) were used and the excitation and emission slit width was set to 4 nm.

The membrane binding affinity of IM30 was calculated by the binding fit (6) (Heidrich et al., 2016).

$$GP = GP_{min} + \frac{\Delta GP}{1 + \frac{K_D}{c_{IM30}}} \quad (6)$$

3.2.4.7. ANS fluorescence spectroscopy

The surface polarity of IM30 was analyzed using the fluorescent dye 8-anilinonaphthalene-1-sulfonic acid (ANS). ANS can bind to both hydrophobic and hydrophilic areas of proteins. The fluorescence intensity increases strongly in a non-polar environment compared to polar solvents. Additionally, the emission maximum of 500 nm is blue-shifted (LaPorte et al., 1980). Here, ANS spectroscopy was used to analyze the surface hydrophobicity of IM30 in absence and presence of Mg^{2+}.

For the measurements, 1 µM IM30 was mixed with 7.5 µM ANS (Sigma-Aldrich, Munich, GER) in 20 mM HEPES buffer (pH 7.6). The samples were incubated in the dark for at 15 min at RT. After addition of 7.5 mM Mg^{2+}, the samples were further incubated for 30 min at RT in the dark. The measurements were performed using a Fluoromax-4 spectrometer (Horiba Scientific, Kyoto, JPN) and quartz crystal suprasil cuvettes (3 mm; Hellma Analytics, Jena, GER). The excitation wavelength was 370 nm (slit widths 4 nm), the emission wavelength ranged from 400 to 650 nm (slit widths 4 nm). Fluorescence intensities of three independent measurements were averaged and the spectra of ANS in the respective buffer in absence of the protein were subtracted.

3.2.4.8. Tryptophan fluorescence spectroscopy

Tryptophan, phenylalanine and tyrosine are fluorescent amino acids. The fluorescence of a protein is mainly attributed to tryptophan, since it has the highest quantum yield. The fluorescence of tryptophan is sensitive to the polarity of the environment. When e.g. exposed to a hydrophobic environment, the tryptophan spectrum is blue-shifted and the fluorescence intensity is increased (Hellmann and Schneider, 2019).

To analyze the change of the tryptophan spectrum, the spectral center of mass <λ> was analyzed, which includes changes of the emission maximum, but also the spectral shape (Royer et al., 1993).

$$<\lambda> = \frac{\sum \lambda \cdot I}{\sum I} \tag{7}$$

Here, λ refers to the wavelength and I refers to the fluorescence intensity.

For the measurements, 1.6 µM IM30 in 200 µL HEPES (20 mM, pH 7.6) were incubated for 30 min at 25 °C. Tryptophan fluorescence spectra were recorded at 25 °C from 300 to 450 nm (slit width 5 nm) upon excitation at 280 nm (slit width 5 nm) using quartz crystal suprasil cuvettes (3 mm; Hellma Analytics, Jena, GER). The measurements were performed using a Fluoromax-4 spectrometer (Horiba Scientific, Kyoto, JPN).

3.2.4.9. Membrane fusion assay

Membrane fusion of MGDG/DOPG liposomes was measured using a Förster resonance energy transfer (FRET)-based assay (Hennig et al., 2015). To do so, unlabeled liposomes were mixed in 10-fold excess with labeled liposomes containing the lipid-coupled FRET dyes NBD and Liss-Rhod. Upon fusion of labeled with unlabeled liposomes, the dyes redistribute over the membrane by lateral diffusion. The consequently decreasing FRET is measured as increasing donor emission intensity. As a positive control, liposomes containing only a 10^{th} of the fluorescently labeled lipids were used to simulate complete membrane fusion.

IM30 was preincubated with Mg^{2+} for ~ 5 min. After addition of the MGDG/DOPG (40/60 %) liposomes, the measurement was immediately started. The final concentrations were 2.5 µM IM30, 7.5 mM Mg^{2+} and 0.1 mM lipid. All components were dissolved in 20 mM HEPES (pH 7.6). The measurements were performed for 1000 s at 25 °C using a Fluoromax-4 spectrometer (Horiba Scientific, Kyoto, JPN). The slit widths were set to 5 nm for excitation at 460 and emission at 535

nm. The raw fluorescence data was converted to a fusion rate by equation 2 using the intensities of the negative control (I_0), the positive control (I_M) and the measured sample (I) at each time point t.

$$NBD\ fluorescence\ (t) = \frac{I_t - I_{t,0}}{I_{t,M} - I_{t,0}} \quad (8)$$

The initial fusion rate was determined by the slope of the fusion curve over the first 50 s.

4. Results and Discussion

4.1. GTP hydrolysis by *Synechocystis* IM30 does not decisively affect its membrane remodeling activity

4.1.1. Publication

Junglas B. [#], Siebenaller C. [#], Schlösser L., Hellmann N. and Schneider, D. (2020) GTP hydrolysis by Synechocystis IM30 does not decisively affect its membrane remodeling activity, Sci. Rep. 10, 9793

The author affiliations are listed in chapter VII.

The study has been originally published in *Scientific reports* (Appendix VIII.2) (Junglas et al., 2020c). The author contributions according to the *CRediT taxonomy* (Allen et al., 2014) are listed in Table 4.1.1.

Table 4.1.1: Author contributions to *GTP hydrolysis by Synechocystis IM30 does not decisively affect its membrane remodeling activity*

Study conception	Complete study	**CS**, BJ, NH, DS
Writing	Complete study	**CS**, BJ, NH, DS
Supervision, Project administration, Funding acquisition, Resources	Complete study	NH, DS
Figures (numbers refer to the original publication)	**Methodology, Investigation, Formal analysis**	**Data visualization**
Fig. 1 A, B	BJ, LS	**CS**, BJ
Fig. 1 C-F	BJ	**CS**, BJ
Fig. 2 A, B	BJ	**CS**, BJ
Fig. 3 A	BJ, LS	**CS**, BJ
Fig. 3 B	BJ	**CS**, BJ
Fig. 3 C	BJ, NH	**CS**, BJ
Fig. 4 A-C	**CS**	**CS**, BJ
Fig. 5 A, B	**CS**	**CS**, BJ
Fig. S1	BJ, LS	**CS**, BJ
Fig. S2	**CS**	**CS**, BJ
Fig. S3 A-D	BJ, NH	**CS**, BJ, NH
Fig. S4 A-D	BJ, NH	**CS**, BJ, NH

[#] These authors contributed equally.

4.1.2. Summary

The physiological function of IM30 in cyanobacteria and chloroplasts is under debate since more than 15 years. While the significance of IM30 for TM biogenesis and/or maintenance is generally acknowledged, diverse specific functions have been suggested, including lipid transport, protein complex formation or membrane remodeling (Zhang and Sakamoto, 2013; Heidrich et al., 2017; Siebenaller et al., 2019).

IM30 shares certain features with other membrane-active proteins such as dynamin-like proteins (Jilly et al., 2018), since it is likely involved in membrane fusion and protection/stabilization and oligomerizes into higher-ordered structures (Fuhrmann et al., 2009b; Hennig et al., 2015; Zhang and Sakamoto, 2015; Saur et al., 2017). As membrane remodeling is often associated with nucleotide hydrolysis (McNew et al., 2013), it was not unreasonable to suspect a nucleotide hydrolyzing activity for IM30. Indeed, in 2018, a GTPase activity of IM30 of *Arabidopsis thaliana* was revealed *in vitro*, albeit IM30 shows no further classical GTPase features, such as a G-domain, suggesting that IM30 belongs to a new class of membrane-remodeling GTPases (Ohnishi et al., 2018). Still, all membrane-related functions of IM30 have been observed before in absence of nucleotides, giving rise to the question if and how GTP binding/hydrolysis actually affects the activity of IM30.

In the project part "GTP hydrolysis by *Synechocystis* IM30 does not decisively affect its membrane remodeling activity" it has been investigated whether the observed GTPase activity is conserved also in IM30 of *Synechocystis*. It has been shown that also *Synechocystis* IM30 hydrolyzes GTP followed by the release of phosphate. Yet, Mg^{2+} appears not to be essential for GTP hydrolysis. Furthermore, the IM30 GTPase activity has no decisive influence on membrane interaction of IM30. Consequently, the GTP hydrolyzing activity appears not to be essential for IM30´s membrane remodeling function.

4.1.2.1. IM30 has GTP hydrolyzing activity in presence and absence of Mg^{2+}

The potential GTPase activity of the cyanobacterial IM30 was analyzed using different assays based on either the detection of inorganic phosphate (P_i) or GTP, respectively.

The malachite green assay, which was also used for the analysis of *Arabidopsis* IM30 (Ohnishi et al., 2018), and a fluorescence-based, continuous phosphate release assay (Brune et al., 1994) are both based on the detection of P_i, which is released upon GTP hydrolysis. In presence of 2.5 mM Mg^{2+}, *Synechocystis* IM30 showed a rather low GTPase activity. Using the Hill-equation, the k_{cat} of 2.16 ± 0.33 min^{-1} was determined in the malachite green assay, which is e.g. similar to the k_{cat} of

dynamin in absence of membranes (k_{cat} 2.60 ± 0.98 min^{-1}) (Song et al., 2004). But in contrast to dynamin, the GTPase activity of IM30 did not increase in presence of lipid membranes. Furthermore, a K_M of 0.65 ± 0.14 mM and a Hill coefficient of 1.29 ± 0.14 mM were determined. In contrast to other GTPases, such as dynamins (K_D ~0.5-5 µM), or GTPases from the *ras* superfamily (subnanomolar K_D), the affinity of IM30 for GTP is rather weak (Shan et al., 2009). The GTPase activity of IM30 could be modulated by the addition of the non-hydrolyzable GTP analog GMP-PCP. In presence of GMP-PCP, the analysis revealed strong cooperativity (Hill coefficient n = 5.19 ± 3.64), potentially involving more than 4 binding sites. Still, the data do not allow to distinguish between allosteric and competitive inhibition. Since the analysis of the malachite green assay is based on an average of the experimental time and does not account e.g. for substrate limitation or inhibition, a continuous phosphate release assay was used to determine the kinetics of P_i release. The analysis revealed a k_{cat} of approximately 0.0179 ± 0.02 min^{-1}, taking into account the necessary experimental conditions of 0.1 µM IM30 and 10 µM GTP, which results in the very low saturation level of IM30 of about 0.5 %.

The results were further supported by a luciferase-coupled GTPase assay, which directly depends on the GTP concentration. The results show that the before measured P_i release indeed originates from GTP hydrolysis and not from a release of P_i that was initially bound to IM30. Noteworthy, using an established enzyme-coupled GTPase assay, including Pyruvate Kinase (PK) and Lactic Dehydrogenase (LDH) (Ingerman and Nunnari, 2005), no GTP hydrolyzing activity of IM30 was detected. This might be caused by an inhibition of any reaction step of the assay by IM30 or by a very slow k_{off} rate. Nevertheless, IM30 clearly showed GTP-hydrolyzing activity in all other assays.

Surprisingly, the GTPase activity of IM30 was not Mg^{2+}-dependent, which is rather uncommon for classical GTPases. In case of other Mg^{2+}-independent GTPases, such as FtsZ or the Rho family, the presence of Mg^{2+} does at least strongly increase the GTPase activity (De Boer et al., 1992; Zhang et al., 2000), which was not observed for IM30-mediated GTP hydrolysis. Still, increased cooperativity was observed in presence of Mg^{2+}, which may be explained by the alteration of the oligomeric structure of IM30 induced by Mg^{2+}-binding (Heidrich et al., 2018).

4.1.2.2. GTP hydrolysis depends on the oligomeric state of IM30

The first α-helix of IM30 was claimed to be essential for the GTPase activity of IM30, since its deletion in *Arabidopsis* IM30 resulted in the loss of the GTP hydrolyzing activity (Ohnishi et al., 2018). Noteworthy, this deletion also results in disassembly of the IM30 ring/rod-like structure in case of *Arabidopsis* IM30 (Otters et al., 2013; Ohnishi et al., 2018), but not in case of IM30 from

Synechocystis or *Chlamydomonas* (Gao et al., 2015; Thurotte and Schneider, 2019). When the truncated IM30 variant lacking helix 1 (IM30 H27) was analyzed using the malachite green assay, GTPase activity was still observed. This implies that not specifically helix 1 is crucial for the GTPase activity, but likely the oligomeric structure. This assumption was supported by analysis of the IM30 mutant IM30*, which was shown to only form smaller oligomers instead of ring/rod structures (Heidrich et al., 2016) and was not able to hydrolyze GTP. A species-dependent difference of this aspect seems unlikely, as a conserved function of the IM30 helices can be assumed. IM30 does not contain any currently known GTP binding sites, such as a G-domain or P-loop motif, respectively. While other proteins, such as Tubulin or FtsZ, also miss a P-loop motif, they still have a highly conserved nucleotide binding site (Nogales et al., 1998; Wittinghofer and Vetter, 2011), which cannot be found within the IM30 sequence. The observations from this publication suggested that the putative GTP binding sites are localized between adjacent IM30 monomers/smaller oligomers in the intact ring structure. This idea is now supported by the recently published IM30 structure, where an ADP-molecule was found stably bound between the layers 1 and 2 of the ring (Gupta et al., 2021). The GTP binding site of IM30 is novel, and the furthermore missing typical Mg^{2+}-dependency of canonical GTPases suggests that IM30 may found a new class of GTPases (Ohnishi et al., 2018).

4.1.2.3. GTP binding and/or hydrolysis do not critically affect IM30-mediated membrane remodeling

After showing that also *Synechocystis* IM30 has a GTPase activity, the impact of GTP hydrolysis on the activity of IM30 was studied. The physiological function of IM30 is not clear yet, but in *in vitro* experiments it has clearly been shown that IM30 binds to negatively charged membranes, which can result in membrane fusion at specific conditions (Hennig et al., 2015; McDonald et al., 2015; Heidrich et al., 2016). Since membrane remodeling is often accompanied by nucleotide hydrolysis (McNew et al., 2013), the influence of GTP hydrolysis on the membrane interactions of IM30 was analyzed next.

In absence of Mg^{2+}, IM30 binds to negatively charged membranes, which can be monitored via Laurdan fluorescence spectroscopy (Hennig et al., 2015; Heidrich et al., 2016). The fluorescence emission of the membrane-integrating dye Laurdan is sensitive to the polarity of the environment and therefore reflects e.g. changes in the lipid order (Parasassi et al., 1998), which are discussed to be induced by IM30 (Heidrich et al., 2016). The Laurdan fluorophore was incorporated into liposomes (PG, 100 %) and incubated with the nucleotides GTP or GDP and/or IM30. The experiment showed already minor changes even in absence of IM30, indicating some interaction of the

nucleotides with the liposomes. Nevertheless, the observed changes in presence of IM30 were considerably larger, allowing to analyze the impact of the nucleotides on IM30 membrane binding. Here, no significant changes were observed, showing that GTP binding/hydrolysis does not affect IM30 membrane binding, at least in absence of Mg^{2+}.

Mg^{2+} directly interacts with both PG membranes (Mondal Roy and Sarkar, 2011) and IM30 (Heidrich et al., 2018). In presence of Mg^{2+}, IM30 mediates membrane fusion of TM model membranes (PG/MGDG, 40 %/60 %). Consequently, the influence of GTP binding/hydrolysis on IM30 membrane binding cannot be analyzed completely independent from side-effects caused by membrane fusion. The impact of GTP binding and/or hydrolysis on the IM30 membrane fusion activity was analyzed using a FRET-based liposome fusion assay (Hennig et al., 2015). Here, no major changes of the initial fusion rate were observed, albeit the kinetics were marginally altered. While the fusion rates slightly increased in presence of GTP, the rate decreased to some extent in presence of GDP.

Noteworthy, the analysis of the fusion assay results was challenging, since the fusion process involves multiple equilibria between IM30, Mg^{2+}, liposomes and nucleotides, which are constantly changing during the membrane fusion process. The concentration of Mg^{2+} was experimentally adjusted, as GTP and GDP both bind Mg^{2+}, yet to different extents (Rudack et al., 2012), and consequently lowered the effective free Mg^{2+} concentration. The analysis might thus be biased by this experimental approach and must be taken with caution, since the Mg^{2+} concentration is crucial in the membrane fusion process (Hennig et al., 2015). Additionally, a direct impact of the nucleotides on the lipid bilayer structure was not considered in the analysis. While direct binding of nucleotides to DOPC membranes has already been observed, the nucleotide-membrane interaction could also be mediated by Mg^{2+} bridging the negatively charged PG headgroups and the phosphate groups of the nucleotides, as e.g. discussed in case of DNA-membrane interactions (Liang et al., 2005; Antipina and Gurtovenko, 2016). Taking all these considerations into account, the observed small differences of the membrane fusion kinetics rather hint for a minor influence of GTP binding and/or hydrolysis on IM30-mediated membrane fusion.

The results suggest that GTP binding/hydrolysis by IM30 likely is no key regulator of IM30´s membrane binding and membrane fusion activity, since it neither abolishes nor exclusively triggers membrane interactions. This is perfectly in line with various previous results, since nucleotides were never present in any study analyzing membrane interaction of IM30 (Otters et al., 2013; Hennig et al., 2015; McDonald et al., 2015; Heidrich et al., 2016; Hennig et al., 2017; McDonald et al., 2017; Heidrich et al., 2018). Based on the observed small effects on the fusion kinetics, a modulating effect

of the fusion process cannot be excluded, but may also be caused by the discussed experimental complications.

Taken together, *Synechocystis* IM30 clearly showed GTPase activity *in vitro*. Yet, IM30 differs from typical GTPases, since it misses a known nucleotide binding site and is independent of Mg^{2+}. The results of this study show no impact of GTP binding and hydrolysis on membrane interaction of IM30, at least *in vitro,* and the physiological relevance of this function remains to be shown.

4.2. Binding and/or hydrolysis of purine-based nucleotides is not required for IM30 ring formation

4.2.1. Publication

Siebenaller C., Schlösser, L., Junglas B., Schmidt-Dengler M., Jacob D., Hellmann N., Sachse C., Helm M. and Schneider D. (2021) Binding and/or hydrolysis of purine-based nucleotides is not required for IM30 ring formation, FEBS Letters, 595(14), 1876-1885.

The author affiliations are listed in chapter VII.

The study has been originally published in *FEBS Letters* (Appendix VIII.3) (Siebenaller et al., 2021). The author contributions according to the *CRediT taxonomy* (Allen et al., 2014) are listed in Table 4.2.1.

Table 4.2.1: Author contributions of *Binding and/or hydrolysis of purine-based nucleotides is not required for IM30 ring formation*

Study conception	Complete study	**CSi**, NH, MH, CSa, DS
Writing	Complete study	**CSi**, DJ, BJ, DS
Supervision, Project administration, Funding acquisition, Resources	Protein characterization Nucleotide analysis Electron Microscopy	NH, DS MH CSa
Figures (numbers refer to the original publication)	**Methodology, Investigation, Formal analysis**	**Data visualization**
Fig. 1 A	**CSi**, LS	**CSi**, LS
Fig. 1 B	LS, BJ	**CSi**, LS
Fig. 2 A, B	**CSi**, SM, DJ	**CSi**
Fig. 2 C	**CSi**, BJ	**CSi**, BJ
Fig. 3 A	**CSi**, LS	**CSi**
Fig. 3 B	**CSi**, LS	**CSi**
Fig. 3 C	**CSi**, BJ	**CSi**, BJ
Fig. S1	**CSi**, SM, DJ	**CSi**
Fig. S2	LS	**CSi**, LS

4.2.2. Summary

GTP hydrolyzing activity has been suggested as a function of IM30 as shown in chapter 4.1. (Ohnishi et al., 2018; Junglas et al., 2020c). Noteworthy, the IM30 protein does not contain any canonical domains or motifs involved in GTP-binding, and GTP-binding/hydrolysis does not seem to regulate IM30 membrane interactions decisively (Junglas et al., 2020c, chapter 4.1).

The formation of homo-oligomeric ring/rod structures with masses >1 MDa is a characteristic feature of PspA/IM30 family members (reviewed in Siebenaller et al., 2019). While the height of IM30 rings is constant, diameters of 22-35 nm are observed caused by varying rotational symmetries (Saur et al., 2017; Gupta et al., 2021; Junglas et al., 2021; Liu et al., 2021). The high-resolution cryo-EM analyses show that the mainly α-helical monomers are arranged horizontally and form interwoven ring layers. Between the first and the second layer of the IM30 ring, a stably bound ADP molecule was detected. Based on this, it has been suggested that the formation of IM30 rings budding off from membrane surfaces requires ATP-binding and/or hydrolysis (Gupta et al., 2021).

To address this suggestion, the study analyzed whether GTP-binding/hydrolysis affects the formation of IM30 rings. The results show that *Synechocystis* IM30 rings self-assemble in absence of any nucleotides, suggesting that nucleotide binding and/or hydrolysis is not required for ring formation. Furthermore, the study demonstrates that IM30 is actually an NTPase that hydrolyzes the purine-based nucleotides ATP and GTP with similar rates, but not the pyrimidine-based CTP and UTP.

4.2.2.1. IM30 hydrolyzes purine-based, but not pyrimidine-based nucleotides

The specificity of the NTP-hydrolyzing activity of purified IM30 was analyzed *in vitro* using a well-established malachite green-based assay. While the purine-based nucleotides GTP and ATP were hydrolyzed to a similar extent, the pyrimidine-based nucleotides CTP and UTP were only slightly hydrolyzed (Fig. 1). This shows that IM30 is actually not a GTPase, but an NTPase, which specifically hydrolyzes purine-based nucleotides. The results are perfectly in line with the recently observed ADP bound to IM30 rings and the originally observed GTPase activity (Junglas et al., 2020c (chapter 4.1); Gupta et al., 2021; McCullough and Sundquist, 2020). While thus far solely the interaction of the nucleotide´s phosphate groups with IM30 side chains was discussed to be involved in nucleotide binding, the results here imply that also interactions of the nucleotide bases are crucial. Consequently, the nucleotide binding pocket appears to be specific for the larger purine-heterocycle of NTPs.

Still, the NTPase activity of IM30 is unusual. A substrate promiscuity has also been observed for other ATP/GTPases, such as the predicted GTP-binding protein HflX or YchF, but is rather uncommon (Dutta et al., 2009; Cheung et al., 2016). It is discussed that during evolution, the GTPase activity has switched to an ATPase activity in some cases (Leipe et al., 2002; Leipe et al., 2004). Still, in contrast to IM30, these proteins contain canonical nucleotide binding motifs in their sequence. The GTP-binding affinity and GTPase activity of IM30 is relatively low when compared to other GTP-hydrolyzing enzymes (Junglas et al., 2020c, chapter 4.1). The low activity could be explained by a very slow k_{off} rate for ADP and GDP from the IM30 binding pocket. This seems in line with the in the IM30 cryo-EM structure identified stably bound ADP (Gupta et al., 2021), and explains why no free GDP could be detected in the enzyme-coupled GTPase assay described in chapter 4.1. (Junglas et al., 2020c).

4.2.2.2. IM30 nucleotide binding is not required for IM30 ring formation

The structural analysis of IM30, in which the ADP molecule was detected, was performed with a protein that was incubated with ATP-containing solutions during the protein purification (Gupta et al., 2021). In this study, it was first analyzed by LC-MS whether IM30 purified without an ATP-including washing step contains any nucleotides, which could originate from the *E. coli* cells used for protein expression. Here, no nucleotides were observed (Fig. 2 A, B). Next, it was analyzed by EM whether the nucleotide-free IM30 still forms ring/rod structures (Fig. 2 C). Since this was the case, it was concluded that nucleotide binding is not essential for the stabilization of the ring structure.

As the IM30 ring formation might already take place in *E. coli* during protein expression, these observations do not completely exclude that nucleotide binding could be a crucial step triggering ring formation. Still, IM30 likely forms a monomer or lower-ordered oligomer during the purification (Saur et al., 2017), and the monomers/oligomers are partially unfolded when not organized as a ring (Junglas et al., 2020b). Furthermore, the N-terminally fused chitin-binding domain, which was used in Gupta *et al.* for protein purification, likely prevents ring formation prior to removal of the fusion domain (Gupta et al., 2021).

Nevertheless, the structure of IM30, which was completely denatured during the first purification steps was next further analyzed using CD-spectroscopy (Fig. 3 A). Noteworthy, due to denaturation any potential nucleotide binding sites are likely not properly formed. The complete absence of nucleotides in the purified protein sample was confirmed via LC/MS analysis (Fig. S1). Since the

overall secondary structure of IM30 purified under denaturing conditions did not differ after refolding from IM30 purified under native conditions (Fig. 3 A), the protein seems to correctly refold. Since smaller IM30 oligomers are partially unfolded (Junglas et al., 2020b), this is a first hint for ring formation. This was supported by SEC, where only high molecular weight oligomers were detected (Fig. 3 B). Using EM, it was finally shown that nucleotide-free IM30 still forms the prototypical ring and rod structures (Fig. 3 C).

Consequently, IM30 unambiguously self-assembles into ring structures without nucleotide binding and/or hydrolysis.

The ADP observed in the cryo-EM structure likely originates from the ATP-including washing step applied during protein purification (Gupta et al., 2021). The ADP molecule was only detected between the first and the second layer of the ring, where the monomers have a somewhat distorted structure due to the basket-like ring structure (Gupta et al., 2021). This suggests that nucleotide binding might cause a distortion of the IM30 structure, and/or ATP/GTP bind only to slightly distorted IM30 structures. In fact, PspA rods, which were purified under denaturing conditions, looked even more regular than PspA purified under native conditions (Junglas et al., 2021). Since minor structural changes of IM30 cannot be excluded, it was next analyzed whether *in vitro* refolded IM30 still has nucleotide hydrolyzing activity. Here, no measurable ATP or GTP hydrolysis was observed (Fig. S2), which might be caused by minor changes of the IM30 structure close to the putative ADP binding site. As the NTPase-inactive proteins are neither overall misfolded (Fig. 3 A), nor have impaired oligomerization/ring formation (Fig. 3 B, C), the relevance of nucleotide binding for the IM30 structure appears to be low.

In vivo, nucleotide hydrolysis can only be relevant when an IM30 ring has already formed, since the nucleotide binding site involves three adjacent IM30 monomers within the ring structure (Gupta et al., 2021). In line with this, oligomerization-impaired mutants were shown to not hydrolyze GTP at all in chapter 4.1 (Junglas et al., 2020c). Since IM30 rings dissociate on the membrane (Junglas et al., 2020b), the idea that ring formation is initiated on the membrane by ATP/GTP appears to be rather unlikely. Moreover, the thermal stability of IM30´s secondary structure was shown to be decreased in presence of GTP (chapter 4.1, Junglas et al., 2020c), which does not support the idea of ring stabilization by nucleotide binding.

Since this study showed that nucleotide binding/hydrolysis is not relevant for IM30 ring formation, and the previous results suggest that it is not relevant for membrane remodeling *in vitro* (Junglas et al., 2020c, chapter 4.1.), the results suggest that nucleotide hydrolysis by IM30 does not significantly affect the *in vivo* function of IM30.

4.3. Proton leakage is sensed by IM30 and activates IM30-triggered Membrane Fusion

4.3.1. Publication

Siebenaller C. [#]*, Junglas B.*[#]*; Lehmann A., Hellmann N. and Schneider D. (2020) Proton Leakage Is Sensed by IM30 and Activates IM30-Triggered Membrane Fusion,* Int. J. Mol. Sci. 21*(12), 4530*

# These authors contributed equally.

The author affiliations are listed in chapter VII.

The study belongs to the Special Issue *Membrane Fusion 2.0* of the *International Journal of Molecular Sciences* (Appendix VIII.4) (Siebenaller et al., 2020). The author contributions according to the *CRediT taxonomy* (Allen et al., 2014) are listed in Table 4.3.1.

Table 4.3.1: Author contributions to *Proton Leakage Is Sensed by IM30 and Activates IM30-Triggered Membrane Fusion*

Study conception	Complete study	**CS**, BJ, NH, DS
Writing	Complete study	**CS**, BJ, NH, DS
Supervision, Project administration, Funding acquisition, Resources	Complete study	NH, DS
Figures (numbers refer to the original publication)	**Methodology, Investigation, Formal analysis**	**Data visualization**
Fig. 1 A-D	BJ	**CS**, BJ
Fig. 2 A, B	BJ	**CS**, BJ
Fig. 2 C, D	**CS**	**CS**
Fig. 3	BJ	**CS**, BJ
Fig. 4 A, B	BJ, AL	**CS**, BJ
Fig. 5 A, B	**CS**	**CS**
Fig. S1	BJ	**CS**, BJ
Fig. S2	**CS**	**CS**
Fig. S3	BJ, AL	**CS**, BJ
Fig. S4	**CS**	**CS**

[#] These authors contributed equally.

4.3.2. Summary

IM30 is essential for the development and/or maintenance of TMs in oxygenic photosynthetic organisms, involving plants, cyanobacteria and algae (Vothknecht et al., 2012). It is localized in the cyanobacterial cytoplasm or the chloroplast stroma, respectively, as well as at the TMs and the CM or chloroplast inner envelope, respectively (Li et al., 1994; Fuhrmann et al., 2009a). IM30 is discussed to have at least a dual function, i.e. membrane protection/stabilization and membrane remodeling (Heidrich et al., 2017; Siebenaller et al., 2019).

The membrane-remodeling activity appears to be specific for photosynthetic organisms. Membrane remodeling includes membrane fusion events, and IM30 indeed induces the fusion of TM model membranes *in vitro* upon activation by Mg^{2+}-binding (Hennig et al., 2015; Heidrich et al., 2018; Thurotte and Schneider, 2019). Consequently, IM30 could be involved in the continuous rearrangement of the TM system *in vivo*, e.g. in order to adapt to changing light conditions, which regulate the cytoplasmic/stromal Mg^{2+}-concentration (Chuartzman et al., 2008; Nagy et al., 2011; Nestler et al., 2012; Liberton et al., 2013a; Pohland and Schneider, 2019). The membrane protective/stabilizing function is conserved in the IM30/PspA protein family (Thurotte et al., 2017). PspA is known to stabilize membranes of Gram-negative bacteria to maintain the proton motive force (PMF) (Kleerebezem et al., 1996; Kobayashi et al., 2007; Joly et al., 2010). In cyanobacteria and chloroplast, maintaining the electrochemical gradient across the TM is of special importance, since the ΔpH is used for ATP production (Belkin et al., 1987). The TM is prone to oxidative damage, especially in curvature-stressed TM regions (Foyer, 2018; Junglas and Schneider, 2018). In recent *in vivo* studies, IM30 was found to localize preferentially at highly curved TM regions under high light-stress, likely forming protective IM30 assemblies (Thurotte et al., 2017; Gutu et al., 2018; Junglas and Schneider, 2018). As these regions bear the risk of protons leaking out of the acidified TM lumen, IM30 is potentially exposed to a lower pH at these regions. While all previous studies were performed at a pH of ~7.6, essentially nothing is known about the IM30 structure and function at acidic conditions.

In this study it is demonstrated that the IM30 structure differs at a mildly acidic pH of ~ 5 from the structure observed at pH 7.6, and that membrane binding and membrane fusion are enhanced at pH 5.5. Consequently, IM30 is suggested to sense and seal proton leaks at defective TM regions.

4.3.2.1. The IM30 structure is modulated at acidic pH

The structure of the IM30 protein was analyzed using CD-spectroscopy, ANS- and Trp-fluorescence at pH values ranging from 7.6 to 2.2. The experiments showed an at least biphasic structural rearrangements of the protein´s secondary and tertiary structure in this pH range.

While the secondary structure initially changed with decreasing pH to an unconventional structure at ~ pH 5.5, an apparently regular α-helical structure was regained after further lowering the pH. The observed unusual CD spectrum at ~pH 5.5 had an only minor contribution of the 208 nm minimum, and the typical minima at 208 nm and 222 nm were additionally shifted to higher wavelengths. This spectrum may be attributed to atypical secondary structural elements, such as β-turns or distorted forms of α-helical spectra. While absorption flattening due to light scattering could cause such a distortion (Duysens, 1956; Urry and Ji, 1968), no increased scattering was observed when the pH was decreased. A different explanation is the formation of at least partially unconventional beta-sheet structures as shown for some lectins (McCubbin et al., 1971). Similar shifts of beta-sheet minima have also been reported for selected peptides upon pH alteration or TFE treatment (Bañares-Hidalgo et al., 2014). Finally, it is not clear which structure was acquired at this pH. Since the changes of the CD-spectrum are most pronounced at pH 5.5 and regain a regular spectrum at pH 4.0, further protonation of particular amino acid side chains seems to destabilize the atypical structure forming at ~pH 5.5.

Besides the secondary structure, also the tertiary structure of IM30 changed upon acidification, as measured by ANS-fluorescence. This dye binds to hydrophobic areas of the protein surface, which results in a blue shift of the spectrum accompanied by a fluorescence intensity increase (LaPorte et al., 1980). While the hydrophobicity of IM30´s surface first increased between pH 7.6 and ~pH 4.5, a small decrease was observed below pH 4, clearly showing a change in the tertiary structure of IM30. This was supported by Trp-Fluorescence measurements using the sole Trp residue (Trp71), which is located in the center of the coiled-coil forming helices 2 and 3 (Saur et al., 2017). Interestingly, the environment of Trp71 did also change upon acidification. While the fluorescence intensity was almost unaltered, the spectral shape changed in a biphasic manner with a minimum at ~pH 6 and a maximum at ~pH 4. This indicates a structural alteration of the coiled-coil region of IM30, suggesting a slightly more hydrophobic environment at mildly acidic pH. Yet, the rather minor changes exclude major structural alterations, such as protein denaturation.

Taken together, the overall structure of IM30 was shown to be highly pH-dependent with an atypical structure at a ~pH 5.5.

Interestingly, the structural changes observed at pH 5.5 were similar to structural changes observed in presence of Mg^{2+} (Heidrich et al., 2018). Mg^{2+}-binding to IM30 also causes secondary structure rearrangements and increased surface hydrophobicity, albeit the effects were not as pronounced as reported here. More specifically, the amplitude of the 208 nm peak of the IM30 CD-spectrum was also decreased to some extent in presence of Mg^{2+} at pH 7.6, but no shift of the typical minima was observed. At pH 5.5, Mg^{2+}-binding did induce a slight increase of the 208 nm peak, resulting in a similar CD spectrum for IM30 at pH 5.5. and 7.6 in presence of Mg^{2+}. Still, IM30 appears to interact with Mg^{2+} also at pH 5.5., followed by a structural rearrangement.

4.3.2.2. Membrane interaction of IM30 is influenced by a low pH

Since IM30 may be locally exposed to a low pH close to the TMs, membrane interaction of IM30 was next analyzed via fluorescence spectroscopy. As the structural rearrangement appears most pronounced at pH 5.5, the binding propensity and membrane fusion activity were analyzed at pH 5.5 and compared to pH 7.6.

Laurdan fluorescence was monitored using TM-mimicking liposomes (PG/MGDG, 40/60 %). The Laurdan dye is sensitive to changes of the membrane fluidity, which causes changes of the emission spectrum that can be characterized by the GP-value. IM30 membrane binding was discussed to induce ordering of the lipid head group region, observed by an increase of the GP value (Hennig et al., 2015; Heidrich et al., 2016). In the now performed experiments, the membrane binding affinity was calculated from binding curves determined at pH 5.5 and 7.6, respectively. At pH 5.5, a higher membrane binding affinity (K_d = 1.8 ± 0.4) was observed in comparison to pH 7.6 (K_d = 9.8 ± 5.8 µM).

Results from QCM-experiments further support this interpretation. With this technique, binding to a solid supported lipid bilayer (SLB) is measured by monitoring the change of the resonance frequency and damping of the quartz crystal. If the absorbed mass is rigid, the change of the resonance frequency is proportional to the absorbed mass (Sauerbrey, 1959; Reviakine et al., 2011). Binding of IM30 to an SLB (PG/PC, 20 %/80 %) was observed over 3500s. At pH 5.5, the shift of the resonance frequency and damping were substantially larger, indicating increased binding of IM30 at pH 5.5. As the frequency and damping changed by about the same factor, a major change of the viscoelasticity is unlikely, which finally allows a quantitative analysis. This result was somewhat unexpected, since usually electrostatic interactions are discussed for IM30 membrane binding (Hennig et al., 2015; Heidrich et al., 2016). These new results now hint at least for a partial

contribution of hydrophobic interactions. At low pH, the increased proton concentration potentially leads to protonation of the PG lipid, which results in a reduction of the surface charge. The beforehand observed increased exposure of hydrophobic patches at low pH seems to promote hydrophobic interactions with the membrane, which appears to outweigh the weakened electrostatic interactions.

IM30-induced membrane fusion depends on IM30 activation via Mg^{2+}-binding (Hennig et al., 2015; Heidrich et al., 2018). As the structural changes of IM30 observed upon lowering the pH resemble changes caused by Mg^{2+} binding (Heidrich et al., 2018), it was next investigated to what extent an acidic pH influences the IM30 fusion activity. Actually, when decreasing the pH from 7.6 to 5.5, IM30-mediated membrane fusion was strongly enhanced in contrast to control measurements (Mg^{2+}-induced membrane fusion). The increased fusion activity at pH 5.5 might be partially caused by the observed increased membrane binding affinity. In addition, IM30-induced membrane fusion was triggered even in the absence of Mg^{2+} at pH 5.5. Nevertheless, the addition of Mg^{2+} did further increase the membrane fusion activity, showing that Mg^{2+} is not mandatory, but supports membrane fusion at this condition. This appears to be in line with the observed similar secondary structure at pH 5.5 and, in presence of Mg^{2+}, at pH 7.6. The results from the fusion assay indicate that the similar structure observed at the two conditions likely represents the fusion-competent structure of IM30. Both, protons and Mg^{2+}, probably interact with negatively charged amino acid side-chains, which likely causes the structural rearrangements. However, since the IM30 structure seems to be considerably more affected at pH 5.5 than in presence of Mg^{2+} at pH 7.6, protonation appears to be more effective than Mg^{2+} binding.

4.3.2.3. Physiological implications of a pH-responsive IM30 structure and function

All proteins of the PspA/IM30 family seem to be involved in membrane stabilization, albeit the underlying mechanism is currently rather enigmatic (Thurotte et al., 2017). While the complete *phage shock protein (psp)* stress response system of e.g. *E. coli* or *Yersinia enterocolitica* contains the membrane-defect sensing proteins PspB and PspC as well as the effector protein PspA (Darwin, 2005), other bacteria appear to require only a PspA homolog for both recognizing and stabilizing membrane defects (Vrancken et al., 2008). Also in case of IM30, no PspB or PspC homologs have been identified in cyanobacteria or chloroplasts thus far, giving rise to the assumption that IM30 may be able to both sense and stabilize/repair defects.

The TM system of cyanobacteria is an entirely separated compartment (Schneider et al., 2007). The pH of the thylakoid lumen is distinctly lower than the pH of the cyanobacterial cytoplasm, since

electron transfer reactions drive proton translocations across the TM during photosynthesis (Belkin et al., 1987). The ΔpH across the TM is essential for energy production. In the thylakoid lumen at dark light conditions, the pH is about 4.5-5.5, whereas the pH of the cytoplasm is about 7-8 (Falkner et al., 1976; Masamoto and Nishimura, 1977; Padan and Schuldiner, 1978; Gibson, 1981; Kallas and Dahlquist, 1981; Belkin et al., 1987). In the light, the pH of the lumen is further increased by ~0.5 pH units (Scherer et al., 1984; Nitschmann and Peschek, 1985). The destabilization of the TM integrity is endangered e.g. under conditions of curvature- or light-induced oxidative stress. The IM30 protein appears to stabilizes the TMs in chloroplasts and cyanobacteria (Vothknecht et al., 2012; Zhang and Sakamoto, 2013; Zhang and Sakamoto, 2015). As the IM30 protein is usually located either at TMs or the CM, or in the cytoplasm, it is usually exposed to a pH of 7-9 (Bryan et al., 2014; Gutu et al., 2018). Under stress conditions, the TM may lose its integrity, which can cause spatio-temporal formation of damaged membrane regions where protons leak out of the thylakoid lumen. In this case, IM30 located near the proton leak experiences a lowered pH.

Since the IM30 structure is pH-responsive with a maximum effect at pH 4-5, IM30 is hypothesized to “sense” and “repair” such membrane defects triggered by the structural rearrangement. The molecular mechanism is unclear so far, yet most likely, protonation of ionizable amino acid side chains affects both electrostatic interactions as well as the net surface charge (Pace et al., 2009). As a consequence of these alterations, the membrane binding affinity and fusion capacity of IM30 was distinctly enhanced. In line with this, IM30 assemblies have been observed *in vivo* at highly curved membrane regions (Gutu et al., 2018). These were discussed to have a protective function (Thurotte et al., 2017; Junglas and Schneider, 2018). As membrane fusion includes partial membrane destabilization, the observed enhanced membrane fusion competence of IM30 at low pH is at first glance contradictory to a protective function. Finally, the study suggests that IM30 actively promotes membrane sealing at the TM defects by membrane fusion of an intact membrane patch to the defective area. At destabilized membrane regions, the energy cost for membrane remodeling is already lowered, which allows to expect an increased membrane fusion activity of IM30. A similar physiological role has been discussed for the bacterial membrane fusion protein DynA in *B. subtilis* (Sawant et al., 2016; Guo and Bramkamp, 2019) or for several eukaryotic proteins (Zhen et al., 2021).

4.4. IM30 IDPs form a membrane-protective carpet upon super-complex disassembly

4.4.1. Publication

Junglas B., Orru R., Axt A., Siebenaller C., Steinchen W., Heidrich J., Hellmich U.A., Hellmann N., Wolf E., Weber S. and Schneider D. (2020) IM30 IDPs form a membrane-protective carpet upon super-complex disassembly, Nature Comm. Biol. 3, 595

The author affiliations are listed in chapter VII.

The original publication is added as Appendix VIII.5 (Junglas et al., 2020b). The author contributions according to the *CRediT taxonomy* (Allen et al., 2014) are listed in Table 4.4.1.

Table 4.4.1: Author contributions to *IM30 IDPs form a membrane-protective carpet upon super-complex disassembly*

Study conception	Protein characterization Atomic force microscopy Small-angle X-ray scattering	BJ, **CS**, JH, UH, WS, NH, DS BJ, AA, SW BJ, RO, EW
Supervision, **Project administration,** **Funding acquisition,** **Resources**	Protein characterization NMR AFM SAXS HDX	NH, DS UH SW EW WS
Writing	Original Draft Review and Editing	BJ, NH, DS BJ, **CS**, NH, DS
Special tasks	AFM data collection SAXS data collection NMR data collection HDX data collection	BJ, AA RO UH WS

Table 4.4.1: Author contributions to *IM30 IDPs form a membrane-protective carpet upon super-complex disassembly*

Figures (numbers refer to the original publication)	**Methodology, Investigation, Formal analysis**	**Data visualization**
Fig. 1 A	JH, NH, **CS**	BJ, **CS**
Fig. 1 B	BJ, AA	BJ, AA
Fig. 1 C, D	BJ	BJ
Fig. 1 E	**CS**	**CS**
Fig. 2 A-D	BJ, RO	BJ
Fig. 2 E, F	BJ	BJ
Fig. 3 A	BJ, RO	BJ
Fig. 3 B	BJ, WS	BJ
Fig. 3 C, D	BJ	BJ
Fig. S1 A, B	**CS**	BJ, **CS**
Fig. S2 A-G	BJ	BJ
Fig. S3 A, B	BJ	BJ
Fig. S4 A-D	BJ, AA	BJ, AA
Fig. S4 E, F	BJ, NH	BJ
Fig. S5 A, B	BJ, AA	BJ, AA
Fig. S6 A, B	BJ	BJ
Fig. S7 A, B	BJ, RO	BJ
Fig. S8 A-C	BJ, WS	BJ
Fig. S8 C	BJ, WS	BJ, WS
Fig. S9 A	BJ, UH	BJ
Fig. S9 B, C	BJ, RO	BJ
Fig. S10 A, B	BJ	BJ
Fig. S10 C, D	BJ	BJ
Fig. S11 A, B	BJ	BJ
Fig. S12	BJ	BJ
Fig. S13 A, B	BJ	BJ

4.4.2. Summary

IM30 clearly is a membrane-active protein that binds to negatively charged membranes both *in vivo* and *in vitro* (Fuhrmann et al., 2009a; Hennig et al., 2015; McDonald et al., 2015; Heidrich et al., 2016).

A characteristic feature of PspA/IM30 family members is their intrinsic propensity to form homo-oligomeric ring- or rod-like structures with masses >1 MDa (Aseeva et al., 2004; Hankamer et al., 2004; Liu et al., 2007; Fuhrmann et al., 2009a; Wolf et al., 2010; Male et al., 2014; Gao et al., 2015; Saur et al., 2017). Recently, the cryo-EM structure of soluble IM30 has been published (Gupta et al., 2021). Yet, in contrast to the analysis of IM30 in solution, the structure of membrane-bound IM30 is currently much less investigated. *In vitro* experiments show that the ring structure, as well as smaller oligomers, bind to membranes, whereby the smaller oligomers even bind with higher affinity (Heidrich et al., 2016). Therefore, it has been hypothesized that IM30 rings disassemble upon membrane binding by a thermodynamically driven process (Junglas and Schneider, 2018). Nevertheless, the mechanism of this potential super-complex disassembly is entirely unknown so far. *In vivo* experiments using GFP-tagged IM30 suggest the formation of IM30 assemblies at TM margins of chloroplasts and cyanobacteria (Zhang et al., 2012; Bryan et al., 2014; Gutu et al., 2018). These assemblies are discussed to have a membrane-stabilizing function, as membrane-protective effects have been observed in *Arabidopsis thaliana* chloroplasts (Zhang et al., 2012; Zhang and Sakamoto, 2013; Zhang and Sakamoto, 2015; Zhang et al., 2016).

In the publication "IM30 IDPs form a membrane-protective carpet upon super-complex disassembly" it is now shown for the first time that IM30 rings disassemble upon membrane binding, resulting in formation of a membrane-protective carpet. Ring disassembly involves unfolding the C-terminal domain, resulting in intrinsically disordered IM30 regions.

4.4.2.1. IM30 membrane binding is followed by dissociation of the oligomeric ring structure

When analyzing the IM30 fragments upon tryptic digestion in absence and presence of negatively charged liposomes (PG, 100 %), a different fragmentation pattern has been observed. This was a first hint for a rearrangement of the IM30 structure upon membrane binding. The potential structural change was further analyzed via following FRET between CFP- and Venus-labeled IM30, which allows to draw conclusions about the relative distance of the IM30 monomers during and after

membrane binding. A decrease of the FRET signal was observed when IM30 was incubated with liposomes (PG, 100 %), indicating an increasing distance of the IM30 monomers. This suggests at least partial disassembly of the ring structure on the membrane. Consequently, IM30 membrane binding seems to be associated with a structural rearrangement of the protein.

To analyze the structure of membrane-bound IM30 in greater detail, membrane interaction of IM30 was visualized via AFM. On a mica surface, ring structures with dimensions similar to those found for IM30 in negative staining TEM studies have been observed. In contrast, several hundred nm^2 large carpet-like structures were observed when IM30 bound to a supported lipid bilayer (SLB) (PG, 100 %). These carpets were also detected on an SLB with a physiological surface charge of the TM (PG/PC, 40 %/60 %). The height of the carpet structures (average: ~0.9 nm) did clearly not match the ring height of 13-15 nm (Saur et al., 2017) or 20 nm (Gupta et al., 2021), and thus carpets did not form via simple lateral association of multiple IM30 rings. Instead, a major reorganization of the oligomeric structure was required. A non-ring-forming mutant (IM30*) did also form carpet-like structures on the membrane similar to the IM30 wt. This implies that the ring formation is not a prerequisite for carpet development.

The here observed protein carpets on the membrane likely correspond to the *in vivo* observed assemblies of IM30 on the TM margins (Zhang et al., 2012; Bryan et al., 2014; Gutu et al., 2018). It is therefore likely that IM30 ring disassembly upon membrane binding is a physiologically relevant mechanism.

4.4.2.2. IM30 membrane binding involves unfolding of C-terminal domains

The assemblies of IM30 on the TM are involved in stress response in cyanobacteria and chloroplasts (Zhang et al., 2012; Bryan et al., 2014; Gutu et al., 2018). A fluorescence-based proton leakage assay was used to analyze if the here observed IM30 assemblies on the membrane indeed protect the membrane integrity, as suggested (Junglas and Schneider, 2018). Liposomes (PG, 100 %) with a proton gradient across the membrane were incubated with isopropanol, resulting in membrane destabilization. Consequently, an increased proton flux into the liposomes was observed. In the presence of IM30, the influx was strongly decreased, indicating decreased membrane permeability. An even stronger effect was observed in presence of the dimeric mutant IM30*. As faster membrane binding kinetics were observed for this mutant, binding of IM30 rings likely is slower than binding of smaller oligomers. This might originate in the increased number of individual particles when IM30

is organized as a small oligomer instead of a ring at identical monomer concentration. Upon ring disassembly, similar membrane binding may also be achieved for the IM30 wt.

Similarly, an increased membrane binding affinity has also been observed for the isolated coiled-coil fragment IM30 H23 recently (Thurotte and Schneider, 2019). As the coiled-coil structure is usually buried in the ring structure (Gupta et al., 2021; Liu et al., 2021), efficient membrane binding via exposure of the coiled-coil may only be accomplished after ring disassembly. Thus, ring disassembly likely is a crucial step in carpet formation. The faster membrane binding and larger membrane-protective effect of IM30* can therefore probably be explained by the missing necessity of the dimeric IM30* to disassemble in the initial step. Noteworthy, interactions of the C-terminal region of IM30 seem crucially involved in the membrane-protective activity, as the isolated IM30 H23 destabilizes membranes (Thurotte and Schneider, 2019).

4.4.2.3. Intrinsic disorder is the structural basis for the membrane-protective function of IM30

The dimeric structure of IM30* could be an intermediate structure in the process of IM30 membrane binding and ring disassembly. Consequently, the structure of IM30* was of potential interest and was therefore determined using *small-angle X-ray scattering coupled to size exclusion chromatography* (SEC-SAXS). The results suggest an elongated shape of IM30* dimers and a partially flexible structure with considerable amounts of unstructured regions. The extent of these unstructured regions was confirmed by *circular dichroism* (CD) spectroscopy. In contrast to the IM30 wt (~80% α-helix) (Fuhrmann et al., 2009a; Otters et al., 2013; Gao et al., 2015), an α-helical content of only ~40% was determined for IM30*. Limited proteolysis and *hydrogen-deuterium exchange* (HDX) coupled to LC-MS measurements of IM30* were performed to identify the potential unstructured regions of IM30. In the limited proteolysis analysis, a stable IM30 fragment (~17 kDa) was found, which consisted of parts of helix 1 to about half of helix 4. This indicates that helix 1 and helix 4-7 are highly protease accessible and likely flexible parts of the IM30* structure. The HDX/LC-MS analysis showed only little H/D exchange for the expected coiled-coil structure of helix 23, whereas considerable amounts of H/D exchange were detected for the residual helices. A comparison with the IM30 wt showed vastly more H/D exchange in the region of helix 1, 4 and 5/6. This indicates that in the mutant the N-terminal domain as well as in large parts of the C-terminal domain (helix 4-7) are unstructured when compared to the wt protein, whereby helix 7 appears to be unstructured to some extent in the IM30 wt as well. The disordered nature of the isolated C-terminal domain (IM30 H4-7) was confirmed by CD and 1D-1H-NMR spectroscopy.

Based on the SAXS-data and the PspA X-ray structure of the stable coiled-coil region, a model for the IM30 structure that includes the flexibility of the IM30* C-terminus was generated. In a fragmentation-based modeling approach, starting from a recent structure model (Saur et al., 2017), several potential dimeric model structures were obtained, likely representing different conformations of the IM30* dimer. To analyze the dimeric interface of IM30*, *SEC coupled with multi-angle laser light scattering* (SEC-MALS) was performed with the isolated IM30 fragments H23 and H47. IM30 H23 was determined to be monomeric, whereas the IM30 H47 fragment was dimeric. Thus, the dimer interface of IM30* is most likely located in the C-terminal region. This is further supported by SDS-PAGE analysis of IM30*and IM30 wt after Cys-crosslinking in the C-terminal region (A227C). The SDS-PAGE analysis showed covalently linked dimers for both proteins, suggesting close contact of the C-termini of two neighboring monomers.

The results of the structural analysis of IM30* and IM30 H47 allow to draw conclusions about the IM30 wt structure. While the IM30 H23 fragment requires no further helices to form a stable coiled-coil structure (Osadnik et al., 2015; Thurotte and Schneider, 2019), the isolated C-terminal region H47 is not able to form α-helices. In contrast, the combination of H23 and H47 in the full-length IM30 wt, where individual IM30 monomers interact in the ring structure, is largely α-helical. Consequently, oligomerization of IM30 monomers seems to induce the folding of beforehand disordered IM30 domains. In the dimeric IM30*, the C-terminal domain is also unstructured in the full-length protein, most likely due to missing interactions with neighboring monomers caused by the mutation of conserved amino acids (FERM cluster) in helix 4. Consequently, when organized as a monomer/smaller oligomer, the IM30 wt is most likely also unstructured in the C-terminal region.

4.4.2.4. Conclusion

IM30 super-complex formation seems to be a new example for self-assembling IDPs (intrinsically disordered proteins), which form higher-ordered oligomers accompanied by the folding of disordered regions. The disordered character of certain domains and the consequently large interaction surface thereby enable interactions with various binding partners (Muiznieks et al., 2010; Rauscher and Pomès, 2017; Uversky, 2017). Interactions of disordered C-termini are probably important for both IM30 oligomerization and super-complex formation as well as carpet formation after membrane binding.

Carpet-formation on membranes has also been observed e.g. for proteins involved in Alzheimer's or Parkinson's disease, although the protein carpet leads to membrane-destabilization in these cases

(Uversky and Eliezer, 2009; Fabiani and Antollini, 2019). This contradicts the membrane-stabilizing function of the IM30 assemblies on the membrane, which, however, is perfectly in line with the observed *in vivo* formation of IM30 assemblies at stressed TM regions (Zhang et al., 2012; Bryan et al., 2014; Gutu et al., 2018) and the membrane-protective activity of IM30 on *Arabidopsis thaliana* chloroplasts (Zhang et al., 2012; Zhang and Sakamoto, 2013; Zhang and Sakamoto, 2015; Zhang et al., 2016). Scaffold-like, membrane-protective structures have also been discussed for the related PspA-protein (Kobayashi et al., 2007; Standar et al., 2008). The functional complementation of *E. coli pspA* null mutant by *im30* expression (DeLisa et al., 2004) is a further hint for a conserved membrane-stabilizing activity of both proteins.

The study *IM30 IDPs form a membrane-protective carpet upon super-complex disassembly* suggests for the first time a so far unknown structural basis for the physiological function of IM30 (summarized in Fig. 4.4.1).

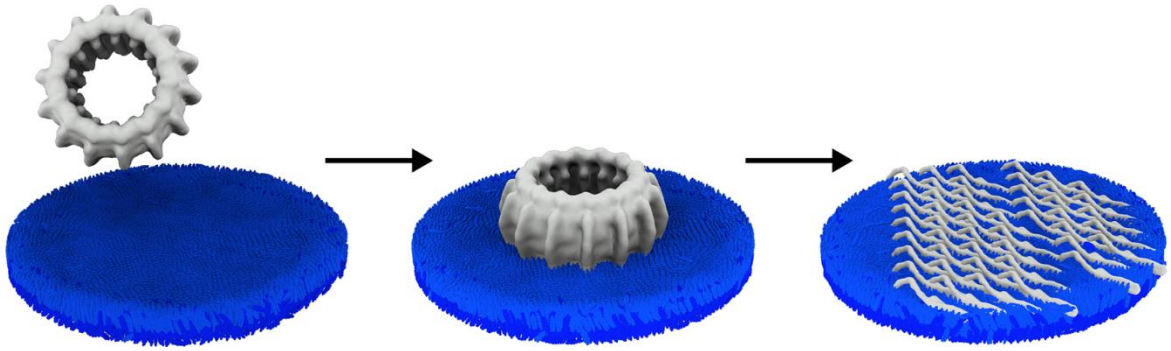

Figure 4.4.1: Model for IM30 membrane binding followed by ring disassembly.

Binding of IM30 to negatively charged membranes involves (at least) 2 steps: In the initial binding step, the predominantly ring-like IM30 wt binds to the membrane, likely accompanied by minor structural changes and ring destabilization. In a second step, the IM30 ring structure disassembles and rearranges to a flat, membrane-protective carpet structure. The disassembly of the ring is likely coupled to unfolding of the IM30 C-terminal domain.

4.5. Mg^{2+}-binding to the *Synechocystis* IM30 (Vipp1) protein results in membrane destabilization and pore formation

Junglas B.[#], Axt A.[#], Siebenaller C.[#], Sonel H., Hellmann N., Weber S. and Schneider D. (2020) Mg^{2+}-binding to the Synechocystis IM30 (Vipp1) protein results in membrane destabilization and pore formation, in preparation.

The author affiliations are listed in chapter VI.

A previous version of this study has been published as an unreviewed preprint on the bioRxiv server (Junglas et al., 2020a). The author contributions according to the *CRediT taxonomy* (Allen et al., 2014) are listed in Table 4.5.1.

Table 4.5.1: Author contributions to *Mg^{2+}-binding shifts the IM30 activity from membrane protection to membrane destabilization*

Study conception	Protein characterization Atomic force microscopy	**CS**, BJ, NH, DS BJ, AA, SW
Writing	Complete study	**CS**, BJ, AA, SW, NH, DS
Supervision, Project administration, Funding acquisition, Resources	Protein characterization AFM	DS SW
Figures	**Methodology, Investigation, Formal analysis**	**Data visualization**
Fig. 4.5.1 A-E	**CS**	**CS**
Fig. 4.5.2	**CS**, HS	**CS**, HS
Fig. 4.5.3 A-C	BJ, NH	**CS**, BJ
Fig. 4.5.4 A-C	BJ, AA, NH	AA
Fig. 4.5.4 D-E	BJ, AA, NH	AA, NH
Fig. 4.5.5 A-C	BJ, AA	BJ, AA
Fig. 4.5.6	n.a.	**CS**, BJ

[#] These authors contributed equally.

4.5.1. Introduction

While a membrane protecting activity of IM30 has been observed in the previous chapter in absence of Mg^{2+}, IM30 triggers membrane fusion when Mg^{2+} is present (Hennig et al., 2015). Notably, in chloroplasts and cyanobacteria, Mg^{2+} flux across the thylakoid membrane is used to counterbalance the light-induced formation of a proton gradient across the TM (recently reviewed in (Pohland and Schneider, 2019)). In the light, the Mg^{2+} concentration in the chloroplast stroma increases from below 1 to 2-3 mM (Lin and Nobel, 1971; Portis and Heldt, 1976; Portis, 1981; Ishijima et al., 2003). Once Mg^{2+} has entered the chloroplast stroma or cyanobacterial cytoplasm, respectively, out of the thylakoid lumen, it allosterically regulates the activity of several enzymes and proteins (Ashton, 1998; Hazra et al., 2015). In fact, Mg^{2+} directly binds also to IM30 in solution with a K_D in the range of 1 mM (Heidrich et al., 2018). Mg^{2+}-binding to IM30 induces several structural rearrangements, resulting in increased surface hydrophobicity and increased protease resistance of the protein´s C-terminal domain (Heidrich et al., 2018). Thus, IM30-triggered membrane remodeling is potentially controlled via Mg^{2+}-binding to IM30. However, while the organization of membrane-protecting IM30 species on the membrane surface has been elucidated in chapter 4.4 (Junglas et al., 2020b), critical steps of the membrane fusion/remodeling process are still unclear. How does Mg^{2+}-binding to IM30 affect the interaction of the protein with membranes and the membrane structure and how does it induce membrane fusion?

The study here shows that IM30 binds more strongly to native as well as to model membranes when Mg^{2+} is present. Importantly, membrane adsorption onto solid-supported bilayers substantially differs in the presence of Mg^{2+} from membrane adsorption in the absence of Mg^{2+}, as shown here via AFM: Upon binding of Mg^{2+}-loaded IM30 (short: IM30/Mg^{2+}) to membrane surfaces, the emergence of membrane defects in close proximity to the IM30 binding region was observed. Membrane destabilization by IM30/Mg^{2+} and the formation of membrane defects now explain the recently observed Mg^{2+}-dependent membrane fusogenic activity of IM30. Thus, IM30 has two (seemingly opposing) functions, and Mg^{2+}-binding to IM30 switches the protein function from “membrane protection” to a “membrane fusion” activity.

4.5.2. Results

4.5.2.1. IM30 membrane binding is followed by dissociation of the oligomeric ring structure

Binding of Mg^{2+} to IM30 alters the structure of IM30 and triggers membrane fusion (Hennig et al., 2015; Heidrich et al., 2018). Due to the exposure of an increased hydrophobic surface upon Mg^{2+}-binding (Heidrich et al., 2018), the structural changes induced by Mg^{2+}-binding potentially enhance its membrane binding affinity. To test this assumption, it was first analyzed whether binding of IM30 to native TMs depends on the cytosolic Mg^{2+} concentrations. To address this, the amount of membrane-bound IM30 was determined in the presence of different Mg^{2+} concentrations using cellular extracts of the cyanobacterium *Synechocystis* via SD gradient centrifugation and subsequent immuno-detection of membrane-attached IM30 (Fig. 4.5.1 A). When increasing concentrations of Mg^{2+} were added to the *Synechocystis* cell lysate, an increasing amount of native IM30 was found to colocalize with membranes in the sucrose gradient, strongly indicating increased membrane binding (Fig. 4.5.1 A). In contrast, the amount of IM30 colocalizing with the TM in a control, where endogenous Mg^{2+} was removed via EDTA, was below the detection limit of the immunoblots. Thus, Mg^{2+}-binding to IM30 clearly enhances its ability to interact with cyanobacterial membranes.

To test whether IM30 binds directly to membranes rather than to exposed proteins or protein domains that were copurified with the *Synechocystis* membrane, negatively charged model membranes were analyzed next (100 % PG liposomes). Therefore, SD gradient centrifugation and subsequent immunological detection of the protein were performed at increasing Mg^{2+} concentrations (0-10 mM) (Fig. 4.5.1 B). As shown before (Hennig et al., 2015), colocalization of a small IM30 fraction with liposomes in the absence of Mg^{2+} was observed, indicating low-affinity binding of IM30 to liposomes in absence of Mg^{2+}. Based on Western blot analyses (Fig. 4.5.1 B), only ~15% of IM30 colocalized with the liposomes (fraction 1 to 3, 4.5.1 C,D), whereas the majority of the protein was found in the pellet fraction, as the high molecular mass IM30 assemblies sedimented during centrifugation. However, increasing the Mg^{2+} concentration to up to 10 mM largely increased the liposome-bound fraction, finally resulting in ~80% bound IM30 at 10 mM Mg^{2+} (Fig. 4.5.1 B).

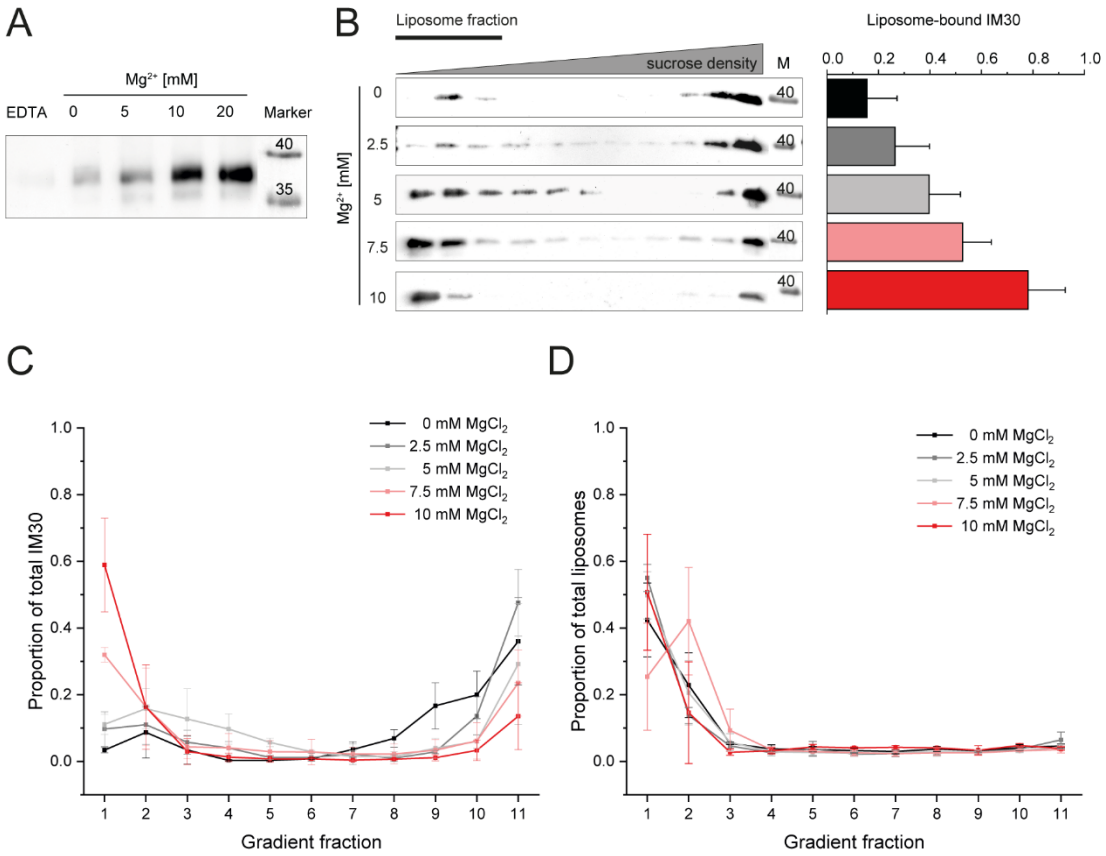

Figure 4.5.1: The membrane binding propensity of IM30 is increased in the presence of Mg^{2+}.

A: The amount of IM30 bound to TMs in the presence of increasing Mg^{2+} concentrations was estimated via SD gradient centrifugation of *Synechocystis* cell lysate and subsequent immunoblotting of the TM fraction. Endogenous IM30 was not detected to colocalize with TMs when 20 mM EDTA was present to remove any endogenous Mg^{2+}. At concentrations of 5 mM Mg^{2+} or higher, increasing amounts of IM30 were detected. **B:** Interaction of IM30 with 100% PG liposomes in presence of 0 to 10 mM Mg^{2+} was examined via SD gradient centrifugation. Localization of IM30 in the density gradient was monitored via immunoblotting, and liposomes were localized using the incorporated fluorescent lipid dye NBD-PE. The amount of liposome-bound IM30 was quantified via densitometric analysis of the immunoblot bands (bar chart). An increasing amount of IM30 colocalizes with liposomes with increasing concentrations of Mg^{2+}. Error bars represent SD, n=3. **C:** Localization of IM30 in the SD gradient was monitored via immunoblotting of the individual gradient fractions. The amount of IM30 was quantified via densitometric analysis. N=3, error bars represent SD. **D:** The localization of the liposomes within the gradient was analyzed via the incorporated fluorescent lipid dye NBD-PE. N=3, error bars represent SD.

Next, binding of IM30 to lipid membranes was directly visualized using PG/PC (20/80) giant unilamellar vesicles (GUVs) in the absence and presence of Mg^{2+} via fluorescence microscopy (Fig. 4.5.2). IM30 C-terminally fused to CFP (IM30-CFP) was recombinantly produced and purified, and the GUVs were labeled by doping the membranes with Atto633-PE. In absence of Mg^{2+}, binding of the protein to the GUVs was not detectable (Fig. 4.5.2). However, upon addition of 5 mM Mg^{2+}, binding of IM30-CFP to the GUVs was clearly visible, and the CFP-fluorescence was evenly distributed over the GUV area (Fig. 4.5.2). Note that the GUVs were highly unstable at higher

concentrations of negatively charged lipids and/or >5 mM Mg^{2+} concentrations. Thus, the experiment was limited to lower ratios of PG in the GUVs and lower Mg^{2+} concentrations compared to the centrifugation assay. Nevertheless, the amount of IM30 bound to negatively charged GUVs was also clearly increased in the presence of Mg^{2+}. Thus, Mg^{2+}-binding to IM30 clearly boosts its ability to bind to native as well as to model membranes.

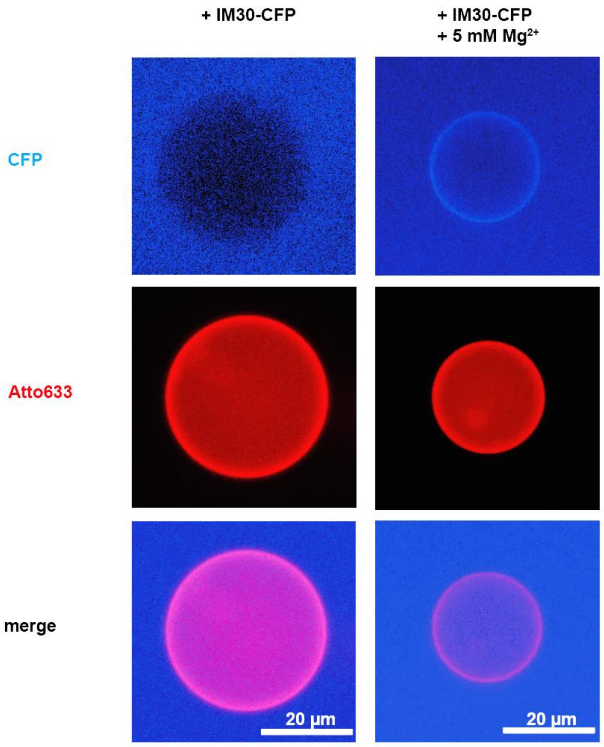

Figure 4.5.2: Increasing amounts of IM30 bind to GUVs in presence of Mg^{2+}.

Adsorption of IM30-CFP to PG/PC (20/80) GUVs in absences *vs* presence of Mg^{2+} was visualized using fluorescence microscopy. GUVs were detected by the fluorescence signal of the incorporated lipid dye Atto-633-PE. IM30-CFP was visualized via monitoring the CFP fluorescence. The amount of adsorbed IM30 was increased at 5 mM Mg^{2+} when compared to Mg^{2+}-free buffer, as indicated by the increased CFP fluorescence intensity localized on the GUV surface.

4.5.2.2. IM30 membrane binding is followed by dissociation of the oligomeric ring structure

To further analyze the impact of Mg^{2+} on IM30 membrane binding, QCM was performed to follow the binding of IM30 to a solid supported lipid bilayer (SLB) (20% PG / 80% PC), as above described in the absence of Mg^{2+} (Siebenaller et al., 2020, chapter 4.3). In QCM experiments, the resonance frequency of a quartz crystal and its damping behavior is determined. The resonance frequency changes when additional material binds to the crystal. Hence, binding of any material, *e.g.* IM30, to the SLB (which is attached to the quartz crystal) leads to a frequency shift towards lower resonance frequencies. If the adsorbed material is rigid and sufficiently thin (significantly smaller than the penetration depth of the oscillation, which is ≈ 250 nm for the present case), the total mass bound to the crystal can be determined using the Sauerbrey equation (Sauerbrey, 1959; Reviakine et al., 2011). However, if a viscoelastic or very thick layer is formed on the crystal, the oscillation is damped, leading to a decreased frequency shift, and the mass determined based on the Sauerbrey equation then underestimates the mass actually adsorbed. The Sauerbrey equation is assumed to be applicable

only if the damping signal in Hz is much smaller than the frequency shift. If this is not the case, a quantitative determination of the amount of bound protein is not possible anymore. Yet, it still is possible to employ the damping/frequency ratio as a qualitative indicator for changes in the viscoelastic properties of the adsorbed layer (Du and Johannsmann, 2004).

As can be seen in Figure 4.5.3 A, binding of IM30 to the SLB caused a shift of the resonance frequency, associated with increased damping of the resonance oscillation in the absence of Mg^{2+}. The frequency shift reached a constant level at about -80 Hz after ~2500 s, as already shown previously (Siebenaller et al., 2020, chapter 4.3). In stark contrast, in presence of Mg^{2+} the frequency signal change was only ~25 % of the signal change observed in the absence of Mg^{2+} (Fig. 4.5.3 A). The reduced frequency shift in presence of Mg^{2+} could be caused by a lower amount of mass attached to the membrane surface and/or an increase in viscoelasticity, leading to a stronger impact of the missing mass effect. According to the results of the SD centrifugation experiments described above, the actual amount of protein attached to the SLB is expected to be higher in presence of Mg^{2+}, rendering an increased viscoelasticity more likely. This hypothesis is supported by the larger magnitude of the damping/frequency shift ratio (Fig. 4.5.3 C). Of note, this ratio was constant in time, in contrast to the experiments performed in absence of Mg^{2+}. In the latter case, the contribution of viscoelastic properties to the oscillation actually appears to get smaller with progress of the binding process, as indicated by the different slopes when the damping is plotted *vs* the frequency shift (Fig. 4.5.3 B,C). The observation that IM30 initially binds as a ring to the membrane, which then converts into flat carpet structures representing a more rigid layer with lower damping (chapter 4.4, Junglas et al., 2020b), nicely explains the here observed decrease in viscoelasticity: Binding of ring-shaped proteins to a surface is expected to show viscoelastic behavior because the layer formed is not homogenous (Reviakine et al., 2011). Dissociation of the rings decreases not only the height of the layer, but also leads to a more homogenous layer, decreasing the damping signal. On the other, the actual mass bound to the surface decreases upon ring dissociation, due to release of the water trapped inside the rings and potentially between the rings (Reviakine et al., 2011). This process decreases both the damping and the frequency shift, but not the ratio of both (Du and Johannsmann, 2004). Thus, the data indicate that the membrane-bound ring is less prone to disassemble in presence of Mg^{2+}, in accordance with the observation that Mg^{2+} binding to IM30 stabilizes the ring in solution (Heidrich et al., 2018).

In summary, the QCM measurements clearly indicate a different mode of interaction of IM30 with membrane surfaces in absence *vs* presence of Mg^{2+}.

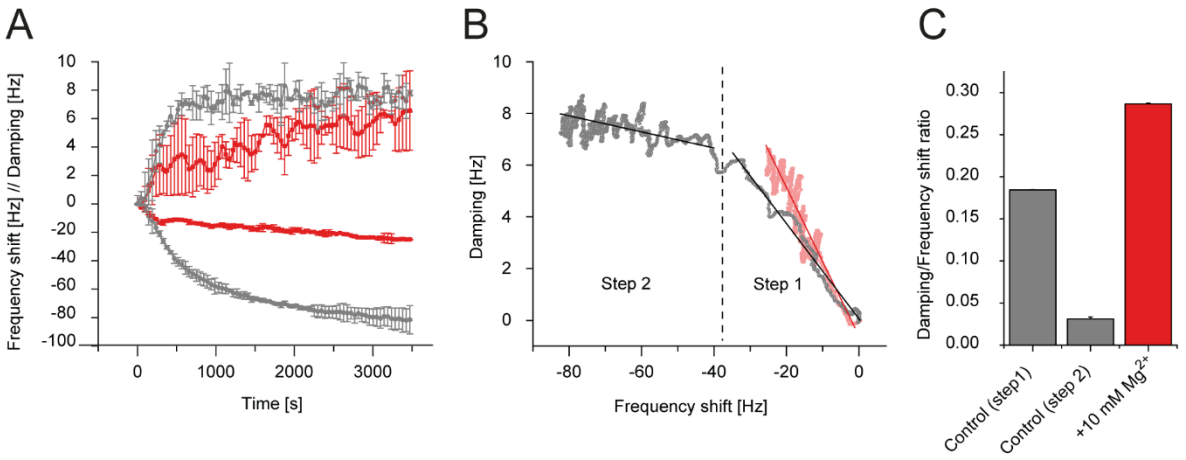

Figure 4.5.3: The viscoelastic properties of membrane-bound IM30 differ in presence and absence of Mg^{2+}.

A: The frequency shift (negative values) and damping (in terms of the resonance peak's full width at half maximum; positive values) of QCM measurements of IM30 binding to an SLB (80% PC/20% PG) in the absence (dark grey) and presence (red line) of 10 mM Mg^{2+} are shown. IM30 binding to the SLB in the presence of Mg^{2+} caused a smaller frequency shift than in the absence of Mg^{2+}. The damping signals reached about the same levels. N=3, error bars represent SD. For a better overview, only every 30th data point is shown. **B:** A plot of the frequency shift *vs* the damping of IM30 binding to an SLB reveals a shift in viscoelastic properties during protein binding in the absence of Mg^{2+} (dark grey) and a single phase in the presence of Mg^{2+} (red). The regimes were determined by the slopes of linear fits: Step 1 in the absence of Mg^{2+}: m=-0.1844±0.0002; (R^2=0.99959); Step 2 in the absence of Mg^{2+}: m=-0.031±0.002; (R^2=0.8976); Step 1 in the presence of Mg^{2+}: m=-0.28742±0.0008; (R^2=0.98384). N=3, error bars represent SD. **C:** A comparison of the damping/frequency shift ratio (slope in B) in the absence (dark grey, step 1 and step 2) and presence of Mg^{2+} (red) is shown. Error bars represent errors from the linear fit of the slopes in B.

4.5.2.3. Mg^{2+} triggers IM30-induced formation of bilayer defects

To better understand how IM30 affects the membrane structure when Mg^{2+} is present, and *vice versa*, membrane adhesion of IM30 was next analyzed on a nanometer-scale using AFM on SLBs. All AFM measurements were performed using 100% PG SLB on mica. Due to technical limitations, the first image after injection of IM30 could only be scanned after at least 10 minutes. Therefore, processes happening in the first 10 minutes after injection were not observed.

After membrane adhesion of IM30, particles of variable heights and diameters were observed on the bilayer in the absence as well as in the presence of Mg^{2+}, but the dimensions of the particles differed (Fig. 4.5.4 B,C). Therefore, a statistical analysis of the particle size was performed, only taking into account particles that were larger than one pixel and extracted the particle properties with the AFM analysis software GWYDDION (Fig. 4.5.4 D). Neither the diameter nor the height is normally distributed, therefore the analysis is based on medians and quantiles. In absence of Mg^{2+}, IM30

particles have a median diameter of 34 nm and a median height of 0.6 nm (Fig. 4.5.4 D). 67 % of the particles have diameters between ~20 nm and 40 nm. These values are in line with diameters of IM30 rings determined via TEM (~20 – 35 nm (Saur et al., 2017; Gupta et al., 2021)) as well as IM30 rings bound directly to the *mica* surface and visualized via AFM (outer diameter ~30 – 60 nm (Fig. 4.5.4A, (Junglas et al., 2020b)). Yet, the height of the particles does not match previous findings: TEM analyses reveal a height of about 20 nm for the rings (Gupta et al., 2021), and recent AFM studies in liquid environments report a height of 15-25 nm for IM30 rings attached to *mica* surfaces (Junglas et al., 2020b). The low height of the particles, together with the slightly increased diameter, potentially indicates the beginning or partial disassembly of IM30 ring structures on the membrane surface. In fact, the stability of IM30 rings appear to depend on the buffer conditions, and while rings are essentially stable in *e.g.* TRIS/HCl buffer, where they, however, lose their activity (Junglas et al., 2020b), rings (partially) disassemble upon binding to mica surfaces in HEPES/NaOH buffer, as previously observed (Junglas et al., 2020b) and confirmed here (Fig. 4.5.4 A). The results of the QCM measurements also indicated ring disassembly (Fig. 4.5.3 B,C), in line with the finding that in the absence of Mg^{2+}, IM30 rings disassemble upon membrane binding and rearrange into large and flat membrane protecting carpets upon prolonged interaction with PG bilayers (Junglas et al., 2020b).

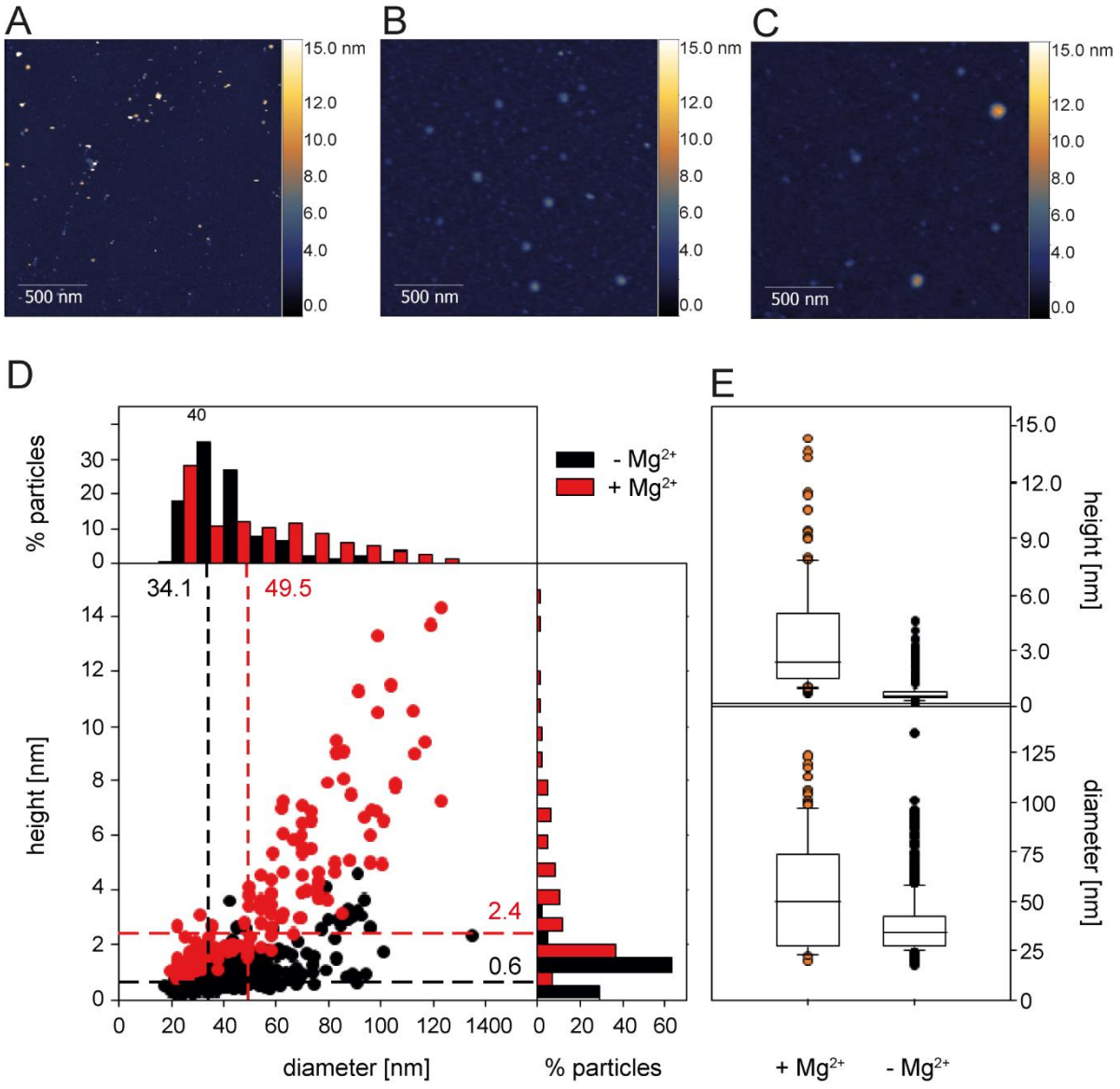

Figure 4.5.4: Dimensions of membrane-bound IM30 particles as determined from AFM topography images.

A: IM30 on mica in the absence of Mg^{2+}. **B:** IM30 on a PG SLB in the absence of Mg^{2+}. **C:** IM30 on a PG SLB in presence of Mg^{2+}. Heights are indicated in the AFM images using a false-color ruler in A, B, C. **D:** Correlation between height and diameter of IM30 *punctae* on the PG SLB in the absence (black n=614), and the presence of 10 mM Mg^{2+} (red, n=156) determined using GWYDDION particle analysis. The normalized histograms at the sides show the distribution of the particle dimensions. The dashed lines indicate the median particle dimensions: median particle diameter was 34.1 nm and 49.5 nm in absence and presence of Mg^{2+}, respectively. The median particle height was 0.6 nm and 2.4 nm, respectively. The number of particles in the absence of Mg^{2+} is higher since these layers were more stable, and a larger surface area per measurement could be scanned. Noteworthy, only *punctae* that did not show signs of defect formation (compare Fig. 4.5.5) were taken into account for the statistical analysis. **E:** The median, the 25% and the 75% quantiles are indicated by boxes, the 10% and 90% quantiles by whiskers; symbols represent outliers. Since the data are not normally distributed, the Mann-Whitney Rank Sum Test was applied. For both parameters, diameter and height, the difference in the median values between the two groups is greater than would be expected by chance, with a significance level of P = <0.001. The statistical calculations were performed with SigmaPlot (Systat Software GmbH).

In stark contrast, when membrane binding of IM30 was analyzed via AFM in presence of 10 mM Mg^{2+}, the median particle diameter was 49 nm and the distribution of diameters was very broad (Fig. 4.5.4 D).

A statistical analysis based on a rank test indicates that the difference in the median values is larger than would be expected if occurring by chance (Fig. 4.5.4 E). A similar result was found for the height distribution: the median height of the particles in presence of Mg^{2+} (2.4 nm) was significantly larger than the height in absence of Mg^{2+} based on a rank test (Fig. 4.5.4 E). Still, the determined height is smaller than the height of intact rings (Saur et al., 2017), indicating ring rearrangement and/or disassembly on the membrane surface also in presence of Mg^{2+}, albeit to a lower extent than in absence. In fact, in presence of Mg^{2+} IM30 rings are stabilized and increased ring-stacking and formation of double rings were observed in solution (Heidrich et al., 2018). The increased height of membrane-attached IM30 in presence of Mg^{2+} likely originates from stabilization of IM30 supercomplexes and membrane attachment of higher-ordered IM30 structures, explaining the higher viscoelasticity observed in the QCM measurements (Fig. 4.5.3 B,C).

In contrast to the situation in absence of Mg^{2+} (Junglas et al., 2020b, chapter 4.4), the formation of carpet structures on the membrane surface was not observed here when Mg^{2+} was present. Instead, in presence of Mg^{2+}, individual *punctae* started to flatten out over time and seem to initiate formation of a lipid bilayer defect (Fig. 4.5.5 B,C). These defects grew in size and depth and ranged from 10 - 36 nm diameter pores to larger defects spanning several hundred nm of the SLB. Some *punctae* started to form pores shortly after their appearance on the bilayer (~20–30 min), whereas other *punctae* converted into pores only after prolonged incubation times (1 – 2 h) and others remained stable over the whole experiment (5 – 6 h). Noteworthy, in absence of IM30 no membrane defects were observed (Fig. 4.5.5 A).

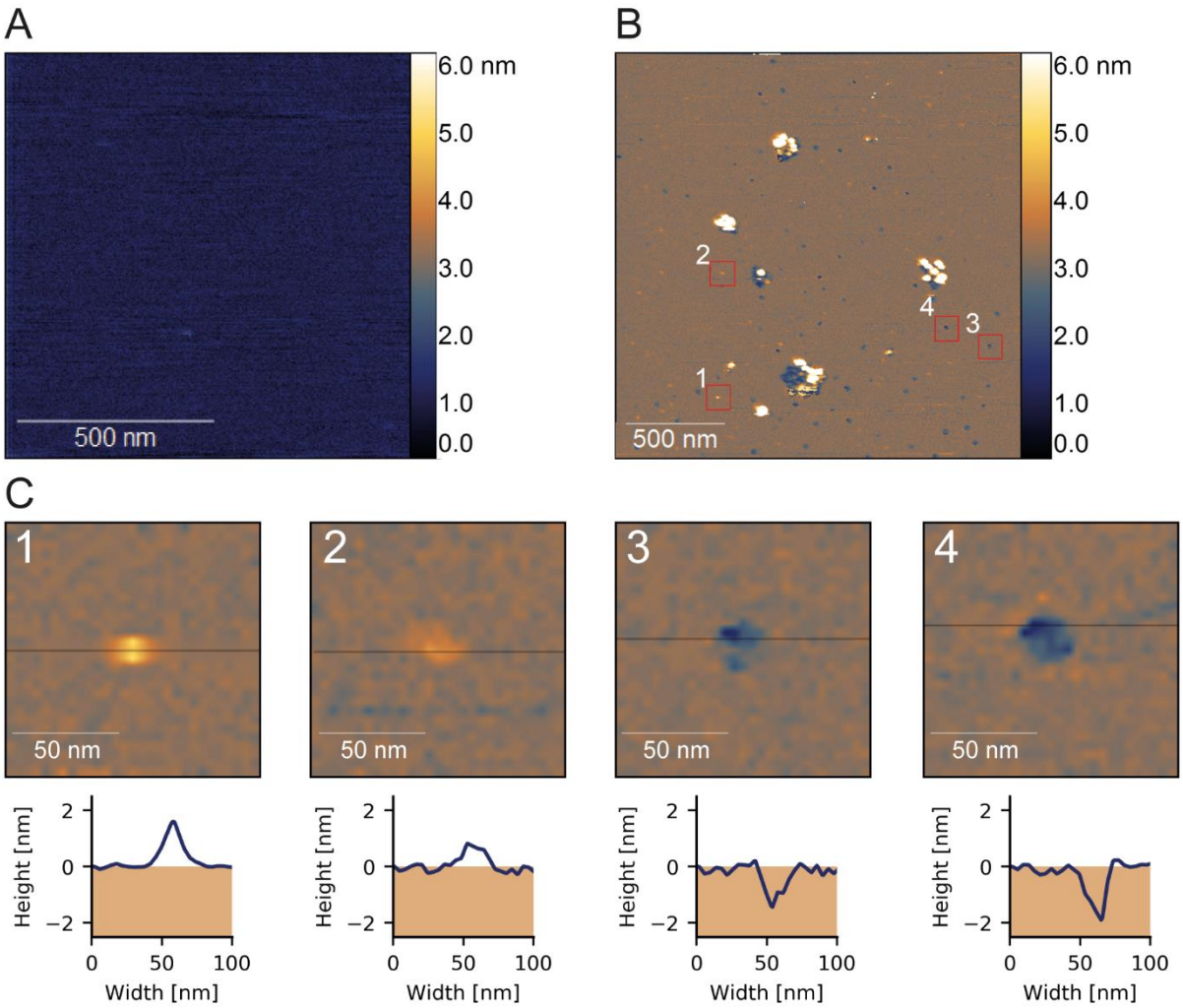

Figure 4.5.5: IM30 induces bilayer defects in the presence of Mg^{2+}.

A: AFM topography image of a PG SLB in presence of Mg^{2+} and absence of IM30: No bilayer defects were observed. **B:** AFM topography image of IM30 on a PG SLB in the presence of Mg^{2+} are shown together with false-color rulers indicating the height. Profile lines indicate the position of the cropped images shown in C**. C:** A series of details are shown with their corresponding height profiles, illustrating representative steps of IM30-mediated formation of bilayer defects.

4.5.3. Discussion

In chapter 4.4., it has been shown that IM30 forms carpet structures on negatively charged membrane surfaces that can stabilize membranes (Junglas et al., 2020b). This observation is in perfect agreement with a membrane protecting activity suggested before for IM30 and PspA family members, as well as with the formation of large membrane covering structures under (membrane) stress conditions observed *in vivo* (Gutu et al., 2018; Junglas and Schneider, 2018). Yet, IM30 has also been shown to mediate membrane fusion, at least *in vitro*, which involves membrane destabilization. However, as shown recently, Mg^{2+} is required for IM30 acting as a membrane fusion protein (Hennig et al., 2015; Heidrich et al., 2018).

Binding of IM30 to negatively charged membranes has been observed using small PG liposomes, PC/PG GUVs, and PG SLBs in the absence of Mg^{2+} (Fig. 4.5.1-4). Membrane interaction of IM30 clearly is enhanced at increased Mg^{2+} concentrations, both in case of artificial, PG-containing membranes as well as isolated cyanobacterial membranes (Fig. 4.5.1 and 2). Mg^{2+} directly binds to IM30 (Heidrich et al., 2018), resulting in a rearrangement of the IM30 structure, involving exposure of extended hydrophobic surface regions on IM30 rings, which is expected to promote membrane binding (Heidrich et al., 2018). Further effects of Mg^{2+} binding to the negatively charged membrane surface, *e. g.* formation of a "bridge" between the negatively charged lipid head groups and negatively charged residues at the protein surface, cannot be excluded. However, a mere increase in affinity would not be able to switch the function of IM30 from a membrane-stabilizing to a membrane fusion protein. Indeed, the present study shows that the structures of membrane-bound IM30 in presence *vs* absence of Mg^{2+} clearly differ: In the presence of Mg^{2+} the small-diameter *punctae* initially forming have an increased height when compared to *punctae* formed in the absence of Mg^{2+} (Fig. 4.5.4). Furthermore, the viscoelastic contribution as determined from the damping/frequency shift ratio in the QCM experiments is higher in presence of Mg^{2+} (Fig. 4.5.3 C). As described above, binding of individual rings is supposed to show more pronounced viscoelastic properties than a flattened-out carpet structure forming on the membrane surface. Thus, the observed increase in the damping/frequency shift ratio likely is related to the overall increased stability and compactness of IM30 rings observed in solution upon addition of Mg^{2+} (Heidrich et al., 2018). The mere observation that differences in the viscoelastic properties exist in presence *vs* absence of Mg^{2+} strongly indicates a difference in the IM30 structure, albeit the exact nature of these differences cannot be exactly deduced solely based on the changes in viscoelastic properties. However, via AFM, large structural changes were observed in presence of Mg^{2+}, after sufficiently long incubation times: While IM30 forms large membrane-stabilizing carpet structures on a PG membrane surface in the absence of Mg^{2+} (Junglas et al., 2020b), it induces localized bilayer defects in the presence of Mg^{2+}. These defects start as small holes within individual IM30 *puncta* and expand to larger defect structures (Fig. 4.5.5 B,C). It is fair to assume that the processes observed in the AFM measurements took also place during the time course of the QCM measurements. This explains why addition of Mg^{2+} not only decreases the contribution of viscoelasticity but also the absolute value of the frequency shift, possibly not only due to loss of trapped water but also due to the local loss of lipid material.

At present, the results here can only suggest the sequence of events leading to formation of large membrane defects (Fig. 4.5.6.). However, the AFM micrographs are in agreement with the assumption that IM30/Mg^{2+} initially binds to and stabilizes spontaneously occurring small and transient bilayer defects. Sequential local accumulation of more IM30 protomers potentially

promotes growth of the bilayer defects and might finally result in a bilayer-spanning toroidal or barrel-stave pore (Fig. 4.5.6). Similar mechanisms for pore formation were suggested for membrane destabilization via antimicrobial peptides (AMPs) (Wimley, 2010) and were in fact monitored using AFM (Hammond et al., 2020). The irregularities in size and shape of the pores support a toroidal pore model, where peptides or proteins pull lipid head groups inwards to line an inner pore wall and thus the resulting pores are lined with both peptides and lipids (Gilbert et al., 2013; Pfeil et al., 2018). Noteworthy, also formation of bilayer defects via a detergent-like lipid solubilization mechanism is discussed for many AMPs (Bechinger and Lohner, 2006; Wimley, 2010; Patel et al., 2014), and it is not yet clear which is the prevailing mechanism.

However, it is also possible that membrane-bound IM30 actively induces, rather than recognizes, bilayer defects by the charge and surface tension imbalance that goes along with asymmetric bilayer binding. Such an impact of asymmetric bilayer binding has been described for membrane remodeling intrinsically disordered proteins, which can effectively induce membrane curvature by steric/lateral pressure due to their larger steric volume compared to compact folded proteins (Fakhree et al., 2019). Indeed, IM30 appears to unfold its C-terminal part upon disassembly of the ring (chapter 4.4). Thus, it is well possible that IM30 locally bends membranes due to its asymmetric membrane binding: the soluble, intrinsically disordered IM30 domains are localized exclusively on the surface of one bilayer leaflet, and accumulation of larger protein domains at only one membrane face could result in increased steric repulsion on the membrane, inducing curvature and finally resulting in local membrane rupture.

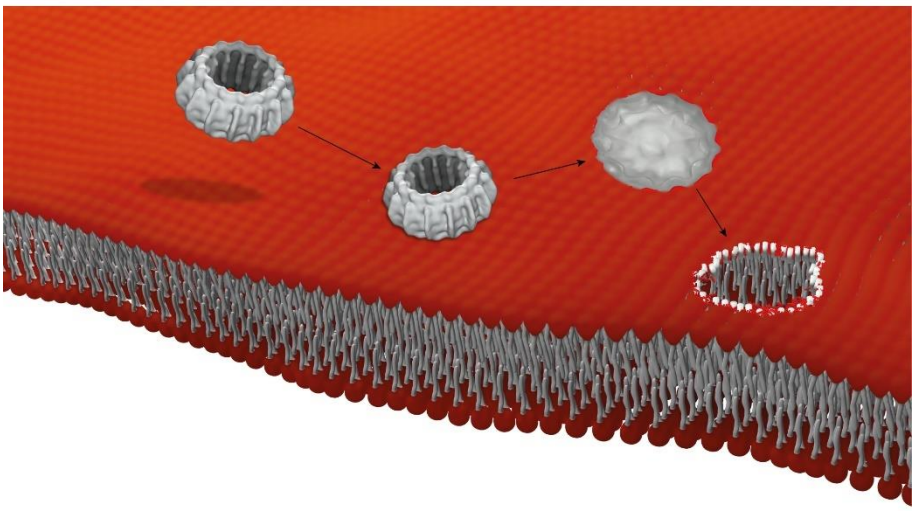

Figure 4.5.6: IM30 generates bilayer defects in the presence of Mg^{2+}.

Upon membrane binding, IM30 rings likely disassemble to a flat unordered assembly of small oligomers and a membrane pore starts to form that is likely stabilized by small IM30 oligomers at the bilayer edges. The models were created using BLENDER and CHIMERAX.

Conclusion

Mg^{2+} binding to IM30 results in an increased membrane binding propensity of IM30 as well as in an altered structure of membrane-bound IM30. While IM30 forms a membrane-protecting surface carpet in the absence of Mg^{2+}, the observations now reveal that IM30 induces bilayer defects in the presence of Mg^{2+}. The bilayer defects observed on SLBs likely trigger liposome fusion in solution. Consequently, IM30 has two (opposing) functions that are spatiotemporally controlled via Mg^{2+}-binding. In photosynthetic organisms, at low Mg^{2+} concentration in the cytosol/lumen, IM30 might mainly fulfill its membrane-chaperoning function. When the Mg^{2+} concentration increases (*e.g.* at increasing light intensity) IM30 becomes membrane fusion-competent and eventually triggers membrane remodeling. Thus, Mg^{2+}-binding switches the IM30 function from membrane protection to membrane destabilization. As the Mg^{2+} concentration within the chloroplast stroma and cyanobacterial cytoplasm, as well as the structure of TMs changes in response to alternating light conditions (Pohland and Schneider, 2019), IM30 potentially is a Mg^{2+}-controlled key component involved in the regulation of TM dynamics.

4.6. Trp71 is crucial for IM30´s membrane fusion activity

Parts of the results have been generated in a previous master thesis as listed in Table 4.6.1 under the supervision of Jennifer Heidrich (Siebenaller, 2016).

Table 4.6.1: Results of *Trp71 is crucial for IM30´s membrane fusion activity*.

Figure numbers	**Methodology, Investigation, Formal analysis**	**Data visualization**
Fig. 4.6.1-3, 4.6.7-9 Fig. 4.6.4-6	**this thesis** **CS** (Siebenaller, 2016)	**this thesis** **this thesis**

4.6.1. Introduction

Until recently, only limited information on the tertiary structure of IM30 was available. A PspA fragment (amino acids 1-144) has been crystallized in 2015 (Osadnik et al., 2015), and cryo-EM structures of IM30 are only available since 2021 (Gupta et al., 2021; Junglas et al., 2021; Liu et al., 2021). The high-resolution structures now confirm, that the IM30 helices 2 and 3 form a large coiled-coil structure as suggested earlier (Saur et al., 2017), and that this region is an essential part of the IM30 layer-like structure. Still, the resolution of the cryo-EM structure does not allow to completely analyze intramolecular interactions of amino acids within the ring. Thus, a useful tool to identify structural and functional important amino acids still is to mutate highly conserved amino acids and monitor changes in the structure and activity of IM30.

This study demonstrates that the IM30 residue Trp71 is highly conserved in members of the PspA/IM30-family and is crucial for the IM30 structure and function. Two Arg residues were identified as potential interaction partners, which likely contribute to the stabilization of the coiled-coil region of IM30 via cation-π-interactions. The relevance of the amino acids Trp71, Arg74 and Arg93 for the IM30 structure, Mg^{2+}- and membrane interactions was analyzed *in vitro*. The results show that the mutations W71A, R74A and R93A impair the IM30 stability as well as IM30 oligomerization. Finally, it was shown that Trp71 is crucial for the membrane fusion activity of IM30 *in vitro*.

4.6.2. Results

4.6.2.1. Trp71 is highly conserved in IM30/PspA

In this study, highly conserved amino acids with potential relevance for the structure and function of IM30 were identified via sequence alignment of the PspA/IM30 family members. The coiled-coil hairpin region of helix 2 and 3 is so far the best-studied structure of IM30/PspA (Osadnik et al., 2015; Thurotte and Schneider, 2019) and forms the core of the ring structure (Gupta et al., 2021; Junglas et al., 2021; Liu et al., 2021). Noteworthy, also proteins of the related ESCRT III-family have a similar coiled-coil structure (Liu et al., 2021). Thus, the focus of my analysis was set on this protein region.

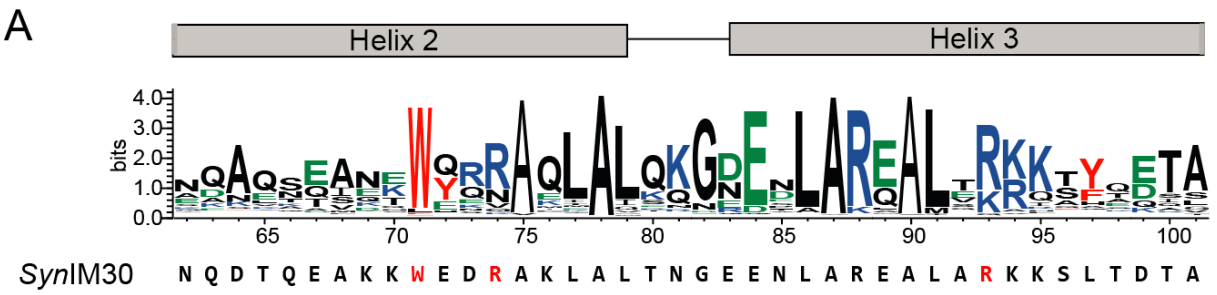

B

*Syn*IM30	N Q D T Q E A K K W E D R A K L A L T N G E E N L A R E A L A R K K S L T D T A
*Ara*IM30	K A A Q Q S S D D W Y K R A Q L A L A K G D E D L A R E A L K R R K S F A D N A
*Cr*IM30	K Q A Q T T A D D W L R R A E L A V Q K G E D D L A K E A L K R R K T Y Q E Q A
*Syn*PspA	D A Q Q L I A Q R W Y E K A Q A A L D R G N E Q L A R E A L G Q R Q S Y Q S H T
*Eco*PspA	E Q A S A R E V E W Q E K A E L A L L K E R E D L A R A A L I E K Q K L T D L I

Figure 4.6.1: Sequence analysis of the PspA/IM30 helix 23 region.

A: Sequence alignment of cyanobacterial PspA/IM30 family members was performed using the PFAM database (protein family PF04012, cyanobacteria: 322 sequences, 132 species) (El-Gebali, Sara et al, 2019). The secondary structure prediction is shown above the sequence logo representation. A high conservation was revealed for Trp71 (*Synechocystis* IM30 counting). The sequence logo representation was prepared using WebLogo3 (Crooks et al., 2004). A score of 4.32 bits reflects full conservation, a score of 0 no conservation of the amino acid at this position. Color code: red = aromatic residue, blue = positively charged, green = negatively charged. **B:** Trp71 is conserved in various IM30/PspA sequences from cyanobacteria, plants and algea (*Syn*IM30: *Synechocystis* sp. PCC 6803 (Uniprot Q55707), *Ara*IM30: *Arabidopsis thaliana* (Uniprot O80796), *Cr*IM30: Chlamydomonas rheinhardtii (Uniprot Q66YD0), *Syn*PspA: *Synechocystis* sp. PCC 6803 (Uniprot P74717), *Eco*PspA: *Escherichia coli* K-12 (Uniprot P0AFM6).

The sequence analysis of the cyanobacterial PspA/IM30 family revealed a highly conserved Trp located at the end of helix 2 (*Synechocystis* IM30: Trp71) (Fig. 4.6.1 A) (El-Gebali et al., 2019). While Trp71 is the only highly conserved amino acid in the region ranging from amino acid 62 to 74, an overall strong sequence conservation was observed from amino acid 75 to 95. As expected, Trp71 can also be found in IM30 from plants (*Ara*IM30), algae (*Cr*IM30), and even in PspA of *Synechocystis* or *E. coli* (*Syn*PspA, *Eco*PspA) (Fig. 4.6.1 B). As the structure and function of IM30 and PspA are assumed to be conserved to some extent in the whole protein family, the conservation of Trp71 in various species is a strong indication for the functional and/or structural relevance of this amino acid.

4.6.2.2. Arg74 and Arg93 are potential interaction partners of Trp71

To analyze potentially interacting amino acids of the highly conserved Trp71, the IM30 structure derived from recent cryo-EM studies was used (Gupta et al., 2021). Since IM30 forms rings with variable rotational symmetries, the monomer structures differ to some extent depending on the ring symmetry. As the structure of the IM30 ring with C16-symmetry is best resolved so far, this structure was used to analyze Trp71 in the following (PDB 7O3Y).

The IM30 monomers are mainly α-helical and have an elongated shape. As predicted before, helices 2 and 3 form a coiled-coil structure, which differs only minorly depending on the IM30 layer. According to the now available structure, Trp71 (helix 2) is located between helix 2 and 3, but the indol-ring of the Trp is actually not located at the direct interface (Fig. 4.6.2 A). The Arg residues Arg74 on helix 2 and Arg93 on the opposing helix 3 were identified in close distance (<5 Å) to the Trp side chain as potential interaction partners in all layers. Hence, the amino groups of the Arg residues could form a cation-π-interaction with the aromatic indol-ring of the Trp (Gallivan and Dougherty, 1999). Noteworthy, the resolution of the structure required molecular dynamics to model the orientation of the amino acid residues. Consequently, the orientation might be different to some extent.

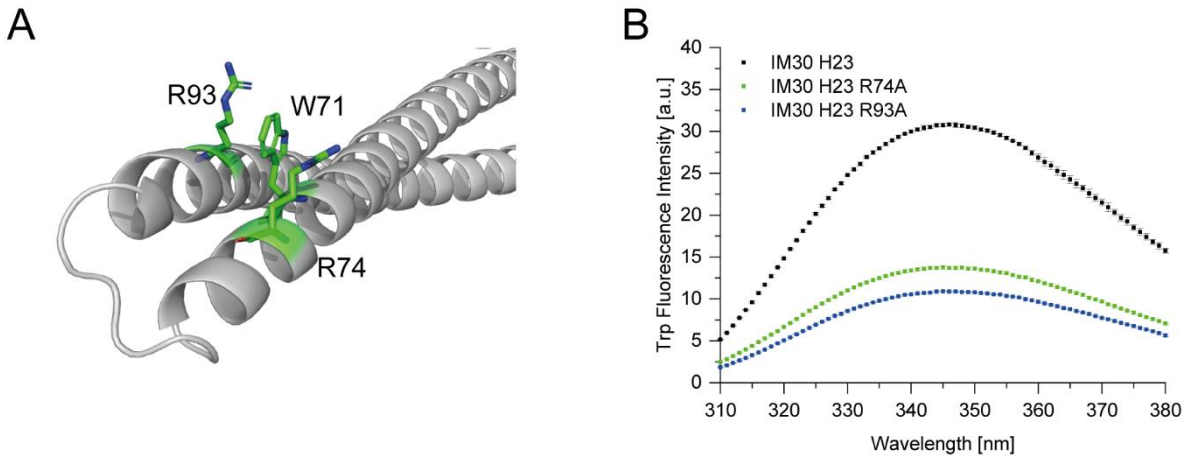

Figure 4.6.2: Arg74 and Arg93 are potential interaction partners of Trp71.

A: The figure shows the IM30 monomer of layer 1 from an IM30 ring with C16-symmetry (PDB 7O3Y). Trp71, Arg74 and Arg93 are located in between helices 2 and 3, but not at the direct interface. Trp71 and Arg74 or Arg93 are in close distance (Trp71-Arg93: 4.71 Å, Trp71- Arg74: 3.85 Å) and can potentially interact via cation-π-interaction. **C:** The Trp fluorescence emission intensity is reduced in the shortened IM30 variants IM30 H23 R74A and IM30 H23 R93A. This indicates a change in the Trp micro-environment.

The IM30 intrinsic Trp fluorescence was monitored to experimentally confirm the proximity of the Arg residues to the Trp in IM30. As changes of the intrinsic Trp fluorescence typically reflect changes in the Trp microenvironment (Hellmann and Schneider, 2019), the replacement of interacting amino acids most likely leads to an altered Trp fluorescence. Note that Trp71 is the only Trp in IM30, which allows to directly draw conclusions on its defined microenvironment. To analyze the Trp environment, IM30 variants containing only the coiled-coil forming helix 2 and 3 (IM30 H23) with mutations of Arg74 or Arg93 to the small, uncharged amino acid Ala were heterologously expressed in *E. coli and* purified. (Thurotte and Schneider, 2019). Since the IM30 IM30 H23 variant was shown to form only monomers or dimers instead of larger ring structures (Thurotte and Schneider, 2019), the influence of a potentially altered oligomerization caused by the R74A/R93A mutation was minimized. Indeed, a drastically changed Trp fluorescence of IM30 H23 R74A and IM30 H23 R93A was observed when compared to IM30 H23 (Fig. 4.6.2 B). The Trp fluorescence intensity was strongly decreased in case of both IM30 variants, which is typically ascribed to an increased solvent exposure of the Trp (Hellmann and Schneider, 2019).

These results indicate that Arg74 and Arg93 likely interact with Trp71 in the isolated coiled-coil structure. Still, since the IM30 variant IM30 H23 also forms dimers, it cannot be completely excluded that a potentially missing dimerization causes the observed change of the Trp environment. Although Arg74 and Arg93 are not as specifically conserved as Trp71, nevertheless high conservation of

positively charged amino acids around region 73-74 and 93-95 was observed in the sequence alignment of the cyanobacterial IM30/PspA family (Fig. 4.6.1 A, B).

4.6.2.3. Trp71, Arg74, and Arg93 stabilize the IM30 H23 coiled-coil structure

To analyze a potential impact of a Trp71 interaction with Arg 74 or 93 on the stability of the helix 23 hairpin, the structure of the short-length IM30 variants with the mutations W71A, R74A or R93A was analyzed via CD-spectroscopy.

At 20 °C, the spectra of all IM30 H23 proteins exhibited the minima at 208 nm and 222 nm characteristic for an α-helix, while the shape of the spectra was altered to some extent (Fig. 4.6.3 A). The thermodynamic stability of the secondary structure was investigated next via monitoring the secondary structure from 15 to 95 °C. Unfolding of IM30 was monitored using the α-helical peak at 222 nm. For IM30 H23 W71A and R74A, a drastic decrease of the thermal stability was observed in comparison to the not mutated IM30 H23 protein (Fig. 4.6.3 B,C). While all denaturation curves show the typical sigmoidal shape (Fig. 4.6.3 C), a shift to lower temperatures was observed for the IM30 H23 mutants. The transition point T_m of the IM30 H23 denaturation curve was calculated to be 52.3 ± 0.5 °C. In contrast, the T_m of the W71A and R93A mutants did strongly decrease to 44.1 ± 0.4 °C or 47.3 ± 0.2 °C, respectively (Fig. 4.6.3 C). In contrast, the R74A mutant showed no altered T_m (53.6 ± 0.6 °C).

Thus, (at least) the amino acids Trp71 and Arg93 seem to contribute to the intramolecular stability of the isolated coiled-coil of helices 2 and 3.

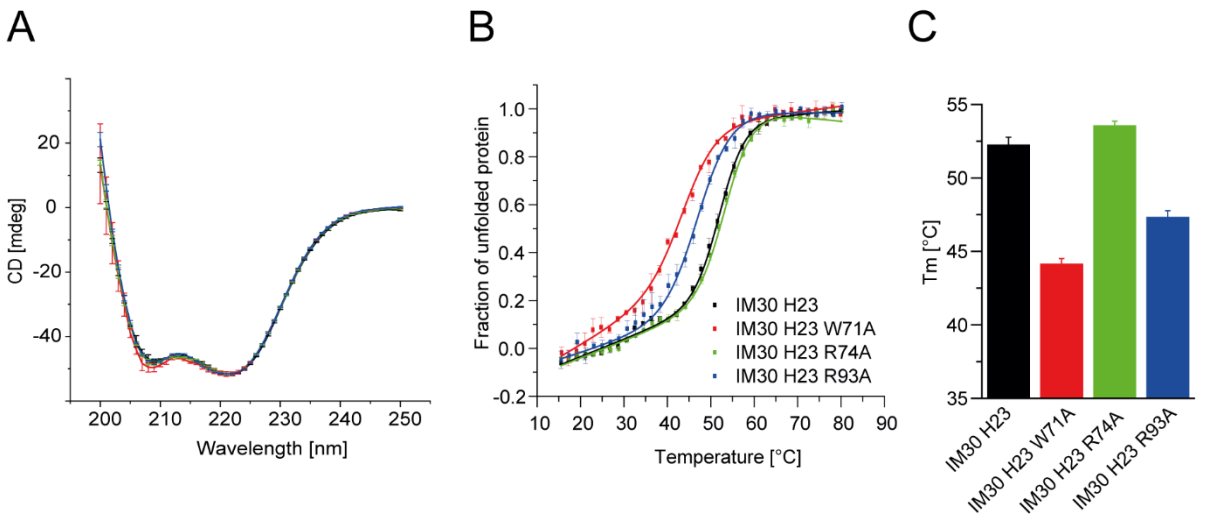

Figure 4.6.3: Trp71, Arg74, and Arg93 stabilize the IM30 secondary structure of isolated IM30 coiled-coil structure.

A: The structure of IM30 H23, H23 W71A, R74A and R93A was analyzed via CD-spectroscopy. For all proteins, a spectrum typical for α-helices was observed. **B:** Thermal denaturation of IM30 H23 wt, W71A, R74A and R93A was monitored by CD-spectroscopy following the signal at 222 nm at increasing T´s. The raw signal was converted to the fraction of unfolded protein. N=3, error bars represent SD. **C:** Fitting the data with an adapted Boltzmann-fit yielded the following T_m´s: 52.3 ± 0.5 °C (IM30 H23), 44.1 ± 0.4 °C (IM30 H23 W71A), 53.6 ± 0.6 °C (IM30 H23 R74A) and 47.3 ± 0.2 °C (IM30 H23 R93A). Error bars represent errors from the fitting of the data.

4.6.2.4. Trp71, Arg74, and Arg93 stabilize the IM30 secondary structure

We next analyzed the influence of Trp71, Arg74 and Arg93 on the structure and function of the full-length IM30. As IM30 forms oligomeric ring structures, analyzes of the full-length protein might differ from the analysis of the isolated coiled-coil structure.

IM30 is a largely α-helical protein (Fuhrmann et al., 2009a; Gupta et al., 2021; Liu et al., 2021). Consequently, at 20 °C the CD-spectra of all here analyzed IM30 variants indicated a mainly α-helical structure with small differences of the shape (Fig. 4.6.4 A). This suggests that all full-length proteins are correctly folded.

We next analyzed the thermodynamic stability of the full-length proteins using a temperature gradient from 15 to 95 °C. For all mutants, a strong decrease of the thermal stability was observed in comparison to the wt protein (Fig. 4.6.4 B,C). The transition point T_m of the IM30 wt denaturation curve was calculated to be 59.8 ± 0.2 °C. In contrast, the T_m of the W71A and R93A mutants did decrease to 51.4 ± 0.3 °C or 53.5 ± 0.2 °C, respectively (Fig. 4.6.4 C). The mutant R74A showed a moderately reduced T_m of 56.4 ± 0.2 °C.

Thus, the amino acids W71A, R74A and R93A seem to contribute to the stabilization of the full-length IM30.

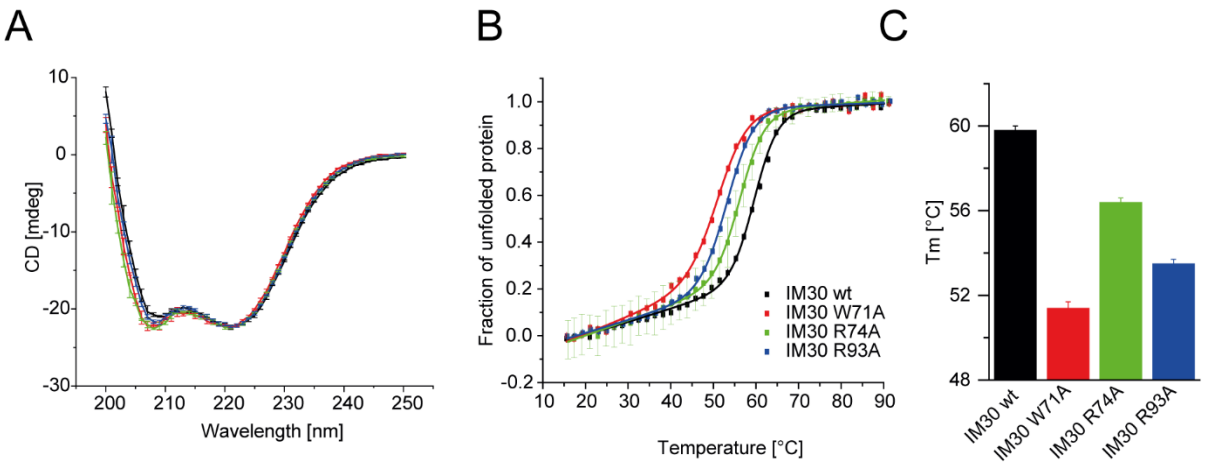

Figure 4.6.4: Trp71, Arg74, and Arg93 stabilize the full-length IM30 protein.

A: The structure of IM30 wt, W71A, R74A and R93A was analyzed via CD-spectroscopy. For all proteins, a spectrum typical for α-helices was observed. **B:** Thermal denaturation of IM30 wt, W71A, R74A and R93A was monitored by CD-spectroscopy at 222 nm. The raw signal was converted to the fraction of unfolded protein. N=3, error bars represent SD. **C**: Fitting the data with an adapted Boltzmann-fit yielded T_m`s of: 59.8 ± 0.2 °C (IM30 wt), 51.4 ± 0.3 °C (W71A), 56.4 ± 0.2 °C (R74A) and 53.5 ± 0.2 °C (R93A). Error bars represent errors from the fitting of the data.

4.6.2.5. IM30 mutants display an impaired oligomerization tendency

Oligomerization into large, ring-like structures is a characteristic feature of all members of the PspA/IM30-family (Thurotte et al., 2017). The oligomerization state likely has an impact on the IM30 function (recently reviewed in Siebenaller et al., 2019).

We analyzed the oligomeric structure of the full-length IM30 wt protein as well as of the W71A, R74A and R93A mutants using negative-stain EM (Fig. 4.6.5 A). Micrographs of IM30 wt show predominantly the typical ring structures with diameters of about 30 nm and small rod-like structures. Considerably less ring structures were observed for the IM30 W71A, R74A and R93A mutants. Instead, lots of smaller particles were detected with a size of about 10 nm. Those particles may consist of smaller oligomers, possibly unable to oligomerize further into ring structures. In case of IM30 R74A and R93A, even high amounts of large malformed aggregates were observed. This

further hints for an impaired oligomerization of the IM30 mutants, showing the high relevance of the Trp71, Arg74 and Arg93 for oligomerization of IM30.

As the TEM micrographs only represent a small fraction of the whole sample, the mean particle size was next analyzed via dynamic light scattering (DLS) (Fig. 4.6.5 B). The mean diameter of the IM30 wt particles was determined as 38 ± 7 nm, which is in good agreement with the ring-diameter of about 30 nm determined by EM, taking into consideration that the determined diameter corresponds to a hypothetical sphere with the same diffusion coefficient. The mean diameter of the W71A and R74A mutants was strongly reduced to 15 ± 2 nm and 20 ± 12 nm, respectively. The mean diameter of the R93A mutant was only minor reduced to 30 ± 10 nm. Note that this does not necessarily correspond to correctly formed ring structures, but eventually also to malformed aggregates.

These results, combined with the observations from the EM imply that the W71A, R74A and R93A mutations strongly affect the oligomerization of IM30.

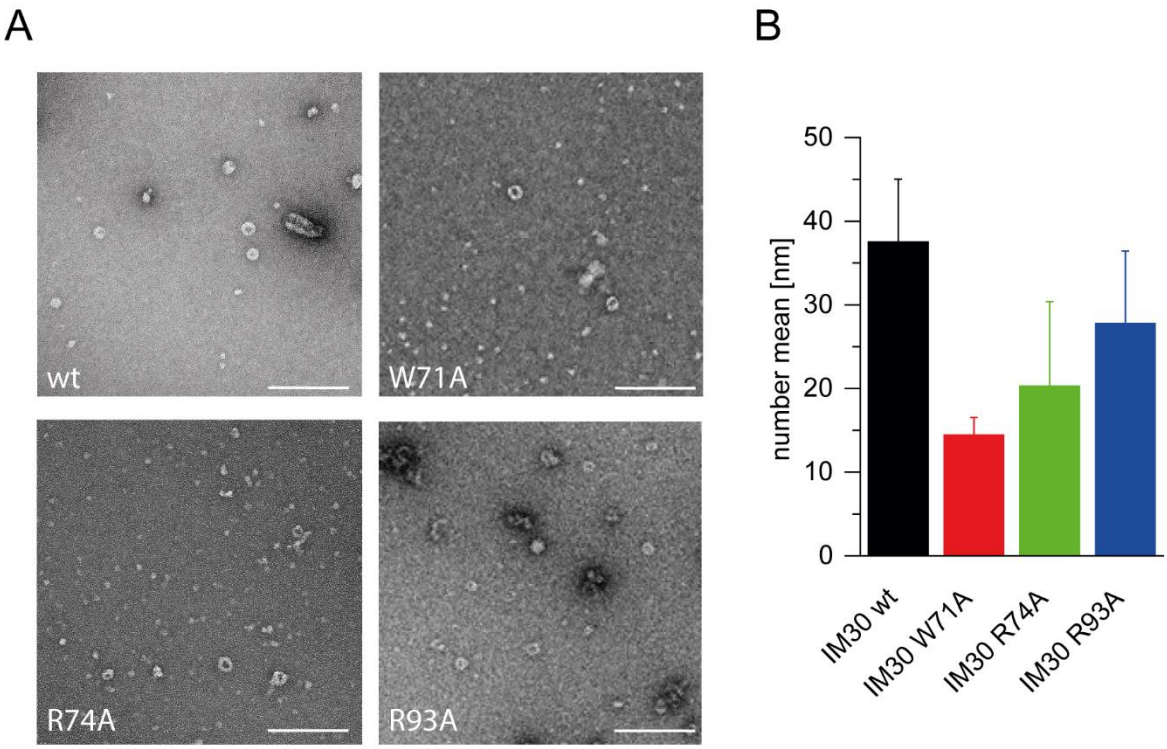

Figure 4.6.5: The oligomerization of IM30 W71A, R74A and R93A is impaired.

A: The structure of IM30 wt, W71A, R74A and R93A was analyzed via negative stain electron microscopy. While all mutants show some IM30-typical ring structures, also smaller aggregates were observed. The scale bar represents 200 nm. The experiments were performed in cooperation with Dr. Wolfgang Gebauer. **B:** The mean particle diameter was determined by dynamic light scattering (DLS). The particle size analyzed by the number mean of the mutants IM30 W71A, R74A and R93A was reduced in comparison to the IM30 wt. N=9, error bars represent SD.

4.6.2.6. The W71A, R74A and R93A mutations do not affect Mg^{2+}-induced structural rearrangement of IM30 oligomers

The membrane fusion activity of IM30 depends on Mg^{2+} (Hennig et al., 2015). Mg^{2+} is not only necessary for the membrane fusion process in general, but also binds to IM30 followed by a structural rearrangement of the protein structure (Heidrich et al., 2018). As this seems to be a prerequisite for membrane fusion, it was next analyzed whether a mutation of Trp71, Arg74 or Arg93 interferes with the IM30-Mg^{2+} interaction.

The interaction of IM30 with Mg^{2+} leads to an increase of hydrophobic surfaces, which can be monitored via following ANS fluorescence as shown previously (Heidrich et al., 2018). In absence of Mg^{2+} a decreased ANS fluorescence was observed in case of the W71A, R74A and R93A mutants compared to the IM30 wt protein (Fig. 4.6.6). This indicates that the mutants might have less exposed hydrophobic surfaces, due to changes in their oligomeric assembly state, as indicated by the negative-staining electron micrographs (Figure 4.6.5). Nevertheless, after addition of Mg^{2+}, all mutants showed the typical increase in the ANS fluorescence, as observed with the IM30 wt protein (Fig. 4.6.6 B), showing that all proteins do interact with Mg^{2+} accompanied by an increase of exposed hydrophobic surfaces.

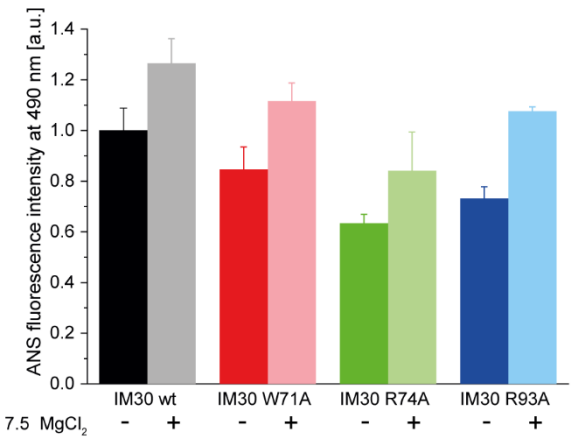

Figure 4.6.6: The interaction of IM30 wt, W71A, R74A and R93A with Mg^{2+} leads to an increased exposure of hydrophobic surfaces.

The exposure of hydrophobic surfaces was analyzed via monitoring ANS fluorescence. The addition of Mg^{2+} leads to an increased exposure of hydrophobic surfaces of IM30 wt, W71A, R74A and R93A. This indicates binding of Mg^{2+} to all here analyzed IM30 variants. N=3, error bars represent SD.

4.6.2.7. W71A, R74A and R93A mutation affect IM30 membrane binding

IM30 binds to membranes containing negatively charged lipids (Hennig et al., 2015). In order to evaluate the membrane fusion activity of the IM30 W71A, R74A and R93A mutants, their membrane binding affinities were studied and compared to the IM30 wt next. As shown before, IM30 binding to liposomes can be determined via following the Laurdan fluorescence. The ΔGP calculated from the Laurdan fluorescence spectra typically reflect changes of the lipid order as e.g. occurs when IM30 is binding to membranes (Heidrich et al., 2016).

We used Laurdan-labeled liposomes (40:60 PG/MGDG) as TM-mimicking model membranes (Hennig et al., 2015). The results show increasing GP-values with increasing concentrations of the IM30 wt and mutants which clearly indicates membrane binding. Via fitting (Heidrich et al., 2016) a K_D of 4.5 ± 1.1 µM was determined for the IM30 wt protein. In case of the W71A and R74A mutants, a lowered membrane binding affinity was observed with a K_D of about 10.6 ± 1.6 µM (W71A) and 10.0 ± 1.6 µM (R74A). Binding of the IM30 R93A mutant to the membrane seems to be rather weak, and no K_D can be calculated at the used experimental conditions. Despite the impaired membrane binding affinities of the W71A, R74A and R93A mutants, all mutants are still able to bind to TM model membranes.

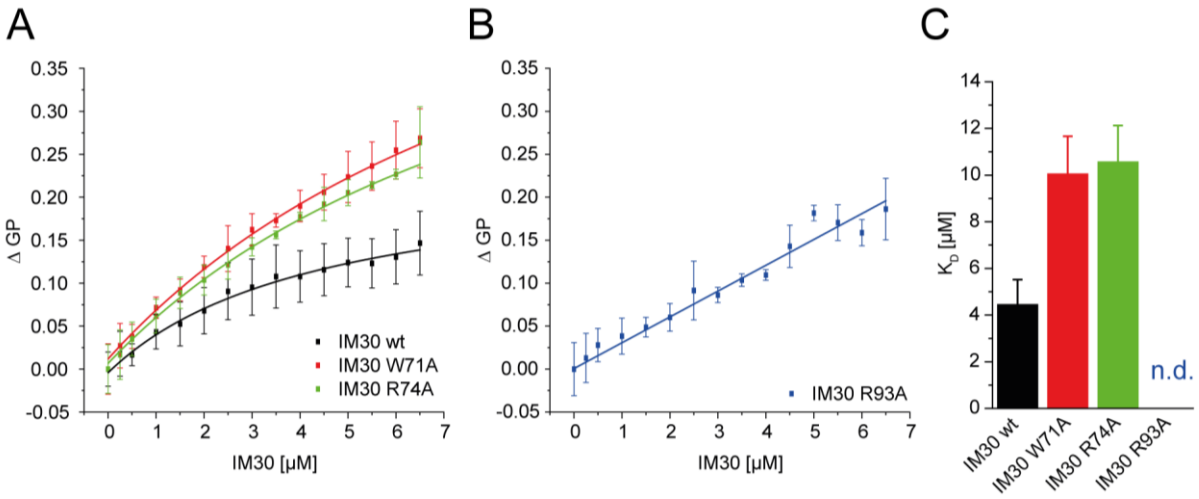

Figure 4.6.7: The membrane binding affinity of IM30 W71A and R74A is 2fold lower than the IM30 wt.

A, B: Steady-state membrane binding of IM30 was measured via monitoring changes in the Laurdan fluorescence using IM30 wt (black), W71A (red), R74A (green), all shown in (A) and R93A (blue) shown in (B). The Laurdan ΔGP values at constant 0.1 mM lipid (40% PG/60% MGDG) and 0–6 µM IM30 were increased for the mutant proteins compared to the wt. (Heidrich et al., 2016). N=3, error bars represent SD. **C:** IM30 wt binds to the model membranes with a K_D = 4.5 ± 1.1. For IM30 W71A a K_D = 10.6 ± 1.6, and for IM30 R74A a K_D of 10.0 ± 1.6 was calculated. For the interaction of IM30 R93A with the PG/MGDG membrane (B), no K_D could be calculated under the used experimental conditions. N=3, error bars represent SD.

4.6.2.8. Trp71 is crucial for the membrane fusion activity of IM30

IM30 triggers membrane fusion in presence of Mg^{2+}, at least *in vitro* (Hennig et al., 2015). Consequently, the membrane fusion activity of the W71A, R74A and R93A mutants was analyzed next. As shown before, the mutants seem to fulfill the basic requirements needed for membrane fusion: membrane binding and Mg^{2+} interaction. Thus, fusion was next analyzed by a FRET-based liposome fusion assay (Hennig et al., 2015).

Actually, no membrane fusion activity was observed for the IM30 W71A mutant (Fig. 4.6.8). The initial fusion rate was calculated as 0.018 ± 0.003 % s^{-1}. In contrast, the rate of the IM30 wt was calculated as 0.133 ± 0.027 % s^{-1}. The IM30 R74A and R93A mutants showed very low fusion rates of 0.028 ± 0.014 % s^{-1} or 0.025 ± 0.017 % s^{-1}, respectively. While IM30 wt-induced membrane fusion reached about 100% after 1000 s, the mutants triggered membrane fusion to less than 20%.

In summary, it could be shown that the highly conserved residue Trp71 is crucial for the IM30 protein structure, which is significantly affecting the membrane fusion activity of IM30. The results further indicate that the potentially interacting amino acids Arg74 and Arg93 seem to be important for the IM30 structure and fusion function.

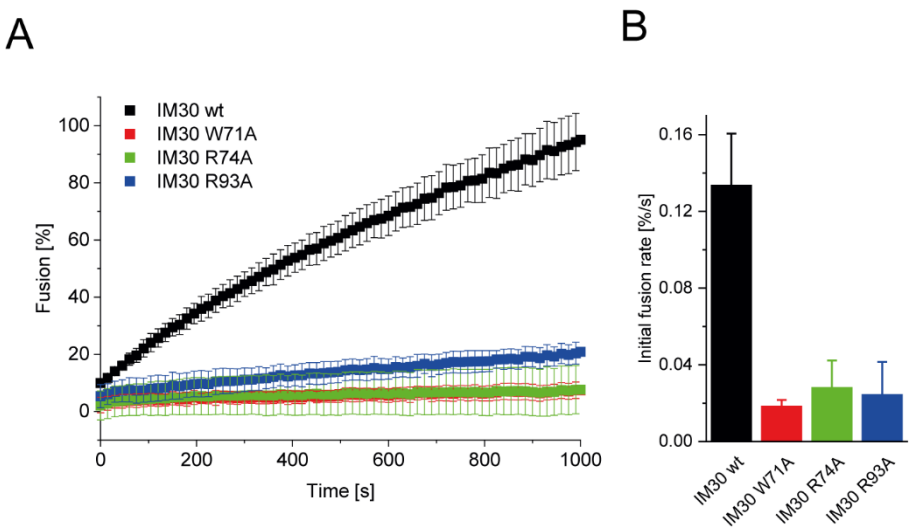

Figure 4.6.8: Trp71, Arg74 and Trp93 are crucial for membrane fusion.

A: 2.5 µM IM30, 7.5 mM Mg^{2+} and 0.1 mM PG/MGDG (40:60) liposomes were mixed and analyzed by a FRET-based membrane fusion assay. In contrast to the IM30 wt, the IM30 mutants W71A, R74A and R93A show only little membrane fusion activity. N=3, error bars represent SD. **B:** The initial fusion rates were calculated as the slope of the fusion curves in the first 50 s. N=3, error bars represent SD.

4.6.3. Discussion

4.6.3.1. Trp71 is highly conserved in PspA/IM30

Our analysis shows that Trp71 is a highly conserved within members of the cyanobacterial IM30/PspA family (Fig. 4.6.1). While Trp71 was not identified as a highly conserved and structural important amino acid in a previous report (Osadnik et al., 2015), Trp71 is also present in IM30 of *Arabidopsis thaliana* or *Chlamydomonas rheinhardtii* or even in PspA of *Synechocystis* or *E. coli* (Fig. 4.6.1. B). With focus on helix 2 and 3, Trp71 can be considered as a highly conserved amino acid, especially taking into account the overall low conservation of the amino acids 62-74 in cyanobacterial IM30 (Fig. 4.6.1. A), but also within the entire IM30/PspA family (Osadnik et al., 2015).

Interestingly, based on the recently published IM30 structure (Gupta et al., 2021), the position of the indol ring of Trp71 is in between the helices 2 and 3 (Fig. 4.6.2), possibly enabling an intramolecular stabilization of the coiled-coil region via interactions with other residues. A previous report assumed Trp71 to be buried within the IM30 structure and not exposed to the surface, which is a clear hint for intramolecular interactions (Heidrich et al., 2018). Although Trp71 is actually not located directly at the interface between helices 2 and 3, the results here suggest an important role of this residue for the structure of IM30.
Because of its very pronounced position and the high conservation of Trp71, the putative role of this amino acid for the structure and function of IM30 was analyzed using the full-length IM30 protein as well as the isolated IM30 coiled-coil forming helices 2 and 3.

4.6.3.2. Trp71 is important for the structure of IM30

The secondary structure of IM30 W71A is mainly α-helical (Fig. 4.6.4 A), as reported for the IM30 wt protein (e.g. Heidrich et al., 2018) indicating correct folding of the mutant.

Yet, the thermodynamic stability of the W71A mutant was strongly decreased compared to the wt, again for the H23 fragment as well as the full-length IM30 (Fig. 4.6.3 C,D; Fig. 4.6.4 C,D). A possible explanation is that the stability of the secondary structure is decreased upon mutation because of the weakened interaction between the coiled-coil forming helices 2 and 3. Yet, the missing contribution of only 1 or 2 cation-π-interactions may not cause the observed drastic difference in the T_m of about 10 °C (Fig. 4.6.4 D). A different explanation could be the observed impaired oligomerization of the W71A mutant (Fig. 4.6.5). It seems reasonable that ring formation increases

the thermodynamic stability of IM30 because of additional interactions establishing between the monomers, as discussed recently (Thurotte and Schneider, 2019). Yet, also in case of the short-length mutants a decreased thermodynamic stability was observed for the H23 W71A protein, which likely only forms monomers or dimers (Thurotte and Schneider, 2019). These results clearly show the importance of Trp71 for the structural stability of the coiled-coil forming helix 23, but also of the oligomeric structure of the protein. Consequently, a correctly folded H23 hairpin seems to be essential for the correct ring formation and a stabilized monomer structure.

An impaired oligomerization of IM30 W71A has been observed via electron microscopy and in DLS analysis (Fig. 4.6.5). While IM30 wt showed the typical ring structures (Saur et al., 2017), IM30 W71A showed fewer ring structures and additionally small particles. These particles could resemble small oligomeric structures. Hypothetically, these smaller oligomers could be the result of an impaired ring assembly. The decreased hydrophobic surface of the mutant, as seen in the ANS fluorescence analysis (Fig. 4.6.6), is a further hint for a different oligomeric state.

4.6.3.3. Trp71 is crucial for the IM30 membrane fusion function

IM30 is able to fuse TM model membranes in presence of Mg^{2+} (Hennig et al., 2015). The interaction of IM30 with Mg^{2+} and with TM mimicking membranes is a prerequisite for this function. While no major difference in the IM30-Mg^{2+} interaction was observed for the IM30 W71A mutant (Fig. 4.6.7), a lowered membrane binding affinity was determined for the W71A mutant. Although it has been observed that the formation of higher oligomers in general reduces the membrane binding affinity (Heidrich et al., 2016), the results here show that the lower oligomeric structures of Trp71 do not have an increased membrane binding propensity. This might be due to malformed small oligomers/aggregates that bury the membrane interacting regions within the complex. Nevertheless, IM30 W71A was still able to bind to the membrane with an about 2fold lower affinity (Fig. 4.6.7).

As shown in Fig. 4.6.9, the hairpin is facing the outside of the ring. This is not in line with previous models, which assumed this region to be at the bottom of the ring (Saur et al., 2017). If IM30 is binding to the membrane first as a ring, as suggested by earlier studies, this region is at first not directly exposed to the membrane, questioning the importance of this region for membrane binding. Yet, since IM30 de-oligomerizes on the membrane (Junglas et al., 2020b, chapter 4.4), this region might still interact directly with the membrane, which could explain the reduced membrane binding affinity of the W71A, R74A and R93A mutants.

Despite the general ability of the IM30 W71A mutant to interact with Mg^{2+} and the membrane, the IM30 mutant was not at all able to trigger membrane fusion of the TM model membranes in presence of Mg^{2+} (Fig. 4.6.8). The results suggest that the missing fusion activity of IM30 W71A is based on the impaired oligomeric structure. This further supports the assumption that an intact IM30 ring structure is absolutely necessary for IM30-mediated membrane fusion as discussed recently (Siebenaller et al., 2019). IM30 W71A does neither form a sufficient amount of correctly folded ring structures (Fig. 4.6.5) nor expose the fusogenic H23 region that triggers membrane fusion without the context of IM30 rings (Thurotte and Schneider, 2019).

4.6.3.4. Arg74 and Arg93 likely interact with Trp71

Via inspection of a modeled IM30 structure (Fig. 4.6.2), Arg74 and Arg93 were identified as amino acids potentially interacting with Trp71. Both are in distance of less than 5 Å to Trp71, which is usually assumed to be close enough for cation-π-interactions. Still, since the orientation of the amino acid side chains was modeled via molecular dynamic simulations, this might not represent the exact structure. Experimentally, a change of the Trp71 microenvironment was demonstrated when the wt helical hairpin H 23 as well as the H23 mutants R74A and R93A were analyzed (Fig. 4.6.2 C,D), which is a clear hint for the close distance of the Arg residues to the Trp.

As Arg74 is located on helix 2 together with Trp71, interaction between these two amino acid side-chains can probably only stabilize the position of Trp71. In contrast, Arg93 is located on helix 3 and interaction with Trp71 could actually mediate a connection between helix 2 and 3.
We further analyzed the full-length and the H23 IM30 variants R74A and R93A to evaluate whether an absence of the Trp71 indole side-chain alone or missing potential interactions are responsible for the impaired structure and function of a W71A mutant. Whereas the observed effects on the structure and function were, in general, more pronounced for the W71A mutant, also the R74A and R93A mutants showed impaired thermal stability (Fig. 4.6.3; Fig. 4.6.4), decreased oligomerization tendency (Fig. 4.6.5) and decreased membrane binding and fusion (Fig. 4.6.7; Fig. 4.6.8). In case of R93A, the membrane binding affinity was even lower compared to IM30 W71A. This might be due to a high amount of malformed aggregates that were observed in EM images and probably the cause for the relatively large diameter detected via DLS (Fig. 4.6.5). Based on the results, it can be hypothesized that interactions of Trp71 are important for the structure and function of IM30, and that Arg74 and Arg93 might contribute by stabilizing the orientation of Trp71 between helix 2 and 3.

4.6.3.5. Trp71 might interact with Phe191 or Glu194

Since the impacts of the W71A, R74A and R93A mutations on the IM30 structure might not exclusively be explained by missing cation-π-interactions in the coiled-coil structure of a monomer, I additionally tried to identify further putative interactors within the IM30 oligomer (C16-ring symmetry) (Fig. 4.6.9).

The region encompassing Trp71-Arg93 is located at the outside of the ring within the spike structure (Fig. 4.6.9 A). In the cross-section of the ring, the relevance of this region for the ring structure is obvious, since the helical hairpin is in close contact with helix 5/6 of the upper layer (L+1). Analysis of this region revealed that amino acids residues around 190-196 are possible interactions. This region is located close to the linker between helix 4 and 5/6, which is differently structured to some extent in the various layers of an IM30 ring (Fig. 4.6.9 B).

The distance between the hairpin and the region encompassing the residues 190-196 of the monomer from layer L+1, and also the orientation of the residues is different depending on the layer, as can be seen by comparison of the interaction site between layer 1 and 2, layer 3 and 4 and layer 5 and 6 (Fig. 4.6.9 D). Between layer 1 and 2, the distance between Phe191 and Arg74 and Phe191 and Trp71 is about 5 Å and the distance between Glu194 and Arg93 is about 6 Å, possibly enabling π-π-stacking, cation-π-interactions or electrostatic interactions (Fig. 4.6.9 C). At the interface of layer 3 and 4, the amino acid side chains seem to be oriented in a different direction. Between layer 5 and 6 the distance between Phe191 and the Trp71 is increased to about 8 Å, and Glu194 is even not close to the interaction site anymore due to a helix-to coil transition of this region. Consequently, the here identified (putative) interactions might be more relevant in the upper region of the ring. Noteworthy, this interaction site is not only present in the IM30 ring with 16-fold rotational symmetry, but also in the ring structures of other rotational symmetries, which are not shown here.

These interactions might explain the strong effects on the stability of the secondary structure of the IM30 mutants at increasing temperatures, since Trp71 not only interacts within the monomer, but between the different layers. Analysis of IM30 variants with mutations of Phe191 and Glu194 have to be performed in the future to confirm or discard the proposed interaction with Trp71. As the secondary structure of IM30 is less α-helical when not organized as a ring (Junglas et al., 2020b, chapter 4.4.), the weakened interaction between the IM30 layers could result in the observed decreased coiled-coil stability.

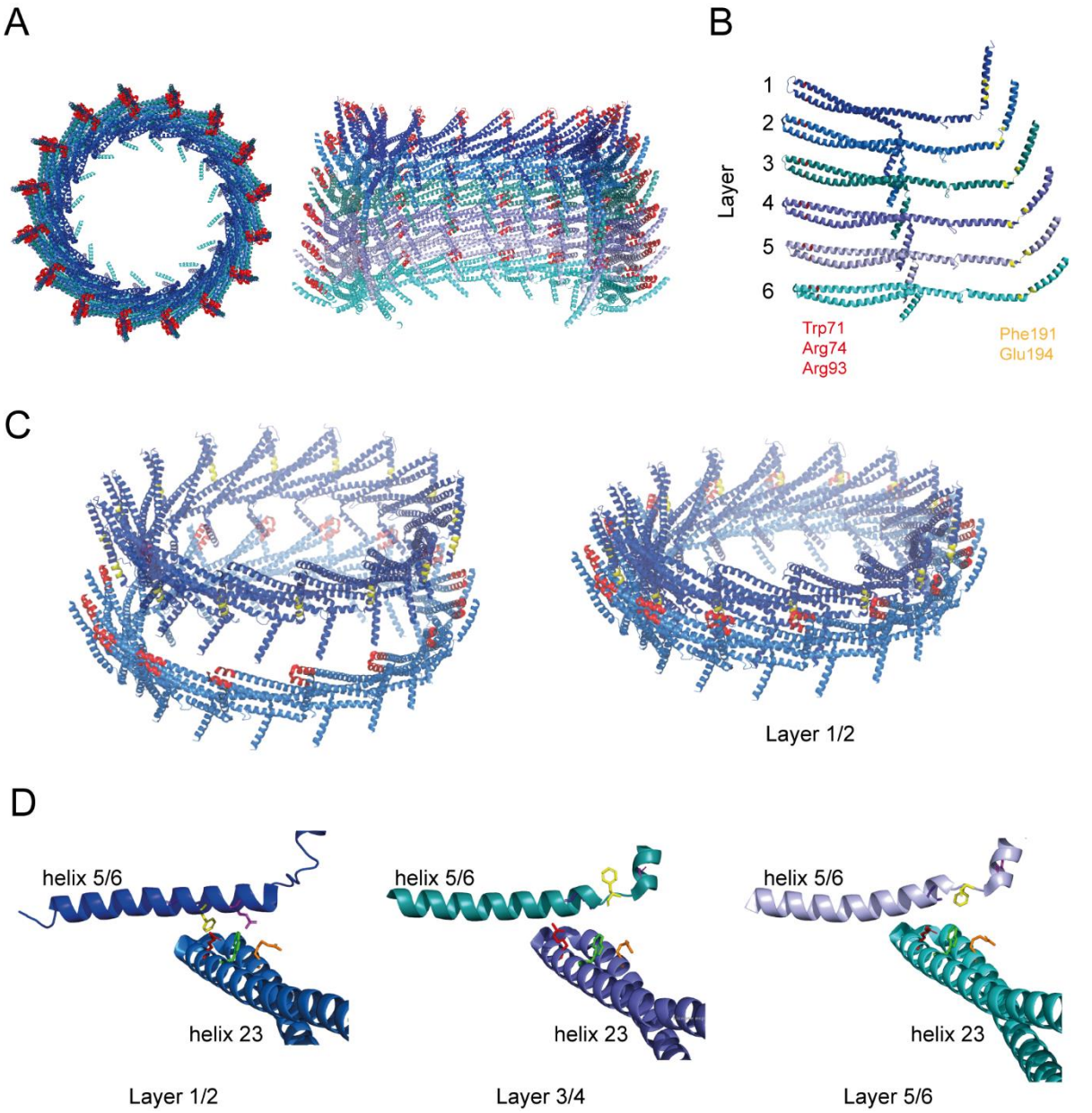

Figure 4.6.9: The helix 23 coiled-coil interacts with helix 5/6 from layer L+1.

A: Top view and a cross-section of an IM30 ring with C16-symmetry (PDB 7O3Y). The amino acids 71-93 in the coiled-coil region are highlighted in red. **B**: Stacking of IM30 monomers in the individual layers is shown. Trp71, Arg74 and Arg93 are highlighted in red, Phe191 and Glu194 are highlighted in orange. The structures differ mainly in helix 4 and 5/6. **C**: Interaction between layer 1 and 2 may be mediated by the coiled-coil of layer 2 (red) and the helix 5/6 of layer 1 (orange). **D**: Detail view of putative interactions within layers 1/2., 3/4 and 5/6 indicate potential interacting amino acids (Trp71 green, Arg74 red, Arg93 orange, Phe191 yellow, Glu194 pink).

4.6.3.6. Conclusion

We propose that the IM30 residues Trp71, Arg74 and Arg93 contribute via cation-π-interactions to stabilization of the helix 23 coiled-coil. Furthermore, these amino acids are potentially also important for interaction of individual IM30 layers within the ring structure. Trp71 is highly relevant for correct oligomerization of IM30 and consequently for its membrane fusion activity. Because of the high conservation, Trp71 likely is also crucial in IM30 proteins of other organisms.

4.7. IM30-mediated membrane fusion depends on the membrane lipid composition

4.7.1. Introduction

The TM is essential for photosynthesis in (almost) all cyanobacteria and chloroplasts. The lipid composition of the TM is unique, since it contains large amounts of glycolipids with galactose as a sugar moiety (galactolipids). In *Synechocystis*, the membrane consists of 54 % monogalactosyldiacylglycerol (MGDG), 18 % digalactosyldiacylglycerol (DGDG), 15 % sulfoquinovosyldiacylglycerol (SQDG) and 13 % of the only phospholipid phosphatidylglycerol (PG), respectively (Wada and Murata', 1989). While MGDG and DGDG have a neutral charge, the headgroups of SQDG and PG are negatively charged. DGDG, SQDG and PG are known to form lamellar lipid phases. MGDG, on the other hand, forms lipid bilayers only in the presence of other lipids or membrane proteins (Shipley et al., 1973; Simidjiev et al., 2000). For this reason, MGDG is discussed to be highly relevant for the stabilization of membrane regions with concave membrane curvature and furthermore for the formation of stacked TMs (Murphy, 1982; Seiwert et al., 2018; Yu et al., 2020). Consequently, MGDG is of general importance for the special TM architecture, which adopts various shapes including highly curved membrane regions as well as flat membranes (Liberton et al., 2006).

The principles guiding TM biogenesis are not completely understood yet, but clearly include a regulated transport of lipids, proteins, pigments and cofactors. Direct contacts between the TM and the cytoplasmic membrane as well as vesicular processes are controversially discussed to be involved in material transfer (reviewed in Heidrich et al., 2017; Lindquist and Aronsson, 2018). However, both processes likely include the fusion of membranes or vesicles. This could be mediated by IM30, since IM30 has been shown to fuse TM-mimicking membranes in presence of Mg^{2+} (Hennig et al., 2015). While previous studies focused on the influence of nucleotides (Junglas et al., 2020c, chapter 4.1), pH (Siebenaller et al., 2020, chapter 4.3), Mg^{2+} (Hennig et al., 2015) or individual IM30 helices (Thurotte and Schneider, 2019) on the membrane fusion process, this study focusses on the membrane properties crucial for IM30-triggered membrane fusion.

This study analyzes the membrane fusion activity of IM30 using membranes with different lipid compositions and curvatures. It is demonstrated that MGDG is necessary for IM30-mediated membrane fusion due to its non-bilayer-forming character as well as its galacto-headgroup. Furthermore, the study shows that high membrane curvature supports IM30-mediated membrane fusion.

4.7.2. Results

4.7.2.1. MGDG is necessary for efficient IM30-mediated membrane fusion

Interaction of IM30 with the TM is essential for its proposed *in vivo* functions (reviewed in Zhang and Sakamoto, 2015; Siebenaller et al., 2019). *In vitro*, the IM30 protein of *Synechocystis* induces fusion of TM-mimicking membranes containing 40 % of the negatively charged phospholipid PG and 60 % of the neutral galactolipid MGDG in presence of Mg^{2+} (Hennig et al., 2015; Thurotte and Schneider, 2019; Siebenaller et al., 2020).

Since IM30 is known to bind preferentially to negatively charged lipids, such as PG, and not to MGDG (Hennig et al., 2015; McDonald et al., 2015), I first aimed to investigate whether IM30 triggers the fusion of negatively-charged membranes if MGDG is not present. Therefore, an established FRET-based liposome-fusion assay was used. The membrane fusion curves over 500 s (Fig. 4.7.1 A,B) and the initial fusion rates (Fig. 4.7.1 C) were compared upon addition of Mg^{2+}, IM30 or a combination of Mg^{2+} and IM30.

As divalent cations like Mg^{2+} are known to induce fusion of negatively charged membranes at sufficiently high concentrations (reviewed in Mondal Roy and Sarkar, 2011), IM30-independent fusion of the membranes was analyzed at Mg^{2+} concentrations of 7.5 mM and 15 mM. At a concentration of 7.5 mM, the TM-mimicking liposomes (MGDG/PG) did not fuse at all (Fig. 4.7.1 A,C), consistent with previous reports (e.g. Hennig et al., 2015). In contrast, liposomes containing 100 % PG did fuse to some extent with a rate of ~ 0.15 % s^{-1}. By adding 15 mM Mg^{2+}, the TM model liposomes did fuse with an initial fusion rate of 1.38 ± 0.34 % s^{-1}, while the PG liposomes did fuse with a lower rate of 0.91 ± 0.16 % s^{-1}. While the TM model membranes reached ~100 % after 500 s, the PG liposomes fused to about 80 % after 500 s (Fig. 4.7.1 A,B). Thus, 100 % PG membranes have a higher fusion propensity at low Mg^{2+}-concentrations than the TM model membrane. To next analyze IM30-induced membrane fusion, 7.5 mM Mg^{2+} and 2.5 µM IM30 were added. While the TM mimicking membranes fused with a rate of 0.58 ± 0.0.05 % s^{-1}, the initial fusion rate of the PG liposomes (0.18 ± 0.09 % s^{-1}) was substantially lower. Taking into consideration the relatively high intrinsic fusion rate of PG in presence of solely 7.5 mM Mg^{2+}, IM30 does seem to only slightly increase the fusion of PG liposomes, if at all, reaching only 40 % fusion after 500 s (Fig. 4.7.1 B).

Since it cannot be excluded that the low fusion rate is caused simply by less binding of IM30 to the membranes, the binding affinity of IM30 was calculated for PG liposomes in contrast to PG/MGDG liposomes using the fluorescent dye Laurdan as a probe, as described previously (Heidrich et al.,

2016). From the binding curves (Fig. 4.7.1 D), the affinity of IM30 to MGDG/PG was calculated as K_D = 5.0 ± 0.7 µM, whereas the affinity to PG was determined as K_D= 1.4 ± 0.2 µM. Consequently, the low IM30-induced fusion of PG liposomes cannot be simply explained by a lowered binding affinity of IM30 to the PG liposomes. While increased IM30-triggered membrane fusion is clearly related to increased membrane binding at TM model membranes (Hennig et al., 2015), these experiments now show that the membrane lipid composition has not only additional, but a decisive impact on the membrane fusion process.

Since the TM mimicking membranes contain only 40 % of negatively charged lipids, the fusion assay was next performed with liposomes containing only 40 % of the negatively charged PG and additionally 60 % of the net-neutral phospholipid PC instead of MGDG. At these experimental conditions, no membrane fusion was observed upon addition of 7.5 mM Mg^{2+} and/or 2.5 µM IM30 (Fig. 4.7.1 C). At 15 mM Mg^{2+}, a low fusion rate of 0.09 ± 0.05 % s^{-1} was detected, showing that IM30 does not trigger fusion of the PG/PC liposomes. Similar effects were observed when PG was exchanged by the other negatively charged TM lipid SQDG (Fig. 4.7.1 C). These observations indicate that not only PG, but also the TM lipid MGDG is required for efficient IM30-mediated membrane fusion.

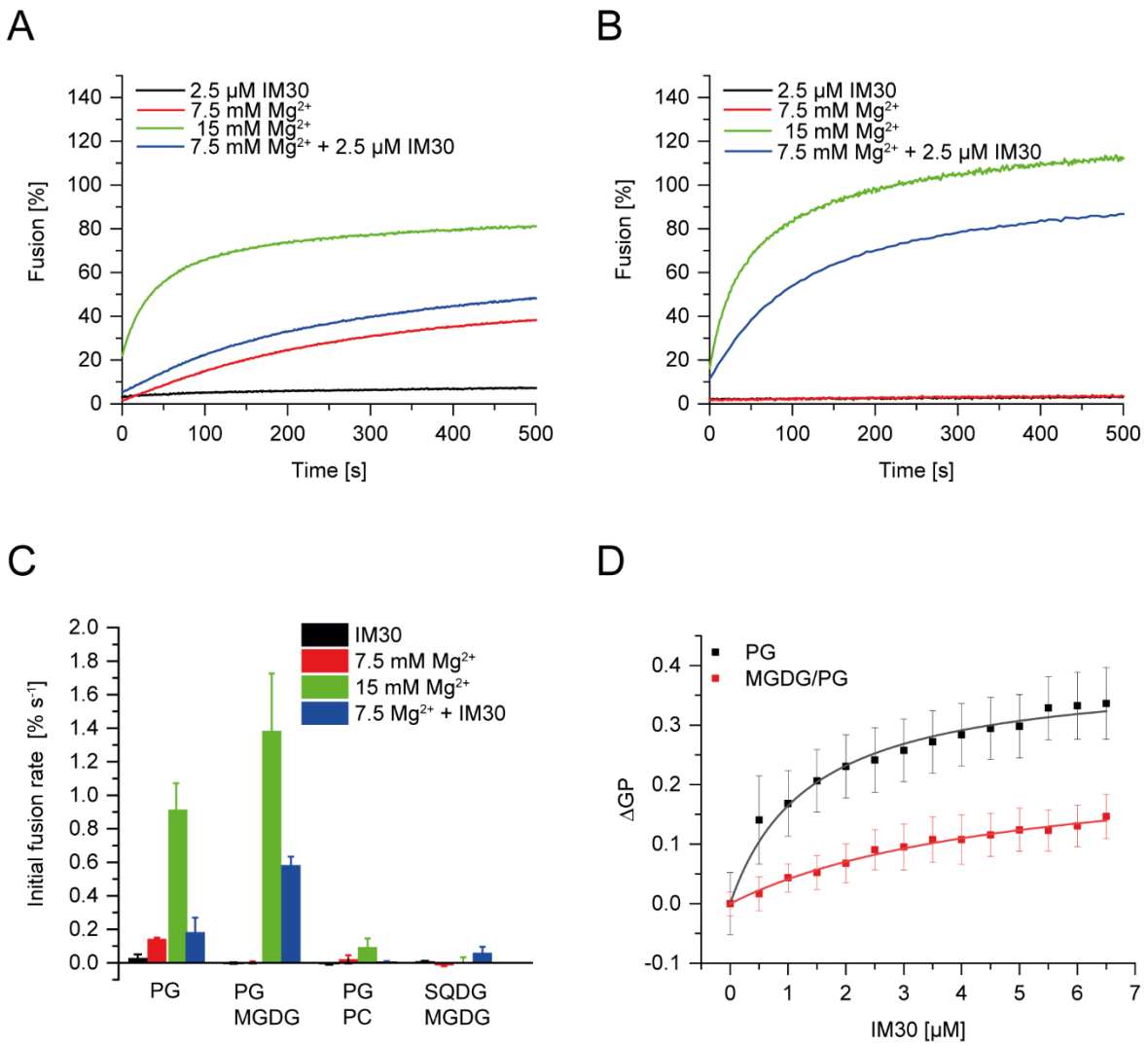

Figure 4.7.1: PG and MGDG are both essential for efficient IM30-mediated membrane fusion.

A: Membrane fusion of 100 % PG liposomes was measured using a FRET-based liposome fusion assay. Fusion was monitored over 500 s in presence of 2.5 µM IM30 (black), 7.5 mM Mg^{2+} (red), 15 mM Mg^{2+} (green) or 2.5 µM IM30 + 7.5 mM Mg^{2+} (blue). The addition of IM30 did only slightly increase the fusion induced by 7.5 mM Mg^{2+}. The curves represent the average of 3 independent measurements. **B:** Membrane fusion of PG/MGDG (40/60) liposomes was measured using a FRET-based liposome fusion assay. The fusion was monitored over 500 s in presence of 2.5 µM IM30 (black), 7.5 mM Mg^{2+} (red), 15 mM Mg^{2+} (green) or 2.5 µM IM30 + 7.5 mM Mg^{2+} (blue). Addition of IM30/Mg^{2+} did strongly increase membrane fusion. The curves represent the average of 3 independent measurements. **C:** Membrane fusion was measured using pure PG, PG/MGDG (40/60), PG/PC (40/60) and SQDG/MGDG (40/60) liposomes, respectively. The initial fusion rates upon addition of 2.5 µM IM30 (black), 7.5 mM Mg^{2+} (red), 15 mM Mg^{2+} (green) or 2.5 µM IM30 + 7.5 mM Mg^{2+} (blue), respectively, were calculated as the slope from 0-25 s of the measured fusion curves. N=3, error bars represent SD. **D:** Membrane binding of IM30 to pure PG (black) and MGDG/PG (red) membranes, respectively, was measured under steady-stare conditions. The Laurdan ΔGP at 0.1 mM lipid + 0–6.5 µM IM30 increases when IM30 binds to liposomes. The data were fitted using a binding fit (Heidrich et al., 2016). N=3, error bars represent SD.

4.7.2.2. The non-bilayer forming character and the lipid headgroup of MGDG are crucial for IM30-mediated membrane fusion

MGDG forms inverse hexagonal structures rather than (prototypical) lamellar bilayers, and, thus, was classified as a non-bilayer forming lipid (Shipley et al., 1973). These lipids are often discussed to be important for membrane remodeling processes (*i.e.* membrane fusion), which is in line with the above presented results. Furthermore, MGDG is a galactolipid, which is present in TMs in high amounts. Thus, the question arose, if also the galacto-headgroup of MGDG is relevant for the IM30-induced membrane fusion. Consequently, membrane fusion was analyzed using a different non-bilayer-forming lipid, PE (which is in contrast to MGDG a phospholipid), in combination with PG (40 % PG, 60 % PE).

First, Mg^{2+} was added in concentrations of 2-15 mM to analyze potential fusion of the pure liposomes in absence of IM30. The PG/PE liposomes had a high intrinsic fusion propensity, and fusion was induced already at 3 mM of Mg^{2+}. The initial fusion rates could not be calculated, since the starting point was not detectable at the used experimental conditions. In contrast, the TM model membranes did not fuse even at 7.5 mM Mg^{2+} (Fig. 4.7.1). Nevertheless, to analyze the IM30-mediated membrane fusion, 2.5 µM IM30 was added to the maximal tolerable Mg^{2+} concentration (2 mM), where liposomes did not significantly fuse (Fig. 4.7.2 B). Addition of IM30 increased the initial fusion rate only slightly from ~ 0.01 to 0.02 s^{-1}, reaching ~ 20 % liposome fusion after 500 s (Fig. 4.7.2 B). For better comparison, the fusion curves of the TM mimicking membranes at the maximal tolerable Mg^{2+} concentration (7.5 mM) are shown in Fig. 4.7.2 B, clearly demonstrating that IM30 triggers fusion of PE/PG membranes to a much lesser extent than fusion of MGDG/PG liposomes at the respective maximum tolerable Mg^{2+} concentration. Note that the difference in the Mg^{2+} concentration clearly also has impact on the Mg^{2+}-interaction with IM30 (Heidrich et al., 2018).

At least at low Mg^{2+}concentrations, the PE/PG liposomes are not fused by the combined addition of IM30 and Mg^{2+}, demonstrating that the non-bilayer forming characteristics of MGDG and PE alone are not interchangeable in IM30-mediated membrane fusion. This indicates that other features, such as the lipid headgroup, might be important for this process.

The low stability of the PG/PE liposomes in presence of Mg^{2+} was somewhat surprising, since it was assumed that only the amount of the negatively charged lipid PG would be relevant for the interaction with the divalent cation. To analyze whether the galacto-headgroup is relevant for the low membrane stability at high Mg^{2+} concentrations, a special lipid composition of constant 40 % non-bilayer forming lipid PE, constant 20 % of negatively charged PG and 40 % of the lipids PC and

DGDG in variable ratios was used. PC and DGDG are both neutral and bilayer-forming lipids, but have different lipid headgroups.

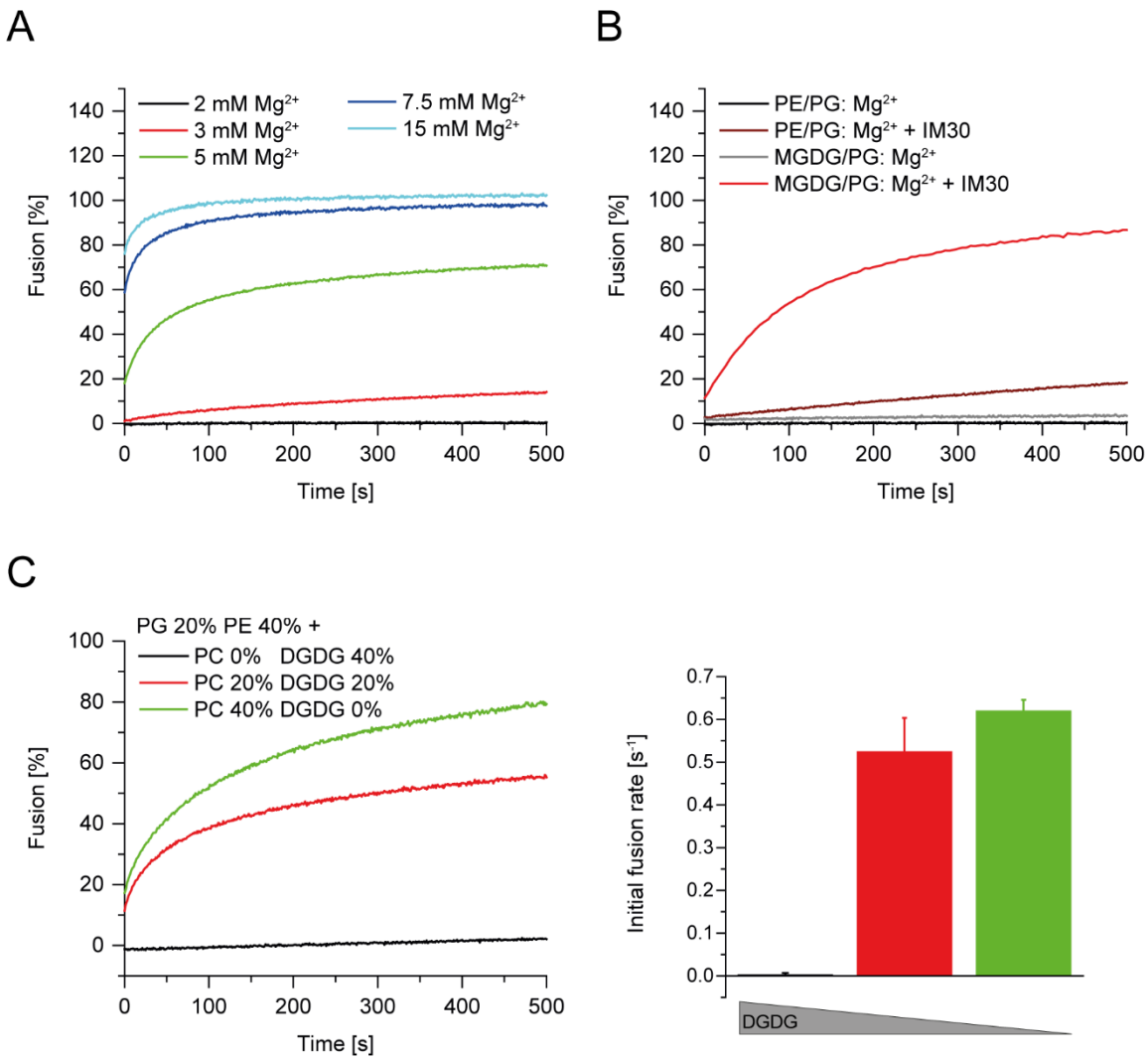

Figure 4.7.2: The galacto-headgroups of MGDG and DGDG lipids stabilizes negatively charged membranes at high Mg^{2+} concentrations.

A: Membrane fusion of PG/PE (40/60) liposomes was measured (in absence of IM30) using a FRET-based liposome fusion assay. Fusion was monitored over 500 s in presence of 2-15 mM Mg^{2+}. The curves represent the average of 3 independent measurements. **B:** Membrane fusion of PE/PG (60/40) and MGDG/PG (60/40) liposomes was monitored over 500 s in presence of the respective maximum tolerable Mg^{2+} concentration. After addition of IM30/Mg^{2+}, only fusion of the MGDG/PG liposomes was observed. The curves represent the average of 3 independent measurements. **C:** Membrane fusion of PG/PE (20/40 %) with DGDG (40 %) (black), PC/DGDG (20/20 %) (red) or PC (40 %) (green) liposomes, respectively, was monitored using a FRET-based liposome fusion assay. The initial fusion rates were calculated as the slope from 0-25 s of the measured fusion curves. The curves represent the average of 3 independent measurements. N=3, error bars represent SD.

While DGDG is a galactolipid, PC is a phospholipid. When analyzing these liposomes with the fusion assay in presence of 7.5 mM Mg^{2+} and absence of IM30, the liposomes containing 40% PC fused with a rate of 0.62 ± 0.02 % s^{-1} (Fig. 4.7.2 C). A lower rate of 0.53 ± 0.08 % s^{-1} was detected for liposomes containing 20% PC and 20% DGDG, while almost no fusion was observed with liposomes containing 40% DGDG (0.003 % s^{-1}) (Fig. 4.7.2 C). This shows that the higher amounts of galacto-headgroups introduced by DGDG indeed decrease the fusogenic properties at high Mg^{2+} concentrations, likely similar to MGDG headgroups. The special importance of MGDG for IM30-mediated membrane fusion is therefore potentially caused not only by its non-bilayer forming character but also by the galacto-headgroup.

4.7.2.3. IM30-triggered liposome fusion depends on membrane curvature

The TM does not only have a unique lipid composition, but also a special architecture with partially highly curved membrane regions (see introduction, Fig. 1.2.2). Interestingly, IM30 appears to especially accumulate at these regions in living *Synechocystis* cells (Gutu et al., 2018), and a higher membrane binding affinity was suggested at highly curved membranes (McDonald et al., 2015). Hence, the membrane fusion activity of IM30/Mg^{2+} was next analyzed using TM mimicking liposomes with diameters ranging from 50 to 800 nm. While the liposomes having 50 or 80 nm diameter fused to about 80 % after 500 s, the liposomes with 100 or 200 nm diameter reached only ~60 % fusion. Liposomes having 400 or 800 nm even only fused to less than 40 % (Fig. 4.7.3 A). Also, the initial fusion rates decrease from smaller to larger liposomes, demonstrating that IM30 triggers faster fusion of highly curved liposomes.

To analyze whether this dependence on the liposome diameters might be caused by a general higher fusion propensity of small MGDG/PG liposomes, fusion was induced by the addition of solely 14 mM Mg^{2+}. In this case, no decreasing trend was observed with increasing liposome diameter, showing that the observed trend is indeed IM30-specific.

Since the lipid concentration, yet not the liposome number was held constant during the performed fusion assay, it was next analyzed whether the lowered number of potentially colliding liposomes at high diameters had an impact on the observations. Therefore, the fusion assay was repeated with liposomes having a 50 nm diameter at constant IM30/Mg^{2+} concentration, but lowered lipid concentrations, which correspond to the number of liposomes at 100 and 200 nm. Also in this case, no decreasing trend was observed (Fig. 4.7.3 D), showing that the number of liposomes has no decisive impact on the IM30-mediated membrane fusion.

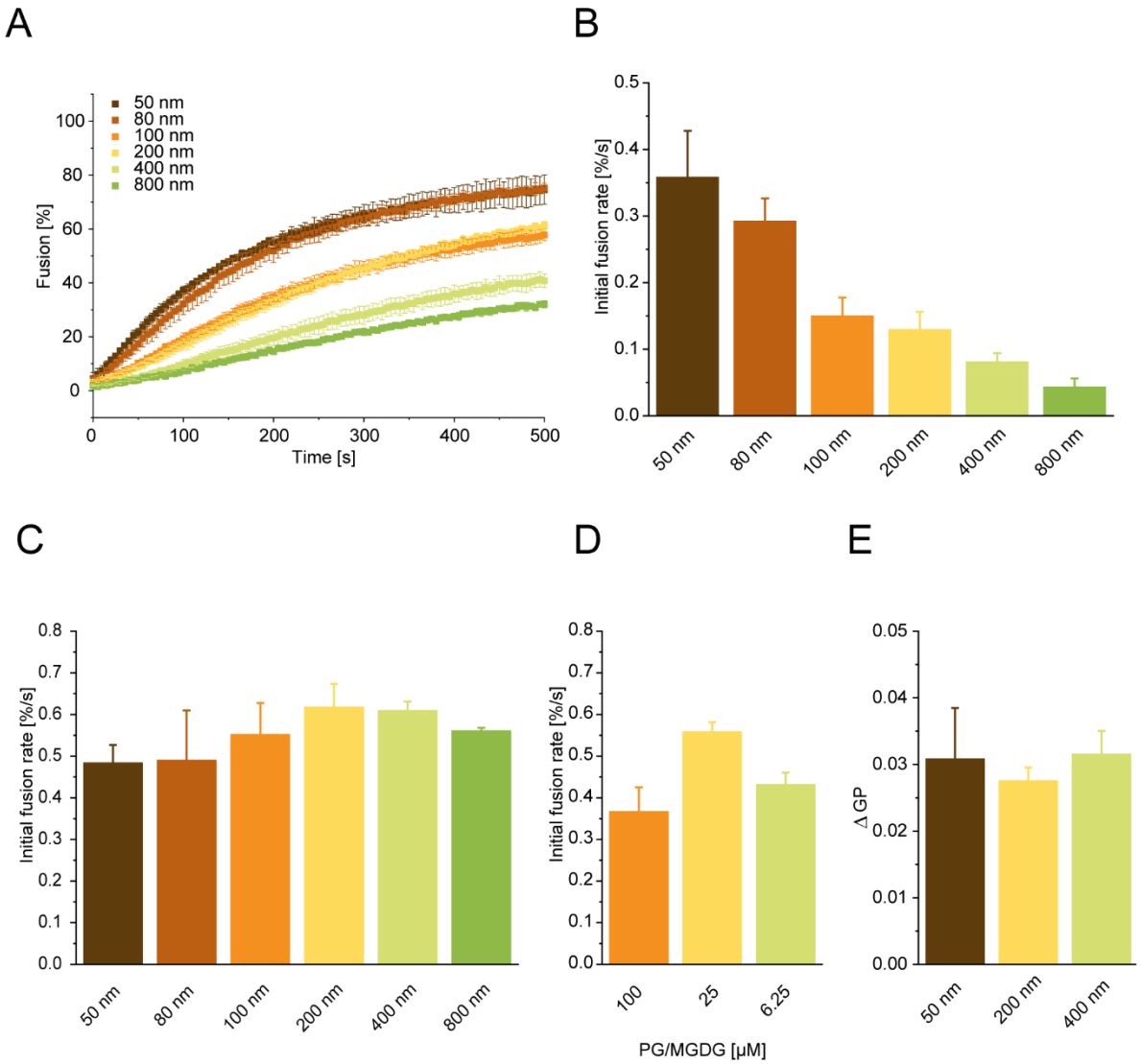

Figure 4.7.3: The membrane fusion activity of IM30 is curvature-dependent.

A: IM30/Mg^{2+}-induced fusion of PG/PE (40/60) liposomes was measured using a FRET-based liposome fusion assay using liposomes with diameters ranging from 50 to 800 nm. Increased membrane fusion was observed with decreasing liposome size. The curves represent the average of 3 independent measurements. **B:** The initial fusion rates were calculated as the slope from 0-25 s of the measured fusion curves. N=3, error bars represent SD. **C:** Mg^{2+}-induced membrane fusion of PG/PE (40/60) liposomes was measured in absence of IM30 using a FRET-based liposome fusion assay and liposomes with diameters from 50 – 800 nm. No trend was observed with decreasing liposome size. N=3, error bars represent SD. **D:** IM30/Mg^{2+}-induced membrane fusion PG/PE (40/60) using 100 µM, 25 µM or 6.25 µM lipid. No decreasing trend was observed with lower lipid concentration. N=3, error bars represent SD. **E:** Steady-state membrane binding of IM30 was measured via monitoring changes in the Laurdan fluorescence emission using liposomes having 50, 200 or 400 nm diameter. The Laurdan ΔGP does not differ, indicating similar binding of IM30 to differently curved membranes. N=3, error bars represent SD.

To analyze whether IM30 binding to liposomes of different sizes is altered at the experimental conditions (2.5 µM IM30 and 0.1 mM lipid), steady-state Laurdan fluorescence spectra were measured additionally. The ΔGP, which reflects the change of the spectrum, was not decreasing when using liposomes having 50, 200 or 400 nm diameter, respectively. This indicates that the amount of protein bound to the liposomes is, at least in absence of Mg^{2+}, not critically affected by the curvature of the liposomes. This suggests that the reason for the increased membrane fusion observed at highly curved membranes is caused by the membrane fusion process itself and not simply by more protein binding to the surface.

4.7.3. Discussion

4.7.3.1. The TM lipids MGDG and PG support IM30-mediated membrane fusion

The distinct lipid composition of the TM is necessary for efficient IM30-mediated membrane fusion

The membrane fusion activity of IM30 has been shown multiple times in *in vitro* assays using liposomes consisting of 60 % MGDG and 40 % PG (Hennig et al., 2015; Heidrich et al., 2016; Hennig et al., 2017; Thurotte and Schneider, 2019; Junglas et al., 2020c; Siebenaller et al., 2020).

Even though the exact mechanism of IM30-induced membrane fusion is still unclear, membrane fusion is generally characterized by the basic steps: (1) close membrane contact, (2) outer leaflet mixing and (3) inner leaflet mixing. Between the second and the third step, a hemifused membrane might be an intermediate structure (Marsden et al., 2011; Mondal Roy and Sarkar, 2011). A requirement for step 1 is to overcome the strong repulsive forces caused by electrostatic, steric and/or hydration forces between two membranes, which finally results in membrane fusion caused by the *van der Waal´s* attractive interaction of the lipid acyl chains (Cevc, 1987). Membranes containing negatively charged lipids, such as PG or phosphatidylserine (PS), show strong electrostatic repulsion, which results in a natural distance between biological membranes and inhibits spontaneous membrane fusion, but can be lowered by adjusting the dielectric constant of the surrounding medium (*i.e.* by higher salt concentrations) (Marsden et al., 2011). In the second and third step, a temporary disorder of the lipid bilayer results in complete fusion of the vesicles, and parts of the membrane undergo a transition from the lamellar membrane structure to an inverted hexagonal structure. This transition is strongly supported by conically shaped lipids, such as MGDG or PE (Kinnunen, 1996). It seems therefore reasonable to assume that the lipid MGDG strongly support the second and third step of IM30-mediated membrane fusion (Fig. 4.7.1 A-C). It has been speculated that IM30 binding causes a local accumulation of MGDG in the inside of the ring,

resulting in bilayer destabilization (Heidrich et al., 2017). Consistent with this idea, cryo-EM analysis of *Synechocystis* revealed structures close to the thylakoid membrane, which likely resemble IM30 and encapsulate the membrane (Gupta et al., 2021).

Divalent cations, such as Ca^{2+} and Mg^{2+}, are known to induce fusion of negatively charged membranes (Mondal Roy and Sarkar, 2011). It is assumed that in case of cation-induced membrane fusion, the major energy needed for fusion is derived from screening of electric charges on the membrane, increased surface tension and removal of structural water from the membrane surface. While the charge screening causes close contact of the membranes, the increased surface tension is likely causing membrane defects necessary for destabilization of the bilayer. In the context of Ca^{2+}-induced fusion in presence of other fusogens, the divalent cation is believed to simply fasten the fusion process by streaming inside the liposomes (Ahkong et al., 1975). In case of IM30-induced fusion, Mg^{2+} clearly not only supports the membrane fusion process via interactions with the lipids, but also causes a major structural rearrangement of the protein (Heidrich et al., 2018) and increased membrane binding, which results in bilayer destabilization (chapter 4.5). This is discussed to activate the membrane fusion activity of IM30.

A negatively charged lipid (e.g. PG) is necessary for binding of IM30 to the membrane (Hennig et al., 2015; McDonald et al., 2015). Although membrane binding of IM30 clearly is a prerequisite for membrane fusion, and increased binding to TM mimicking membranes enhances membrane fusion (Hennig et al., 2015), the results here show that liposomes containing only PG are not fused properly by IM30/Mg^{2+} (Fig. 4.7.1 A) despite the increased membrane binding affinity of IM30 (Fig. 4.7.1 B). The observed low IM30-induced fusion of pure PG membranes can not simply be explained by the larger electrostatic repulsion of the PG liposomes compared to the PG/MGDG liposomes, which might hinder the collision and also close association of the liposomes. Since liposomes containing the same amount of negative charges as the prototypical TM mimicks (40 % PG and 60 % of the neutral lipid PC) did also not fuse upon addition of IM30/Mg^{2+} (Fig. 4.7.1), MGDG clearly is important for IM30-induced membrane fusion.

While IM30 is known to also bind to membranes containing the other negatively charged TM lipid SQDG (Hennig et al., 2015), no fusion was observed when SQDG/MGDG liposomes were analyzed (Fig. 4.7.1). A reason for this could be the steric repulsion of the membranes, since both lipids contain the large galacto-headgroup instead of the smaller PG headgroup. While 100 % PG liposomes fused in presence of 15 mM Mg^{2+}, PG/PC and SQDG/MGDG liposomes did not fuse at all. In case of PG/PC liposomes this might be caused by the lower negative surface charge and consequently less Mg^{2+}-affected surface tension.

Since a characteristic of the TM is the high amount of galactolipids, the importance of the galactolipid headgroup for IM30-mediated membrane fusion was investigated by exchanging MGDG with PE, another non-bilayer forming lipid. Interestingly, the PG/PE membrane fused already at much lower Mg^{2+} concentrations compared to PG/MGDG liposomes. To assess the effect of IM30 on the fusion process, the fusion was analyzed at the maximal tolerable Mg^{2+} concentration, *i.e.* 2 mM for PG/PE membranes. At these conditions, only very little membrane fusion was observed (Fig. 4.7.2). Noteworthy, at ~ 2 mM Mg^{2+}, also the TM model membrane is not fusing in presence of IM30 (Hennig et al., 2015). This appears to be reasonable, since 2 mM Mg^{2+} is not sufficient to induce structural changes in the IM30 protein, which are assumed to be necessary for its fusogenicity (Heidrich et al., 2018). A potential enhancement of the membrane fusion by IM30 at high Mg^{2+} concentrations in presence of PE/PG membranes can unfortunately not be investigated, since the initial phase of the fusion cannot be analyzed with the used experimental setup. Still, the performed experiment highlights the importance of the galacto-headgroup, and not only the non-bilayer-forming character of MGDG specifically for membrane fusion induced by IM30.

The addition of the galactolipid DGDG to PE/PG liposomes did reduce the spontaneous membrane fusion (Fig. 4.7.3), similar to MGDG. This suggests that the galacto-headgroups shield the negatively charged PG headgroups from interacting with Mg^{2+} and thereby prevent Mg^{2+}-mediated membrane fusion, in turn allowing sufficiently high concentrations of Mg^{2+} to activate IM30 for fusion. Since MGDG and DGDG are discussed to be important for the stacking of TM via formation of hydrogen bonds between the polar headgroups (Demé et al., 2014), this actually counterbalances the electrostatic repulsion by the negatively charged lipids. Although the resulting close membrane contact actually favors membrane fusion, it has also been observed before that MGDG or DGDG-containing liposomes do not fuse/aggregate in presence of negatively charged lipids (Webb and Green, 1990). This might be relevant *in vivo*, since the Mg^{2+} concentrations of the cyanobacterial cytoplasm or the chloroplast stroma, respectively, increase at high light conditions (Portis and Heldt, 1976; Pohland and Schneider, 2019), and the TM needs to stay intact also at these conditions.

Not only the lipid composition of the TM is unique but also its diverse 3-dimensional architecture. The TM contains large regions of flat membranes, as well as highly curved membrane regions, e.g. at converging zones close to the cytoplasmic membrane in *Synechocystis* (Liberton et al., 2006). Interestingly, IM30 has been shown to localize at these highly curved regions in high concentrations in *Synechocystis* (Gutu et al., 2018). In agreement with this, IM30 has been shown to bind to membranes in a curvature-dependent manner *in vitro* (McDonald et al., 2015). As suggested in chapter 4.3., IM30 might be necessary at these regions to prevent proton leakage from the TM (Siebenaller et al., 2020).

IM30-mediated membrane fusion has so far been studied using liposomes having a diameter of 100 nm (Hennig et al., 2015; Heidrich et al., 2016; Thurotte and Schneider, 2019; Junglas et al., 2020c; Siebenaller et al., 2020). The results of this study now show strongly decreased membrane fusion rates when increasing the liposome diameter from 50 nm to 800 nm (Fig. 4.7.3). Nevertheless, IM30 mediated fusion of all liposome sizes to some extent, showing that membrane curvature has no decisive, but a supporting impact on membrane fusion. The IM30-mediated fusion is likely supported by membrane defects, which are caused by increased binding of IM30 to the membrane in presence of Mg^{2+} (chapter 4.5). Membrane defects caused by high membrane curvature (Nir et al., 1982) might explain the faster fusion of small liposomes.

The results of this study furthermore show that increased fusion of highly curved liposomes is not a general trend for MGDG/PG liposomes, at least not for Mg^{2+}-triggered membrane fusion (Fig. 4.7.3 B), yet appears to be IM30 specific. This is somewhat surprising, since smaller liposomes are generally known to have a high fusion propensity (Nir et al., 1982). Nevertheless, the relevance of e.g. curvature-induced membrane defects depends on the exact membrane fusion mechanism, which likely differs when membrane fusion is induced by Mg^{2+} alone or Mg^{2+}/IM30. Unfortunately, since the mechanism of IM30-mediated membrane fusion remains unclear so far, exactly suitable control experiments are impossible yet. In contrast to the literature (McDonald et al., 2015), no increased membrane binding of IM30 was observed when liposomes with different diameters were analyzed (Fig. 4.7.4 D). Note that binding was analyzed in absence of Mg^{2+}, since Mg^{2+} interferes with the Laurdan measurements (Heidrich et al., 2018). Since the affinity to bind to MGDG/PG liposomes in absence of Mg^{2+} was quite low (Fig. 4.7.1 D), the differences in membrane binding might not be detectable at the performed experiment. Furthermore, it is possible that the probe Laurdan is not suitable to measure binding to highly curved membranes, since the polarity of the lipid headgroup region might differ depending on the membrane curvature. Analyzing binding via sucrose-density gradients including Mg^{2+}, as described in chapter 4.5, may be helpful to finally analyze the effect of membrane curvature on IM30 membrane binding and membrane fusion.

The results of this study suggest that IM30 mediates membrane fusion *in vivo* preferentially at highly curved membrane regions, which generally contain high amounts of MGDG (Murphy, 1982; Sprague and Staehelin, 1984; Giroud and Siegenthaler, 1988; Seiwert et al., 2018). For example, elevated levels of MGDG at TMs result in highly curved regions in DGDG-defective chloroplasts (Dörmann et al., 1995). In highly curved TM regions, conically shaped lipids, such as MGDG, are suggested to stabilize the inner membrane leaflet because of their intrinsic negative curvature (Murphy, 1982). The intrinsic negative curvature furthermore supports a potential hemifused intermediate structure, which further suggests that these regions are prone to membrane fusion processes.

4.7.3.2. Conclusion

In summary, the analyses shows that PG as well as MGDG support IM30-mediated membrane fusion. PG seems to be important due to its interaction with Mg^{2+} which induces close contact of adjacent membranes, and additionally due to mediating interaction with IM30, which destabilizes the membrane. In contrast to PG, the larger headgroup of the negatively charged TM lipid SQDG seems to sterically hinder membrane fusion. In contrast to the negatively charged lipids, MGDG does not directly interact with IM30, yet is highly relevant for IM30-mediated membrane fusion because of its non-bilayer forming character and its galacto-headgroup, which stabilize the membrane against spontaneous fusion at high Mg^{2+} concentrations. Furthermore, the results of this study suggest that IM30-mediated membrane fusion preferentially occurs at highly curved membrane regions, where the highly abundant MGDG supports the membrane fusion process. This local restriction of possible fusion sites seems physiologically relevant, since membrane fusion has to be highly controlled on several levels to prevent unintended membrane damage.

4.8. Protein (De)phosphorylation regulates IM30-mediated membrane fusion

4.8.1. Introduction

The phosphorylation of proteins by specific kinases, which alters the protein activity, is a common response of bacteria to changing environmental conditions and to ensure survival (Stock et al., 1989; Dworkin, 2015). In *Synechocystis*, the phosphorylation of proteins has been observed e.g. in response to hyper- and hypoosmotic salt shock (Hagemann et al., 1993), bicarbonate uptake (Bloye et al., 1992) or nitrogen starvation (Spät et al., 2015; Spät et al., 2018).

In an extensive phosphoproteomic study, the site-specific phosphorylation of various proteins have been shown to be highly dynamic after nitrogen starvation of *Synechocystis* cells, suggesting that phosphorylation is crucial during the redevelopment of cellular functions (Spät et al., 2015). Upon nitrogen starvation, the acclimation process is characterized by a degradation of photosynthetic pigments (chlorosis), accompanied by the down-tuning of metabolic activities and degradation of cellular proteins (Krasikov et al., 2012). The cyanobacteria finally reach a resting state, in which they can survive for prolonged periods (Görl et al., 1998). Upon addition of nitrate to chlorotic cultures, the TMs redevelop in a 2-phase process. While the first phase completely depends on respiration, the cells gradually regain full photosynthetic activity in the second phase (Neumann et al., 2021).

Interestingly, IM30 was found to be phosphorylated during the first phase of resuscitation from chlorosis at eight different sites (Spät et al., 2018). Two potential phosphorylation sites were located on helix 3: Ser96 or Thr98, and Thr106. Six further phosphorylation sites were located at the end of helix 4 and beginning of helix 5/6: Thr155, Thr161, Ser162, Ser163, Thr165 and Ser166. The phosphorylation of IM30 was maintained for 24 h after addition of nitrogen, and ended with the reemergence of the first TMs, accompanied by increased IM30 concentrations (Spät et al., 2015; Klotz et al., 2016; Spät et al., 2018).

To analyze effects of the phosphorylation on the IM30 structure and membrane interactions, Ser96 or Thr155 were mutated to the phosphomimetic amino acid Asp. Furthermore, mutations of these amino acids to Ala were analyzed to differentiate the phosphomimetic effect from unspecific effects. After heterologous expression in *E. coli*, the IM30 structure, Mg^{2+}- and membrane interactions were analyzed *in vitro*. The study demonstrates that IM30 variants with phosphomimetic mutations have low membrane-fusogenic activity. Consequently, phosphorylation of IM30 might trigger IM30 activation *in vivo*.

4.8.2. Results

4.8.2.1. Purification of IM30 with mutations Ser96 and Thr155

The IM30 protein of *Synechocystis* is phosphorylated *in vivo* upon resuscitation from chlorosis at eight different sites, which cluster in two different sequence regions. In each region, only one site is occupied at the same time (Spät et al., 2018). From these potential phosphorylation sites, Serine 96 (Ser96) and Threonine 155 (Thr155) were analyzed in this study.

Ser96 or Thr155 were exchanged to the phosphomimetic Asp or the neutral Ala as a control via site-directed mutagenesis of the expression plasmid. After heterologous expression in *E. coli* and purification by Ni-NTA affinity chromatography, the purity of the proteins was confirmed by SDS-PAGE (Fig. 4.8.1).

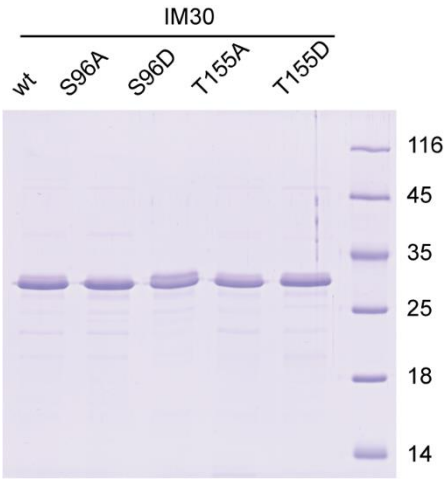

Figure 4.8.1: IM30 variants can be heterologously expressed and purified.

The 6x His-tagged proteins IM30 wt, S96A, S96D, T155A and T155D were heterologously expressed and purified via Ni-NTA chromatography. The SDS-PAGE analysis shows that the proteins were obtained in high purity. Marker (right): Pierce Unstained protein MW Marker (unit: kDa) (Thermo Fisher)

4.8.2.2. IM30 Ser96 and Thr155 are likely important for IM30 oligomerization

For analysis of potential intramolecular interaction sites close the IM30 phosphorylation sites, the structure of an IM30 ring with C16-symmetry was used, as it is best resolved IM30 ring structure thus far (Gupta et al., 2021).

Ser96 is located in the coiled-coil region of IM30 on helix 3 (Fig. 4.8.2). In this region, the monomer structures differ only minor depending on the ring layer (Gupta et al., 2021). In contrast, Thr155 is located in the flexible linker between helix 3 and 4, which structure is different to some extent in each layer.

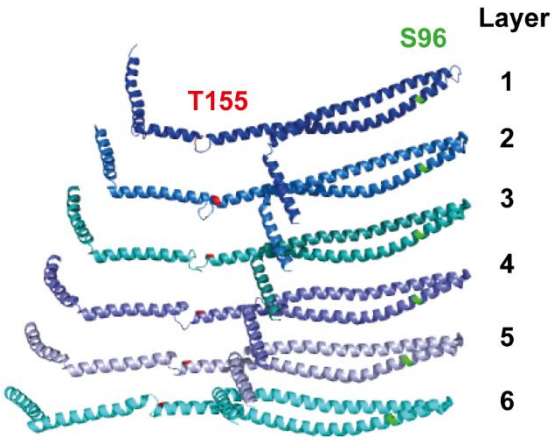

Figure 4.8.2: Localization of the IM30 phosphorylation sites Thr155 and Ser96

The position of Thr155 (red) and Ser96 (green) in the IM30 structure (C16 symmetry, PDB 7O3Y) is shown in the asymmetrical assembly of the monomers. While Ser96 is located in the stable coiled-coil region on helix 3, Thr155 is located close to the flexible linker between helix 3 and 4.

In the ring structure, Ser96 and Thr155 are in close contact (~5-15 Å) to adjacent monomers from the same layer, but also to monomers from adjacent layers. This suggests that Ser96 and Thr155 may be important for the oligomerization of IM30. While Ser96 is in close distance to amino acids 120-130 from helix 3 of the neighboring left monomer (M-1), the distance between Ser96 to monomers from the layer above and below is > 15 Å. Within the individual IM30 layers, Thr155 from monomer M is in close contact to the amino acids 180-190 (helix 4) from the left monomer M-1, and further in close distance to amino acids 30-40 of helix 2 from the right monomer M+1 (Fig. 4.8.3).

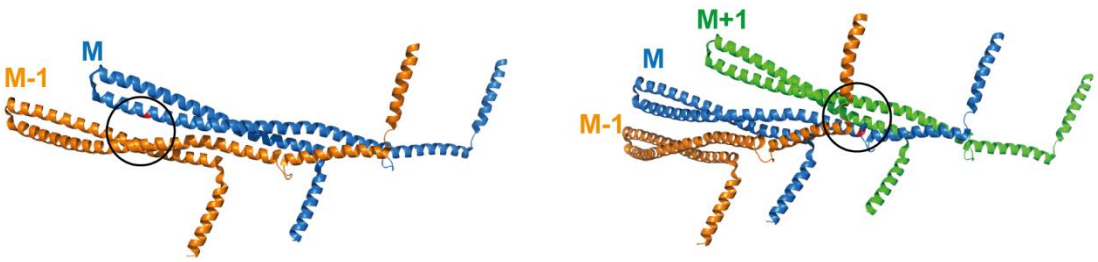

Figure 4.8.3: Interaction of IM30 monomers within layer 2.

The IM30 monomer structure is taken from layer 2 of a C16-ring (PDB: 7O3Y). **Left**: The putative interaction between Ser96 (highlighted red) from monomer M and helix 3 from monomer M-1 is highlighted (black circle). **Right**: The putative interaction between Thr155 (highlighted red) from monomer M, helix 4 from monomer M-1 and helix 2 from monomer M+1 is highlighted (black circle).

Furthermore, Thr155 from the monomer of layer L potentially interacts with helix 1 (amino acids 1-10) from the upper layer (L+1) and helix 2 (amino acids 38 -48) from the lower layer (L-1) (Fig. 4.8.4).

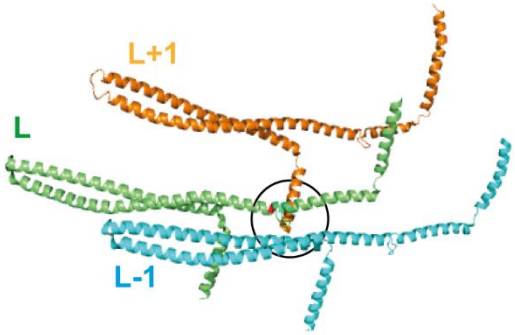

Figure 4.8.4: Interaction of IM30 Thr155 with monomers from adjacent layers.

The IM30 monomer structure is taken from layer 2-4 of a C16-ring (PDB: 7O3Y). The putative interaction between Thr155 (highlighted red) from layer L, helix 1 from layer L+1 and helix 2 from layer L-1 is highlighted.

4.8.2.3. IM30 variants with phosphomimetic mutation have an intact oligomeric ring structure

Oligomerization of IM30 into large, ring structures seems to be highly important for the function of the IM30 protein (recently reviewed in Siebenaller et al., 2019).

Since the IM30 structure suggests that phosphorylation of Ser96 and Thr155 is important for oligomerization, the structure of the IM30 variants S96A, S96D, T155A and T155D was first analyzed via negative-stain EM and AFM (Fig. 4.8.5).

In the EM-analysis (Fig. 4.8.5 A), the typical ring-like structures were observed for all proteins. The diameter of the rings was determined to be ~ 30 nm. Note that the quality of the images from IM30 S96A was not as high as the quality of the other images. But still, similar structures could be observed. This suggests that all mutants are able to form correctly folded oligomers, despite the introduced mutations.

Since IM30 wt rings have been observed also on mica surfaces via AFM (Junglas et al., 2020b, chapter 4.4), the EM observations were further confirmed using this technique (Fig. 4.8.2 B). Again, ring structures were observed for all mutant proteins. The diameter of the rings was varying, ranging from 30 – 50 nm. Similar dimensions have been observed before for the IM30 wt rings (Junglas et al., 2020b). Note that the ring structures observed with AFM were distorted, especially in case of IM30 S96A, which is caused by a drift during the measurement. Therefore, the ring structures

obtained by EM seem more reliable. Still, the height of the rings can only be analyzed using AFM, and was determined to be 10-15 nm, which is consistent with previous reports (Saur et al., 2017; Junglas et al., 2020b).

These results from EM and AFM studies imply that the phosphomimetic mutations, as well as the control mutations, do not affect oligomerization of IM30 into ring structures.

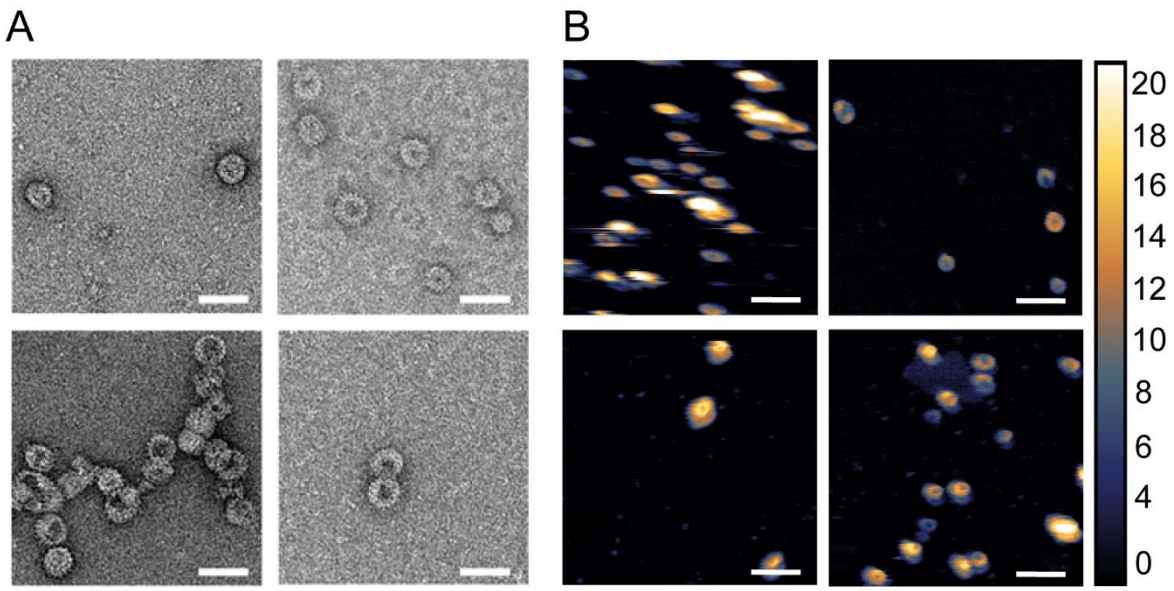

Figure 4.8.5: IM30 variants form IM30-typical ring structures.

A: The structure of IM30 S96A (upper left), S96D (upper right), T155A (bottom left) and T155D (bottom right) was analyzed using negative-stain EM. All mutants show IM30-typical ring structures. The scale bar represents 50 nm. The experiments were performed in cooperation with Dr. B. Junglas. **B:** The structure of IM30 S96A (upper left), S96D (upper right), T155A (bottom left) and T155D (bottom right) was analyzed using AFM. Typical ring structures were observed. The false-color ruler displays the height of the bound substances (unit: nm). The experiments were performed in cooperation with N. Quarta.

4.8.2.4. The oligomeric structure of IM30 is not affected by phosphomimetic mutations

Although EM and AFM analysis clearly showed the formation of the prototypical oligomeric ring structures, potentially formed smaller oligomers, such as e.g. dimers or tetramers, might not be detected by these techniques. Consequently, the oligomeric state of the IM30 mutants was additionally analyzed by size exclusion chromatography (SEC) (Fig. 4.8.6). Since IM30 forms large complexes of > 2 MDa, IM30 is usually eluted in the void volume of all common columns. Still, smaller oligomers with a size < 300 kDa can be detected, as has e.g. been shown for IM30 tetramers (Junglas et al., 2020c, chapter 4.1). The SEC analysis showed that all IM30 mutants elute in the void volume as the IM30 wt, with no further peak at higher volumes. This shows that no smaller oligomers are formed by the IM30 variants. Consequently, the phosphomimetic mutations do not affect the oligomeric structure of IM30.

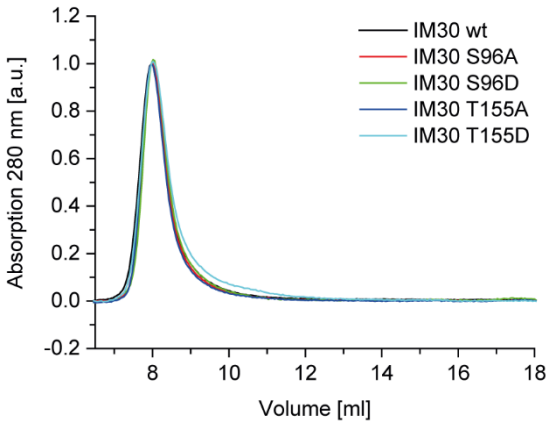

Figure 4.8.6: IM30 mutants do not form lower-ordered oligomeric complexes.

The oligomeric state of IM30 wt (black), S96A (red), S96D (green), T155A (blue) and T155D (cyan) was determined by SEC (Superose 12 10/300 GL column). The elution volume of IM30 wt and mutants was 8.0 mL, which corresponds to the void volume of the column.

4.8.2.5. IM30 variants with phosphomimetic mutation have a reduced thermal stability

We next analyzed the secondary structure of the IM30 variants with phosphomimetic mutation using CD-spectroscopy. IM30 is a largely α-helical protein (Gupta et al., 2021). At 20 °C, the CD-spectra of all IM30 proteins were characterized by the typical minima at 222 nm and 208 nm (Fig.3.8.7 A). The CD analysis suggests that all proteins are correctly folded, whereby small structural differences may be possible in case of all mutant proteins.

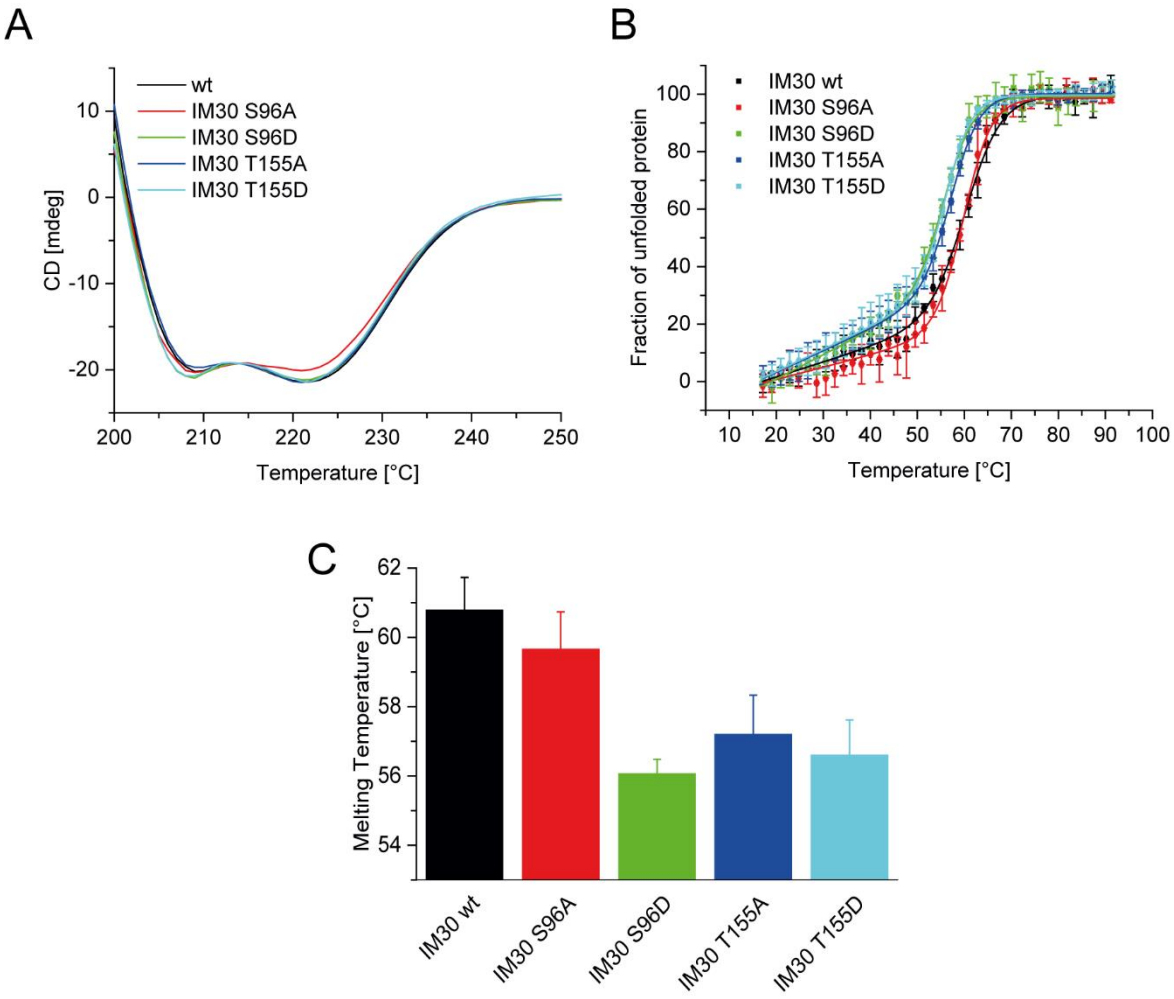

Figure 4.8.7: The thermodynamic stability of IM30 mutants is reduced

A: The secondary structure of IM30 wt (black), S96A (red), S96D (green), T155A (blue) and T155D (cyan) was analyzed with CD-spectroscopy. For all proteins, an spectrum typical for α-helices was observed. **B:** Thermal denaturation of IM30 wt, S96A, S96D, T155A and T155D was monitored by CD-spectroscopy at 222 nm. The raw signal was converted to the fraction of unfolded protein. N=3, error bars represent SD. **C:** Fitting the curves shown in (C) with an adapted Boltzmann-fit yielded the following T_m`s: 60.8 ± 0.9 °C (IM30 wt), 59.7 ± 1.0 °C (S96A), 56.1 ± 0.4 °C (S96D), 57.2 ± 1.1 °C (T155A) and 56.6 ± 1.0 °C (T155D). Error bars represent errors from the fitting of the data.

We next analyzed the stability of the secondary structure using a temperature gradient from 15 to 95 °C. The transition point T_m of the denaturation curve was calculated to be 60.8 ± 0.9 °C for the IM30 wt protein. In contrast, the T_m of the mutants S96D with 56.1 ± 0.4 °C and T155D with 56.6 ± 1.0 °C were remarkably lower. While the T_m of the mutant S96A (control) was decreased only minorly to 59.7 ± 1.1 °C, the T_m of the second control IM30 T155A was comparable to T155D (57.2 ± 1.1 °C).

The results indicate that the phosphomimetic mutations reduce the thermal stability of IM30. Still, in case of Thr155, the destabilization is likely caused by a general importance of Thr155 for the IM30 structure.

4.8.2.6. IM30-membrane binding is not crucially influenced by phosphomimetic mutations

The interaction of IM30 with negatively charged membranes seems to be essential for the *in vivo* function, including membrane protection and membrane remodeling via membrane fusion (Bryan et al., 2014; Hennig et al., 2015; Gutu et al., 2018).

To analyze the effect of phosphorylation on the membrane fusion function, membrane binding in absence of Mg^{2+} was analyzed first. Therefore, binding to neutral liposomes (100 % PC) and to negatively charged liposomes (100 % PG) was investigated using Laurdan fluorescence measurements (Hennig et al., 2015). The GP calculated from the Laurdan spectra reflects changes of the lipid order, as can e.g. be observed when IM30 is binding to negatively charged membrane surfaces (Heidrich et al., 2016).

When analyzing binding to PC liposomes, only minor changes of the calculated ΔGP were observed after addition of the IM30 variants (Fig. 4.8.8 A). This indicates a very low affinity for binding to PC liposomes, consistent with previous reports (Hennig et al., 2015; McDonald et al., 2015). No differences between IM30 wt and the mutants were detectable.

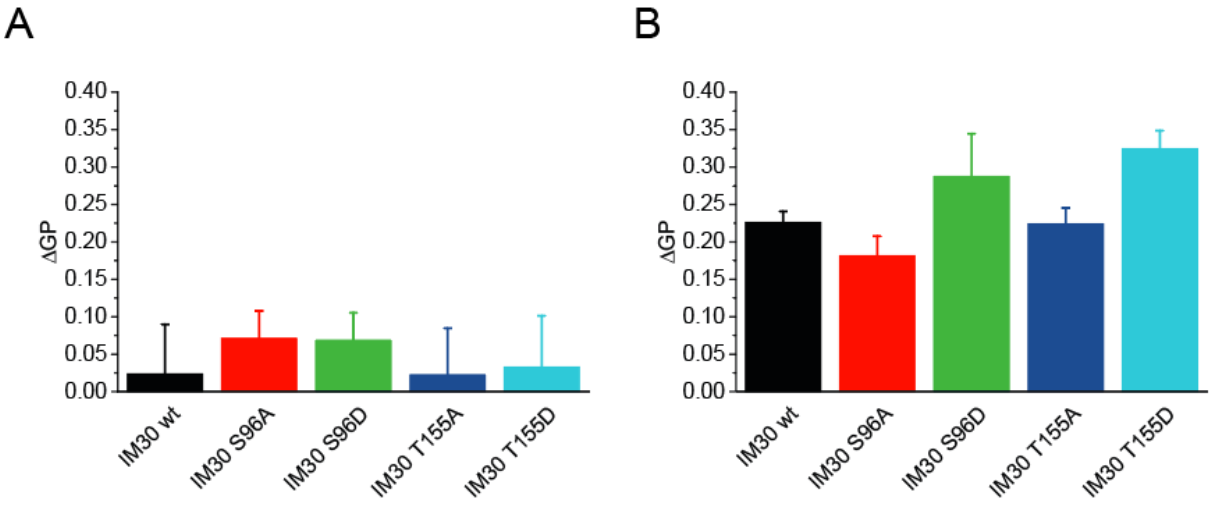

Figure 4.8.8: IM30 wt and mutants bind to negatively charged membranes.

Membrane binding of IM30 was measured using Laurdan fluorescence signals for IM30 wt (black), S96A (red), S96D (green), T155A (blue) and T155D (cyan). **A:** The Laurdan ΔGP was determined using 0.1 mM lipid (100 % PC) and 2.5 µM IM30. N=3, error bars represent SD. **B:** The Laurdan ΔGP was determined using 0.1 mM lipid (100 % PG) and 2.5 µM IM30. N=3, error bars represent SD.

In contrast, the observed ΔGP upon addition of IM30 wt and variants to PG liposomes was remarkably larger (Fig. 4.8.8 B). While the ΔGP was comparable when adding IM30 wt and the controls IM30 S96A and T155A, the variants with phosphomimetic mutation caused a significantly larger increase of the GP-value, indicating increased binding of these proteins at the used experimental conditions. Still, the binding affinity for the PG membrane cannot be analyzed in detail, since the experiment was only performed at a constant protein concentration. Nevertheless, all IM30 variants clearly bind to PG liposomes, as expected.

4.8.2.7. Phosphomimetic mutations do not affect Mg^{2+}-induced structural rearrangement of IM30

The IM30-triggered membrane fusion depends on Mg^{2+} (Hennig et al., 2015). While Mg^{2+} clearly supports membrane fusion in general, it also directly binds to IM30. This is associated with a structural rearrangement of the protein, which includes increased exposure of hydrophobic surfaces (Heidrich et al., 2018). This structural change is discussed to activate IM30 for membrane fusion.

Consequently, it was next analyzed whether the IM30 variants with phosphomimetic mutation still interact with Mg^{2+}. The increase in hydrophobic surfaces was determined via following the ANS fluorescence, as shown previously (Heidrich et al., 2018). ANS binding to hydrophobic surfaces of a protein is typically associated with a blue shift of the spectrum and an increased fluorescence intensity.

The shift of the ANS spectrum was analyzed by comparing the spectral center of mass, which is a characteristic for the spectral shape (Fig. 4.8.9 A). The spectral center of mass did differ for each IM30 variant, suggesting that all proteins have a different surface hydrophobicity. Still, after addition of Mg^{2+}, a blue shift of the ANS spectrum was observed for all proteins. Furthermore, when analyzing the ANS fluorescence intensity (Fig. 4.8.9 B), the typical increase was observed for IM30 variants.

This indicates that the phosphomimetic mutations have no influence on Mg^{2+} binding in general, while differences in the affinity of the Mg^{2+}-IM30 interaction cannot be excluded.

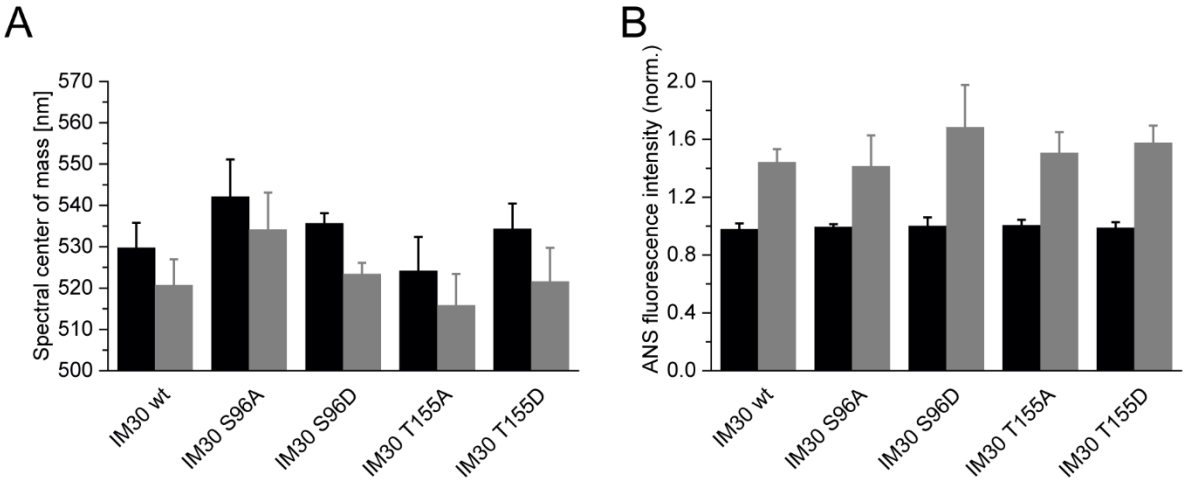

Figure 4.8.9: The interaction of IM30 wt and mutants with Mg^{2+} leads to an increased exposure of hydrophobic surfaces.

The exposure of hydrophobic surfaces upon addition of Mg^{2+} was analyzed via following ANS fluorescence. IM30: black, IM30 + Mg^{2+}: gray. **A:** The spectral center of mass is decreased upon addition of Mg^{2+}. **B:** The addition of Mg^{2+} leads to an increased ANS fluorescence intensity. N=3, error bars represent SD.

4.8.2.8. IM30 variants with phosphomimetic mutation have decreased membrane fusion activity

After showing that IM30 variants with phosphomimetic mutation interact with Mg^{2+} and bind to negatively charged membranes, it was next analyzed whether the mutations influence IM30-mediated membrane fusion (Fig. 4.8.10).

In fact, strongly reduced membrane fusion was observed for both phosphomimetic IM30 variants. In contrast, the fusion induced by the control mutants S96A and T155A was only slightly modulated. While the initial fusion rate of IM30 wt was calculated to be 1.13 ± 0.39 % s^{-1}, the initial fusion rates of IM30 S96D and IM30 T155D were 0.10 ± 0.05 % s^{-1} and 0.16 ± 0.09 % s^{-1}, respectively. While the initial fusion rate of IM30 T155A was even higher compared to the IM30 wt (1.70 ± 0.24 % s^{-1}), the rate observed when adding IM30 S96A was comparable to the wt protein (0.94 ± 0.56 % s^{-1}). While the IM30 wt and the control mutants fused the liposomes to > 80 % after 500 s, the liposomes fused by phosphomimetic mutants were fused to < 50 %.

The results show that the mutations of Ser96 or Thr155 clearly affect the membrane fusion activity of IM30 *in vitro*. These results indicate that IM30 phosphorylation might regulate the IM30 function *in vivo*.

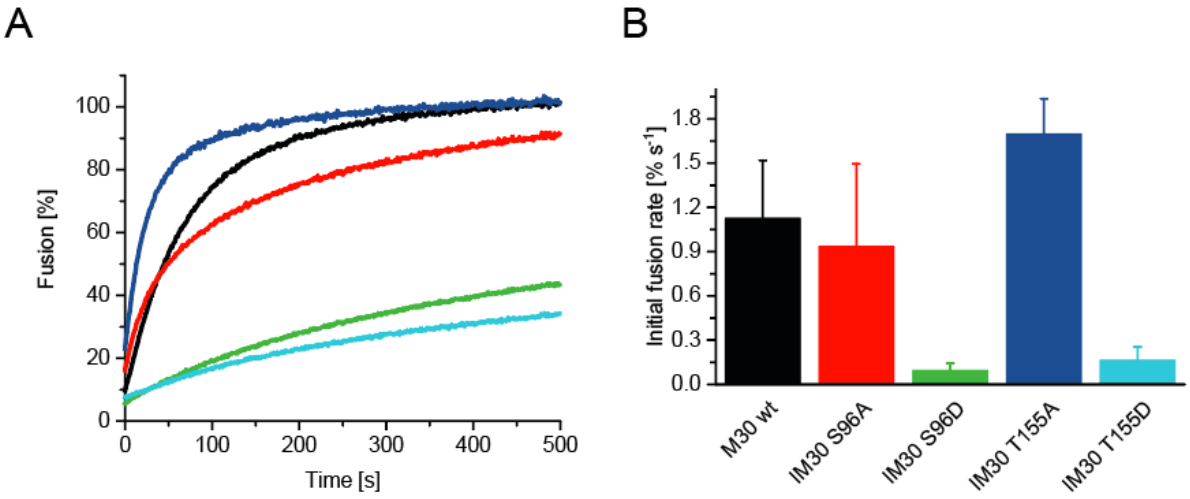

Figure 4.8.10: IM30 variants with phosphomimetic mutation have a decreased membrane fusion activity.

Membrane fusion was monitored by a FRET-based assay containing 2.5 µM IM30, 7.5 mM Mg^{2+} and 0.1 mM PG/MGDG (40:60) liposomes. Fusion induced by IM30 wt (black), S96A (red), S96D (green), T155A (blue) and T155D (cyan) was analyzed over 500s. **A:** The phosphomimetic mutations S96D and T155D showed decreased fusogenic activity. The curves represent the average of 3 independent measurements. **B:** The initial fusion rate was calculated as the slope of the fusion curve in the first 25 s. N=3, error bars represent SD.

4.8.3. Discussion

3.6.1.1. IM30 variants with phosphomimetic mutation form destabilized ring structures

The oligomeric ring structure is discussed to be important for the *in vivo* function of IM30 (Siebenaller et al., 2019).

In the ring structure, the phosphorylation sites Ser96 and Thr155 interact with neighboring monomers within a ring layer, but also with adjacent monomers from the upper or lower layer (Fig. 4.8.3-4). Ser96 likely interacts with helix 3, and Thr155 potentially interacts with helix 1, 2 and 4 from 4 different neighboring monomers. While this suggests an important role of these amino acids for oligomerization of the monomer, the IM30 mutants did still form the typical ring structures based on AFM and EM studies (Fig. 4.8.5). Furthermore, SEC experiments suggest that additionally to the high molecular weight structures, no further smaller oligomers were formed (Fig. 4.8.6). In agreement to that, the CD spectroscopic analyses indicated that the IM30 mutants were in general correctly folded, (Fig. 4.8.7 A,B).

Noteworthy, the thermal stability of the secondary structure of IM30 S96D and IM30 T155D was reduced in comparison to the IM30 wt protein (Fig. 4.8.7 B,C). While the effect seems to be specific for the phosphomimetic mutation of Ser96, a comparable low stability was observed for the two mutants IM30 T155A and T155D. Decreased thermal stability has only been observed for IM30 mutants with impaired oligomerization, such as IM30* or IM30 W71A so far (chapter 4.6). Yet, the results from this study imply that the phosphomimetic mutations destabilize the IM30 structure, which is, however, still able to oligomerize correctly into ring-like structures. It might be possible that the ring-like structure of the mutants can dissociate faster, as is suggested to happen when IM30 binds to membranes (Junglas et al., 2020b, chapter 4.4).

A reason for the structure destabilization could be a repulsion of the IM30 monomers within the ring. The repulsion is likely caused by the introduction of a negative charge by the phosphomimetic mutation, which repels other negatively charged amino acids, such as aspartic acid and glutamic acid. In the vicinity of Ser96 (Fig. 4.8.3), E126 might be responsible for the repulsion. In the vicinity of Thr155 in the ring structure (Fig. 4.8.3-4), Asp5, Glu30, Asp38, Asp39 and Glu187 could be relevant for the repulsion. Still, since destabilization of the ring structure by mutating Thr155 seems not phosphorylation specific, missing interactions of the Thr residue e.g. with Arg residues Arg6, Arg9 and Arg44 might be even more relevant. As the exact orientation of the amino acid side chains cannot be determined due to the quality of the IM30 structure, and the structures differ to some extent depending on the ring size and layer, the interacting amino acids need to be confirmed experimentally in the future.

3.6.1.2. Phosphomimetic mutations decrease the membrane fusion activity of IM30

IM30 has been shown to fuse thylakoid mimicking membranes in presence of Mg^{2+}, at least *in vitro* (Hennig et al., 2015). While the mutants IM30 S96D and T155D interact with Mg^{2+} (Fig. 4.8.8) and with negatively charged membranes (Fig. 4.8.9), the membrane fusion activity was strongly reduced (Fig. 4.8.10). In contrast, the controls IM30 S96A and T155A did trigger membrane fusion similar to the IM30 wt.

Both phosphomimetic mutations S96D and T155D had the same effect on membrane fusion, albeit the mutated residues are located at different positions within the ring structure (Fig. 4.8.10). Consequently, the reason for decreased fusion seems to be not site-specific, but rather caused by a similar effect on the IM30 structure or interactions.

The exact mechanism of the membrane fusion by IM30 is not known so far. It is assumed, that Mg^{2+} binding to the IM30 ring results in a structural rearrangement (Heidrich et al., 2018), which induces increased binding of IM30 rings to the membrane, accompanied by bilayer defects. Thus, Mg^{2+} seems to switch the function of IM30 from membrane-stabilizing to membrane remodeling (chapter 4.5). While membrane protection is likely associated with ring disassembly and the formation of a carpet-like structure on the membrane (Junglas et al., 2020b, chapter 4.4), membrane fusion is typically associated with the ring-like structure (Siebenaller et al., 2019). Since the phosphomimetic mutants still form rings, but with decreased stability, these rings might dissociate faster on the membrane, suggesting a potential role of phosphorylation in membrane stabilization. In contrast, the rings might not be stable enough to efficiently trigger membrane fusion, although they apparently still form rings (Fig. 4.8.5). Noteworthy, also other IM30 variants were not able to fuse membranes, although they (at least partially) form ring structures (chapter 4.7).

The interaction of the IM30 mutants with Mg^{2+} was investigated via analyzing changes in the ANS fluorescence (Fig. 4.8.8). These experiments clearly suggest an interaction of the IM30 variants with Mg^{2+}. But the affinity cannot be calculated quantitatively from the performed experiments. A future analysis on the affinity will clearly help to evaluate the low fusogenic activity. Interestingly, Thr155 is located close to a putative ADP binding site in IM30, in which also a Mg^{2+}-ion is coordinated (Gupta et al., 2021). Hence, the phosphorylation of Thr155 could sterically impair the coordination of the ADP/Mg^{2+} molecule. Nevertheless, as shown in chapter 4.1, nucleotide binding is clearly not necessary for membrane fusion (Junglas et al., 2020c), and the position of additional Mg^{2+} binding sites in IM30 is unclear so far.

A different explanation for the decreased fusion function could be decreased membrane binding. Phosphorylation of IM30 might impair binding to negatively charged lipids because of the charge repulsion of the PG lipid and the phosphorylated protein. Still, the membrane-interacting amino acids are not known in detail yet, and binding to membranes most likely includes multiple electrostatic interactions, as well as hydrophobic interactions. Since the membrane binding experiments were performed only at a single protein concentration, the membrane binding affinity cannot be determined quantitatively. Yet, if the IM30 wt and mutants interact the same way with the membrane, the increased change of the GP rather hints for increased membrane binding of the phosphomutant proteins (Fig. 4.8.9). Still, membrane binding experiments were performed in absence of Mg^{2+}, which has been shown to drastically increase membrane binding of IM30 wt (chapter 4.5).

In summary, the experiments suggest that IM30 phosphorylation might inhibit membrane fusion *in vivo*. Since IM30 is phosphorylated *in vivo* at both sites at the same time, the double mutation S96D and T155D could give further insight to the possible inactivation of IM30. Noteworthy, the analysis of the remaining six phosphorylation sites is also necessary in the future to fully understand the effect of phosphorylation on the IM30 structure and function.

3.6.1.3. Physiological implications

The function of IM30 is linked to TM biogenesis/maintenance, as the emergence of TMs is evolutionarily coupled to the development of the IM30 protein (Vothknecht et al., 2012). IM30 seems to be essential for the development of a TM system, as it is conserved in almost all oxygenic photosynthetic organisms (Westphal et al., 2001a; Vothknecht et al., 2012). IM30 seems to have at least a dual function: membrane protection and membrane remodeling.

While the membrane-protective function seems to be conserved in the PspA/IM30 family, the membrane remodeling activity has typically been ascribed to IM30. Nevertheless, also the bacterial ancestor PspA has recently been suggested to trigger membrane remodeling in absence of Mg^{2+} (Junglas et al., 2021). Clearly, IM30 has acquired additional functions in cyanobacteria and chloroplasts, since PspA cannot replace IM30 (Westphal et al., 2001; Aseeva et al., 2004; Bultema et al., 2010; Vothknecht et al., 2012). When shifting cyanobacterial cells from dark into light growth conditions, the expression of IM30 was suggested to be important (Gutu et al., 2018). During these conditions, the TMs need to be dynamically adapt to the changing light intensity (Chuartzman et al., 2008; Nagy et al., 2011; Liberton et al., 2013b). IM30 was suggested to be important for this extensive membrane remodeling, since IM30 can trigger fusion of TM model membranes (Hennig et al., 2015). Noteworthy, the suggested functions contradict each other on the first view, since membrane fusion usually involves membrane destabilization. Mg^{2+} release *e.g.* at high-light conditions might potentially control the respective activities (Junglas and Schneider, 2018). Still, further control is not known so far. The results of this study suggest that also IM30 phosphorylation might be a regulator of the IM30 function, since the IM30 variants with phosphomimetic mutation have strongly impaired fusogenic activities.

Since phosphorylation of IM30 has been observed *in vivo* during the first phase of resuscitation of chlorotic *Synechocystis* cells, but not during the second phase (Spät et al., 2015; Spät et al., 2018), the question arose why an altered fusogenic activity would be beneficial at these physiological conditions.

Interestingly, the first phase of resuscitation (~16-24 h) completely depends on glycogen consumption and oxygen-dependent respiration. In the second phase of resuscitation (24-48 h), the TMs are reconstructed *de novo*, and the cells regain photosynthetic activity gradually until they finally reach a photoautotrophic metabolism. In the first phase, the basic components of the metabolic machinery, such as ribosomal proteins, are synthesized (Spät et al., 2018). While the IM30 phosphorylation pattern in the first phase is rather complex with eight different sites on two different protein regions, the phosphorylation of all sites decreases with the emergence of the first TMs after 24 h, and is further accompanied by an accumulation of newly synthesized IM30. It has been suggested, that IM30 phosphorylation inactivates the protein (Spät et al., 2015; Spät et al., 2018). This idea is strongly supported by the here reported data, which show decreased membrane fusion activity of phosphomimetic mutants. Still, the data do not allow to conclude that IM30´s membrane-protective function is also reduced. In contrast, since membrane binding was still observed, IM30 might not be inactivated, but still fulfill the protective function. The potential destabilization of the IM30 ring structure could be a hint for the formation of carpet-like structures on the membrane. In the second phase, IM30 might indeed initiate the TM biogenesis by its membrane remodeling function.

Consequently, besides the already known trigger Mg^{2+}, IM30 (de)phosphorylation could be a further regulator of the IM30 function. Since other physiological conditions, such as changing light conditions, also have a huge impact on the TM dynamics, analysis of the phosphorylation status of IM30 during different physiological conditions could help to further unravel the regulation of the dual IM30 function.

3.6.1.4. Conclusion

In summary, this study shows that the phosphomimetic mutations S96D and T155D do not affect IM30 ring formation in general, but destabilize the IM30 ring structure. While interaction of IM30 with the membrane in presence of Mg^{2+} was not affected, the fusogenic activity of the phosphomimetic mutants was strongly reduced. The results suggest that IM30 phosphorylation inactivates the membrane remodeling activity of IM30, which is *e.g.* necessary in the 1st phase of resuscitation from chlorosis.

5. Conclusion

The *inner membrane-associated protein of 30 kDa* (IM30) is crucially involved in the biogenesis and dynamics of TMs, and consequently vital for all oxygenic photosynthetic organisms. Understanding the function, structure and regulation of this protein will help to understand the development of photosynthetic organisms, which enabled the evolution of aerobic life on earth. The observations presented in this thesis now help to better understand several aspects of the IM30 regulation and the mechanism of IM30-mediated membrane fusion.

The described observations give novel insights into the structural basis of the dual IM30 function. The oligomeric ring structure of IM30 was shown to dissociate when binding to a membrane in absence of Mg^{2+} (**chapter 4.4**). It was demonstrated that it forms carpet-like structures on the membrane, which consist of smaller oligomers. These smaller oligomers were shown to efficiently stabilize the membrane. Consequently, the membrane-protective function is most likely related to the carpet structures of IM30, and not to the ring structure. In contrast, the IM30 rings did not dissociate in presence of Mg^{2+}(**chapter 4.5**). The interaction with Mg^{2+} results in increased membrane binding of IM30, coupled with pore formation. Destabilization of the membrane is clearly relevant for the fusogenic activity of IM30. Thus, Mg^{2+} binding seems to regulate the dual IM30 function. Moreover, my research shows that, albeit IM30 ring formation appears to be essential for membrane fusion, ring-forming IM30 variants do not necessarily fuse membranes (**chapter 4.6, 4.7**).

Furthermore, the presented results help to better evaluate the cryptic GTPase activity of IM30. Although experimental proof was missing, it was suggested in the literature that nucleotide binding/hydrolysis plays an important role for IM30 oligomerization and function. The results presented here now show that neither the ring structure (**chapter 4.2**) nor the membrane interactions (**chapter 4.1**) are decisively affected. Furthermore, the results show that IM30 is actually an NTPase with specificity for purine-based nucleotides. Yet, the physiological relevance of the nucleotide interactions remains to be shown.

Importantly, the presented results indicate when and where IM30-mediated membrane fusion might be relevant *in vivo*. First of all, IM30 was found to have an increased membrane binding affinity and fusion activity at mildly acidic pH (**chapter 4.3**). This suggests that e.g. at high-light stress, IM30-mediated membrane fusion might be relevant to seal TM leaks, where protons are leaking out of the lumen. Furthermore, highly curved TM regions could be prone to IM30-mediated membrane remodeling processes, since highly curved liposomes fuse significantly faster in presence of IM30

(**chapter 4.7**). In accordance with this observation, the TM lipid MGDG, which is highly abundant in curved membrane regions, was found to be especially important for the membrane fusion process (**chapter 4.7**). The observations presented in this thesis further underline the idea that membrane fusion is relevant during TM development (**chapter 4.8**). Development of TMs is *e.g.* necessary during resuscitation of chlorotic cyanobacteria, but only after an initial phase of about 24 h. Here, IM30 was found to be phosphorylated, and the here presented results suggest that IM30 has a distinctly lower membrane fusion activity under these conditions. Consequently, phosphorylation might be an important trigger regulating the IM30 activity. Future analysis of the *in vivo* phosphorylation of IM30 under various environmental conditions can potentially largely increase our knowledge about the IM30 activity.

In summary, the results presented in this thesis contribute to better understand membrane remodeling processes in cyanobacteria and chloroplasts. Since IM30 has recently been shown to be part of the conserved ESCRT III-family, the research on IM30 may even help to better understand ESCRT III-dependent membrane remodeling processes in eukaryotic cells.

6. Literature

CC BY 4.0 Creative Commons—Attribution 4.0 International. http://creativecommons.org/licenses/by/4.0/

Ahkong QF, Fisher D, Tampion W, Lucy JA (1975) Mechanisms of cell fusion. Nat 1975 2535488 **253**: 194–195

Allen L, Brand A, Scott J, Altman M, Hlava M (2014) Credit where credit is due. Nature **508**: 312–313

Anderson JM, Goodchild DJ, Boardman NK (1973) Composition of the photosystems and chloroplast structure in extreme shade plants. BBA - Bioenerg **325**: 573–585

Antipina AY, Gurtovenko AA (2016) Molecular-level insight into the interactions of DNA with phospholipid bilayers: Barriers and triggers. RSC Adv **6**: 36425–36432

Aoki M, Sato N, Meguro A, Tsuzuki M (2004) Differing involvement of sulfoquinovosyl diacylglycerol in photosystem II in two species of unicellular cyanobacteria. Eur J Biochem **271**: 685–693

Aseeva E, Ossenbühl F, Eichacker LA, Wanner G, Soll J, Vothknecht UC (2004) Complex formation of Vipp1 depends on its α-helical PspA-like domain. J Biol Chem **279**: 35535–35541

Ashton AR (1998) A simple procedure for purifying the major chloroplast fructose-1,6-bisphosphatase from spinach (Spinacia oleracea) and characterization of its stimulation by sub-femtomolar mercuric ions. Arch Biochem Biophys **357**: 207–224

Bañares-Hidalgo A, Pérez-Gil J, Estrada P (2014) Acidic pH triggers conformational changes at the NH2-terminal propeptide of the precursor of pulmonary surfactant protein B to form a coiled coil structure. Biochim Biophys Acta - Biomembr **1838**: 1738–1751

Barthel S, Bernat G, Seidel T, Rupprecht E, Kahmann U, Schneider D (2013) Thylakoid Membrane Maturation and PSII Activation Are Linked in Greening Synechocystis sp. PCC 6803 Cells. Plant Physiol **163**: 1037–1046

Bechinger B, Lohner K (2006) Detergent-like actions of linear amphipathic cationic antimicrobial peptides. Biochim Biophys Acta - Biomembr **1758**: 1529–1539

Belkin S, Mehlhorn RJ, Packer L (1987) Proton gradients in intact cyanobacteria. Plant Physiol **84**: 25–30

Benning C (2008) A role for lipid trafficking in chloroplast biogenesis. Prog Lipid Res **47**: 381–389

Benning C, Beatty JT, Prince RC, Somerville CR (1993) The sulfolipid sulfoquinovosyldiacylglycerol is not required for photosynthetic electron transport in Rhodobacter sphaeroides but enhances growth under phosphate limitation. Proc Natl Acad Sci U S A **90**: 1561–1565

Benning C, Xu C, Awai K (2006) Non-vesicular and vesicular lipid trafficking involving plastids. Curr Opin Plant Biol **9**: 241–247

Bloye S, Silman N, Mann N, Carr N (1992) Bicarbonate Concentration by Synechocystis PCC6803 : Modulation of Protein Phosphorylation and Inorganic Carbon Transport by Glucose. Plant Physiol **99**: 601–606

De Boer P, Crossley R, Rothfield L (1992) The essential bacterial cell-division protein FtsZ is a GTPase. Nature **359**: 254–256

Bohuszewicz O, Liu J, Low HH (2016) Membrane remodelling in bacteria. J Struct Biol **196**: 3–14

Bradford MM (1976) A rapid and sensitive method for the quantitation of microgram quantities of protein utilizing the principle of protein-dye binding. Anal Biochem **72**: 248–254

Bramkamp M (2012) Structure and function of bacterial dynamin-like proteins. Biol Chem **393**: 1203–1214

Brissette JL, Russel M, Weiner L, Model P (1990) Phage shock protein, a stress protein of Escherichia coli. Proc Natl Acad Sci U S A **87**: 862–866

Brissette JL, Weiner L, Ripmaster TL, Model P (1991) Characterization and sequence of the Escherichia coli stress-induced psp operon. J Mol Biol **220**: 35–48

Brune M, Hunter JL, Corrie JET, Webb MR (1994) Direct, Real-Time Measurement of Rapid Inorganic Phosphate Release Using a Novel Fluorescent Probe and Its Application to Actomyosin Subfragment 1 ATPase. Biochemistry **33**: 8262–8271

Bryan SJ, Burroughs NJ, Shevela D, Yu J, Rupprecht E, Liu LN, Mastroianni G, Xue Q, Llorente-Garcia I, Leake MC, et al (2014) Localisation and interactions of the Vipp1 protein in cyanobacteria. Mol Microbiol **94**: 1179–1195

Bultema JB, Fuhrmann E, Boekema EJ, Schneider D (2010) Vipp1 and PspA. Commun Integr Biol **3**: 162–165

Cevc G (1987) How membrane chain melting properties are regulated by the polar surface of the lipid bilayer. Biochemistry **26**: 6305–6310

Chapman DJ, De-Felice J, Barber J (1983) Growth Temperature Effects on Thylakoid Membrane Lipid and Protein Content of Pea Chloroplasts. Plant Physiol **72**: 225–228

Cheung MY, Li X, Miao R, Fong YH, Li KP, Yung YL, Yu MH, Wong KB, Chen Z, Lam HM (2016) ATP binding by the P-loop NTPase OsYchF1 (an unconventional G protein) contributes to biotic but not abiotic stress responses. Proc Natl Acad Sci U S A **113**: 2648–2653

Chuartzman SG, Nevo R, Shimoni E, Charuvi D, Kiss V, Ohad I, Brumfeld V, Reicha Z (2008) Thylakoid membrane remodeling during state transitions in Arabidopsis. Plant Cell **20**: 1029–1039

Chung CT, Niemela SL, Miller RH (1989) One-step preparation of competent Escherichia coli: transformation and storage of bacterial cells in the same solution. Proc Natl Acad Sci U S A **86**: 2172–2175

Crooks GE, Hon G, Chandonia JM, Brenner SE (2004) WebLogo: A sequence logo generator. Genome Res **14**: 1188–1190

Darwin AJ (2005) The phage-shock-protein response. Mol Microbiol **57**: 621–628

DeLisa MP, Lee P, Palmer T, Georgiou G (2004) Phage Shock Protein PspA of Escherichia coli Relieves Saturation of Protein Export via the Tat Pathway. J Bacteriol **186**: 366–373

Demé B, Cataye C, Block MA, Maréchal E, Jouhet J (2014) Contribution of galactoglycerolipids to the 3-dimensional architecture of thylakoids. FASEB J **28**: 3373–3383

Dörmann P, Hoffmann-Benning S, Balbo I, Benning C (1995) Isolation and characterization of an Arabidopsis mutant deficient in the thylakoid lipid digalactosyl diacylglycerol. Plant Cell **7**: 1801–1810

Du B, Johannsmann D (2004) Operation of the quartz crystal microbalance in liquids: Derivation of the elastic compliance of a film from the ratio of bandwidth shift and frequency shift. Langmuir **20**: 2809–2812

Dutta D, Bandyopadhyay K, Datta AB, Sardesai AA, Parrack P (2009) Properties of HflX, an enigmatic protein from escherichia coli. J Bacteriol **191**: 2307–2314

Duysens LN (1956) The flattening of the absorption spectrum of suspensions, as compared to that of solutions. Biochim Biophys Acta **19**: 1–12

Dworkin J (2015) Ser/Thr phosphorylation as a regulatory mechanism in bacteria. Curr Opin Microbiol **24**: 47

El-Gebali, Sara; Mistry, Jaina; Bateman, Alex; Eddy, Sean R.; Luciani, Aurélien; Potter, Simon C.; Quereshi, Matloob; Richardson, Lorna J.; Salazar, Gustavo A.; Smart, Alfredo; Sonnhammer, Erik L. L.; Hirsh, Layla; Paladin, Lisanna; Piovesan, Damiano; Tosatto RD (2019) The Pfam protein families database in 2019. J Nucleic ACids Res **47**: D427–D432

Essigmann B, Güler S, Narang RA, Linke D, Benning C (1998) Phosphate availability affects the thylakoid lipid composition and the expression of SQD1 a gene required for sulfolipid biosynthesis in Arabidopsis thaliana. Proc Natl Acad Sci U S A **95**: 1950–1955

Fabiani C, Antollini SS (2019) Alzheimer's disease as a membrane disorder: Spatial cross-talk among beta-amyloid peptides, nicotinic acetylcholine receptors and lipid rafts. Front Cell Neurosci **13**: 309

Fakhree MAA, Blum C, Claessens MMAE (2019) Shaping membranes with disordered proteins. Arch Biochem Biophys **677**: 108163

Falke S, Betzel C (2019) Dynamic Light Scattering (DLS): Principles, Perspectives, Applications to Biological Samples. Radiat Bioanal **8**: 173

Falkner G, Horner F, Werdan K, Heldt HW (1976) pH Changes in the Cytoplasm of the Blue-Green Alga Anacystis nidulans Caused by Light-dependent Proton Flux into the Thylakoid Space . Plant Physiol **58**: 717–718

Foyer CH (2018) Reactive oxygen species, oxidative signaling and the regulation of photosynthesis. Environ Exp Bot **154**: 134–142

Fuhrmann E, Bultema JB, Kahmann U, Rupprecht E, Boekema EJ, Schneider D (2009a) The vesicle-inducing protein 1 from Synechocystis sp. PCC 6803 organizes into diverse higher-ordered ring structures. Mol Biol Cell **20**: 4620–4628

Fuhrmann E, Gathmann S, Rupprecht E, Golecki J, Schneider D (2009b) Thylakoid membrane reduction affects the photosystem stoichiometry in the cyanobacterium Synechocystis sp. PCC 6803. Plant Physiol **149**: 735–744

Galetovic A, Seura F, Gallardo V, Graves R, Cortés J, Valdivia C, Nuñez J, Tapia C, Neira I, Sanzana S, et al (2020) Use of phycobiliproteins from atacama cyanobacteria as food colorants in a dairy beverage prototype. Foods. doi: 10.3390/foods9020244

Gallivan JP, Dougherty DA (1999) Cation-π interactions in structural biology. Proc Natl Acad Sci U S A **96**: 9459–9464

Gao F, Wang W, Zhang W, Liu C (2015) α-Helical Domains Affecting the Oligomerization of Vipp1 and Its Interaction with Hsp70/DnaK in *Chlamydomonas*. Biochemistry **54**: 4877–4889

Gaysina LA, Saraf A, Singh P (2019) Cyanobacteria in Diverse Habitats. Cyanobacteria From Basic Sci to Appl 1–28

Gibson J (1981) Movement of acetate across the cytoplasmic membrane of the unicellular cyanobacteria Synechococcus and Aphanocapsa. Arch Microbiol **130**: 175–179

Gilbert RJC, Mikelj M, Dalla Serra M, Froelich CJ, Anderluh G (2013) Effects of MACPF/CDC proteins on lipid membranes. Cell Mol Life Sci **70**: 2083–2098

Giroud C, Siegenthaler P (1988) Development of Oat Prothylakoids into Thylakoids during Greening Does Not Change Transmembrane Galactolipid Asymmetry but Preserves the Thylakoid Bilayer. Plant Physiol **88**: 412–417

Gohre V, Göhre V, Ossenbühl F, Crèvecoeur M, Eichacker LA, Rochaix JD (2006) One of two Alb3 proteins is essential for the assembly of the photosystems and for cell survival in Chlamydomonas. Plant Cell **18**: 1454–1466

Görl M, Sauer J, Baier T, Forchhammer K (1998) Nitrogen-starvation-induced chlorosis in Synechococcus PCC 7942: adaptation to long-term survival. Microbiology **144 (Pt 9**: 2449–2458

Gounaris K, Sundby C, Andersson B, Barber J (1983) Lateral heterogeneity of polar lipids in the thylakoid membranes of spinach chloroplasts. FEBS Lett **156**: 170–174

Gray MW (1999) Evolution of organellar genomes. Curr Opin Genet Dev **9**: 678–687

Guo L, Bramkamp M (2019) Bacterial dynamin-like protein DynA mediates lipid and content mixing. FASEB J **33**: 11746–11757

Gupta TK, Klumpe S, Gries K, Heinz S, Wietrzynski W, Ohnishi N, Niemeyer J, Spaniol B, Schaffer M, Rast A, et al (2021) Structural basis for VIPP1 oligomerization and maintenance of thylakoid membrane integrity. Cell **184**: 3643-3659.e23

Gutu A, Chang F, O'Shea EK (2018) Dynamical localization of a thylakoid membrane binding protein is required for acquisition of photosynthetic competency. Mol Microbiol **108**: 16–31

Hagemann M, Golldack D, Biggins J, Erdmann N (1993) Salt-dependent protein phosphorylation in the cyanobacterium Synechocystis PCC 6803. FEMS Microbiol Lett **113**: 205–209

Hammond K, Ryadnov MG, Hoogenboom BW (2020) Atomic force microscopy to elucidate how peptides disrupt membranes. Biochim Biophys Acta - Biomembr **1863**: 183447

Hankamer BD, Elderkin SL, Buck M, Nield J (2004) Organization of the AAA+ Adaptor Protein PspA Is an Oligomeric Ring. J Biol Chem **279**: 8862–8866

Hazra S, Henderson JN, Liles K, Hilton MT, Wachter RM (2015) Regulation of Ribulose-1,5-bisphosphate Carboxylase/Oxygenase (Rubisco) Activase. J Biol Chem **290**: 24222–24236

Heidrich J, Junglas B, Grytsyk N, Hellmann N, Rusitzka K, Gebauer W, Markl J, Hellwig P, Schneider D (2018) Mg2+ binding triggers rearrangement of the IM30 ring structure, resulting in augmented exposure of hydrophobic surfaces competent for membrane binding. J Biol Chem **293**: 8230–8241

Heidrich J, Thurotte A, Schneider D (2017) Specific interaction of IM30/Vipp1 with cyanobacterial and chloroplast membranes results in membrane remodeling and eventually in membrane fusion. Biochim Biophys Acta - Biomembr **1859**: 537–549

Heidrich J, Wulf V, Hennig R, Saur M, Markl J, Sönnichsen C, Schneider D (2016) Organization into Higher Ordered Ring Structures Counteracts Membrane Binding of IM30, a Protein Associated with Inner Membranes in Chloroplasts and Cyanobacteria. J Biol Chem **291**: 14954–14962

Hellmann N, Schneider D (2019) Hands On: Using Tryptophan Fluorescence Spectroscopy to Study Protein Structure. Methods Mol. Biol. Humana Press Inc., pp 379–401

Hennig R, Heidrich J, Saur M, Schmüser L, Roeters SJ, Hellmann N, Woutersen S, Bonn M, Weidner T, Markl J, et al (2015) IM30 triggers membrane fusion in cyanobacteria and chloroplasts. Nat Commun **6**: 7018

Hennig R, West A, Debus M, Saur M, Markl J, Sachs JN, Schneider D (2017) The IM30/Vipp1 C-terminus associates with the lipid bilayer and modulates membrane fusion. Biochim Biophys Acta - Bioenerg **1858**: 126–136

Hitchcock A, Hunter CN, Canniffe DP (2020) Progress and challenges in engineering cyanobacteria as chassis for light-driven biotechnology. Microb Biotechnol **13**: 363–367

Huokko T, Ni T, Dykes GF, Simpson DM, Brownridge P, Conradi FD, Beynon RJ, Nixon PJ, Mullineaux CW, Zhang P, et al (2021) Probing the biogenesis pathway and dynamics of thylakoid membranes. Nat Commun 2021 121 **12**: 1–14

Ikeuchi M, Tabata S (2001) Synechocystis sp. PCC 6803 — a useful tool in the study of the genetics of cyanobacteria. Photosynth Res 2001 701 **70**: 73–83

Ingerman E, Nunnari J (2005) A continuous, regenerative coupled GTPase assay for dynamin-related proteins. Methods Enzymol. Academic Press Inc., pp 611–619

Ishijima S, Uchibori A, Takagi H, Maki R, Ohnishi M (2003) Light-induced increase in free Mg2+ concentration in spinach chloroplasts: Measurement of free Mg2+ by using a fluorescent probe and necessity of stromal alkalinization. Arch Biochem Biophys **412**: 126–132

Jahn R, Scheller RH (2006) SNAREs - Engines for membrane fusion. Nat Rev Mol Cell Biol **7**: 631–643

Jiang Y-Y, Kong D-X, Qin T, Li X, Caetano-Anollés G, Zhang H-Y (2012) The Impact of Oxygen on Metabolic Evolution: A Chemoinformatic Investigation. PLOS Comput Biol **8**: e1002426

Jilly R, Khan NZ, Aronsson H, Schneider D (2018) Dynamin-like proteins are potentially involved in membrane dynamics within chloroplasts and cyanobacteria. Front Plant Sci **9**: 206

Johannsmann D, Langhoff A, Leppin C (2021) Studying Soft Interfaces with Shear Waves: Principles and Applications of the Quartz Crystal Microbalance (QCM). Sensors (Basel). doi: 10.3390/S21103490

Joly N, Engl C, Jovanovic G, Huvet M, Toni T, Sheng X, Stumpf MPH, Buck M (2010) Managing membrane stress: The phage shock protein (Psp) response, from molecular mechanisms to physiology. FEMS Microbiol Rev **34**: 797–827

Junge W, Nelson N (2015) ATP synthase. Annu Rev Biochem **84**: 631–657

Junglas B, Axt A, Siebenaller C, Sonel H, Hellmann N, Weber SAL, Schneider D, Gutenberg J, Mainz U (2020a) Mg 2+-binding shifts the IM30 activity from membrane protection to membrane destabilization. bioRxiv 2020.09.25.313916

Junglas B, Huber ST, Heidler T, Schlösser L, Mann D, Hennig R, Clarke M, Hellmann N, Schneider D, Sachse C (2021) PspA adopts an ESCRT-III-like fold and remodels bacterial membranes. Cell **184**: 3674-3688.e18

Junglas B, Orru R, Axt A, Siebenaller C, Steinchen W, Heidrich J, Hellmich UA, Hellmann N, Wolf E, Weber SAL, et al (2020b) IM30 IDPs form a membrane-protective carpet upon super-complex disassembly. Commun Biol **3**: 595

Junglas B, Schneider D (2018) What is Vipp1 good for? Mol Microbiol **108**: 1–5

Junglas B, Siebenaller C, Schlösser L, Hellmann N, Schneider D (2020c) GTP hydrolysis by Synechocystis IM30 does not decisively affect its membrane remodeling activity. Sci Rep **10**: 1–14

Kallas T, Dahlquist FW (1981) Phosphorus-31 Nuclear Magnetic Resonance Analysis of Internal pH during Photosynthesis in the Cyanobacterium Synechococcus. Biochemistry **20**: 5900–5907

Kaneko T, Sato S, Kotani H, Tanaka A, Asamizu E, Nakamura Y, Miyajima N, Hirosawa M, Sugiura M, Sasamoto S, et al (1996) Sequence analysis of the genome of the unicellular cyanobacterium synechocystis sp. strain PCC6803. II. Sequence determination of the entire genome and assignment of potential protein-coding regions. DNA Res **3**: 109–136

Kelly SM, Jess TJ, Price NC (2005) How to study proteins by circular dichroism. Biochim Biophys Acta - Proteins Proteomics **1751**: 119–139

Kenneth Hoober J, Boyd CO, Paavola LG (1991) Origin of thylakoid membranes in Chlamydomonas reinhardtii y-1 at 38°C. Plant Physiol **96**: 1321–1328

Khan Z, Bhadouria P, Bisen P (2005) Nutritional and Therapeutic Potential of Spirulina. Curr Pharm Biotechnol **6**: 373–379

Kinnunen PKJ (1996) On the molecular-level mechanisms of peripheral protein-membrane interactions induced by lipids forming inverted non-lamellar phases. Chem Phys Lipids **81**: 151–166

Kirchhoff H (2014) Structural changes of the thylakoid membrane network induced by high light stress in plant chloroplasts. Philos Trans R Soc B Biol Sci. doi: 10.1098/rstb.2013.0225

Kleerebezem M, Crielaard W, Tommassen J (1996) Involvement of stress protein PspA (phage shock protein A) of Escherichia coli in maintenance of the protonmotive force under stress

conditions. Embo J **15**: 162–171

Klotz A, Georg J, Bučinská L, Watanabe S, Reimann V, Januszewski W, Sobotka R, Jendrossek D, Hess WR, Forchhammer K (2016) Awakening of a Dormant Cyanobacterium from Nitrogen Chlorosis Reveals a Genetically Determined Program. Curr Biol **26**: 2862–2872

Knoll AH (2008) Cyanobacteria and Earth History. Caister Academic Press

Kobayashi R, Suzuki T, Yoshida M (2007) Escherichia coli phage-shock protein A (PspA) binds to membrane phospholipids and repairs proton leakage of the damaged membranes. Mol Microbiol **66**: 100–109

Krasikov V, Aguirre von Wobeser E, Dekker HL, Huisman J, Matthijs HCP (2012) Time-series resolution of gradual nitrogen starvation and its impact on photosynthesis in the cyanobacterium Synechocystis PCC 6803. Physiol Plant **145**: 426–439

Kroll D, Meierhoff K, Bechtold N, Kinoshita M, Westphal S, Vothknecht UC, Soll J, Westhoff P (2001) VIPP1, a nuclear gene of Arabidopsis thaliana essential for thylakoid membrane formation. Proc Natl Acad Sci U S A **98**: 4238–4242

LaPorte DC, Wierman BM, Storm DR (1980) Calcium-induced exposure of a hydrophobic surface on calmodulin. Biochemistry **19**: 3814–3819

Lea-Smith DJ, Bombelli P, Vasudevan R, Howe CJ (2016) Photosynthetic, respiratory and extracellular electron transport pathways in cyanobacteria. Biochim Biophys Acta - Bioenerg **1857**: 247–255

Leipe DD, Koonin E V., Aravind L (2004) STAND, a class of P-loop NTPases including animal and plant regulators of programmed cell death: Multiple, complex domain architectures, unusual phyletic patterns, and evolution by horizontal gene transfer. J Mol Biol **343**: 1–28

Leipe DD, Wolf YI, Koonin E V., Aravind L (2002) Classification and evolution of P-loop GTPases and related ATPases. J Mol Biol **317**: 41–72

Li H, Kaneko Y, Keegstra K (1994) Molecular cloning of a chloroplastic protein associated with both the envelope and thylakoid membranes. Plant Mol Biol **25**: 619–632

Liang H, Harries D, Wong GCL (2005) Polymorphism of DNA-anionic liposome complexes reveals hierarchy of ion-mediated interactions. Proc Natl Acad Sci U S A **102**: 11173–11178

Liberton M, Collins AM, Page LE, O'Dell WB, O'Neill H, Urban VS, Timlin JA, Pakrasi HB (2013a) Probing the consequences of antenna modification in cyanobacteria. Photosynth Res

118: 17–24

Liberton M, Howard Berg R, Heuser J, Roth R, Pakrasi H (2006) Ultrastructure of the membrane systems in the unicellular cyanobacterium Synechocystis sp. strain PCC 6803. Protoplasma **227**: 129–138

Liberton M, Page LE, O'Dell WB, O'Neill H, Mamontov E, Urban VS, Pakrasi HB (2013b) Organization and flexibility of cyanobacterial thylakoid membranes examined by neutron scattering. J Biol Chem **288**: 3632–3640

Lin DC, Nobel PS (1971) Control of photosynthesis by Mg2+. Arch Biochem Biophys **145**: 622–632

Lindquist E, Aronsson H (2018) Chloroplast vesicle transport. Photosynth Res **138**: 361–371

Lindquist E, Solymosi K, Aronsson H (2016) Vesicles Are Persistent Features of Different Plastids. Traffic **17**: 1125–1138

Liu C, Willmund F, Golecki JR, Cacace S, Heß B, Markert C, Schroda M (2007) The chloroplast HSP70B-CDJ2-CGE1 chaperones catalyse assembly and disassembly of VIPP1 oligomers in Chlamydomonas. Plant J **50**: 265–277

Liu C, Willmund F, Whitelegge JP, Hawat S, Knapp B, Lodha M, Schroda M (2005) J-domain protein CDJ2 and HSP70B are a plastidic chaperone pair that interacts with vesicle-inducing protein in plastids 1. Mol Biol Cell **16**: 1165–1177

Liu H, Naismith JH (2008) An efficient one-step site-directed deletion, insertion, single and multiple-site plasmid mutagenesis protocol. BMC Biotechnol 2008 81 **8**: 1–10

Liu J, Tassinari M, Souza DP, Naskar S, Noel JK, Bohuszewicz O, Buck M, Williams TA, Baum B, Low HH (2021) Bacterial Vipp1 and PspA are members of the ancient ESCRT-III membrane-remodeling superfamily. Cell **184**: 3660-3673.e18

Liu L-N (2016) Distribution and dynamics of electron transport complexes in cyanobacterial thylakoid membranes. Biochim Biophys Acta **1857**: 256

Lo SM, Theg SM (2012) Role of vesicle-inducing protein in plastids 1 in cpTat transport at the thylakoid. Plant J **71**: 656–668

Luan G, Zhang S, Lu X (2020) Engineering cyanobacteria chassis cells toward more efficient photosynthesis. Curr Opin Biotechnol **62**: 1–6

Lutkenhaus J, Pichoff S, Du S (2012) Bacterial cytokinesis: From Z ring to divisome. Cytoskeleton **69**: 778–790

Male AL, Oyston PCF, Tavassoli A (2014) Self-Assembly of Escherichia coli Phage Shock Protein A. Adv Microbiol **04**: 353–359

Marsden HR, Tomatsu I, Kros A (2011) Model systems for membrane fusion. Chem Soc Rev **40**: 1572–1585

Masamoto K, Nishimura M (1977) Estimation of internal pH in cells of blue-green algae in the dark and under illumination. J Biochem **82**: 483–7

McCubbin WD, Oikawa K, Kay CM (1971) Circular dichroism studies on concanavalin A. Biochem Biophys Res Commun **43**: 666–674

McCullough J, Sundquist WI (2020) Membrane Remodeling: ESCRT-III Filaments as Molecular Garrotes. Curr Biol **30**: R1425–R1428

McDonald C, Jovanovic G, Ces O, Buck M (2015) Membrane stored curvature elastic stress modulates recruitment of maintenance proteins pspa and vipp1. MBio **6**: e01188-15

McDonald C, Jovanovic G, Wallace BA, Ces O, Buck M (2017) Structure and function of PspA and Vipp1 N-terminal peptides: Insights into the membrane stress sensing and mitigation. Biochim Biophys Acta - Biomembr **1859**: 28–39

McKenney PT, Driks A, Eichenberger P (2012) The Bacillus subtilis endospore: assembly and functions of the multilayered coat. Nat Rev Microbiol 2012 111 **11**: 33–44

McNew JA, Sondermann H, Lee T, Stern M, Brandizzi F (2013) GTP-Dependent Membrane Fusion. Annu Rev Cell Dev Biol **29**: 529–550

Van De Meene AML, Hohmann-Marriott MF, Vermaas WFJ, Roberson RW (2006) The three-dimensional structure of the cyanobacterium Synechocystis sp. PCC 6803. Arch Microbiol **184**: 259–270

Mehta P, Jovanovic G, Ying L, Buck M (2015) Is the cellular and molecular machinery docile in the stationary phase of escherichia coli? Biochem Soc Trans **43**: 168–171

Mim C, Unger VM (2012) Membrane curvature and its generation by BAR proteins. Trends Biochem Sci **37**: 526–533

Mondal Roy S, Sarkar M (2011) Membrane Fusion Induced by Small Molecules and Ions. J Lipids **2011**: 1–14

Muiznieks LD, Weiss AS, Keeley FW (2010) Structural disorder and dynamics of elastin. Biochem. Cell Biol. National Research Council of Canada, pp 239–250

Mullineaux CW (2014) Co-existence of photosynthetic and respiratory activities in cyanobacterial thylakoid membranes. Biochim Biophys Acta - Bioenerg **1837**: 503–511

Mullineaux CW (1999) The thylakoid membranes of cyanobacteria: structure, dynamics and function. Funct Plant Biol **26**: 671677

Murata N (1989) Low-temperature effects on cyanobacterial membranes. J Bioenerg Biomembr **21**: 61–75

Murphy DJ (1982) The importance of non-planar bilayer regions in photosynthetic membranes and their stabilisation by galactolipids. FEBS Lett **150**: 19–26

Nagy G, Posselt D, Kovács L, Holm JK, Szabó M, Ughy B, Rosta L, Peters J, Timmins P, Garab G (2011) Reversible membrane reorganizations during photosynthesis in vivo: Revealed by small-angle neutron scattering. Biochem J **436**: 225–230

Nestler H, Groh KJ, Schönenberger R, Eggen RIL, Suter MJF (2012) Linking proteome responses with physiological and biochemical effects in herbicide-exposed Chlamydomonas reinhardtii. J Proteomics **75**: 5370–5385

Neumann N, Doello S, Forchhammer K (2021) Recovery of Unicellular Cyanobacteria from Nitrogen Chlorosis: A Model for Resuscitation of Dormant Bacteria. Microb Physiol **31**: 78–87

Nickelsen J, Rengstl B, Stengel A, Schottkowski M, Soll J, Ankele E (2011) Biogenesis of the cyanobacterial thylakoid membrane system - an update. FEMS Microbiol Lett **315**: 1–5

Nir S, Wilschut J, Bentz J (1982) The rate of fusion of phospholipid vesicles and the role of bilayer curvature. Biochim Biophys Acta - Biomembr **688**: 275–278

Nitschmann WH, Peschek GA (1985) Modes of proton translocation across the cell membrane of respiring cyanobacteria. Arch Microbiol **141**: 330–336

Nordhues A, Schottler MA, Unger A-K, Geimer S, Schonfelder S, Schmollinger S, Rutgers M, Finazzi G, Soppa B, Sommer F, et al (2012) Evidence for a Role of VIPP1 in the Structural Organization of the Photosynthetic Apparatus in Chlamydomonas. Plant Cell Online **24**: 637–659

Ohnishi N, Zhang L, Sakamoto W (2018) VIPP1 involved in chloroplast membrane integrity has GTPase activity in vitro. Plant Physiol **177**: pp.00145.2018

Osadnik H, Schöpfel M, Heidrich E, Mehner D, Lilie H, Parthier C, Risselada HJ, Grubmüller H, Stubbs MT, Brüser T (2015) PspF-binding domain PspA1-144and the PspA·F complex: New insights into the coiled-coil-dependent regulation of AAA+ proteins. Mol Microbiol **98**: 743–759

Otters S, Braun P, Hubner J, Wanner G, Vothknecht UC, Chigri F (2013) The first α-helical domain of the vesicle-inducing protein in plastids 1 promotes oligomerization and lipid binding. Planta **237**: 529–540

Pace CN, Grimsley GR, Scholtz JM (2009) Protein ionizable groups: pK values and their contribution to protein stability and solubility. J Biol Chem **284**: 13285–13289

Padan E, Schuldiner S (1978) Energy transduction in the photosynthetic membranes of the cyanobacterium (blue-green alga) Plectonema boryanum. J Biol Chem **253**: 3281–3286

Parasassi T, Krasnowska EK, Bagatolli L, Gratton E (1998) Laurdan and Prodan as Polarity-Sensitive Fluorescent Membrane Probes. J Fluoresc **8**: 365–373

Parasassi T, Stasio G De, d'Ubaldo A, Gratton E (1990) Phase fluctuation in phospholipid membranes revealed by Laurdan fluorescence. Biophys J **57**: 1179

Patel H, Huynh Q, Bärlehner D, Heerklotz H (2014) Additive and synergistic membrane permeabilization by antimicrobial (LIPO)peptides and detergents. Biophys J **106**: 2115–2125

Pathak J, Rajneesh, Maurya PK, Singh SP, Häder D-P, Sinha RP (2018) Cyanobacterial Farming for Environment Friendly Sustainable Agriculture Practices: Innovations and Perspectives. Front Environ Sci **0**: 7

Peschek GA (1999) Photosynthesis and Respiration of Cyanobacteria. The Phototrophic Prokaryotes. Springer, Boston, MA, pp 201–209

Pfeil MP, Pyne ALB, Losasso V, Ravi J, Lamarre B, Faruqui N, Alkassem H, Hammond K, Judge PJ, Winn M, et al (2018) Tuneable poration: host defense peptides as sequence probes for antimicrobial mechanisms. Sci Rep **8**: 14926

Pleshakova TO, Bukharina NS, Archakov AI, Ivanov YD (2018) Atomic Force Microscopy for Protein Detection and Their Physicochemical Characterization. Int J Mol Sci. doi: 10.3390/IJMS19041142

Pohland AC, Schneider D (2019) Mg2+ homeostasis and transport in cyanobacteria - at the crossroads of bacterial and chloroplast Mg2+ import. Biol Chem **400**: 1289–1301

Porra RJ, Thompson WA, Kriedemann PE (1989) Determination of accurate extinction coefficients and simultaneous equations for assaying chlorophylls a and b extracted with four different solvents: verification of the concentration of chlorophyll standards by atomic absorption spectroscopy. BBA - Bioenerg **975**: 384–394

Portis AR (1981) Evidence of a Low Stromal Mg 2+ Concentration in Intact Chloroplasts in the Dark. Plant Physiol **67**: 985–989

Portis AR, Heldt HW (1976) Light-dependent changes of the Mg2+ concentration in the stroma in relation to the Mg2+ dependency of CO2 fixation in intact chloroplasts. BBA - Bioenerg **449**: 434–446

Praefcke GJK, McMahon HT (2004) The dynamin superfamily: Universal membrane tubulation and fission molecules? Nat Rev Mol Cell Biol **5**: 133–147

Rast A, Heinz S, Nickelsen J (2015) Biogenesis of thylakoid membranes. Biochim Biophys Acta - Bioenerg **1847**: 821–830

Rauscher S, Pomès R (2017) The liquid structure of elastin. Elife. doi: 10.7554/eLife.26526

Reviakine I, Johannsmann D, Richter RP (2011) Hearing What You Cannot See and Visualizing What You Hear: Interpreting Quartz Crystal Microbalance Data from Solvated Interfaces. Anal Chem **83**: 8838–8848

Rexroth S, Mullineaux CW, Ellinger D, Sendtko E, Rögner M, Koenig F (2011) The Plasma Membrane of the Cyanobacterium Gloeobacter violaceus Contains Segregated Bioenergetic Domains. Plant Cell **23**: 2379

Richter G (2003) Praktische Biochemie Grundlagen und Techniken.

Rippka R, Waterbury J, Cohen-Bazire G (1974) A cyanobacterium which lacks thylakoids. Arch Microbiol 1974 1001 **100**: 419–436

Royer CA, Mann CJ, Matthews CR (1993) Resolution of the fluorescence equilibrium unfolding profile of trp aporepressor using single tryptophan mutants. Protein Sci **2**: 1844

Rudack T, Xia F, Schlitter J, Kötting C, Gerwert K (2012) The role of magnesium for geometry and charge in GTP hydrolysis, revealed by quantum mechanics/Molecular mechanics simulations. Biophys J **103**: 293–302

Rueden CT, Schindelin J, Hiner MC, DeZonia BE, Walter AE, Arena ET, Eliceiri KW (2017) ImageJ2: ImageJ for the next generation of scientific image data. BMC Bioinformatics **18**: 529

Sato N, Tsuzuki M, Matsuda Y, Ehara T, Osafune T, Kawaguchi A (1995) Isolation and Characterization of Mutants Affected in Lipid Metabolism of Chlamydomonas Reinhardtii. Eur J Biochem **230**: 987–993

Sauerbrey G (1959) Verwendung von Schwingquarzen zur Wägung dünner Schichten und zur Mikrowägung. Zeitschrift für Phys **155**: 206–222

Saur M, Hennig R, Young P, Rusitzka K, Hellmann N, Heidrich J, Morgner N, Markl J, Schneider D (2017) A Janus-Faced IM30 Ring Involved in Thylakoid Membrane Fusion Is Assembled from IM30 Tetramers. Structure **25**: 1380-1390.e5

Sawant P, Eissenberger K, Karier L, Mascher T, Bramkamp M (2016) A dynamin-like protein involved in bacterial cell membrane surveillance under environmental stress. Environ Microbiol **18**: 2705–2720

Scherer S, Stürzl E, Böger P (1984) Oxygen-dependent proton efflux in cyanobacteria (blue-green algae). J Bacteriol **158**: 609–14

Schmidt O, Teis D (2012) The ESCRT machinery. Curr Biol **22**: R116

Schneider D, Fuhrmann E, Scholz I, Hess WR, Graumann PL (2007) Fluorescence staining of live cyanobacterial cells suggest non-stringent chromosome segregation and absence of a connection between cytoplasmic and thylakoid membranes. BMC Cell Biol. doi: 10.1186/1471-2121-8-39

Seiwert D, Witt H, Ritz S, Janshoff A, Paulsen H (2018) The Nonbilayer Lipid MGDG and the Major Light-Harvesting Complex (LHCII) Promote Membrane Stacking in Supported Lipid Bilayers. Biochemistry **57**: 2278–2288

Shan SO, Schmid SL, Zhang X (2009) Signal recognition particle (SRP) and SRP receptor: A new paradigm for multistate regulatory GTPases. Biochemistry **48**: 6696–6704

Shaul O (2002) Magnesium transport and function in plants: The tip of the iceberg. BioMetals **15**: 309–323

Shipley GG, Green JP, Nichols BW (1973) The phase behavior of monogalactosyl, digalactosyl, and sulphoquinovosyl diglycerides. Biochim Biophys Acta - Biomembr **311**: 531–544

Siebenaller C (2016) Einfluss von Tryptophan 71 auf die Struktur und Funktion des IM30-Proteins aus Synechocystis sp. PCC 6803. Johannes Gutenberg University Mainz

Siebenaller C, Junglas B, Lehmann A, Hellmann N, Schneider D (2020) Proton Leakage Is Sensed by IM30 and Activates IM30-Triggered Membrane Fusion. Int J Mol Sci **21**: 4530

Siebenaller C, Junglas B, Schneider D (2019) Functional Implications of Multiple IM30 Oligomeric States. Front Plant Sci. doi: 10.3389/fpls.2019.01500

Siebenaller C, Schlösser L, Junglas B, Schmidt-Dengler M, Jacob D, Hellmann N, Sachse C, Helm M, Schneider D (2021) Binding and/or hydrolysis of purine-based nucleotides is not required for IM30 ring formation. FEBS Lett 1873-3468.14140

Simidjiev I, Stoylova S, Amenitsch H, Jávorfi T, Mustárdy L, Laggner P, Holzenburg A, Garab G (2000) Self-assembly of large, ordered lamellae from non-bilayer lipids and integral membrane proteins in vitro. Proc Natl Acad Sci U S A **97**: 1473

Song BD, Leonard M, Schmid SL (2004) Dynamin GTPase domain mutants that differentially affect GTP binding, GTP hydrolysis, and clathrin-mediated endocytosis. J Biol Chem **279**: 40431–40436

Song T, Mårtensson L, Eriksson T, Zheng W, Rasmussen U (2005) Biodiversity and seasonal variation of the cyanobacterial assemblage in a rice paddy field in Fujian, China. FEMS Microbiol Ecol **54**: 131–140

Spät P, Klotz A, Rexroth S, Maček B, Forchhammer K (2018) Chlorosis as a Developmental Program in Cyanobacteria: The Proteomic Fundament for Survival and Awakening. Mol Cell Proteomics **17**: 1650

Spät P, Maček B, Forchhammer K (2015) Phosphoproteome of the cyanobacterium Synechocystis sp. PCC 6803 and its dynamics during nitrogen starvation. Front Microbiol **6**: 248

Sprague S, Staehelin L (1984) A rapid reverse phase evaporation method for the reconstitution of uncharged thylakoid membrane lipids that resist hydration. Plant Physiol **75**: 502–504

Standar K, Mehner D, Osadnik H, Berthelmann F, Hause G, Lünsdorf H, Brüser T (2008) PspA can form large scaffolds in Escherichia coli. FEBS Lett **582**: 3585–3589

Stock JB, Ninfa AJ, Stock AM (1989) Protein phosphorylation and regulation of adaptive responses in bacteria. Microbiol Rev **53**: 450

Theis J, Gupta TK, Klingler J, Wan W, Albert S, Keller S, Engel BD, Schroda M (2019) VIPP1

rods engulf membranes containing phosphatidylinositol phosphates. Sci Rep **9**: 8725

Thurotte A, Brüser T, Mascher T, Schneider D (2017) Membrane chaperoning by members of the PspA/IM30 protein family. Commun Integr Biol **10**: e1264546

Thurotte A, Schneider D (2019) The Fusion Activity of IM30 Rings Involves Controlled Unmasking of the Fusogenic Core. Front Plant Sci **10**: 108

Urry DW, Ji TH (1968) Distortions in circular dichroism patterns of particulate (or membranous) systems. Arch Biochem Biophys **128**: 802–807

Uversky V, Eliezer D (2009) Biophysics of Parkinsons Disease: Structure and Aggregation of α- Synuclein. Curr Protein Pept Sci **10**: 483–499

Uversky VN (2017) Paradoxes and wonders of intrinsic disorder: Stability of instability. Intrinsically Disord Proteins **5**: e1327757

Vega-Cabrera LA, Pardo-López L (2017) Membrane remodeling and organization: Elements common to prokaryotes and eukaryotes. IUBMB Life **69**: 55–62

Vermass WFJ, Rutherford AW, Hansson O (1988) Site-directed mutagenesis in photosystem II of the cyanobacterium Synechocystis sp. PCC 6803: Donor D is a tyrosine residue in the D2 protein. Proc Natl Acad Sci **85**: 8477–8481

Vothknecht UC, Otters S, Hennig R, Schneider D (2012) Vipp1: A very important protein in plastids?! J Exp Bot **63**: 1699–1712

Vrancken K, Van Mellaert L, Anné J (2008) Characterization of the Streptomyces lividans PspA response. J Bacteriol **190**: 3475–3481

Wada H, Murata' N (1989) Synechocystis PCC6803 Mutants Defective in Desaturation of Fatty Acids.

Walter B, Hristou A, Nowaczyk MM, Schünemann D (2015) *In vitro* reconstitution of co-translational D1 insertion reveals a role of the cpSec–Alb3 translocase and Vipp1 in photosystem II biogenesis. Biochem J **468**: 315–324

Webb MS, Green BR (1990) Effects of neutral and anionic lipids on digalactosyldiacylglycerol vesicle aggregation. Biochim Biophys Acta - Biomembr **1030**: 231–237

Weiner L, Brissette JL, Model P (1991) Stress-induced expression of the Escherichia coli phage shock protein operon is dependent on σ54 and modulated by positive and negative feedback mechanisms. Genes Dev **5**: 1912–1923

Westphal S, Heins L, Soll J, Vothknecht UC (2001a) Vipp1 deletion mutant of Synechocystis: a connection between bacterial phage shock and thylakoid biogenesis? Proc Natl Acad Sci U S A **98**: 4243–8

Westphal S, Soll J, Vothknecht UC (2001b) A vesicle transport system inside chloroplasts. FEBS Lett **506**: 257–261

Wimley WC (2010) Describing the mechanism of antimicrobial peptide action with the interfacial activity model. ACS Chem Biol **5**: 905–917

Wolf D, Kalamorz F, Wecke T, Juszczak A, Mäder U, Homuth G, Jordan S, Kirstein J, Hoppert M, Voigt B, et al (2010) In-Depth Profiling of the LiaR Response of Bacillus subtilis. J Bacteriol **192**: 4680–4693

Yu C-W, Lin Y-T, Li H (2020) Increased ratio of galactolipid MGDG : DGDG induces jasmonic acid overproduction and changes chloroplast shape. New Phytol **228**: 1327–1335

Zhang B, Zhang Y, Wang ZX, Zheng Y (2000) The role of Mg2+ cofactor in the guanine nucleotide exchange and GTP hydrolysis reactions of Rho family GTP-binding proteins. J Biol Chem **275**: 25299–25307

Zhang L, Kato Y, Otters S, Vothknecht UC, Sakamoto W (2012) Essential Role of VIPP1 in Chloroplast Envelope Maintenance in Arabidopsis. Plant Cell **24**: 3695–3707

Zhang L, Kondo H, Kamikubo H, Kataoka M, Sakamoto W (2016) VIPP1 has a disordered C-terminal tail necessary for protecting photosynthetic membranes against stress. Plant Physiol **171**: 1983–1995

Zhang L, Sakamoto W (2015) Possible function of VIPP1 in maintaining chloroplast membranes. Biochim Biophys Acta **1847**: 831–837

Zhang L, Sakamoto W (2013) Possible function of VIPP1 in thylakoids: Protection but not formation? Plant Signal Behav. doi: 10.4161/psb.22860

Zhang S, Shen G, Li Z, Golbeck JH, Bryant DA (2014) Vipp1 is essential for the biogenesis of Photosystem I but not thylakoid membranes in Synechococcus sp. PCC 7002. J Biol Chem **289**: 15904–15914

Zhen Y, Radulovic M, Vietri M, Stenmark H (2021) Sealing holes in cellular membranes. EMBO J **40**: e106922

Zhou L, Srisatjaluk R, Justus D., Doyle R. (1998) On the origin of membrane vesicles in Gram-negative bacteria. FEMS Microbiol Lett **163**: 223–228

7. Abbreviations

λ	Wavelength
Å	Angström, 10^{-10} m
A, Ala	Alanine
A	Adenine
A	Absorption
A	Area
ADP	Adenosine diphosphate
AFM	Atomic force microscopy
AMP	Antimicrobial peptide
ANS	8-Anilino-1-naphthalenesulfonic acid
ATP	Adenosine triphosphate
Arabidopsis	*Arabidopsis thaliana*
Atto-633-PE	1,2-Dioleoyl-*sn*-glycero-3-phosphoethanolamine labeled with Atto633
a.u.	Arbitrary unit
c	concentration
C, Cys	Cysteine
C	Cytosine
C-	Carboxy-
CD	Circular Dichroism
CFP	Cyan fluorescent protein
CM	Cytoplasmic membrane
Cr	*Chlamydomonas rheinhardtii*
Chlamydomonas	*Chlamydomonas rheinhardtii*
CPS	Counts per second
d	diameter
D, Asp	Aspartic acid

Da	Dalton
DGDG	Digalactosyldiacylglycerol
DNA	Desoxyribonucleid acid
dNTP	Desoxyribonucleosid triphosphate
DOPC	1,2-dipalmytoyl-*sn*-glycero-3-phosphocholin
DOPE	1,2-dipalmytoyl-*sn*-glycero-3-phosphoethanolamine
DOPG	1,2-dipalmytoyl-*sn*-glycero-3-phosphoglycerol
DGDG	Digalactosyldiacylglycerol
E, Glu	Glutamic acid
e.g.	lat. *exempli gratia*
E. coli	*Escherichia coli*
EM	Electron microscopy
ESCRT	Endosomal sorting complex required for transport
G, Gly	Glycine
G	Guanine
GDP	Guanosine diphosphate
GP	Generalized Polarization
GTP	Guanosine triphosphate
GUV	Giant unilamellar vesicle
H	Helix
H, His	Histidine
HEPES	4-(2-Hydroxyethyl)-1-piperazineethanesulfonic acid
His-Tag	Histidine tag
I, Ile	Isoleucine
I	Intensity
IE	Inner envelope
IM30	Inner-membrane associated protein of 30 kDa
IPTG	Isopropyl-β-thiogalactopyranoside
K, Lys	Lysine

K_D	Dissociation constant
L, Leu	Leucine
LC	Liquid chromatography
Liss-Rhod-PE	1,2-Dioleoyl-*sn*-glycero-3-phosphoethanolamine-*N*-(lissaminerhodamine B sulfonyl)
M, Met	Methione
M	Molarity
M	Marker
m	slope
MGDG	Monogalactosyldiacylglycerol
MS	Mass spectrometry
MWCO	Molecular weight cut off
N, Asn	Asparagine
n	Number of samples
n.a.	Not applicalble
Ni-NTA	Nickel-Nitrilotriacetic acid
norm.	normalized
NBD-PE	1,2-Dioleoyl-sn-glycero-3-phosphoethanolamine-N-(7-nitro-2-1,3-benzoxadiazol-4-yl)
OD	Optical density
P, Pro	Proline
PC	Phosphatidylcholine
PG	Phosphatidylglycerol
pH	Lat.: *potentia Hydrogenii*
PCR	Polymerase chain reaction
PMF	Proton motive force
PS	Photosystem
PspA	Phage-shock protein A
PsP System	Phage shock protein system

PDB	Protein data bank
Q, Gln	Glutamine
QCM	Quartz crystal microbalance
R, Arg	Arginine
rpm	revolutions per minute
Rel.	Relative
RT	Room temperature
S, Ser	Serine
SD	Sucrose density
SD	Standard deviation
SDS-PAGE	Sodium dodecyl sulfate polyacrylamide gel electrophoresis
SEC	Size exclusion chromatography
SLB	Solid supported bilayer
SQDG	Sulfoquinovosyldiacylglycerol
Syn	*Synechocystis* sp. PCC 6803
Synechocystis	*Synechocystis* sp. PCC 6803
Synechococcus	*Synechococcus* sp. PCC 7002
T, Thr	Threonine
T	Thymine
T	Temperature
T_m	Melting temperature
TM	Thylakoid membrane
V, Val	Valine
Vipp1	Vesicle-inducing protein in plastids
wt	wildtype
W, Trp	Tryptophan
Y, Tyr	Tyrosine

8. List of Figures

9. List of Tables

10. Author affiliations

11. Appendix

VIII.1 Siebenaller C.#, Junglas B.# and Schneider D. (2019) Functional implications of multiple IM30 oligomeric states, Front. Plant Sci. 10, 150

VIII.2 Junglas B.#, Siebenaller C.#, Schlösser L., Hellmann N. and Schneider, D. (2020) GTP hydrolysis by *Synechocystis* IM30 does not decisively affect its membrane remodeling activity, Sci. Rep. 10, 9793

VIII.3 Siebenaller C., Schlösser L., Junglas B., Schmidt-Dengler M., Jacob D., Hellmann N., Sachse C., Helm M. and Schneider, D. (2021) Binding and/or hydrolysis of purine-based nucleotides is not required for IM30 ring formation, FEBS let. 595, 14, 1876-1885.

VIII.4 Siebenaller C.#, Junglas B.#; Lehmann A., Hellmann N. and Schneider D. (2020) Proton Leakage Is Sensed by IM30 and Activates IM30-Triggered Membrane Fusion, Int. J. Mol. Sci. 21(12), 4530

VIII.5 Junglas B., Orru R., Axt A., Siebenaller C., Steinchen W., Heidrich J., Hellmich U.A., Hellmann N., Wolf E., Weber S. and Schneider D. (2020) IM30 IDPs form a membrane-protective carpet upon super-complex disassembly, Nature Comm. Biol. 3, 595

# These authors contributed equally.

All articles are licensed under a Creative Commons Attribution 4.0 International License (CC BY 4.0, http://creativecommons.org/licenses/by/4.0/).

The format of the articles was adapted to the style of this thesis. No content was changed.

VIII.1. Functional implications of multiple IM30 oligomeric states

Carmen Siebenaller[#], Benedikt Junglas[#] and Dirk Schneider*

Department of Pharmacy and Biochemistry, Johannes Gutenberg University Mainz, Mainz, Germany

***Correspondence:** Dirk Schneider Dirk.Schneider@uni-mainz.de

# These authors have contributed equally to this work

Received: 21 August 2019, **Accepted**: 29 October 2019, **Published**: 21 November 2019

Edited by: Luning Liu, University of Liverpool, United Kingdom

Reviewed by: Radek Kana, Institute of Microbiology, Czechia Wataru Sakamoto, Okayama University, Japan

Keywords: IM30, Vipp1, PspA, thylakoid membrane, membrane fusion, membrane stabilization, membrane dynamics, heat shock proteins

ABSTRACT

The inner membrane-associated protein of 30 kDa (IM30), also known as the vesicle-inducing protein in plastids 1 (Vipp1), is essential for photo-autotrophic growth of cyanobacteria, algae and higher plants. While its exact function still remains largely elusive, it is commonly accepted that IM30 is crucially involved in thylakoid membrane biogenesis, stabilization and/or maintenance. A characteristic feature of IM30 is its intrinsic propensity to form large homo-oligomeric protein complexes. 15 years ago, it has been reported that these supercomplexes have a ring-shaped structure. However, the in vivo significance of these ring structures is not finally resolved yet and the formation of more complex assemblies has been reported. We here present and discuss research on IM30 conducted within the past 25 years with a special emphasis on the question of why we potentially need IM30 supercomplexes in vivo.

IM30 IS INVOLVED IN TM PROTECTION AND REMODELING

The thylakoid membranes (TMs) of chloroplasts and cyanobacteria harbor the complexes of the photosynthetic electron transfer chain. The emergence of TMs in cyanobacteria is evolutionary coupled to the development of the inner membrane-associated protein of 30 kDa (IM30)/vesicle-inducing protein in plastids 1 (Vipp1)-protein (Vothknecht et al., 2012), and while Vipp1/IM30 is clearly linked to the biogenesis/maintenance of TMs, its exact physiological function still is unclear. As this protein appears to be essential for proper development of a functional TM system and therefore the whole photosynthetic apparatus, clarifying the involvement of Vipp1/IM30 in TM biogenesis/maintenance is vital to understand and eventually reconstruct the photosynthetic machinery, which is the major energy source for life on earth.

The inner membrane-associated protein of 30 kDa (IM30) was first described in 1994 as a protein with a dual localization at the inner envelope (IE) and at TMs in *Pisum sativum* chloroplasts (Li et al., 1994). In 2001, homologs of this protein have been identified and characterized in *Arabidopsis thaliana* and the cyanobacterium *Synechocystis* sp. PCC 6803 (from now on: *Synechocystis*) (Kroll et al., 2001; Westphal et al., 2001). Due to an apparent deficiency in vesicle formation at low temperatures of *Arabidopsis* Vipp1 depletion mutants, IM30 was renamed to *vesicle inducing proteins in plastids* 1 (Vipp1) (Kroll et al., 2001). In recent years, IM30/Vipp1 has been found to be essential for TM formation and IM30/Vipp1 was suggested to be involved in many processes linked to TM maintenance and/or biogenesis (summarized in Heidrich et al., 2017). As the proposed involvement in vesicle formation was not supported by any additional data, we here name the protein as originally proposed, *i.e.* IM30.

IM30 proteins are conserved amongst almost all photosynthetic organisms (Westphal et al., 2001; Vothknecht et al., 2012), and phylogenetic analyses have revealed that IM30 proteins potentially evolved *via* gene duplication from the bacterial phage shock protein A (PspA) during evolution (Westphal et al., 2001). Although sequence identity (~30%) and similarity (~50%) are not too high between PspA and IM30 proteins (Bultema et al., 2010), both proteins appear to share a highly conserved (predicted) secondary structure with an N-terminal core structure of about 220 amino acids consisting of six α-helices (the so-called PspA-like domain, Figure 1A). A major structural difference between PspA and IM30 is an extra C-terminal α-helix in IM30 proteins that is connected to the PspA domain *via* an extended linker region (Westphal et al., 2001; Otters et al., 2013). This extra domain of 20–30 aa possibly discriminated PspA from IM30 proteins and potentially causes the specialized functions of IM30 during TM biogenesis/maintenance, which cannot be accomplished by PspA (Westphal et al., 2001; Aseeva et al., 2004; Bultema et al., 2010; Vothknecht et al., 2012). In contrast, IM30 can functionally replace PspA in *E. coli pspA* null mutants (DeLisa et al., 2004; Zhang et al., 2012), suggesting a conserved function of the PspA domain and a more specific function of the C-terminal IM30 domain in TM biogenesis/maintenance gained during evolution. Nevertheless, due to their similarities, PspA and IM30 together form the PspA/IM30 protein family, together with LiaH, a phage shock protein homolog (Wolf et al., 2010).

An outstanding feature of all members of the PspA/IM30 protein family is their ability to organize into large ring-shaped homo-oligomeric (super)complexes (as further discussed below), which have first been described 15 years ago for both, PspA and IM30 (Aseeva et al., 2004; Hankamer et al., 2004) and were later on also identified for LiaH (Wolf et al., 2010). Interestingly, the occurrence of these IM30 supercomplexes appears to depend on the presence of chaperones/chaperonins, which

are likely involved in assembly and disassembly of the IM30 supercomplexes (at least *ex vivo*) (Liu et al., 2005; Liu et al., 2007; Gao et al., 2015).

The exact physiological function of IM30 monomers and/or oligomers is still not finally resolved yet. In recent years, potential *in vivo* functions of IM30 have mainly been studied using IM30 depleted or deleted cyanobacteria, algae, or plants. In fact, most studies were performed in the cyanobacterium *Synechocystis* sp. PCC 6803, the green alga *Chlamydomonas reinhardtii* or the higher plant *Arabidopsis thaliana* (Table 1).

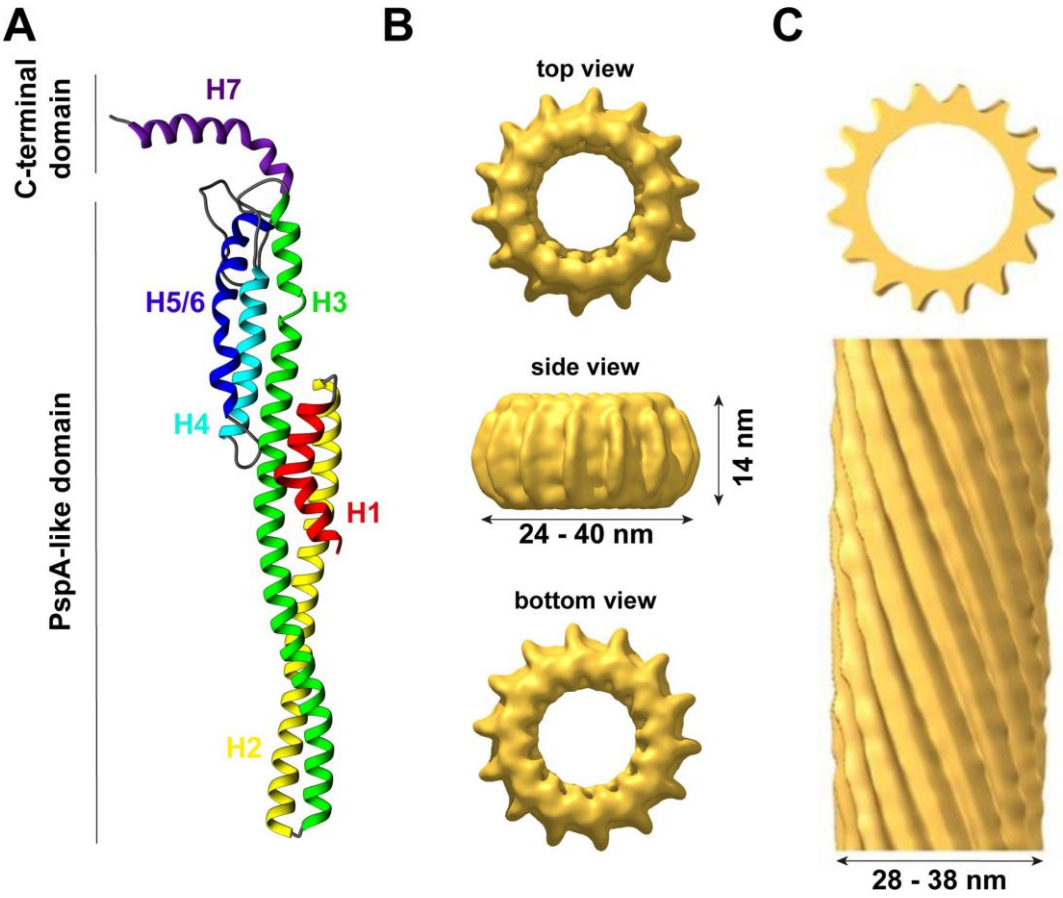

FIGURE 1 The structure of IM30.

(A) IM30 is a predominantly α-helical protein with seven helices. Helix 1–6 form the PspA-like domain. IM30 can be discriminated from PspA by a C-terminal extension, which includes an additional helix. **(B)** IM30 forms ring-like homo-oligomers with diameters ranging from 24 to 40 nm and a height of 14 nm (EMDB:3740). **(C)** IM30 forms rod-like structures with typical diameters of 28–38 nm [adapted from (Theis et al., 2019); open-access license http:// creativecommons.org/licenses/by/4.0/].

TABLE 1: The IM30 supercomplex structures in different species.

Organism	Ultrastructure *in vitro*	Diameter	Ultrastructure *in vivo*	Size
Synechocystis sp. PCC 6803	Mostly rings, (rods) [1,2]	25–33 nm [2]	At membranes: dynamic and static punctae [8,9] In the cytoplasm: diffuse particles [8,9]	100–300 GFP molecules estimated: 100 ± 25 nm [8]
Arabidopsis thaliana	Mostly rings, (rods) [3,4]	40 nm [3]	At membranes: static clusters [4,10] In the stroma: mobile IM30 particles [4,10]	<0.2–1.5 µm [4]
Chlamydomonas reinhardtii	Mostly rods, rings [5,6]	28–37 nm [5]	*n.a.*	*n.a.*
Triticum urartu	Mostly rings, (rods) [7]	~30 nm [7]	*n.a.*	*n.a.*

[1] (Fuhrmann et al., 2009a), [2] (Saur et al., 2017), [3] (Aseeva et al., 2004), [4] (Zhang et al., 2016), [5] (Liu et al., 2007), [6] (Theis et al., 2019), [7] (Gao et al., 2017) [8] (Bryan et al., 2014), [9] (Gutu et al., 2018), [10] (Zhang et al., 2012). n.a. = data not available.

Yet, results obtained after protein depletion were not entirely conclusive. While depleting IM30 in the cyanobacteria *Synechococcus* sp. PCC 7002 or *Synechocystis* sp. PCC 6803 (Westphal et al., 2001; Fuhrmann et al., 2009b; Zhang et al., 2014) as well as in *Arabidopsis* chloroplasts (Aseeva et al., 2007; Vothknecht et al., 2012) resulted in reduced TM networks and a disturbed TM morphology, depleting the protein in *Chlamydomonas* did not affect the TM structure (Nordhues et al., 2012). However, *Chlamydomonas* contains two IM30 paralogs (named Vipp1 and Vipp2), and in Nordhues *et al*. solely expression of one paralog was reduced. Yet, depletion of this paralog resulted already in an altered photosynthetic activity in *Chlamydomonas,* as has also been observed in cyanobacteria, but not in *Arabidopsis*, with photosystem II being affected in *Chlamydomonas* and photosystem I in cyanobacteria (Aseeva et al., 2007; Fuhrmann et al., 2009a; Nordhues et al., 2012; Vothknecht et al., 2012). Noteworthy, in contrast to most other studies, Gao *et al.* describe that depletion of IM30 in *Synechocystis* did lead to a generally reduced photosynthetic activity but not to TM reduction (Gao and Xu, 2009). While these results could indicate different roles of IM30 in different species, even results obtained in the same strain are not conclusive (Gao and Xu, 2009; Fuhrmann et al., 2009b). We believe that the major activity of IM30 remained conserved throughout evolution and that differences were observed due to other species-specific features, e.g., in some photosynthetic organisms certain lipids are essential whereas these can be replaced by other lipids in other species. This has e.g. been well studied in case of sulfoquinovosyldiacylglycerol (SQDG), which can be

replaced by phosphatidylglycerol (PG) to some extent in *Synechococcus*, but not in *Synechocystis* or *Arabidopsis* (Aoki et al., 2004; Kobayashi et al., 2015). As IM30 likely interacts with defined lipids and as lipids are crucial building blocks of TMs as well as part of photosystems, the observed differences could be explained by this. Yet, also other species-specific factors are described to be exclusively involved in TM and/or photosystem biogenesis in chloroplasts or cyanobacteria (Anbudurai et al., 1994; Guskov et al., 2009; Umena et al., 2011; Heinz et al., 2016). Yet, within the last 25 years, besides many others (Kroll et al., 2001; Benning et al., 2006; Göhre et al., 2006; Fuhrmann et al., 2009b; Nordhues et al., 2012; Rütgers and Schroda, 2013; Zhang et al., 2014; Walter et al., 2015) (reviewed in more detail in (Heidrich et al., 2017)), two major physiological functions of IM30 have been suggested, which we briefly introduce here:

(i) Membrane protection:

PspA, the major effector of the bacterial phage shock system, is known to have a membrane stabilizing/protecting function, and binding of PspA to membrane surfaces helps to maintain the proton motive force (PMF) (Kleerebezem et al., 1996; Kobayashi et al., 2007; Joly et al., 2010). Due to the high similarity of PspA and IM30, it appears reasonable to speculate that IM30 also has a membrane-stabilizing/-protecting function (Vothknecht et al., 2012; Zhang et al., 2012; Zhang and Sakamoto, 2013; Zhang and Sakamoto, 2015). Indeed, both, PspA and IM30, bind to negatively charged lipid membranes in a curvature dependent manner *in vitro* (Kobayashi et al., 2007; Hennig et al., 2015; McDonald et al., 2015; Heidrich et al., 2016) and IM30 potentially increases the lipid order upon membrane binding (Hennig et al., 2015; Heidrich et al., 2016). While this suggests that the protein preferentially binds to ordered membrane regions (*i.e.* gel-phase membranes), further experimental proof is missing. Besides these *in vitro* observations, it has been observed that heterologous expression of IM30 from *Synechocystis* and *Arabidopsis* can complement deficiencies in a bacterial Δ*pspA* mutant (DeLisa et al., 2004; Zhang et al., 2012) and that IM30 overexpression can increase the heat stress tolerance in *Arabidopsis* (Zhang et al., 2016). As small IM30 oligomers bind with higher affinity to negatively charged membranes than the large oligomeric ring structures (Heidrich et al., 2016), it has been hypothesized that IM30 and PspA rings disassemble on membranes and function as membrane chaperones by forming a membrane protective structure upon membrane binding (Thurotte et al., 2017; Junglas and Schneider, 2018).

(ii) Membrane remodeling:

While IM30 appears to share its membrane-stabilizing/-protecting activity with PspA, IM30 clearly must have acquired additional functions in cyanobacteria and chloroplasts, as PspA is not able to replace IM30 (Westphal et al., 2001; Aseeva et al., 2004; Bultema et al., 2010; Vothknecht et al.,

2012). Expression of IM30 appears to be of special importance when cyanobacterial cells are shifted from dark to light growth conditions (Gutu et al., 2018), where photosynthetic organisms need to adapt their photosynthetic apparatus to account for the changing light intensities by dynamic rearrangement of the TM system (Chuartzman et al., 2008; Nagy et al., 2011; Liberton et al., 2013). Such TM rearrangements require extensive membrane remodeling, and a likely candidate catalyzing TM remodeling is IM30. IM30 can induce fusion of liposomal membranes, at least *in vitro* (Hennig et al., 2015; Thurotte and Schneider, 2019), a process that appears to be controlled by the cytosolic Mg^{2+} concentration, as Mg^{2+} directly binds to IM30 and thereby triggers the fusion process (Hennig et al., 2015; Heidrich et al., 2018; Thurotte and Schneider, 2019). This is of special importance in TM-containing organisms, as the cytosolic Mg^{2+} concentration varies in the dark *vs.* light and depends on the photosynthetic activity (Pohland and Schneider, 2019). Thus, the IM30-specific membrane remodeling activity appears to be (indirectly) controlled by light. Besides light, GTP binding and hydrolysis were recently suggested to control the IM30 membrane remodeling function (Ohnishi et al., 2018), although IM30 does not contain a canonical G-domain and GTP is not required *per se* for membrane binding and liposome fusion (Hennig et al., 2015). Noteworthy, the suggested membrane-stabilizing and the membrane-remodeling activity of IM30 on the first view contradict each other, at least in part, as membrane fusion processes typically involve membrane destabilization. However, both functions might be relevant *in vivo,* as Mg^{2+}- release or binding to IM30 could control the respective activities (Junglas and Schneider, 2018).

IM30 STRUCTURE: WHAT DO WE (NOT) KNOW SO FAR?

The Monomer Structure

Thus far, the structure of the IM30 monomer is still elusive. The monomer is supposed to have a highly α-helical structure (~80% α-helix) with six helices separated by short linker regions (Fuhrmann et al., 2009a; Gao et al., 2015). Additionally, helix 7 is separated from the PspA(-like) domain by an extended flexible linker (Otters et al., 2013). All these assumptions are based on secondary structure predictions but are supported by CD-spectroscopy and FTIR measurements (Fuhrmann et al., 2009a; Gao et al., 2015; Heidrich et al., 2018). Recently, a model of the IM30 monomer has been reported (see Figure 1A) that is based on the X-ray structure of a PspA fragment (amino acids 1–144) (Osadnik et al., 2015) and homology modeling (Saur et al., 2017). The X-ray structure of the PspA fragment revealed that helix 2 and 3 form an extended hairpin coiled-coil structure (Osadnik et al., 2015), which appears to form the structural core of the PspA domain. Suggested structural and functional roles of each helix were discussed in more detail recently (Heidrich et al., 2017). Studying truncated IM30 variants allowed to deduce the involvement of

individual helices in protein oligomerization (Otters et al., 2013; Gao et al., 2015; Thurotte and Schneider, 2019). Based on these analyses, helix 2 and 3 form the structural core of IM30 that is crucial for supercomplex formation, but by itself does exclusively form monomers (Thurotte and Schneider, 2019).

Adding helix 1 and 4 to the structural core enables the formation of dimers (Thurotte and Schneider, 2019) or intermediate-sized oligomers (800 kDa) (Gao et al., 2015), but not of ring-shaped supercomplexes. At minimum, helices 2–6 are required for the formation of stable ring/supercomplex structures (Thurotte and Schneider, 2019). Hence, the helix 2/3 coiled-coil apparently interacts with helix 4 and/or 5/6 in the supercomplexes.

Small Oligomers

In solution, isolated IM30 has a strong tendency to spontaneously form homo-oligomeric supercomplexes, as further discussed below. Yet, a minor fraction of the protein still forms small oligomers (mostly tetramers and dimers), and also the basic building block of the ring complex appears to be an IM30 tetramer (Liu et al., 2007; Fuhrmann et al., 2009a; Saur et al., 2017). Although some low-resolution data of the structure of the supercomplexes are available, essentially nothing is known about the structure of the small oligomers. Thus far, solely a hypothetical model describing the organization of the monomers in the ring structure, including the tetrameric building block, was suggested (Saur et al., 2017) (Figure 1A).

IM30 Supercomplexes

In 2004, PspA (Hankamer et al., 2004) and IM30 (Aseeva et al., 2004) were reported to form homo-oligomeric supercomplexes with ring-like structures and molecular masses exeeding 1 MDa. In the following 15 years, one main aspect of the research on IM30 was to analyze the structure and implications of these large supercomplexes.

In various experiments, involving size exclusion chromatography (SEC), BN-PAGE, and sucrose gradient centrifugation, members of the PspA/IM30 family were found to mainly organize into high molecular mass complexes in solution, besides a small fraction of dimers/tetramers (Aseeva et al., 2004; Liu et al., 2005; Liu et al., 2007; Fuhrmann et al., 2009a; Gao et al., 2015; Heidrich et al., 2016; Saur et al., 2017). This has been observed for IM30 in cellular extracts of cyanobacteria and chloroplasts of green algae or vascular plants, but also for heterologously expressed and purified proteins (Aseeva et al., 2004; Liu et al., 2005; Liu et al., 2007; Fuhrmann et al., 2009a; Gao et al., 2015; Heidrich et al., 2016; Gao et al., 2017; Saur et al., 2017). As no other proteins appear to be

necessary for IM30 oligomerization, the complexes identified in cellular extracts likely represent homo-oligomeric assemblies.

The size of the *EcoPspA* complex was determined via SEC to be ~1 MDa, indicating that the complex contains 36–37 subunits (Hankamer et al., 2004). For isolated IM30, the molecular mass was determined to be >1 MDa for *Arabidopsis* IM30 (*Ara*IM30) (Aseeva et al., 2004; Otters et al., 2013), for *Chlamydomonas* IM30 (*Cr*IM30) (Liu et al., 2007; Gao et al., 2015) as well as for two IM30 paralogs encoded in Tricum urartu (Gao et al., 2017). The size of *Synechocystis* IM30 (*Syn*IM30) was estimated via SEC to be about 1600–2000 kDa (or even higher) (Fuhrmann et al., 2009a). For the homologous LiaH protein of *B. subtillis*, a molecular mass of at least 1.25 MDa was determined via SEC (Wolf et al., 2010). As these high molecular mass supercomplexes elute in the void volume or close to the void volume in most SEC experiments and as a compact globular shape is assumed in SEC analyzes, which deviates from the partially hollow ring structure of IM30/PspA rings, the determined masses have to be taken with caution. In fact, from a recent 3D-reconstruction of IM30-rings, a molecular mass of about 1.5–2.5 MDa could be roughly estimated by using the volume/shape of the complex (Saur et al., 2017). However, the low resolution of this 3D-reconstruction makes it difficult to set the correct contour level for an exact determination of the volume and thus the exact mass.

Ring-shaped supercomplexes have been observed multiple times via negative stain electron microscopy for purified PspA (Hankamer et al., 2004), LiaH (Wolf et al., 2010) and IM30 from different organisms, involving *Arabidopsis*, *Chlamydomonas* and *Synechocystis* (Aseeva et al., 2004; Liu et al., 2007; Fuhrmann et al., 2009a; Gao et al., 2015). Thus far, the prevailing thesis is that PspA rings solely occur with 9-fold rotational symmetry (from *E. coli*), indicating a 4x9 (= 36 monomers) structure, which is in agreement with the molecular mass estimated via SEC. These *Eco*PspA rings have a diameter of about 20 nm and a height of 8–11 nm (Hankamer et al., 2004). However, *Eco*PspA rings with different diameters have also been observed, although they have not been further characterized (Male et al., 2014). The symmetry and number of monomers of the LiaH rings were identical with the PspA rings described by Hankamer et al. (2004); yet a ring diameter of 25 nm has been determined (Wolf et al., 2010).

In contrast to the supposedly homogeneous PspA and LiaH supercomplex structures, the IM30 ring dimensions are clearly highly variable. The first electron micrographs of heterologously expressed *Ara*IM30 revealed ring-shaped particles with a diameter of about 40 nm and a height of about 14 nm (Figure 1B) (Aseeva et al., 2004). Subsequent more detailed analysis of *Cr*IM30 and *Syn*IM30 revealed a heterogeneous size distribution with rings having diameters of at least 28–37 nm

(*Cr*IM30) (Liu et al., 2007) and 25–33 nm (*Syn*IM30), respectively, resulting in a calculated number of monomers per ring ranging from 48–72 (Fuhrmann et al., 2009a; Saur et al., 2017). While the ring diameter clearly is variable, a constant height of 13–15 nm was observed for all *Syn*IM30 ring structures (Saur et al., 2017). Most electron micrographs of IM30 exhibit a pronounced spike architecture, giving rise to a very well defined rotational symmetry (at least 7 up to 22fold) (Saur et al., 2017). Interestingly, the 3D-reconstructions of the *Syn*IM30 rings suggest that the rings are polar and have two distinct sides (ring top and bottom side) (Figure 1B), with the monomers likely being ordered unidirectional in the ring structure (Saur et al., 2017), possibly enabling the rings to interact with two different interaction partners. This perfectly supports the idea of IM30 rings beeing able to bind/fuse two different membrane surfaces, e.g. different TM sheets or the cyanobacterial cytoplasmic membrane (CM) with the TM (Saur et al., 2017).

Rod-Like Structures

Besides isolated rings, in electron micrographs of purified IM30 and PspA also double rings and elongated rod-like structures were identified (Figure 1C), the latter appear to form via stacking of multiple IM30/PspA rings (Liu et al., 2007; Fuhrmann et al., 2009a; Male et al., 2014; Gao et al., 2015; Saur et al., 2017; Thurotte and Schneider, 2019).

While the formation of rod-like structures is a common feature of IM30/PspA family members, the preference for rings vs. rod-like structures appears to depend on the species (see table 1). *Syn*IM30, the most intensely studied member of the IM30/PspA family in terms of protein structure, does only occasionally form rod-like structures (Fuhrmann et al., 2009a; Saur et al., 2017). Yet, formation of double ring structures is induced by Mg^{2+}-binding to IM30, which alters the surface properties of individual IM30 rings (Heidrich et al., 2018). Additionally, increased formation of rod-like structures has been observed upon removal of the C-terminal helix 7 from *Syn*IM30 (Hennig et al., 2017). This observation suggests that PspA (and/or the PspA core of IM30 proteins) might be more prone to the formation of rod-like structures as they do not contain the (IM30-specific) C-terminal extension. PspA rings were initially observed and analyzed in the presence of chaotropic salts (Hankamer et al., 2004), which might hinder rod formation or disassemble PspA rods. In fact, extensive formation of rod-like structures has recently been reported for *Eco*PspA (Male et al., 2014). Furthermore, truncation of the *Syn*IM30 helix 1 also resulted in an increased formation of rod-like structures (Thurotte and Schneider, 2019), suggesting that helix 1 and helix 7 negatively control rod-formation in *Syn*IM30. Indeed, the removal of helix 1 and helix 7 in combination resulted in the exclusive formation of rod-like structures in the case of *Syn*IM30 (Thurotte and Schneider, 2019). This might

be due to the removal of steric barriers inhibiting rod-formation of the wt protein. Interestingly, helix 7 is known to protrude out of the ring core structure (Otters et al., 2013; Heidrich et al., 2018) and thereby may hinder ring-ring contacts at one side of the ring. However, both helix 1 and 7 seem to have an intrinsic propensity to be unstructured (Osadnik et al., 2015; Zhang et al., 2016; Hennig et al., 2017; McDonald et al., 2017). Thus, they occupy a large conformational space, which might explain why they can create a steric hindrance for ring/supercomplex formation.

Notably, while *Ara*IM30, as well as the two IM30 paralogs of *Triticum urartu*, also appear to have a rather weak tendency to form rod-like structures (to the best of our knowledge, as the experimental evidence on these structures is limited (Otters et al., 2013; Zhang et al., 2016; Gao et al., 2017)), *Cr*IM30 has a pronounced tendency to form rods (Liu et al., 2005; Liu et al., 2007; Theis et al., 2019) (table 1).

Also, deletion of helix 1 has different effects on the ultrastructure of IM30 from different species: While deletion of helix 1 in *Syn*IM30 clearly induced rod formation, deleting helix 1 from *Eco*PspA (Jovanovic et al., 2014) as well as from *Ara*IM30 (Otters et al., 2013; Ohnishi et al., 2018) did even abolish formation of large oligomers (including rings and rods), and thus here helix 1 appears to be essential for the formation of large oligomers as well as rings or rods. In contrast, removal of helix 1 from *Cr*IM30 did not abolish formation of large oligomers, albeit the oligomers appear not to have the prototypical ring structures anymore (Gao et al., 2015). Thus, the exact role of helix 1 for supercomplex formation appears to be species-dependent and has to be analyzed in more detail. Nevertheless, helix 1 and 7 are crucially involved in (de)stabilization of IM30 supercomplexes.

However, while also the physiological relevance of the rod-like structures is not at all clear yet, it has been hypothesized that they might be part of cytoskeleton-like elements with microtubule-like structures (Liu et al., 2007; Rütgers and Schroda, 2013). Recently, it has been shown that *Cr*IM30 rods can engulf phosphatidylinositol phosphate-containing membranes (Theis et al., 2019), and thus, the rod-like structures could well be part of the membrane remodeling machinery of IM30.

THE STRUCTURE OF IM30 CHANGES DYNAMICALLY *IN VIVO*

The *in vivo* structure of IM30 is still enigmatic. It has been shown via fluorescence microscopy that GFP-tagged IM30 forms large clusters close to the TMs in chloroplasts and cyanobacterial cells, seen as punctae (Bryan et al., 2014). These punctae are called “functional Vipp1 particles” (FVPs) in chloroplasts (Zhang et al., 2016) (see Table 1). Additionally, GFP-tagged IM30 has also been identified at the CM and in the cytoplasm of *Synechocystis* (Bryan et al., 2014). Importantly, the localization of IM30 in *Synechocystis* changes when cells are transferred from low-light (LL, 8 µE m-2 s-1 intensity)

to high-light (HL, (600 µE m-2 s-1 intensity) conditions. At LL, the majority of IM30 clusters were found at the cyanobacterial CM, whereas under HL conditions the total number of IM30 puncta strongly increased and the IM30 puncta preferentially form at the TM (Bryan et al., 2014). This dynamic relocalization of IM30 in *Synechocystis* has been investigated more extensively by Gutu et al. At standard light conditions (100 µE m-2 s-1 intensity), *Syn*IM30 was identified in two fractions: (i) a diffuse uniformly distributed fraction and (ii) short-lived puncta closely associated with highly curved TM regions. Yet, at HL conditions, IM30 puncta stably form at and associate with TMs (Gutu et al., 2018), and potential implications of this relocalization were discussed in more detail recently (Junglas and Schneider, 2018). A similar mobility of FVPs has also been observed in chloroplasts when protoplasts from *Arabidopsis* were treated with hypotonic stress (Zhang et al., 2016). As all members of the IM30/PspA family appear to be localized in discrete punctae associated with (probably stressed) cellular membranes (Engl et al., 2009; Yamaguchi et al., 2013; Domínguez-Escobar et al., 2014) the transient formation of clusters at defined membrane regions might be linked to the primordial PspA-function, *i.e.* membrane protection/maintenance.

However, the question arises, how IM30 is structured in these clusters? Unfortunately, the resolution of conventional fluorescence microscopy is limited to roughly 200 nm. Thus, single IM30 rings with typical diameters of 30 to 40 nm will be hardly detectable. Nevertheless, it has been suggested that the so-called FVPs in chloroplasts represent IM30 rings or clusters of IM30 rings (Zhang et al., 2016). In fact, the observed clusters have estimated maximal diameters of <0.2–1.5 µm (Zhang et al., 2016) and are thus too large for single IM30 rings and may consist of assemblies of multiple IM30 rings (Table 1). Notably, the IM30 puncta observed in *Synechocystis* are much smaller than the FVPs (100 ± 25 nm) and contain about 100–300 IM30 molecules (Bryan et al., 2014) (Table 1). Thus, they would consist of at least two to five rings, assuming an average monomer content of the rings of about 60. Taking into account the roughly estimated shape of these puncta, it is rather unlikely that they are formed by rod-like structures, but by multiple IM30 rings sitting next to each other (Junglas and Schneider, 2018). However, it is hard to imagine how membrane attached IM30 rings can stabilize lipid bilayers. Yet, as small IM30 oligomers and/or monomers have a higher membrane binding affinity than rings (Heidrich et al., 2016), it is reasonable to assume that IM30 rings disassemble upon membrane binding. Monomers or small oligomers may then form a protein network on membrane surfaces, similar to the clathrin-like structure that has been described for *Eco*PspA (Standar et al., 2008; Thurotte et al., 2017; Junglas and Schneider, 2018). The assumption that IM30 does not remain ring-structured upon membrane binding is further supported by the recent notion that IM30 rings were not found by template matching in tomograms of *Synechocystis* cells at or close to the highly curved TM ends (Rast et al., 2019), *i.e.* at the regions where the clusters have been

identified via fluorescence microscopy. Furthermore, while not being genuine proof, up to the present day IM30 rings have, to the best of our knowledge, never been observed in any study of isolated TMs via electron microscopy or atomic force microscopy, despite the large ring dimensions (Olive et al., 1981; Kirchhoff et al., 2004; Kirchhoff et al., 2008b; Engel et al., 2015; Kowalewska et al., 2016; Casella et al., 2017; MacGregor-Chatwin et al., 2019; Wietrzynski et al., 2019). Hence, we conclude that the observed clusters most likely are not formed from IM30 rings sitting on membrane surfaces. However, the diffuse particles observed by Gutu et al. potentially represent single IM30 rings in solution (Gutu et al., 2018). Unfortunately, for the diffuse particles, no dimensions were given, possibly because the diffuse particles were too small and too mobile.

DYNAMIC (DIS)ASSEMBLY OF IM30 IS MEDIATED BY CHAPERONES

As observed in the before mentioned *in vivo* studies, the oligomeric state of IM30 appears to be highly dynamic. This dynamic behavior likely involves the activity of chaperones, which have been identified to interact with IM30 proteins (Figure 2). In *Chlamydomonas rheinhardtii*, IM30 was shown to associate with HSP70 chaperones and the co-chaperones CDJ2 and CGE1 in ATP-depleted cell extracts (Liu et al., 2005; Liu et al., 2007). These interactions were thereafter confirmed in solubilized membrane fractions (Heide et al., 2009). Additionally, HSP90 was identified as a supplementary interaction partner of the IM30/HSP70 complex in *Chlamydomonas* (Heide et al., 2009) and in *Arabidopsis* chloroplasts (Feng et al., 2014). In *Synechocystis*, the two HSP70 chaperones DnaK2 and DnaK3 (Rupprecht et al., 2007; Rupprecht et al., 2008; Rupprecht et al., 2010), as well as the HSP60 chaperonin GroL1, were shown to interact with IM30 (Bryan et al., 2014).

Interaction of IM30 with different chaperones significantly impacts the oligomeric state of IM30 (Figure 2). Although IM30 was found in the IM30/CDJ2 complex in a high- and low-molecular-weight fraction (> > 670 kDa and <230 kDa) in ATP-depleted *Chlamydomonas* cell extracts, it was only part of an intermediate-size molecular-weight fraction (about 670 kDa) in ATP-supplemented cell extracts (Liu et al., 2007), clearly suggesting an ATP-dependent assembly and/ or disassembly, as expected when ATP-dependent chaperones are involved. Further analyses showed that also heterologously expressed IM30 can be assembled and disassembled by the HSP70-chaperone machinery in an ATP-dependent manner (Liu et al., 2007). Interestingly, the rod-like structures formed by *Cr*IM30 were also disassembled into IM30 rings and possibly smaller oligomers by the HSP70/CDJ2/CGE1 system when ATP was present (Liu et al., 2007). The bacterial HSP70 *Eco*DnaK was able to replace the *Cr*HSP70 protein in presence of CDJ2 and CGE1 (Liu et al., 2007). Interaction of the *Eco*DnaK protein with the *Cr*IM30 full-length protein was observed directly upon induction of heterologous expression of *Cr*IM30 in *E. coli* cells, suggesting that HSP70s generally recognize and

stabilize IM30 monomers and assist in the formation of IM30 oligomers and supercomplexes. Likely, HSP70s shield IM30 domains to prevent unspecific aggregation. In fact, *Eco*DnaK binds with high affinity to truncated versions of the *Cr*IM30 proteins that form smaller oligomers but no ring structure anymore (Gao et al., 2015). In intact *Synechocystis* cells, GFP-labeled DnaK2, DnaK3, and IM30 were observed via fluorescence microscopy to colocalize in specific TM regions under HL-conditions, but not under LL-conditions (Bryan et al., 2014). Thus, under (HL) stress conditions, IM30 is potentially recruited to DnaK2 and/or DnaK3-enriched regions close to the membrane that activate IM30 via catalyzing assembly/disassembly (Bryan et al., 2014). Such relocalization of proteins under stress conditions has also been observed for PspA of *Yersinia enterocolitica* which can be found in the cytoplasm and at the CM under normal conditions, whereas it forms large static complexes at the CM under stress conditions (Yamaguchi et al., 2013).

In an *Arabidopsis* mutant lacking *Ara*HSP90.5, the ratio of monomeric IM30 to higher molecular weight-oligomers of IM30 (>1000 kDa) was shifted to the oligomeric form, indicating that HSP90.5 is also involved in disassembly of IM30 supercomplexes, possibly together with HSP70 (Feng et al., 2014).

Taken together, IM30 clearly has an intrinsic propensity to spontaneously form large oligomeric structures. HSP70 and HSP90 chaperones have been shown to catalyze disassembly, but also the assembly of IM30 oligomers (Figure 2), at least *ex vivo* and *in vitro*. The chaperones may be required for removal of membrane-bound small IM30 oligomers (Figure 2), as has been described for the uncoating of clathrin complexes by auxilin and HSP70 (Ungewickell et al., 1995). Membrane-associated chaperones are potential candidates for this process. After removal from the membrane, small oligomers may then assemble into oligomers in the cytosol, to finally form the typical ring-shaped IM30 structures and complete the recycling process (Figure 2). Yet, it remains to be shown which physiological conditions trigger the interaction of IM30 with the chaperones.

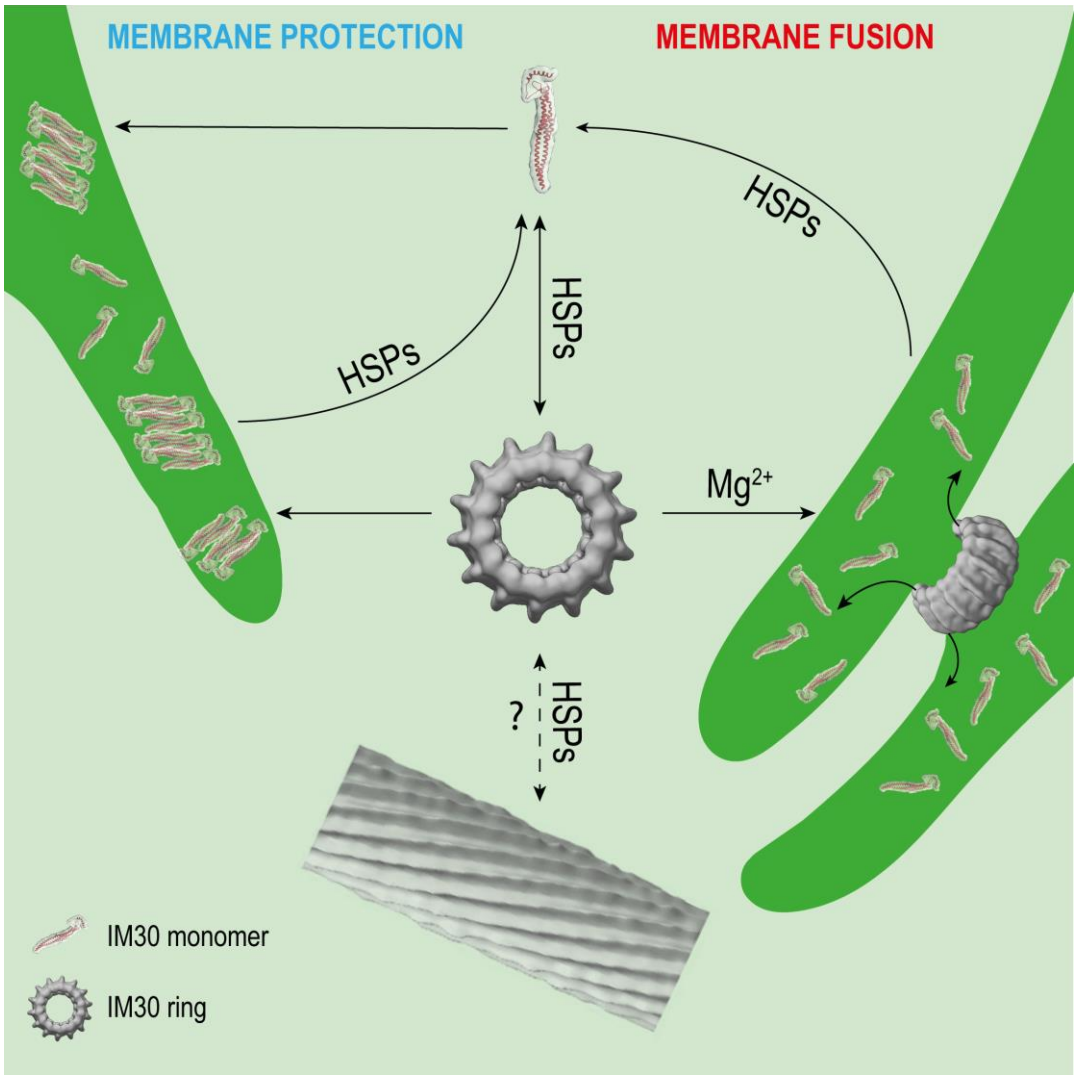

FIGURE 2 Potential interactions of IM30 with membrane and HSPs.

Potential interactions of IM30 with membrane and HSPs. IM30 interacts with the TM as a ring and/or monomer. The monomers possibly rearrange on the TM to form a membrane-protecting structure. In presence of high amounts of Mg2+, the IM30 ring is able to fuse adjacent membranes, which might involve dissociation of the ring into membrane-bound small oligomers/monomers. HSPs may detach the monomers from the membrane and trigger homo-oligomerization and ring formation. The physiological relevance of IM30 rod-like structures is unclear so far. However, HSPs have been shown to disassemble IM30 rods in the presence of ATP in vitro. (Rod structure adapted from (Theis et al., 2019); open-access license http://creativecommons.org/licenses/by/4.0/).

WHY DO WE NEED A RING?

In several models, a need for the formation of IM30 rings and/ or rod-like structures to fulfill their physiological function(s) is implicated. However, the existence and relevance of IM30 supercomplexes *in vivo* still need to be shown, especially because IM30 rings have never been observed in an *in vivo* context so far. But, are IM30 rings really indispensable for the proposed IM30 functions?

The IM30 Ring Structure Enables Efficient Membrane Chaperoning

Formation of IM30/PspA rings is probably not necessary for the proteins´ membrane chaperoning function, as small oligomers bind with higher affinity to membrane surfaces (Heidrich et al., 2016). This observation has triggered the suggestion that IM30 rings disassemble into smaller oligomers (or monomers) upon/ during membrane binding. It has been hypothesized that PspA/ IM30 family proteins act as membrane chaperones by forming a stabilizing network on the membrane surface, as discussed above (Thurotte et al., 2017; Junglas and Schneider, 2018). Possibly, such structures have been imaged via GFP-tagged IM30 in living cells as large IM30 assemblies located at the TM (Zhang et al., 2012; Bryan et al., 2014; Zhang et al., 2016; Gutu et al., 2018; Junglas and Schneider, 2018). Also, the oligomeric PspA structures identified by Standar et al., described as a clathrin-like scaffold (Standar et al., 2008), potentially represent *E. coli* membrane patches coated with PspA.

So, what might the ring structure then be good for, especially in the case of PspA and LiaH proteins that are the main effector proteins of the *psp*/*lia* membrane-stress response system, where their major task is to maintain membranes? Homo-oligomeric protein complexes can provide a highly ordered structure and high stability due to the compactness and cooperativity of highly packed monomers. This might protect the monomeric protein against proteolysis and degradation under harsh conditions, which is especially beneficial for stress-response proteins. Indeed, IM30 rings (more precisely the ring core) are relatively protease-resistant and resistant against chemical and thermal denaturation compared to small oligomers (Gao et al., 2015; Heidrich et al., 2018; Thurotte and Schneider, 2019). Furthermore, the surface of a higher-ordered oligomer is relatively small compared to the monomer. This could be a mechanism to control the IM30 activity, as amphiphilic helices, which are prone to interact with membrane surfaces, are exposed solely when the complexes dissociate. Consequently, the IM30 ring could be a storage form of smaller, active IM30 oligomers/ monomers to prevent a continuous need for shielding the hydrophobic surfaces by chaperones. Additionally, preformation of a highly ordered homo-oligomeric supercomplex ensures a high avidity and an immediate high local concentration of the active small oligomers (or monomers) upon membrane binding, which is likely necessary for membrane attachment and rapid formation of protein networks on membrane surfaces involved in membrane repair and/or protection. The orientation of the monomers in the ring could support e.g. membrane binding if the interacting amino acid residues are positioned in a favorable orientation to the membrane.

The IM30 Ring Is Crucial for Membrane Fusion

Besides the involvement of the IM30 ring structure in membrane protection, the ring seems to be mandatory for the membrane fusion activity of IM30. A membrane fusion protein requires strict control of its activity, as any uncontrolled fusion event is potentially detrimental for the cell because it could e.g. result in a loss of electrical and/or chemical gradients. This is especially relevant for the TM, as any leak by misdirected fusion reduces the proton gradient and the photosynthetic efficiency. Therefore, control of the IM30 activity *via* oligomer formation might be a potential solution. Another regulation mechanism is the dependence of the fusion process on Mg^{2+}, which seems to activate IM30 rings (Heidrich et al., 2018).

The structural features of the IM30 ring structure seem to support the fusion mechanism directly. An oligomeric ring exposes two distinct sides of the monomers, which are orientated unidirectional, as suggested for IM30 (Saur et al., 2017). The opposing sides of the ring can consequently interact *e.g.* with two membranes, as it would be necessary for a membrane fusion activity. This would also be possible with a cylindrically shaped protein, but the hole inside the ring might be important for the formation of a fusion pore(-like structure). A recent model for the IM30-mediated membrane fusion suggests that fusion is initiated by the ring (Heidrich et al., 2017). As the protein binds negatively charged lipids (Hennig et al., 2015), IM30 might recruit such lipids when binding as a ring to a membrane surface. In the center of the ring, the concentration of the non-bilayer forming lipid MGDG becomes locally high, which might result in disruption of an ordered bilayer structure and initial fusion of two interacting membranes. Dissociation of the ring could then lead to lipid mixing, allowing the formation of a stable, now fused membrane (Heidrich et al., 2017). Moreover, a large protein complex would clearly facilitate the formation of a fusion pore at the TM. As the membrane is completely crowded with integral and peripheral membrane proteins (Kirchhoff et al., 2008a; Casella et al., 2017; MacGregor-Chatwin et al., 2019; Wietrzynski et al., 2019), it is hard to imagine that binding of a small protein could provide enough space needed for membrane-membrane contacts and subsequent membrane fusion. Instead, binding of a large ring complex that finally dissociates could generate a fusion platform on the membrane. We, therefore, suggest that the IM30 ring structure is mandatory for the membrane fusion function.

Taken together, the formation of IM30 rings might prevent uncontrolled membrane binding and simultaneously prealigns IM30 monomers for efficient membrane binding. Furthermore, IM30 rings are directly involved in membrane fusion, where Mg^{2+} binding is an additional activation step that renders the rings fusion competent.

WHERE AND WHEN TO FIND IM30 RINGS?

As discussed above, IM30 rings are indispensable for controlled membrane remodeling but are probably also generally useful to ensure proper activity of IM30, *i.e.* increase the local concentration of active small oligomers/monomers or shield them from unwanted interactions when not bound to the membrane. An intriguing question that arises from these assumptions is: When such rings are so important, why do we not see them *in vivo*? While IM30 clusters have been observed on TMs in cyanobacteria and chloroplasts (Zhang et al., 2012; Bryan et al., 2014; Zhang et al., 2016; Gutu et al., 2018), the supramolecular organization of IM30 within these structures is still enigmatic, and rings "sitting" on TMs have not been observed yet. The problem probably is not that IM30 rings are hard to find because of their size and shape. Other proteins of similar or even smaller size have been identified in cryo-TEM tomograms of *Synechocystis* recently (Rast et al., 2019). So the question probably is more: Where and when to find IM30 rings in living cells?

IM30 appears to be a protein with (at least) a dual function, *i.e.* a membrane remodeling and a membrane stabilizing/protecting function. These functions have to be separated spatiotemporally, as they would otherwise cancel out each other. Assuming that both functions have different requirements on the protein structure (as discussed above), IM30 rings are very short-living and can probably only be found on a membrane under certain specific conditions. However, both processes, membrane chaperoning and remodeling, potentially involve binding of IM30 rings to the membrane and ring dissociation, resulting in small membrane-bound oligomers or even monomers (Figure 2). Thus, chances to find IM30 rings on membrane surfaces are probably low. Only at the initial phase of a fusion event, *i.e.* when two adjacent membranes meet each other, rings may be found to connect these (Figure 2). This may only be observed at TM convergence zones under conditions where membrane remodeling is needed, e.g. when cells are shifted from the dark to light. Under HL/stress conditions, IM30 monomers and/or small oligomers will be found on the TM (Thurotte et al., 2017; Gutu et al., 2018; Junglas and Schneider, 2018) (Figure 2), so chances to find rings are also low. Yet, as discussed above, the oligomeric state of IM30 depends on the activity of molecular chaperones, which likely control assembly and disassembly of IM30 oligomers (Figure 2). Indeed, IM30 supercomplexes have been detected in cellular extracts of *Chlamydomonas rheinhardtii* chloroplasts when ATP was depleted (Liu et al., 2007). Thus, IM30 rings might only exist in detectable amounts under conditions of low ATP, e.g. as periodically observed at the (diurnal) dark to light transition in cyanobacteria and chloroplasts (Konno et al., 2012; Saha et al., 2016; Voon et al., 2018). During dark to light transition, where IM30 is necessary for unimpaired growth (Gutu et al., 2018), IM30 rings might be needed for TM remodeling. However, the oligomeric state of IM30 is probably also controlled by altered expression of chaperones, as observed e.g. for DnaK2 under HL, heat,

hyperosmotic and salt stress in *Synechococcus elongatus* PCC 7942 and *Synechocystis* sp. PCC 6803 (Sato et al., 2007; Rupprecht et al., 2008). Under normal growth conditions (no increased chaperone expression), IM30 rings could display an inactive cytosolic storage form. These possibly represent the diffuse particles observed by Gutu et al. (2018). Thus, the cellular ATP levels will likely have only minor effects on the oligomeric state of IM30 when chaperones are not induced.

In summary, we believe that IM30 rings can barely be found on membranes in living cells as they likely represent a short-lived IM30 structure. Assembly and disassembly of the supercomplexes likely are highly controlled and meet cellular demands.

AUTHOR CONTRIBUTIONS

All authors wrote the manuscript.

FUNDING

This work was funded by the Max-Planck graduate center at the Max Planck institutes and the University of Mainz.

ACKNOWLEDGMENTS

We thank Anne-Christin Pohland, Lucas Gewehr, and Hildegard Pearson for carefully reading the manuscript.

REFERENCES

Anbudurai, P. R., Mor, T. S., Ohad, I., Shestakov, S. V., and Pakrasi, H. B. (1994). The ctpA gene encodes the C-terminal processing protease for the D1 protein of the photosystem II reaction center complex. *Proc. Natl. Acad. Sci. U. S. A.* 91, 8082–8086. doi: 10.1073/pnas.91.17.8082

Aoki, M., Sato, N., Meguro, A., and Tsuzuki, M. (2004). Differing involvement of sulfoquinovosyl diacylglycerol in photosystem II in two species of unicellular cyanobacteria. *Eur. J. Biochem.* 271, 685–693. doi: 10.1111/j.1432-1033.2003.03970.x

Aseeva, E., Ossenbühl, F., Eichacker, L. A., Wanner, G., Soll, J., and Vothknecht, U. C. (2004). Complex formation of Vipp1 depends on its alpha-helical PspA-like domain. *J. Biol. Chem.* 279, 35535–35541. doi: 10.1074/jbc.M401750200

Aseeva, E., Ossenbühl, F., Sippel, C., Cho, W. K., Stein, B., and Eichacker, L. A. (2007). Vipp1 is required for basic thylakoid membrane formation but not for the assembly of thylakoid protein complexes. *Plant Physiol. Biochem.* 45, 119–128. doi: 10.1016/J.PLAPHY.2007.01.005

Benning, C., Xu, C., and Awai, K. (2006). Non-vesicular and vesicular lipid trafficking involving plastids. *Curr. Opin. Plant Biol.* 9, 241–247. doi: 10.1016/j. pbi.2006.03.012

Bryan, S. J., Burroughs, N. J., Shevela, D., Yu, J., Rupprecht, E., and Liu, L. N. (2014). Localisation and interactions of the Vipp1 protein in cyanobacteria. *Mol. Microbiol.* 94, 1179–1195. doi: 10.1111/mmi.12826

Bultema, J. B., Fuhrmann, E., Boekema, E. J., and Schneider, D. (2010). Vipp1 and PspA. *Commun. Integr. Biol.* 3, 162–165. doi: 10.4161/cib.3.2.10529

Casella, S., Huang, F., Mason, D., Zhao, G.-Y., Johnson, G. N., and Mullineaux, C. W. (2017). Dissecting the native architecture and dynamics of cyanobacterial photosynthetic machinery. *Mol. Plant* 10, 1434–1448. doi: 10.1016/j.molp.2017.09.019

Chuartzman, S. G., Nevo, R., Shimoni, E., Charuvi, D., Kiss, V., and Ohad, I. (2008). Thylakoid membrane remodeling during state transitions in Arabidopsis. *Plant Cell* 20, 1029–1039. doi: 10.1105/tpc.107.055830

DeLisa, M. P., Lee, P., Palmer, T., and Georgiou, G. (2004). Phage shock protein PspA of Escherichia coli relieves saturation of protein export via the Tat pathway. *J. Bacteriol.* 186, 366–373. doi: 10.1128/JB.186.2.366-373.2004

Domínguez-Escobar, J., Wolf, D., Fritz, G., Höfler, C., Wedlich-Söldner, R., and Mascher, T. (2014). Subcellular localization, interactions and dynamics of the phage-shock protein-like Lia response in Bacillus subtilis. *Mol. Microbiol.* 92, 716–732. doi: 10.1111/mmi.12586

Engel, B. D., Schaffer, M., Kuhn Cuellar, L., Villa, E., Plitzko, J. M., and Baumeister, W. (2015). Native architecture of the Chlamydomonas chloroplast revealed by in situ cryo-electron tomography. *Elife* 4: e04889. doi: 10.7554/eLife.04889

Engl, C., Jovanovic, G., Lloyd, L. J., Murray, H., Spitaler, M., and Ying, L. (2009). In vivo localizations of membrane stress controllers PspA and PspG in Escherichia coli. *Mol. Microbiol.* 73, 382–396. doi: 10.1111/j.1365-2958.2009.06776.x

Feng, J., Fan, P., Jiang, P., Lv, S., Chen, X., and Li, Y. (2014). Chloroplast-targeted Hsp90 plays essential roles in plastid development and embryogenesis in Arabidopsis possibly linking with VIPP1. *Physiol. Plant* 150, 292–307. doi: 10.1111/ppl.12083

Fuhrmann, E., Bultema, J. B., Kahmann, U., Rupprecht, E., Boekema, E. J., and Schneider, D. (2009a). The vesicle-inducing protein 1 from Synechocystis sp. PCC 6803 organizes into diverse higher-ordered ring structures. *Mol. Biol. Cell* 20, 4620–4628. doi: 10.1091/mbc.E09-04-0319

Fuhrmann, E., Gathmann, S., Rupprecht, E., Golecki, J., and Schneider, D. (2009b). Thylakoid membrane reduction affects the photosystem stoichiometry in the cyanobacterium Synechocystis sp. PCC 6803. *Plant Physiol.* 149, 735–744. doi: 10.1104/pp.108.132373

Göhre, V., Ossenbühl, F., Crèvecoeur, M., Eichacker, L. A., and Rochaix, J. D. (2006). One of two Alb3 proteins is essential for the assembly of the photosystems and for cell survival in Chlamydomonas. *Plant Cell* 18, 1454–1466. doi: 10.1105/tpc.105.038695

Gao, H., and Xu, X. (2009). Depletion of Vipp1 in Synechocystis sp. PCC 6803 affects photosynthetic activity before the loss of thylakoid membranes. *FEMS Microbiol. Lett.* 292, 63–70. doi: 10.1111/j.1574-6968.2008.01470.x

Gao, F., Wang, W., Zhang, W., and Liu, C. (2015). α-Helical domains affecting the oligomerization of Vipp1 and its interaction with Hsp70/DnaK in Chlamydomonas. *Biochemistry* 54, 4877–4889. doi: 10.1021/acs.biochem.5b00050

Gao, F., Chen, B., Jiao, J., Jia, L., and Liu, C. (2017). Two novel vesicle-inducing proteins in plastids 1 genes cloned and characterized in *Triticum urartu*. *PloS One* 12, e0170439. doi: 10.1371/journal.pone.0170439

Guskov, A., Kern, J., Gabdulkhakov, A., Broser, M., Zouni, A., and Saenger, W. (2009). Cyanobacterial photosystem II at 2.9-Å resolution and the role of quinones, lipids, channels and chloride. *Nat. Struct. Mol. Biol.* 16, 334–342. doi: 10.1038/nsmb.1559

Gutu, A., Chang, F., and O'Shea, E. K. (2018). Dynamical localization of a thylakoid membrane binding protein is required for acquisition of photosynthetic competency. *Mol. Microbiol.* 108, 16–31. doi: 10.1111/mmi.13912

Hankamer, B. D., Elderkin, S. L., Buck, M., and Nield, J. (2004). Organization of the AAA+ Adaptor Protein PspA is an Oligomeric Ring. *J. Biol. Chem.* 279, 8862–8866. doi: 10.1074/JBC.M307889200

Heide, H., Nordhues, A., Drepper, F., Nick, S., Schulz-Raffelt, M., and Haehnel, W. (2009). Application of quantitative immunoprecipitation combined with knockdown and cross-linking to Chlamydomonas reveals the presence of vesicle-inducing protein in plastids 1 in a common complex with chloroplast HSP90C. *Proteomics* 9, 3079–3089. doi: 10.1002/pmic.200800872

Heidrich, J., Wulf, V., Hennig, R., Saur, M., Markl, J., and Sönnichsen, C. (2016). Organization into higher ordered ring structures counteracts membrane binding of IM30, a protein associated with inner membranes in chloroplasts and cyanobacteria. *J. Biol. Chem.* 291, 14954–14962. doi: 10.1074/JBC.M116.722686

Heidrich, J., Thurotte, A., and Schneider, D. (2017). Specific interaction of IM30/ Vipp1 with cyanobacterial and chloroplast membranes results in membrane remodeling and eventually in membrane fusion. *Biochim. Biophys. Acta - Biomembr.* 1859, 537–549. doi: 10.1016/j.bbamem.2016.09.025

Heidrich, J., Junglas, B., Grytsyk, N., Hellmann, N., Rusitzka, K., and Gebauer, W. (2018). Mg2+ binding triggers rearrangement of the IM30 ring structure, resulting in augmented exposure of hydrophobic surfaces competent for membrane binding. *J. Biol. Chem.* 293, 8230–8241. doi: 10.1074/jbc.RA117.000991

Heinz, S., Liauw, P., Nickelsen, J., and Nowaczyk, M. (2016). Analysis of photosystem II biogenesis in cyanobacteria. *Biochim. Biophys. Acta* 1857, 274– 287. doi: 10.1016/j.bbabio.2015.11.007

Hennig, R., Heidrich, J., Saur, M., Schmüser, L., Roeters, S. J., and Hellmann, N. (2015). IM30 triggers membrane fusion in cyanobacteria and chloroplasts. *Nat. Commun.* 6, 7018. doi: 10.1038/ncomms8018

Hennig, R., West, A., Debus, M., Saur, M., Markl, J., and Sachs, J. N. (2017). The IM30/Vipp1 C-terminus associates with the lipid bilayer and modulates membrane fusion. *Biochim. Biophys. Acta - Bioenerg.* 1858, 126–136. doi: 10.1016/j.bbabio.2016.11.004

Joly, N., Engl, C., Jovanovic, G., Huvet, M., Toni, T., and Sheng, X. (2010). Managing membrane stress: the phage shock protein (Psp) response, from molecular mechanisms to physiology. *FEMS Microbiol. Rev.* 34, 797–827. doi: 10.1111/j.1574-6976.2010.00240.x

Jovanovic, G., Mehta, P., McDonald, C., Davidson, A. C., Uzdavinys, P., and Ying, L. (2014). The N-terminal amphipathic helices determine regulatory and effector functions of phage shock protein A (PspA) in escherichia coli. *J. Mol. Biol.* 426, 1498–1511. doi: 10.1016/j.jmb.2013.12.016

Junglas, B., and Schneider, D. (2018). What is Vipp1 good for?. *Mol. Microbiol.* 108, 1–5. doi: 10.1111/mmi.13924

Kirchhoff, H., Tremmel, I., Haase, W., and Kubitscheck, U. (2004). Supramolecular photosystem II organization in grana thylakoid membranes: evidence for a structured arrangementt. *Biochemistry* 43, 9204–9213. doi: 10.1021/bi0494626

Kirchhoff, H., Haferkamp, S., Allen, J. F., Epstein, D. B. A., and Mullineaux, C. W. (2008a). Protein diffusion and macromolecular crowding in thylakoid membranes. *Plant Physiol.* 146, 1571–1578. doi: 10.1104/pp.107.115170

Kirchhoff, H., Lenhert, S., Büchel, C., Chi, L., and Nield, J. (2008b). Probing the organization of photosystem II in photosynthetic membranes by atomic force microscopy. *Biochemistry* 47, 431–440. doi: 10.1021/bi7017877

Kleerebezem, M., Crielaard, W., and Tommassen, J. (1996). Involvement of stress protein PspA (phage shock protein A) of Escherichia coli in maintenance of the protonmotive force under stress conditions. *EMBO J.* 15, 162–171. doi: 10.1128/JCM.43.1.19

Kobayashi, R., Suzuki, T., and Yoshida, M. (2007). Escherichia coli phage-shock protein A (PspA) binds to membrane phospholipids and repairs proton leakage of the damaged membranes. *Mol. Microbiol.* 66, 100–109. doi: 10.1111/j.1365-2958.2007.05893.x

Kobayashi, K., Fujii, S., Sato, M., Toyooka, K., and Wada, H. (2015). Specific role of phosphatidylglycerol and functional overlaps with other thylakoid lipids in Arabidopsis chloroplast biogenesis. *Plant Cell Rep.* 34, 631–642. doi: 10.1007/ s00299-014-1719-z

Konno, H., Nakane, T., Yoshida, M., Ueoka-Nakanishi, H., Hara, S., and Hisabori, T. (2012). Thiol modulation of the chloroplast ATP synthase is dependent on the energization of thylakoid membranes. *Plant Cell Physiol.* 53, 626–634. doi: 10.1093/pcp/pcs018

Kowalewska, Ł., Mazur, R., Suski, S., Garstka, M., and Mostowska, A. (2016). Three-dimensional visualization of the Tubular-Lamellar transformation of the internal plastid membrane network during runner bean chloroplast biogenesis. *Plant Cell* 28, 875–891. doi: 10.1105/tpc.15.01053

Kroll, D., Meierhoff, K., Bechtold, N., Kinoshita, M., Westphal, S., and Vothknecht, U. C. (2001). VIPP1, a nuclear gene of Arabidopsis thaliana essential for thylakoid membrane formation. *Proc. Natl. Acad. Sci.* 98, 4238–4242. doi: 10.1073/PNAS.061500998

Li, H., Kaneko, Y., and Keegstra, K. (1994). Molecular cloning of a chloroplastic proteinassociated with both the envelope and thylakoid membranes. *Plant Mol. Biol.* 25, 619–632. doi: 10.1007/BF00029601

Liberton, M., Page, L. E., O'Dell, W. B., O'Neill, H., Mamontov, E., and Urban, V. S. (2013). Organization and flexibility of cyanobacterial thylakoid membranes examined by neutron scattering. *J. Biol. Chem.* 288, 3632–3640. doi: 10.1074/ jbc.M112.416933

Liu, C., Willmund, F., Whitelegge, J. P., Hawat, S., Knapp, B., and Lodha, M. (2005). J-domain protein CDJ2 and HSP70B are a plastidic chaperone pair that interacts with vesicle-inducing protein in plastids 1. *Mol. Biol. Cell* 16, 1165–1177. doi: 10.1091/mbc.E04-08-0736

Liu, C., Willmund, F., Golecki, J. R., Cacace, S., Heß, B., and Markert, C. (2007). The chloroplast HSP70B-CDJ2-CGE1 chaperones catalyse assembly and disassembly of VIPP1 oligomers in Chlamydomonas. *Plant J.* 50, 265–277. doi: 10.1111/j.1365-313X.2007.03047.x

MacGregor-Chatwin, C., Jackson, P. J., Sener, M., Chidgey, J. W., Hitchcock, A., and Qian, P. (2019). Membrane organization of photosystem I complexes in the most abundant phototroph on Earth. *Nat. Plants* 5, 879–889. doi: 10.1038/s41477-019-0475-z

Male, A. L., Oyston, P. C. F., and Tavassoli, A. (2014). Self-assembly of Escherichia coli Phage Shock Protein A. *Adv. Microbiol.* 04, 353–359. doi: 10.4236/aim.2014.47042

McDonald, C., Jovanovic, G., Ces, O., and Buck, M. (2015). Membrane stored curvature elastic stress modulates recruitment of maintenance proteins PspA and Vipp1. *MBio* 6, e01188–e01115. doi: 10.1128/mbio.01188-15

McDonald, C., Jovanovic, G., Wallace, B. A., Ces, O., and Buck, M. (2017). Structure and function of PspA and Vipp1 N-terminal peptides: insights into the membrane stress sensing and mitigation. *Biochim. Biophys. Acta - Biomembr.* 1859, 28–39. doi: 10.1016/J.BBAMEM.2016.10.018

Nagy, G., Posselt, D., Kovács, L., Holm, J. K., Szabó, M., and Ughy, B. (2011). Reversible membrane reorganizations during photosynthesis in vivo: revealed by small-angle neutron scattering. *Biochem. J.* 436, 225–230. doi: 10.1042/bj20110180

Nordhues, A., Schottler, M. A., Unger, A.-K., Geimer, S., Schonfelder, S., and Schmollinger, S. (2012). Evidence for a role of VIPP1 in the structural organization of the photosynthetic apparatus in Chlamydomonas. *Plant Cell Online* 24, 637–659. doi: 10.1105/tpc.111.092692

Ohnishi, N., Zhang, L., and Sakamoto, W. (2018). VIPP1 involved in chloroplast membrane integrity has GTPase activity in vitro. *Plant Physiol.* 177, 328–338. doi: 10.1104/pp.18.00145

Olive, J., Wollman, F.-A., Bennoun, P., and Recouvreur, M. (1981). Ultrastructure of thylakoid membranes in C. reinhardtii: Evidence for variations in the partition coefficient of the light-harvesting complex-containing particles upon membrane fracture. *Arch. Biochem. Biophys.* 208, 456–467. doi: 10.1016/0003-9861(81)90532-4

Osadnik, H., Schöpfel, M., Heidrich, E., Mehner, D., Lilie, H., and Parthier, C. (2015). PspF-binding domain PspA1-144and the PspA·F complex: New insights into the coiled-coil-dependent regulation of AAA+ proteins. *Mol. Microbiol.* 98, 743–759. doi: 10.1111/mmi.13154

Otters, S., Braun, P., Hubner, J., Wanner, G., Vothknecht, U. C., and Chigri, F. (2013). The first α-helical domain of the vesicle-inducing protein in plastids 1 promotes oligomerization and lipid binding. *Planta* 237, 529–540. doi: 10.1007/s00425-012-1772-1

Pohland, A.-C., and Schneider, D. (2019). Mg2+ homeostasis and transport in cyanobacteria – at the crossroads of bacterial and chloroplast Mg2+ import. *Biol. Chem.* 400, 1289–1301. doi: 10.1515/hsz-2018-0476

Rütgers, M., and Schroda, M. (2013). A role of VIPP1 as a dynamic structure within thylakoid centers as sites of photosystem biogenesis? *Plant Signal. Behav.* 8, e27037. doi: 10.4161/psb.27037

Rast, A., Schaffer, M., Albert, S., Wan, W., Pfeffer, S., and Beck, F. (2019). Biogenic regions of cyanobacterial thylakoids form contact sites with the plasma membrane. *Nat. Plants* 5, 436–446. doi: 10.1038/s41477-019-0399-7

Rupprecht, E., Gathmann, S., Fuhrmann, E., and Schneider, D. (2007). Three different DnaK proteins are functionally expressed in the cyanobacterium Synechocystis sp. PCC 6803. *Microbiology* 153, 1828–1841. doi: 10.1099/mic.0.2007/005876-0

Rupprecht, E., Fuhrmann, E., and Schneider, D. (2008). "Stress Regulated DnaK Expression in Synechocystis sp. PCC 6803" in *Photosynthesis. Energy from the Sun* (Dordrecht: Springer Netherlands), 1327–1330. doi: 10.1007/978-1-4020-6709-9_286

Rupprecht, E., Duppre, E., and Schneider, D. (2010). Similarities and Singularities of Three DnaK Proteins from the Cyanobacterium Synechocystis sp. PCC 6803. *Plant Cell Physiol.* 51, 1210–1218. doi: 10.1093/pcp/pcq074

Saha, R., Liu, D., Hoynes-O'Connor, A., Liberton, M., Yu, J., and Bhattacharyya- Pakrasi, M. (2016). Diurnal regulation of cellular processes in the Cyanobacterium Synechocystis sp. Strain PCC 6803: insights from transcriptomic, fluxomic, and physiological analyses. *MBio* 7, e00464–e00416. doi: 10.1128/mBio.00464-16

Sato, M., Nimura-Matsune, K., Watanabe, S., Chibazakura, T., and Yoshikawa, H. (2007). Expression analysis of multiple dnaK genes in the cyanobacterium Synechococcus elongatus PCC 7942. *J. Bacteriol.* 189, 3751–3758. doi: 10.1128/JB.01722-06

Saur, M., Hennig, R., Young, P., Rusitzka, K., Hellmann, N., and Heidrich, J. (2017). A Janus-Faced IM30 Ring Involved in Thylakoid Membrane Fusion Is Assembled from IM30 Tetramers. *Structure* 25, 1380–1390.e5. doi: 10.1016/J.STR.2017.07.001

Standar, K., Mehner, D., Osadnik, H., Berthelmann, F., Hause, G., and Lünsdorf, H. (2008). PspA can form large scaffolds in Escherichia coli. *FEBS Lett.* 582, 3585–3589. doi: 10.1016/j.febslet.2008.09.002

Theis, J., Gupta, T. K., Klingler, J., Wan, W., Albert, S., and Keller, S. (2019). VIPP1 rods engulf membranes containing phosphatidylinositol phosphates. *Sci. Rep.* 9, 8725. doi: 10.1038/s41598-019-44259-3

Thurotte, A., and Schneider, D. (2019). The fusion activity of IM30 rings involves controlled unmasking of the fusogenic core. *Front. Plant Sci.* 10, 108. doi: 10.3389/fpls.2019.00108

Thurotte, A., Brüser, T., Mascher, T., and Schneider, D. (2017). Membrane chaperoning by members of the PspA/IM30 protein family. *Commun. Integr. Biol.* 10, e1264546. doi: 10.1080/19420889.2016.1264546

Umena, Y., Kawakami, K., Shen, J. R., and Kamiya, N. (2011). Crystal structure of oxygen-evolving photosystem II at a resolution of 1.9Å. *Nature* 473, 55–60. doi: 10.1038/nature09913

Ungewickell, E., Ungewickell, H., Holstein, S. E. H., Lindner, R., Prasad, K., and Barouch, W. (1995). Role of auxilin in uncoating clathrin-coated vesicles. *Nature* 378, 632–635. doi: 10.1038/378632a0

Voon, C. P., Guan, X., Sun, Y., Sahu, A., Chan, M. N., and Gardeström, P. (2018). ATP compartmentation in plastids and cytosol of Arabidopsis thaliana revealed by fluorescent protein sensing. *Proc. Natl. Acad. Sci. U. S. A.* 115, E10778–E10787. doi: 10.1073/pnas.1711497115

Vothknecht, U. C., Otters, S., Hennig, R., and Schneider, D. (2012). Vipp1: a very important protein in plastids? *J. Exp. Bot.* 63, 1699–1712. doi: 10.1093/jxb/err357

Walter, B., Hristou, A., Nowaczyk, M. M., and Schünemann, D. (2015). In vitro reconstitution of co-translational D1 insertion reveals a role of the cpSec–Alb3 translocase and Vipp1 in photosystem II biogenesis. *Biochem. J.* 468, 315–324. doi: 10.1042/BJ20141425

Westphal, S., Heins, L., Soll, J., and Vothknecht, U. C. (2001). Vipp1 deletion mutant of Synechocystis: a connection between bacterial phage shock and thylakoid biogenesis? *Proc. Natl. Acad. Sci. U. S. A.* 98, 4243–4248. doi: 10.1073/ pnas.061501198

Wietrzynski, W., Schaffer, M., Tegunov, D., Albert, S., Kanazawa, A., and Plitzko, J. M. (2019). Charting the native architecture of thylakoid membranes with single-molecule precision [Preprint]. *bioRxiv*, 759001. doi: 10.1101/759001

Wolf, D., Kalamorz, F., Wecke, T., Juszczak, A., Mäder, U., and Homuth, G. (2010). In-depth profiling of the LiaR response of Bacillus subtilis. *J. Bacteriol.* 192, 4680–4693. doi: 10.1128/JB.00543-10

Yamaguchi, S., Reid, D. A., Rothenberg, E., and Darwin, A. J. (2013). Changes in Psp protein binding partners, localization and behaviour upon activation of the Yersinia enterocolitica phage shock protein response. *Mol. Microbiol.* 87, 656–671. doi: 10.1111/mmi.12122

Zhang, L., and Sakamoto, W. (2013).). Possible function of VIPP1 in thylakoids: Protection but not formation? *Plant Signal. Behav.* 8: e22860. doi: 10.4161/ psb.22860

Zhang, L., and Sakamoto, W. (2015). Possible function of VIPP1 in maintaining chloroplast membranes. *Biochim. Biophys. Acta* 1847: 831–837. doi: 10.1016/j. bbabio.2015.02.013

Zhang, L., Kato, Y., Otters, S., Vothknecht, U. C., and Sakamoto, W. (2012). Essential role of VIPP1 in chloroplast envelope maintenance in Arabidopsis. *Plant Cell* 24, 3695–3707. doi: 10.1105/tpc.112.103606

Zhang, S., Shen, G., Li, Z., Golbeck, J. H., and Bryant, D. A. (2014). Vipp1 is essential for the biogenesis of Photosystem I but not thylakoid membranes in Synechococcus sp. PCC 7002. *J. Biol. Chem.* 289, 15904–15914. doi: 10.1074/ jbc.M114.555631

Zhang, L., Kondo, H., Kamikubo, H., Kataoka, M., and Sakamoto, W. (2016). VIPP1 has a disordered C-Terminal tail necessary for protecting photosynthetic membranes against stress. *Plant Physiol.* 171, 1983–1995. doi: 10.1104/pp.16.00532

CONFLICT OF INTEREST

The authors declare that the research was conducted in the absence of any commercial or financial relationships that could be construed as a potential conflict of interest.

VIII.2. GTP hydrolysis by *Synechocystis* IM30 does not decisively affect its membrane remodeling activity

Benedikt Junglas[1,2], Carmen Siebenaller[1,2], Lukas Schlösser[1], Nadja Hellmann[1] & Dirk Schneider[1*]

[1] Department of Chemistry, Biochemistry, Johannes Gutenberg University Mainz, 55128 Mainz, Germany.

[2] These authors contributed equally.

***Correspondence:** Dirk Schneider, Dirk.Schneider@uni-mainz.de

Received: 22 January 2020; **Accepted**: 26 May 2020; **Published online**: 17 June 2020

ABSTRACT

The function of IM30 (also known as Vipp1) is linked to protection and/or remodeling of the thylakoid membrane system in chloroplasts and cyanobacteria. Recently, it has been revealed that the *Arabidopsis* IM30 protein exhibits GTP hydrolyzing activity *in vitro*, which was unexpected, as IM30 does not show any classical GTPase features. In the present study, we addressed the question, whether an apparent GTPase activity is conserved in IM30 proteins and can also be observed for IM30 of the cyanobacterium *Synechocystis* sp. PCC 6803. We show that *Synechocystis* IM30 is indeed able to bind and hydrolyze GTP followed by the release of Pi. Yet, the apparent GTPase activity of *Synechocystis* IM30 does not depend on Mg^{2+}, which, together with the lack of classical GTPase features, renders IM30 an atypical GTPase. To elucidate the impact of this cryptic GTPase activity on the membrane remodeling activity of IM30, we tested whether GTP hydrolysis influences IM30 membrane binding and/or IM30-mediated membrane fusion. We show that membrane remodeling by *Synechocystis* IM30 is slightly affected by nucleotides. Yet, despite IM30 clearly catalyzing GTP hydrolysis, this does not seem to be vital for its membrane remodeling function.

INTRODUCTION

IM30, the inner membrane-associated protein of 30 kDa (also known as Vipp1 (vesicle-inducing protein in plastids 1)), is present in cyanobacteria as well as in chloroplasts of higher plants and algae[1]. In chloroplasts, the protein has a triple localization: It can be found soluble in the stroma as well as bound to the inner chloroplast envelope membrane and the thylakoid membrane (TM)[2]. Similarly, IM30 is also found in a soluble form as well as bound to the cytoplasmic membrane and TMs of cyanobacteria[3].

IM30 is a predominantly α-helical protein predicted to consist of seven α-helices, which are able to form coiled-coil structures[3-5]. *In vitro*, IM30 monomers assemble to form diverse higher ordered homo-

oligomers with molecular masses exceeding 2 MDa[4-7]. *In vivo*, in cyanobacteria and in chloroplasts, GFP-labeled IM30 forms large dynamic assemblies, which are mainly located at TM regions with high membrane curvature[8-10].

While diverse functions have been attributed to IM30 in the past[1,2,10-24], most observations clearly indicate that the protein is membrane-active and involved in the biogenesis, dynamics and/or stabilization of internal membranes in chloroplasts and cyanobacteria (recently reviewed in[25]). Thus, the physiological function of IM30 appears to be linked to dynamic membrane remodeling[25-27], likely involving membrane fusion/fission events, which have been observed in plant chloroplasts[28-31]. In fact, dynamic rearrangement of the TM system is crucial for adaptation of photosynthetic processes to altering environmental conditions, most importantly in response to altering light intensities[32,33]. While TM dynamics is studied to some extent in chloroplasts, direct observations of TM dynamics in cyanobacteria are still limited, although TMs in cyanobacteria are assumed to be as dynamic as in chloroplasts[34,35]. Nevertheless, a machinery mediating such membrane remodeling processes has not been unambiguously identified yet, neither in chloroplasts nor in cyanobacteria[36], and IM30 is currently the only protein in chloroplast and cyanobacteria recognized to have a membrane fusion activity[23]. Importantly, light not only triggers rearrangement of the TM system but also rearrangement and redistribution of intracellular IM30 clusters at internal membranes[8,26], which again indicates a connection between TM dynamics and IM30 oligomer formation[25].

In several aspects, the membrane activity of IM30 resembles other membrane-active proteins, as IM30 is involved in membrane fusion, protection and/or stabilization[10,15,16,18,23,37,38] and has a strong tendency to oligomerize and to form higher ordered structures[3,4,7]. Yet, in most thus far described systems, membrane remodeling, especially membrane fission and fusion, are typically connected to nucleotide hydrolysis. Thus, it was somewhat intriguing to suspect a nucleotide binding/hydrolysis function also for IM30, a protein that can mediate membrane fusion[23]. Consistent with this idea, Ohnishi *et al.* recently suggested that recombinant *Arabidopsis* IM30 (*Ara*IM30) has an intrinsic GTPase activity despite lacking classical features of GTPases, implying that IM30 belongs to a new class of membrane-remodeling GTPases[39]. Yet, the molecular details of the IM30 membrane activity have been extensively studied *in vitro* in recent years, and all membrane-related activities were already observed in the absence of nucleotides. Thus, the question arises whether GTP binding and/or hydrolysis have any impact on the structure and/or activity of IM30.

In the present study, we have analyzed the apparent GTPase activity of IM30 of the cyanobacterium *Synechocystis* sp. PCC 6803. We have tested the influence of nucleotides on IM30-triggered membrane fusion and lipid organization *in vitro*. Our results suggest that the *Synechocystis* IM30 also has a low GTP hydrolyzing activity, as observed before with the *Arabidopsis* homolog, yet

nucleotides have only minor effects on the *in vitro* membrane remodeling activity of IM30, and therefore nucleotide binding/hydrolysis does not appear to critically affect IM30-triggered membrane remodeling.

RESULTS

SynIM30 has an apparent GTPase activity

The *Arabidopsis* IM30 protein (*Ara*IM30) appears to have a GTPase activity under defined *in vitro* conditions[39]. As this has never been described for any IM30 protein before, we first aimed to elucidate whether this apparent activity is conserved in IM30 proteins. Therefore, we analyzed the interaction of a cyanobacterial IM30 homolog (*Synechocystis* IM30; *Syn*IM30) with GTP.

Initially, we tested whether *Syn*IM30 hydrolyzes GTP, using the malachite green-based assay that has also been used by Ohnishi *et al.* to determine the apparent GTPase activity of *Ara*IM30[39].

Indeed, we observed protein-dependent P_i production, *i.e.* GTP hydrolysis, in perfect agreement with the findings of Ohnishi *et al.*, reaching about 20 µM P_i release at a protein concentration of 2 µg/100 µL (Fig. 1a). To rule out that P_i release of the protein originated from contamination with a GTPase, we analyzed the purity of the protein via SDS-PAGE, whereby no other protein was identified besides IM30 (Fig. 1g). Although this does not finally exclude any contamination with a highly active GTPase, the missing GTPase activity of an IM30 mutant (Fig. 3a), purified following the exact same protocol, is a strong hint that the observed GTPase activity can indeed be exclusively ascribed to IM30, as further discussed below.

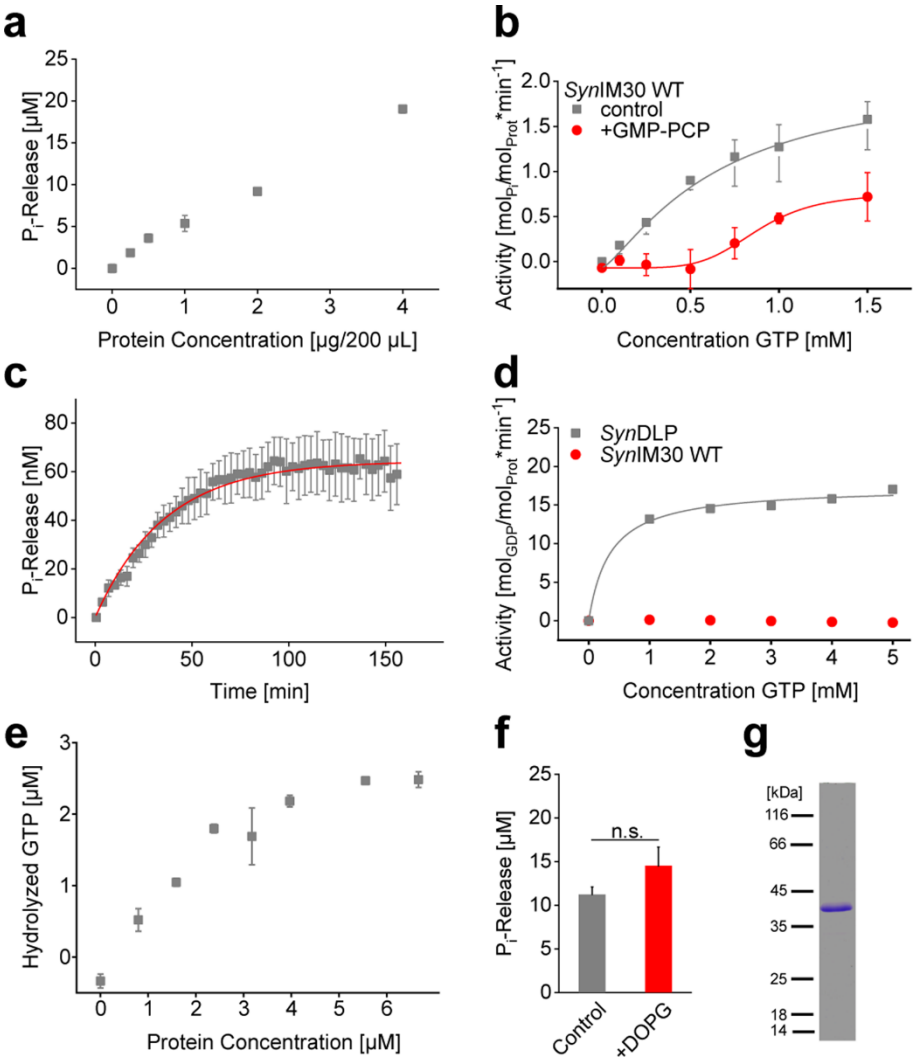

Figure 1: IM30 GTPase activity was characterized by multiple assays.

(a) A malachite green-based assay was used to measure the P_i release catalyzed by *Syn*IM30 WT (0.5 mM GTP; 2.5 mM Mg^{2+}; 30 min at 37 °C). (Error bars represent SD, n = 3). **(b)** The enzymatic properties of the GTP hydrolysis caused by *Syn*IM30 were analyzed with a malachite green-based assay in absence and presence of 0.5 mM GMP-PCP (0.1 µM IM30 WT; 2.5 mM Mg^{2+}; 30 min at 37 °C). Fitting the data with a Hill equation derived model yielded Vmax value of 2.16 ± 0.33 mol GTP per mol IM30 per min, K_m = 0.65 ± 0.14 mM; n = 1.29 ± 0.09 and Vmax = 0.83 ± 0.33 min^{-1}; K_m = 0.88 ± 0.16 mM; n = 5.19 ± 3.64 in presence of GMP-PCP. (R^2 = 0.99835 and R^2 = 0.95888; SD, n = 3). **(c)** A fluorescence-based continuous test for P_i release was used to determine *Syn*IM30 GTPase activity in real-time (0.1 µM IM30 WT; 10 µM GTP; 2.5 mM Mg^{2+}; 37 °C). Fitting the data with a mono-exponential function yielded v_0 = 1.79 ± 0.02 min^{-1} and ηη = 2.79 ± 0.05 *10^{-2} (R^2 = 0.97898; SD, n = 3). **(d)** A PK/LDH-coupled assay was used to determine the GTPase activity independent of the P_i release. *Syn*IM30 WT did not show significant activity (SD, n = 3). As a control, a GTPase with known activity was used (*Syn*DLP; n = 1). (e) A luciferase-coupled GTPase assay was used to measure the amount of hydrolyzed GTP over 120 min at 37 °C in the presence of increasing *Syn*IM30 concentrations (4 µM GTP). (Error bars represent SD, n = 3) **(f)** GTPase activity of IM30 WT was measured by the malachite green-based assay in absence and presence of 30 µM DOPG (2 µg/200 µL protein, 0.5 mM GTP; 2.5 mM Mg^{2+}; 30 min at 37 °C). The GTPase activity is not significantly increased in the presence of the liposomes. (SD, n = 3, two-sample Student´s t-test, significance level p > 0.05). **(g)** The purity of *Syn*IM30 WT heterologously expressed in *E. coli* and purified via Ni^{2+}-affinity chromatography was analyzed by SDS-PAGE.

Subsequently, we used the malachite green-based assay to further characterize the apparent GTPase activity of IM30. The steady-state activity of IM30 in dependence on the GTP concentration could be described by a slightly sigmoidal curve (Fig. 1b). Fitting the experimental data with the Hill-equation (Eq. 2) resulted in a k_{cat} value of 2.16 ± 0.33 mol GTP per mol IM30 per min, a Michaelis-Menten constant of 0.65 ± 0.14 mM and a Hill coefficient of 1.29 ± 0.09. Addition of the non-hydrolyzable GTP analog GMP-PCP, which is expected to act as a competitive inhibitor, strongly increased the cooperativity, as evidenced by the increased Hill coefficient ($n = 5.19 \pm 3.64$) (Fig. 1b).

As the malachite green-based assay is not capable of measuring reaction kinetics, we next applied a continuous assay for P_i release, which is based on a recombinant *E. coli* phosphate-binding protein labeled with the fluorophore MDCC[40]. This assay indeed allowed monitoring the kinetics of the apparent IM30 GTPase activity, measured as the P_i release (Fig. 1c). Fitting the data with a model for non-linear, steady-state enzyme kinetics and assuming a first-order process[41] yielded a k_{cat} (Eqs. 3 and 4) in presence of 10 µM GTP ($1.79 \pm 0.02 * 10^{-2}$ min^{-1}) (Fig. 1c). However, these measurements could be performed solely at very low GTP concentrations, as the P_i sensor has an extremely high sensitivity for P_i.

Although specifically established for measuring NTPase activities, the malachite green-based assay is prone to artifacts, and *e.g.* protein binding to the malachite complex or acids can induce NTP hydrolysis, causing false positive results[42]. Thus, we aimed to apply an established PK/LDH-coupled assay that measured GTP hydrolysis by coupling the regeneration of GTP from GDP to a decline in NADH concentration, which can be monitored by absorbance at 340 nm[43]. Surprisingly, when using this assay we were not able to measure a significant amount of GTP hydrolysis (Fig. 1d). Even doubling the *Syn*IM30 concentration did not produce a detectable signal (data not shown). Based on the P_i release determined with the malachite green assay (20 µM P_i/30 min) we calculated the expected change in absorption at 340 nm, amounting to $\Delta OD = 0.124$ in 30 min. This should be easily detectable if GDP is released. To ensure that the assay works properly, we also analyzed the GTPase activity of *Syn*DLP, a canonical P-loop GTPase of the cyanobacterium *Synechocystis* sp. PCC6803[36], as a positive control (Fig. 1d).

Since we were not able to detect any GTP hydrolysis using the PK/LDH-coupled assay, we wondered whether the observed apparent GTPase activity might be caused by P_i leaking into the reaction mixture, *e.g.* by release of P_i bound to IM30 rather than by GTP hydrolysis. To test this, we used a luciferase-coupled GTPase assay, which directly depends on the GTP concentration rather than P_i-release. In this assay, non-hydrolyzed GTP is enzymatically converted to ATP and the resulting ATP concentration is subsequently measured in the luciferase reaction. Here we observed a steady

decrease of the GTP concentration in the presence of IM30 in a protein concentration-dependent manner, as expected for a GTP hydrolyzing activity (Fig. 1e). Thus, we conclude that *Syn*IM30 can indeed catalyze the hydrolysis of GTP.

The activity of many membrane-active GTPases is modulated when the protein interacts with lipid membranes, and interaction of *e.g.* dynamins with membrane surfaces can increase the GTPase activity by a factor of 40[44,45]. As IM30 binds to negatively charged PG liposome surfaces[23,24,37,46], we next assayed GTP hydrolysis by *Syn*IM30 in absence *vs.* in presence of DOPG liposomes. While our measurements were limited to low lipid concentrations, as the liposomes created a strong background signal in the assay, we did not observe a significant increase in GTP hydrolysis in presence of DOPG liposomes ($p = 0.066$) (Fig. 1f).

In summary, *Syn*IM30 clearly has an apparent GTPase activity *in vitro*, as observed before with the *Ara*IM30 protein. This activity can be modulated by a classical GTPase inhibitor and does not seem to be affected by membranes.

IM30 binds and hydrolyzes GTP in the presence and absence of Mg^{2+}

Thus far, apparent GTP hydrolysis was always tested in presence of Mg^{2+}, as the activity of NTPases typically requires the presence of Mg^{2+}. Notably, the interplay of IM30, Mg^{2+} and GTP is of special interest, as also the membrane fusion activity of IM30 depends on Mg^{2+} [23], and binding of Mg^{2+} to IM30 even causes rearrangement of the IM30 structure[47].

To test the Mg^{2+} dependence of the IM30 GTPase activity we determined GTP hydrolysis rates in the absence of Mg^{2+}. Surprisingly, the K_M value (0.61 ± 0.20 mM) determined for GTP hydrolysis was essentially identical, regardless of the presence of Mg^{2+}. Similarly, the v_{max} value ($1.65 \pm 0.55 min^{-1}$) did not significantly differ from the value determined in the presence of Mg^{2+} ($2.16 \pm 0.33 min^{-1}$) (Fig. 2a). Thus, Mg^{2+} does obviously not have a strong impact on GTP hydrolysis by *Syn*IM30. Yet, cooperativity was strongly increased in absence of Mg^{2+}, reaching a value of 2.00 ± 0.27, which nicely supports the recently described Mg^{2+}-induced change of the IM30 structure and stability[47]. In fact, addition of Mg^{2+} *e.g.* increased the thermal stability of IM30 as indicated by T_m values of 66.6 ± 0.2 °C and 68.7 ± 0.2 °C in absence and presence of 2.5 mM Mg^{2+}, respectively (Fig. 2b). However, an increased stability of *Syn*IM30 was observed when 0.5 mM GTP and 2.5 mM Mg^{2+} were present together (T_m 67.6 ± 0.2 °C) compared to *Syn*IM30 in presence of solely 2.5 mM GTP, where the T_m was as low as 64.6 ± 0.2 °C (Fig. 2b). This suggests that GTP binding affects the structure and stability of IM30 to some extent, and Mg^{2+}

and GTP do not operate synergistically but have opposing effects on the *Syn*IM30 stability. Thus, GTP binding to *Syn*IM30 and *Syn*IM30-mediated GTP hydrolysis appear to be independent of Mg^{2+}, which is rather uncommon for GTPases.

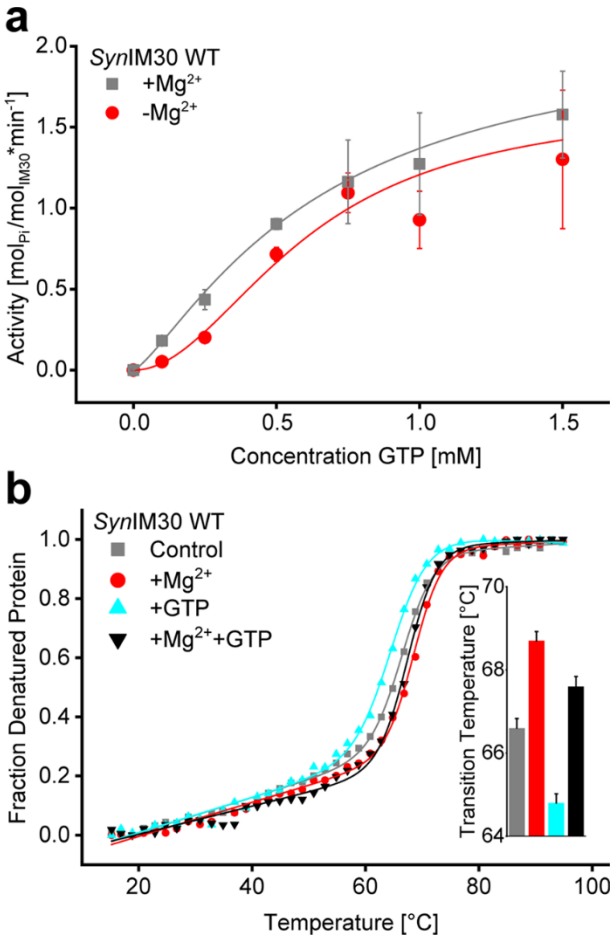

Figure 2: GTP binds to IM30 in presence and absence of Mg^{2+}.

(a) GTP hydrolysis caused by IM30 WT in absence of Mg^{2+} was analyzed using a malachite green-based assay (0.1 µM IM30 WT; 0 mM Mg^{2+}; 30 min at 37 °C). Fitting of the data with a Hill equation derived model yielded VmaxVmax = 1.66 ± 0.55 min^{-1}; K_m = 0.61 ± 0.20 mM; n = 2.00 ± 0.27 in absence of Mg^{2+}. (R^2 = 0.96951; SD, n = 3). Data in presence of Mg^{2+} were taken from Fig. 1b (control). **(b)** Thermal denaturation of IM30 WT in the absence and presence of GTP and Mg^{2+} was monitored by CD-spectroscopy at 222 nm. The raw signal was converted to the fraction of denatured protein (f_D). Fitting the data with an adapted Boltzmann-fit yielded: T_m = 66.6 ± 0.2 °C (0 mM GTP; 0 mM Mg^{2+}) (R^2 = 0.99866); T_m = 68.7 ± 0.2 °C (0 mM GTP; 2.5 mM Mg^{2+}) (R^2 = 0.99841); T_m = 64.8 ± 0.2 °C (0.5 mM GTP; 0 mM Mg^{2+}) (R^2 = 0.99836) and T_m = 67.5 ± 0.2 °C (0.5 mM GTP; 2.5 mM Mg^{2+}) (R^2 = 0.99784). Error bars represent errors from the fitting of the data.

GTP hydrolysis depends on the oligomeric state of IM30

Based on studies using truncated *Ara*IM30 it has been suggested that helix 1 is crucial for GTP binding to *Ara*IM30 and for its apparent GTPase activity[39]. As we assume that the apparent GTPase activity is conserved in IM30 proteins of different origins, we next tested the GTP hydrolyzing activity of the

recently described *Syn*IM30 variant H2-7, where helix 1 was deleted[46]. Although this mutant showed a decreased P_i release rate compared to the wt protein (Fig. 3a), P_i release was decreased only by about 40% (*i.e.* to roughly 60% of the wt levels), whereas the GTPase activity of the *Ara*IM30 protein was completely abolished when helix 1 was deleted[39]. However, the *Ara*IM30 protein does not form high molecular mass oligomers anymore when helix 1 is deleted[4,39], whereas IM30 of *Chlamydomonas rheinhardtii*[5] and the here analyzed *Syn*IM30 do[46], as recently discussed in[25]. Yet, a fraction of smaller oligomers was also identified in SEC analyses of the *Syn*IM30 H27 protein (see Fig. 3b). Thus, the disturbed formation of high molecular mass oligomers might explain the abolished GTPase activity of the *Ara*IM30 H2-7 protein[39], and the reduced amount of released P_i by *Syn*IM30 H2-7 (Fig. 3b). To further test the hypothesis that the decreased oligomeric state, and not deletion of helix 1, has caused the reduced apparent GTPase activity, we next generated a *Syn*IM30 variant that exclusively forms small oligomers (mainly tetramers in buffers with low ionic strength) (*Syn*IM30 FERM_EE) and no high molecular mass oligomers (Fig. 3b). This mutant is based on the *Syn*IM30_FERM variant described recently[7,37], but additionally E83 and E84 in the loop region of helix 2 and 3 were mutated to overcome the problem of unspecific aggregation upon prolonged exposure to HEPES buffer. In line with our hypothesis, this variant had no detectable GTPase activity (Fig. 3a). Note that also *Syn*IM30_FERM does not exhibit detectable GTPase activity (Suppl. Fig. 1).

Thus, we conclude that the IM30 GTPase activity depends on the IM30 oligomeric state, and formation of high molecular mass oligomers is a prerequisite of GTP hydrolysis. A lack of high molecular mass oligomers seems to be the major factor for GTP hydrolysis since helix 1 is unchanged in the tetrameric *Syn*IM30 variant. Together, these results clearly suggest that not helix 1 but the formation of high molecular mass oligomers is crucial for GTP hydrolysis. In addition, the absent GTP hydrolyzing activity of the mutant protein confirms that the GTPase activity observed with the IM30 wt (Fig. 1) was not caused by an (unintended) co-purification of an (unknown) GTPase.

Considering that IM30 forms oligomers, the sigmoidal shape of the GTPase activity in presence of GMP-PCP (Fig. 1b) and in absence of Mg^{2+} (Fig. 2a) might well reflect the interaction of GTP-binding sites within the protein. Indeed, the data describing the GTPase activity of IM30 can be well depicted by a cooperative two-state model (Fig. 3c, see Suppl. Fig. 3 for details). The increase in cooperativity in presence of GMP-PCP can be explained by competitive binding, which would shift the distribution towards the low-affinity state, requiring more GTP to yield measurable activity. Formally, also binding to an allosteric site could explain the data. Both variants of the two-state model describe the data similarly well (see Supplemental Data 3). The number of binding sites interacting, giving rise to the observed cooperativity, is ≥8 (Suppl. Fig. 3d). Thus, these data correspond well with the idea of having multiple subunits interacting with each other during GTP binding/hydrolysis, which explains

the necessity of IM30 rings/high molecular weight complexes for GTPase activity.

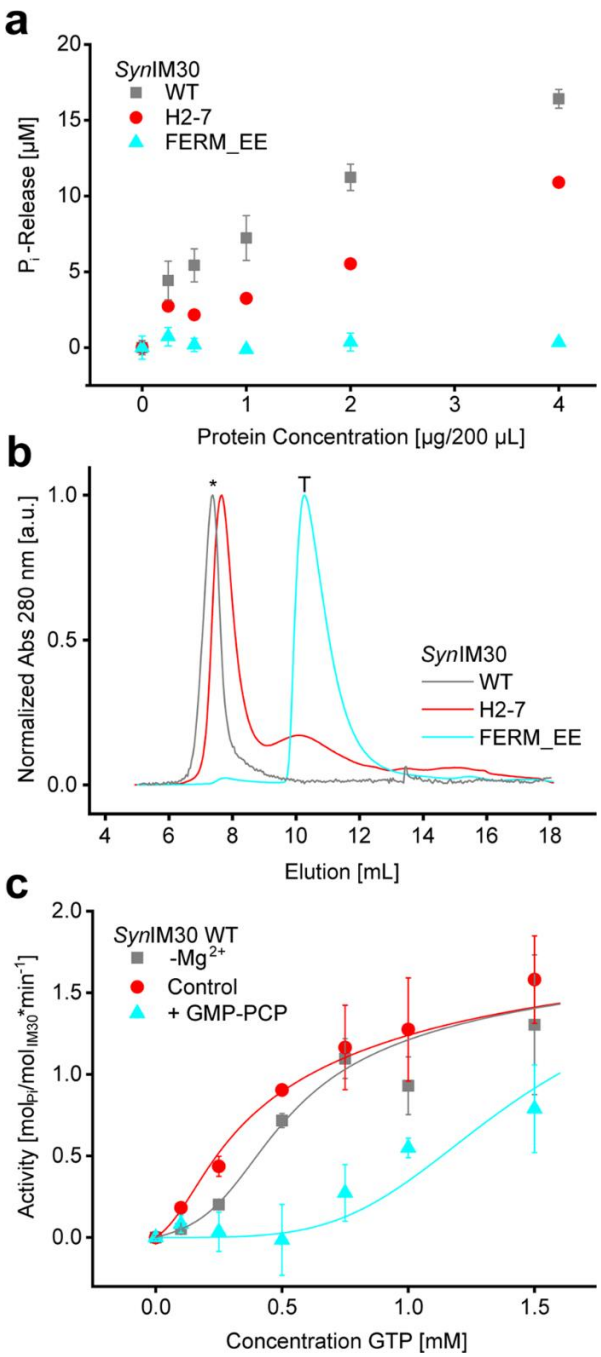

Figure 3: The oligomeric state of IM30 is crucial for GTP hydrolysis.

(a) The malachite green-based assay was used to compare the GTPase activity of IM30 variants with different oligomeric states (0.5 mM GTP; 2.5 mM Mg^{2+}; 30 min at 37 °C). Compared to IM30 WT, H2-7 has a reduced GTPase activity. The tetrameric IM30 FERM_EE has no detectable GTPase activity. (Error bars represent SD, n = 3). **(b)** The oligomeric state of IM30 variants was determined by SEC (Superose 12 10/300 GL column). The elution volumes determined are 7.4 mL for IM30 WT (>300 kDa); 7.7 mL (>300 kDa) and 10.2 mL (105 kDa) for IM30 H2-7 and 10.3 mL (100 kDa) for IM30 FERM_EE. The asterisk marks the position of the void volume. T marks the position of an IM30 tetramer. **(c)** The data of the malachite green assay of IM30 WT in absence and presence of Mg^{2+} and after addition of GMP-PCP were analyzed using a more sophisticated model (described in detail in the Supplemental Data 3), to disentangle the mechanism of GTP-hydrolysis. Error bars represent SD, n = 3. Fit: n = 12, allosteric model (see Supplemental Data 3).

IM30 binding to membrane surfaces is not influenced by GTP

IM30 binds to negatively charged membrane surfaces and is involved in membrane remodeling[16,23,37]. Thus, we next studied the impact of GTP on binding of *Syn*IM30 to negatively charged membrane surfaces.

In the presence of Mg^{2+}, *Syn*IM30 exhibits membrane fusion activity, and such membrane fusion events can disturb other assays, involving IM30 and liposomes[23]. Luckily, GTP binding to *Syn*IM30 and GTP hydrolysis were observed also in absence of Mg^{2+} (Fig. 2a,b). Thus, we were able to analyze the influence of nucleotide binding to *Syn*IM30 on membrane binding independent of the effect on IM30-mediated membrane fusion.

First, we analyzed whether GTP has an impact on the propensity of *Syn*IM30 to interact with negatively charged DOPG liposomes. It has previously been shown that binding of *Syn*IM30 to DOPG membranes can be monitored via steady-state Laurdan fluorescence spectroscopy[23,37]. As shown in Fig. 4a,b, the Laurdan fluorescence emission spectrum was already altered upon addition of solely GTP or GDP, even when *Syn*IM30 was not present, albeit only to a minor extent. Thus, the nucleotides appear to interact with the liposomes, resulting in a minor change of the Laurdan fluorescence emission. However, when *Syn*IM30 was added to the liposomes, the Laurdan fluorescence spectrum changed far more significantly, and an altered fluorescence spectrum was observed in absence as well as in presence of GTP or GDP. All spectra recorded in presence of *Syn*IM30 (Fig. 4a) showed an increased fluorescence emission at 440 nm and a decreased emission at 490 nm, leading to an increase of the GP-value. This indicates a decreased polarity of Laurdan's environment, as occurring when the lipid order increases. The changes in the lipid order, represented by the ΔGP values, showed no significant impact of GTP or GDP on the interaction of *Syn*IM30 with DOPG liposomes (Fig. 4c), indicating that GTP binding and/or hydrolysis by *Syn*IM30 do not affect binding of IM30 to lipid bilayers, at least not in the absence of Mg^{2+}. Unfortunately, it was not possible to analyze *Syn*IM30 binding to DOPG liposomes in the presence of Mg^{2+} due to direct binding of Mg^{2+} to DOPG membranes as well as to to *Syn*IM30[47] and side-effects caused by *Syn*IM30-mediated membrane fusion[23].

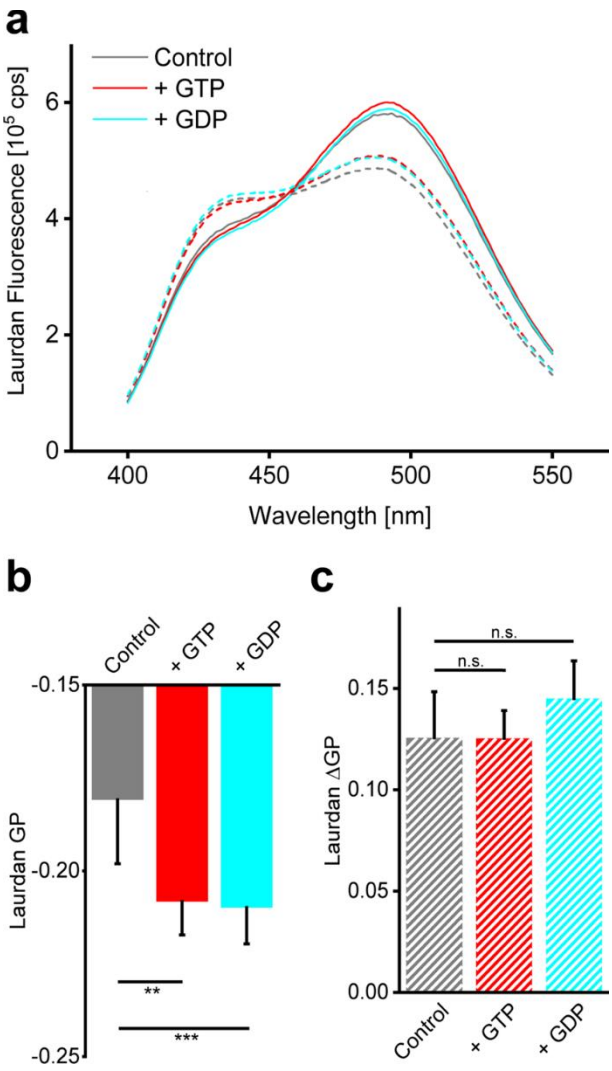

Figure 4: The presence of the nucleotides GTP and GDP does not affect the IM30-mediated change of the DOPG lipid order.

(a) Laurdan fluorescence emission spectra of 0.1 mM DOPG liposomes were recorded in absence and presence of 2.5 mM GTP or GDP and 1 µM SynIM30 WT. Solid lines show the spectra in absence of IM30. Dashed lines show the spectra in the presence of SynIM30 WT. Binding of IM30 leads to a clear shift of the Laurdan fluorescence maximum. **(b)** The GP value was calculated for DOPG liposomes in the presence and absence of GTP and GDP without addition of SynIM30. Addition of the nucleotides leads to a small, but still significant decrease of the GP-value. SD, n = 6 two-sample Student´s t-test, *p < 0.05, **p < 0.01, ***p < 0.005. **(c)** The ΔGP after addition of SynIM30 WT to DOPG liposomes is not significantly changed in the presence of the nucleotides GTP or GDP, respectively. (SD, n = 6 two-sample Student´s t-test).

GTP and GDP do only marginally affect the kinetics of IM30-mediated membrane fusion

*Syn*IM30 has a membrane fusion activity when Mg^{2+} is present (Hennig *et al.*, 2015). Consequently, we next analyzed the potential impact of GTP and GDP on IM30-induced liposome fusion in the presence of Mg^{2+}. Membrane fusion was measured using a FRET-based liposome fusion assay, as described in detail previously[23]. Importantly, in presence of the nucleotides, the concentration of $MgCl_2$ had to

be adjusted, as GTP and GDP coordinate Mg^{2+} via their phosphate groups[48] and thereby lower the effective concentration of "free" Mg^{2+} which clearly influences the membrane fusion process[23]. The concentration of additionally "needed" $MgCl_2$ was determined experimentally in the presence of GTP and GDP, as described in the "Experimental Procedures" section. Note that controls containing exclusively IM30, Mg^{2+}, the nucleotides or the respective Mg^{2+}/nucleotide mixture did not show any membrane fusion activity (data not shown).

In contrast to membrane fusion observed in absence of nucleotides, the fusion assay indicated a slightly increased fusion rate in presence of GTP, while slightly less liposome fusion was observed in presence of GDP (Fig. 5). The initial fusion rate increased from 0.58 ± 0.20%/s in the absence of nucleotides to 0.80 ± 0.22%/s in the presence of GTP. In contrast, addition of GDP lowered the initial fusion rate to 0.33 ± 0.04%/s. However, in all cases the fusion curves appear to level out at approximately the same amount of total fusion.

Clearly, GTP binding/hydrolysis is not unequivocally required for IM30-mediated membrane fusion, and the presence of GTP or GDP does neither abolish nor exclusively trigger membrane fusion. We conclude therefore that the GTP hydrolyzing activity of IM30 is not a key regulator of the membrane fusion process, as it is not switching the IM30 membrane fusion activity from a completely active to an inactive state, or *vice versa*. Yet, as we did observe small effects on the fusion kinetics in the presence of GTP and GDP, we cannot completely rule out the possibility that nucleotide binding and/or GTP hydrolysis modulate IM30-mediated membrane fusion.

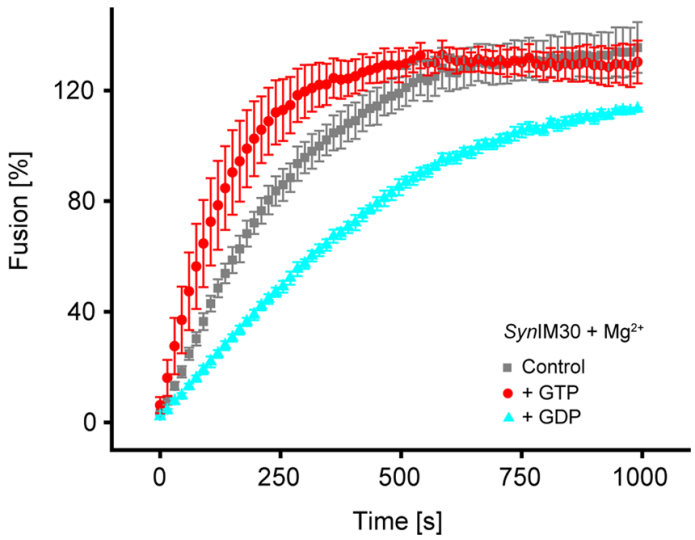

Figure 5: IM30-mediated membrane fusion is modulated to some extent by GTP and GDP.

Liposome fusion was measured in the presence of 1 µM SynIM30 WT, 2.5 mM nucleotide and 6 mM Mg2+. Because of binding of free Mg2+ by the nucleotides, "extra" needed Mg2+, needed to obtain the same membrane destabilization, was also added (2.5 mM for GDP, 4.25 mM for GTP). The presence of GTP leads to a slight increase in the fusion rate, whereas the presence of GDP leads to a slower fusion process. (SD, n = 3).

DISCUSSION

SynIM30 has a low GTP binding affinity and hydrolyzes GTP with low rates in the absence of Mg^{2+}

Involvement of the IM30 protein in membrane protection and/or membrane dynamics in chloroplasts and cyanobacteria has been described in the past, and recently, an apparent GTPase activity of *Ara*IM30 has been observed[39]. Yet, this observation was unexpected, as none of the known IM30 protein sequences does contain predicted domains or amino acid motifs known to be crucial for nucleotide binding and/or hydrolysis (not shown). Thus, the question arose whether the presumed GTPase activity is *Ara*IM30-specific or more generic. Therefore, in the present study, we analyzed the GTPase activity of *Syn*IM30. We here show that *Syn*IM30 can bind GTP, resulting in GTP hydrolysis and release of free P_i. This apparent GTPase activity can be modulated by a classical GTPase inhibitor (GMP-PCP).

In fact, when analyzed with the malachite green assay, *Syn*IM30 has a (rather low) GTPase activity with a k_{cat} of $2.16 \pm 0.33\,min^{-1}$, a value comparable to the activity described for some other membrane remodeling GTPases, such as dynamin in absence of membranes (k_{cat} $2.60 \pm 0.98\ min^{-1}$)[49]. However, it is worth mentioning that the k_{cat}

determined using the malachite green assay (Fig. 1b) is essentially derived from the activity averaged over the entire incubation time, and the determined values do thus not account for any bias on the turnover rates, such as substrate limitation/substrate inhibition, *etc*. In an attempt to address these limitations, we applied a continuous phosphate release assay (Fig. 1c) that is in principle capable of measuring the actual rate of P_i release and can therefore be used to determine the initial, non-biased turnover rate v_0. Unfortunately, when using this assay we were limited to a very small concentration of the substrate (10 µM GTP), which was significantly lower than the K_M value determined for *Syn*IM30 with the malachite green assay (K_M 0.65 ± 0.14 mM). Based on the parameters obtained for the Hill-equation, the saturation level of IM30 at this GTP concentration is about 0.5%. Thus, under these conditions, the expected k_{cat} is about 0.01 min, which is reasonably well in agreement with the experimentally observed k_{cat} ($0.0179 \pm 0.02\ min^{-1}$) (Fig. 1c). However, we were not able to observe GTP hydrolysis when using a PK/LDH-coupled assay (Fig. 1d) that is well-established in the NTPase field. Assuming the same activity as observed with the malachite green assay, we would expect to observe a change of OD 0.124/30 min, which should be easily detectable. This can either be explained by IM30 inhibiting the assay and/or *vice versa* or by slow k_{off} rates for GDP.

Nevertheless, *Syn*IM30 clearly shows GTP hydrolysis activity, as demonstrated by the luciferase-coupled GTPase assay, which directly depends on the decrease of the GTP concentration. Again, the observed rate is in reasonable agreement with the K_M and k_{cat} values obtained from the malachite

green-based assay, taking the low GTP concentration of 4 µM into account. However, IM30 binds GTP rather weakly, compared to K_D values of typical GTPase. *E.g.* GTPases of the *ras* superfamily, which are considered high-affinity GTPases, have K_D values in the subnanomolar range[49], whereas low-affinity GTPases, such as dynamins or the signal recognition particle (SRP), have K_D values in the range of 0.5–5 µM[50]. Thus, typical low-affinity GTPases still bind GTP with at least 100-fold higher affinities than observed here for *Syn*IM30.

Addition of GMP-PCP, a non-hydrolyzable GTP analog, revealed strong cooperative properties of the apparent GTPase activity, which was essentially not observed in the absence of GMP-PCP. Within the frame of an allosteric two-state model, both allosteric and competitive binding could produce such an increase in cooperativity (see Suppl. Fig. 3). While the data did not allow to identify the exact nature of GMP-PCP inhibition, the observations demonstrate that binding of GTP is a cooperative process, probably involving more than four binding sites (see Suppl. Fig. 3d).

While *Syn*IM30 exhibits a GTPase activity, which can be modulated by a non-hydrolyzable GTP analog, this activity clearly is Mg^{2+}-independent (Fig. 2a), which is rather uncommon for canonical GTPases. Typically, Mg^{2+} is required for GDP and GTP binding and hydrolysis. Yet, absence of Mg^{2+} does neither affect GTP binding nor GTP hydrolysis by *Syn*IM30 (Fig. 2), and both K_M and v_{max} were about identical in presence or absence of Mg^{2+} (Fig. 2a). While binding of GTP and an apparent GTPase activity in absence of Mg^{2+} have already been described for other GTPases, involving FtsZ[51] or Rho family GTP-binding proteins[52], in these cases Mg^{2+} addition dramatically increased the hydrolysis rates. In fact, here Mg^{2+} binding was suggested to regulate the kinetics of GTP binding and hydrolysis to achieve high catalytic efficiency and specificity. Thus, a fully Mg^{2+}-independent GTP hydrolyzing activity is rather uncommon. Nevertheless, while v_{max} remained unchanged in presence of Mg^{2+}, the cooperativity of GTP hydrolysis by the oligomeric IM30 was significantly increased. Mg^{2+} is known to directly bind to *Syn*IM30 and to alter the structure of *Syn*IM30 oligomers[47]_bookmark44, which, *vice versa*, *e.g.* results in an increased thermal stability of the protein (Fig. 2b). Thus, a model, where binding of Mg^{2+} leads to a shift in the conformational distribution between different structural states, is reasonable and explains the observed change in cooperativity well, while v_{max} remains constant.

GTP hydrolysis depends on the oligomeric state

While IM30 proteins do not contain any canonical GTPase domain or any motif known to be involved in NTP binding and/or hydrolysis, Ohnishi *et al.* have identified helix 1 of *Ara*IM30 to be crucial for GTP hydrolysis, as deletion of helix 1 resulted in reduced GTP hydrolysis[39]_bookmark36. However, deletion of helix 1 also resulted in disassembly of the typical IM30 high molecular mass complexes in

case of the *Ara*IM30 protein[4,39], and thus the GTP hydrolyzing activity could well be coupled to the oligomeric state of IM30 proteins. In fact, we show here that GTP binding/hydrolysis does depend on the oligomeric state of IM30 but does not crucially involve helix 1. As *Syn*IM30 H2-7 still had considerably high GTP hydrolyzing activity and as we assume a conserved function of the helices in IM30 proteins of different organisms, we rule out the possibility that any amino acid in helix 1 is crucial for GTP binding or hydrolysis. However, the *Ara*IM30 oligomer appears to be less stable than the proteins of *Synechocystis* or *Chlamydomonas reinhardtii*, as in the latter cases helix 1-truncated versions reportedly still form high molecular mass complexes[5,25,46]. Thus, we assumed that oligomer formation, rather than helix 1, is crucial for GTP hydrolysis by IM30 proteins, and we indeed confirmed this assumption by using a *Syn*IM30 full-length mutant protein that forms tetramers but no high molecular mass complexes anymore (Fig. 3b). As this mutant did not hydrolyze GTP anymore, a tetrameric IM30 structure likely is insufficient for GTP hydrolysis and higher oligomeric structures are required, most likely prototypical IM30 rings[7]. As the analyzed *Syn*IM30 mutant forms tetramers, which are considered to be the basic building blocks of IM30 rings[7,37], the putative GTP binding sites are potentially localized within the ring in between adjacent tetrameric building blocks.

GTP binding and hydrolysis do not critically affect IM30-mediated membrane remodeling

While we could clearly establish that *Syn*IM30 high molecular mass oligomers do hydrolyze GTP (also in absence of Mg^{2+}), the important question arose whether this cryptic GTPase activity has any impact on the physiological function of the protein. Unfortunately, the exact function of IM30 is still not finally resolved. Yet, *in vitro* analyses clearly show that the protein binds to negatively charged membrane surfaces and is able to mediate membrane fusion[16,23,24,37,46]. In fact, in many cases a membrane remodeling activity of NTPases is nucleotide-dependent and typically requires nucleotide hydrolysis (reviewed in[53]). Nevertheless, membrane interaction and membrane remodeling by IM30 clearly do not require nucleotide binding and/or hydrolysis, as NTPs were never present in any assay reported thus far[4,16,17,23,24,37,46]. As a stimulating effect of a lipid surface on a protein's GTPase activity has been shown for many other proteins, such as dynamin-like proteins[49], it was well possible that GTP binding and/or hydrolysis modulate the membrane interaction and/or the fusion activity of *Syn*IM30. However, our results suggest that the presence of GTP or GDP does not affect membrane binding of *Syn*IM30, at least in absence of Mg^{2+} (Fig. 4a,b), and also the GTPase activity of *Syn*IM30 is not significantly enhanced in presence of DOPG liposomes (Fig. 1f). However, a minor effect on GTPase activity might have been unnoticed due to the rather low affinity of IM30 to lipid membranes[37], leaving a considerable fraction of the protein unaffected upon presence of the membranes.

Analysis of the fusion events was challenging, as direct binding of Mg^{2+} is necessary for IM30 activation[23,47] as well as for membrane destabilization, when Mg^{2+} is interacting with negatively charged liposomes[54,59]. Thus, while the exact same concentration of "free" Mg^{2+} is necessary for comparing the fusion data, the amount of free Mg^{2+} is clearly altered in the presence of GTP or GDP due to the nucleotide- Mg^{2+} interaction[48].We minimized this effect via experimentally adjusting the concentration of Mg^{2+} specifically when GTP or GDP was present (as described in the "Experimental Procedures" section). Nevertheless, we cannot rule out that the observed differences of the fusion kinetics (Fig. 5) were biased by our approach to experimentally determine the required Mg^{2+} concentrations in presence of GTP or GDP to gain similar fusion curves in absence of IM30 (Suppl. Fig. 4). Thus, the results of the membrane fusion assay have to be treated with caution. Yet, the kinetics of IM30-mediated membrane fusion were somewhat altered in the presence of GDP or GTP. While GTP enhanced the fusion rate, the membrane fusion rate was somewhat decreased in the presence of GDP (Fig. 5).

However, any influence of potential direct interaction of the nucleotides with the lipid bilayer, as possibly observed in the present study (Fig. 4a and b), is not considered in our analysis. In fact, in presence of Mg^{2+}, GTP or GDP could well interact with the negatively charged DOPG head group, as Mg^{2+} can "bridge" the phosphate groups of the nucleotides and the PG head group. This has *e.g.* been discussed for binding of DNA to anionic and zwitterionic membrane surfaces[60,61]. Consequently, nucleotides binding to the membrane surface might directly affect fusion-related membrane properties, which eventually alters fusion kinetics. Furthermore, membrane fusion is affected by multiple, complex equilibria involving IM30, Mg^{2+}, liposomes and the nucleotides that are furthermore constantly changing during membrane fusion and GTP hydrolysis. The small changes in the fusion rate observed here are consequently no decisive hint for any influence on the membrane fusion. Importantly, major impacts on the IM30 (*in vitro*) fusion activity can be detected via the fusion assay, as e.g. observed analyzing IM30 mutants[7].

We conclude that GTP binding and/or hydrolysis are no key regulators of IM30 membrane binding or membrane fusion. If at all, GTP binding/hydrolysis only slightly modulates the kinetics of the membrane fusion process. Hence, membrane remodeling by *Syn*IM30 is vastly nucleotide-independent, despite the cryptic GTP hydrolyzing activity.

IM30 is an atypical GTPase

Besides apparently hydrolyzing GTP, at least *in vitro*, *Syn*IM30 does not exhibit features expected for a canonical GTPase, involving (i) a G-domain and (ii) Mg^{2+} dependent substrate binding.

Although the G-domain or the P-loop motif, respectively, are fingerprints of GTPases, a few examples of G-proteins lacking the P-loop motif are described[62]. The most extensively studied members of such untypical GTPases are Tubulin and FtsZ, which have a highly conserved nucleotide binding site that clearly differs from typical GTPases[63]. While IM30 proteins do not contain any sequences involved in nucleotide binding to any thus far studied protein, we cannot *per se* exclude that GTP binds to a new, currently not described GTP-binding pocket to IM30 proteins. Furthermore, as our results suggest that GTP hydrolysis requires oligomeric structures larger than tetramers, it is well possible that amino acids of different IM30 monomers together form the GTPase site, which would not be easily predictable and could only be visualized in a high-resolution structure of oligomeric IM30. Unfortunately, neither a high-resolution structure of an oligomer nor of the monomer is available for IM30 yet. Thus, structural comparisons are limited to homology modeling based on the structure of the PspA coiled-coil fragment that was solved recently[64]. However, no NTP-binding site was identified in such a model[7].

Furthermore, as outlined above, typically nucleotide binding and hydrolysis depend on Mg^{2+} and in cases where nucleotides are hydrolyzed even in the absence of Mg^{2+}, the hydrolysis rates increased in the presence of Mg^{2+}. In contrast, here we show that the cooperativity of the apparent IM30 GTPase activity is increased when Mg^{2+} is absent, which could well be ascribed to an allosteric action of Mg^{2+} (see Suppl. Fig. 3). Binding of Mg^{2+} to IM30 has been demonstrated recently, and Mg^{2+} binding clearly induces structural rearrangements of oligomeric IM30[47], in line with the allosteric function of Mg^{2+}. These structural rearrangements appear to affect the GTP hydrolysis activity of oligomeric *Syn*IM30, as discussed above. The GTP hydrolyzing activity of *Syn*IM30 was altered in the presence of GMP-PCP, a non-hydrolyzable GTP analog, typically used as a competitive inhibitor. This lead to a further increase in cooperativity, due to an increased population of a low-affinity state.

Taken together, IM30 exhibits many characteristics that clearly separates it from canonical GTPases, such as the missing G-domain and Mg^{2+}-independent GTP hydrolysis. Thus, IM30 might found a new class of GTPases[39]. Yet, GTP binding and hydrolysis clearly have no major effect on the membrane remodeling activity of IM30, at least *in vitro*, and it remains to be shown whether GTP hydrolysis by IM30 proteins is relevant *in vivo*.

EXPERIMENTAL PROCEDURES

Cloning, expression and purification of IM30

Construction of the plasmid used for expression of N-terminally His-tagged *Synechocystis* IM30 (pRSET IM30 WT) was described recently[13]. The plasmid used for expression of helix 1 truncated *Syn*IM30 is described in[46]. The plasmid used for expression of the IM30 FERM_EE mutant was created

via introducing six mutations (E83A, E84A, F168A, E169A, R170A, M171A) into IM30 WT using the Quick-Change method[65,66].

All proteins were expressed in *E. coli* BL21 (DE3) at 37 °C for 3–4 h after induction via the addition of 0.5 mM Isopropyl-β-D-thiogalactopyranoside (IPTG).

Cells were resuspended in lysis buffer (50 mM HEPES pH 7.6, 300 mM NaCl, 20 mM imidazole), lysed via sonification (4 °C) and cell debris was removed by centrifugation (8200 g, 10 min, 4 °C). His-tagged IM30 was isolated via Ni^{2+}-affinity-chromatography (Ni-NTA agarose matrix, 3 wash steps with 20, 50 and 100 mM imidazole, elution with 1000 mM imidazole). After isolation of the protein, the buffer was exchanged to 20 mM HEPES pH 7.6 by gel filtration (Sephadex G25). Where necessary, the protein solution was concentrated using a Centriprep filter unit (MWCO 10 kDa, regenerated cellulose membrane, 3000 g, 30 min, 4 °C). The protein concentration was estimated using a Bradford assay with a BSA standard curve. For storage, the protein solution was mixed 1:1 (v/v) with glycerol and stored at −20 °C. The purification was completed within 8 hours (time from cell lysis to storage at −20 °C).

Malachite green assay

*Syn*IM30 (0.1 µM) was mixed with 0.5 mM (if not stated otherwise) of GTP and Mg^{2+} (2.5 mM if not stated otherwise) in 20 mM HEPES and incubated for 30 min at 37 °C. 200 µL of this sample was transferred to a 96-well plate and mixed with 50 µL of the malachite green reaction mixture ("Gold mix", PiColorLock Gold Phosphate Detection Kit by Innova Biosciences) and incubated for 5 min at RT. Finally, 20 µL of "stabilizer" (PiColorLock Gold Phosphate Detection Kit by Innova Biosciences) was added. Absorbance at 635 nm was measured with an OMEGA FLUOstar Platereader (BMG Labtech). Buffer blank (including the respective GTP concentration) absorbance was subtracted, and the concentration of released phosphate was determined by linear regression from a phosphate standard curve.

The phosphate release value was used to calculate the average NTPase activity A_{NTPase} [min^{-1}] per mol protein:

$$A_{NTPase} = \frac{\Delta[P_i]}{\Delta t} \quad (1)$$

$[P_i]$ refers to the concentration of released phosphate and t to the incubation time of the hydrolysis reaction.

The Michaelis-Menten constant K_M was determined by using a Hill equation-derived fitting model and the resulting V_{max} was used to determine k_{cat}:

$$A_{NTPase} = \frac{V_{max} * [S]^n}{{K_M}^n + [S]^n}$$
$$k_{cat} = \frac{V_{max}}{[IM30]} \quad (2)$$

[S] denotes for the substrate concentration and *n* for the Hill coefficient.

For a more detailed analysis of the dependence of GTPase activity on GTP, Mg^{2+} and GMP-PCP, a two-state model was fitted to the data. This is described in more detail in the supplement.

Continuous phosphate release assay

*Syn*IM30 was mixed with a phosphate sensor (recombinant *E. coli* phosphate-binding protein labeled with the fluorophore MDCC; Sigma Aldrich) [40] and Mg^{2+} in a 96-well plate. The mixture was preincubated at 37 °C and prewarmed GTP was added directly via an automatic titrator prior to the measurement (OMEGA FLUOstar Platereader (BMG Labtech)). The final concentration in the wells were 0.1 µM protein, 2.5 mM Mg^{2+} and 10 µM GTP. Fluorescence of the samples was measured at 37 °C with a 420/10 nm excitation filter and a 460/10 nm emission filter over the indicated timescale.

From the change in the fluorescence signal over time (after subtraction of the fluorescence signal generated by GTP auto-hydrolysis in the buffer), the concentration of released phosphate was determined via linear regression using a phosphate standard curve. The initial, non-biased turnover rate v_0 [min^{-1}] was determined by a monoexponential fit for non-linear, steady-state enzyme kinetics, assuming a first-order process [41]:

$$[P_i](t) = \frac{v_0}{\eta} * (1 - e^{-\eta * t}) \quad (3)$$

[P_i] is the measured concentration of released phosphate and η accounts for a term describing the bias on v_0 that causes non-linearity, *e.g.* reduced velocity due to substrate limitation or product inhibition [41]. v_0 was used to determine the k_{cat}:

$$k_{cat} = \frac{v_0}{[IM30]} \quad (4)$$

PK/LDH-coupled GTPase assay

The reaction buffer containing 5 mM $MgCl_2$, 150 mM NaCl, 7.5 mM KCl, 0.6 mM NADH, 1 mM PEP (phosphoenolpyruvate), PK(final concentration 12 – 20 units/mL)/LDH(final concentration 18 – 28 units/mL) mix (Pyruvate Kinase /Lactic Dehydrogenase mix from Sigma-Aldrich) (and 0-5 mM GTP in 20 mM HEPES pH 7.6 was preincubated at room temperature for 15 min to convert already present GDP to GTP. *Syn*IM30 WT or *Syn*DLP was mixed with the reaction buffer to a final concentration of 0.5 µM. The GTP to GDP turnover rate was determined indirectly via the decrease of NADH absorbance at 340 nm [43] on a timescale of 1 – 2 h at 37 °C with an OMEGA FLUOstar Platereader (BMG Labtech). The decline in NADH concentration is proportional to the concentration of GDP produced. The slope of the measured NADH absorbance was determined via fitting with a linear function. The GTPase activity A_{NTPase} [min^{-1}] was calculated as follows:

$$A_{NTPase} = -\frac{\Delta A_{340}}{\Delta t} * l^{-1} * {\varepsilon_{NADH}}^{-1} \quad (5)$$

With $\frac{\Delta A_{340}}{\Delta t}$ being the linear slope of the absorbance at 340 nm, l the filling height of the well and ε_{NADH} the extinction coefficient of NADH (ε = 6220 M^{-1} cm^{-1}). Data were corrected for autohydrolysis and the 0 mM GTP value was subtracted from all values to account for protein caused perturbations.

The maximum GTP turnover rate V_{max} was determined via equation 2. The GTP turnover rate was used to determine k_{cat}.

Luciferase-coupled GTPase assay

To analyze the GTPase activity of IM30 by directly measuring changes in the GTP concentration, we used a luciferase-coupled GTPase assay (GTPase-Glo Assay Kit by Promega). The assay was performed according to the instructions of the manufacturer. In short, 4 µM GTP and IM30 (0-6.5 µM IM30) were incubated for 120 min at 37 °C. After the reaction, the remaining GTP was converted to ATP by addition of GTPase-Glo Reagent (including ADP and a luciferase) and further incubation for 30 min at 37 °C. After 10 min incubation with the detection reagent at 37 °C, the luminescence was measured in a 384 wellplate using an OMEGA FLUOstar Platereader (BMG Labtech). GTP concentrations were calculated from the luminescence intensities using GTP standards that were treated as the samples.

Size exclusion chromatography (SEC)

Proteins were analyzed on an ÄKTA basic system (GE Healthcare) with a Superose12 10/300 GL column (GE Healthcare) equilibrated with 20 mM HEPES pH 7.6 at 8 °C. Protein elution was monitored via absorbance at 280 nm. The column was calibrated against standards of known size (blue dextran >2000 kDa, β-amylase (200 kDa), alcohol dehydrogenase (150 kDa), albumin (66 kDa), ribonuclease A (13.7 kDa).

Thermal denaturation

Thermal stability of IM30 (3.2 µM) was determined via CD spectroscopy (JASCO-815 CD spectrometer with an MPTC-490S temperature-controlled cell holder) in presence and absence of 0.5 mM GTP and/or 2.5 mM Mg^{2+}. CD spectra were collected from 250 to 200 nm (cell length 0.1 cm, 1 nm data pitch, 5 nm bandwidth, 200 nm/min, 1 s data integration time, averaged over 3 accumulations of the same sample) over a temperature ramp from 15 to 95 °C (2 °C steps, overall heating rate 0.27 °C/min). Spectra were smoothened with a Savitzky-Golay filter. The ellipticity at 222 nm was used as a measure for the folding state of the protein. To estimate the transition temperature T_m of the protein, an indicator for the thermal stability, the resulting melting curve was fitted with an adapted Boltzmann-Fit, which allows linear slopes in the plateau regions of the curve, assuming a simple two-state unfolding mechanism:

$$\theta_{meas}(T) = \frac{(T * m_N + \theta_N) - (T * m_D + \theta_D)}{1 + e^{\frac{T - T_m}{dT}}} + (T * m_D + \theta_D) \quad (6)$$

θ_{meas} refers to the measured ellipticity. T is the temperature, θ_N and θ_D are the ellipticities at the plateaus of native and denatured protein, m_N and m_D are the slopes of the respective plateaus.

Liposome preparation

The lipids DOPG (1,2-dioleoyl-*sn*-glycero-3-phosphoglycerol), MGDG (monogalactosyldiacylglycerol) and the fluorescently labeled lipids NBD-PE (1,2-distearoyl-*sn*-glycero-3-phosphoethanolamine-N-(7-nitro-2-1,3-benzoxadiazol-4-yl) and LissRhod-PE (Lissamine Rhodamine PE; 1,2-Dioleoyl-*sn*-glycero-3-phosphoethanolamine-N-(lissamine rhodamine B sulfonyl) (ammonium salt)) were purchased from Avanti Polar Lipids, Inc. (Birmingham, AL, USA). For liposome preparation, lipids

were dissolved in chloroform/methanol (2:1, v/v). The organic solvent was evaporated under a gentle stream of nitrogen gas followed by overnight vacuum desiccation to remove any traces of solvent. Unilamellar liposomes were prepared by hydration of the dried lipid film with 20 mM HEPES buffer (pH 7.6) and five cycles of freeze-thawing. For the liposome fusion assay, the liposomes were subsequently extruded 15 times through a 100-nm filter, using an extruder from Avanti Polar Lipids, Inc. (Alabaster, AL, USA).

Laurdan fluorescence measurements

Laurdan (6-dodecanoyl-*N*,*N*-dimethyl-2-naphthylamine) is a fluorescent dye that incorporates into lipid bilayers. Its fluorescence is sensitive to changes in the polarity of the environment and is therefore used to report changes of the membrane fluidity. In order to quantify the spectral changes, the Generalized Polarization (GP) value defined by [67] is calculated for each spectrum.

$$GP = \frac{I_{440} - I_{490}}{I_{440} + I_{490}} \quad (7)$$

Here, I_{440} and I_{490} are the fluorescence emission intensities at 440 and 490 nm, respectively.

Laurdan (Sigma, Taufkirchen, Germany) was added to the dissolved lipid DOPG in a molar ratio of 1:500. Unilamellar liposomes were prepared as described before. To analyze the effect of nucleotides on the binding of IM30 to DOPG, 1µM IM30 WT, 0.1 mM liposomes and 2.5 mM GTP (or GDP) were mixed and incubated for 2 h at 25 °C. As the protein was stored in 50% glycerol, the final concentration of glycerol was 15%. For samples without IM30, the corresponding amount of 50% glycerol (20 mM HEPES, pH 7.6) was added.

The fluorescence emission spectra were recorded on a FluoroMax-4 spectrometer (Horiba Scientific, Kyoto, Japan) from 400 to 550 nm with excitation at 350 nm at 25 °C. The slit width was set at 4 nm for excitation and emission of Laurdan.

Liposome fusion assay

The influence of nucleotides on IM30-triggered liposome fusion was measured using a FRET-based assay, as described earlier [23,68]. Unlabeled liposomes were mixed in 10-fold excess with labeled liposomes containing two fluorescent dyes that form a FRET-pair. Upon fusion of labeled with unlabeled liposomes, the FRET dyes redistribute over the membrane and consequently FRET

decreases, resulting in increasing donor emission intensity. To simulate complete membrane fusion, liposomes containing only a 10th of the fluorescently labeled lipids were used as a positive control.

For the fusion assay, 1µM IM30 WT and 0.1 mM liposomes (MGDG/DOPG, 40:60, w/w) were used. As described for the Laurdan measurements, the final concentration of glycerol was 15% for all samples. The concentration of $MgCl_2$ was 6 mM for samples without nucleotides.

The measurements were performed using a Fluoromax-4 spectrometer (Horiba Scientific, Kyoto, Japan). The IM30-containing solutions were preincubated with Mg^{2+} for 15 min, whereas the liposomes were premixed with the nucleotides for about 1 min. After fast mixing of all compounds, the measurement was started immediately. Upon excitation of the FRET-donor NBD-PE at 460 nm, the donor emission was monitored at 525 nm over 1000 s at 25 °C. The slit widths for excitation and emission were set at 5 nm.

The raw fluorescence data was converted to a fusion rate in percentage by equation 9 using the intensities of the negative control (I_{NC}), positive control (I_{PC}) and the measured sample (I) at every point in time t.

$$Fusion\ (t) = \frac{I_t - I_{t,NC}}{I_{t,PC} - I_{t,NC}} \cdot 100\ \% \qquad (8)$$

The initial fusion rate was determined by the first derivative of the fusion curve after 50 s.

Since GTP and GDP bind Mg^{2+} via their phosphate groups, higher concentrations of $MgCl_2$ had to be used to obtain the same amount of free Mg^{2+} in samples containing GTP or GDP as in the control. To determine the additionally needed amount of Mg^{2+}, we made use of the fact that Mg^{2+} alone can induce fusion at a concentration of 10 mM. Increasing amounts of $MgCl_2$ were added to the assay containing 10 mM Mg^{2+} in presence of 2.5 mM GTP or GDP, until the observed fusion rates matched the one obtained in absence of the nucleotides. In the case of GTP, 4.25 mM $MgCl_2$ was additionally needed, in the presence of GDP 2.5 mM $MgCl_2$ (Suppl. Fig. 2).

REFERENCES

1 Vothknecht, U. C., Otters, S., Hennig, R. & Schneider, D. Vipp1: A very important protein in plastids?! *Journal of Experimental Botany* 63, 1699–1712 (2012).

2 Li, H. M., Kaneko, Y. & Keegstra, K. Molecular cloning of a chloroplastic protein associated with both the envelope and thylakoid membranes. *Plant Mol. Biol.* 25, 619–632 (1994).

3 Fuhrmann, E. *et al.* The vesicle-inducing protein 1 from Synechocystis sp. PCC 6803 organizes

into diverse higher-ordered ring structures. *Mol. Biol. Cell* 20, 4620–4628 (2009).

4 Otters, S. *et al*. The first α-helical domain of the vesicle-inducing protein in plastids 1 promotes oligomerization and lipid binding. *Planta* 237, 529–540 (2013).

5 Gao, F., Wang, W., Zhang, W. & Liu, C. α-Helical Domains Affecting the Oligomerization of Vipp1 and Its Interaction with Hsp70/ DnaK in Chlamydomonas. *Biochemistry* 54, 4877–4889 (2015).

6 Aseeva, E. *et al*. Complex formation of Vipp1 depends on its α-helical PspA-like domain. *J. Biol. Chem.* 279, 35535–35541 (2004).

7 Saur, M. *et al*. A Janus-Faced IM30 Ring Involved in Thylakoid Membrane Fusion Is Assembled from IM30 Tetramers. *Structure* 25(1380–1390), e5 (2017).

8 Gutu, A., Chang, F. & O'Shea, E. K. Dynamical localization of a thylakoid membrane binding protein is required for acquisition of photosynthetic competency. *Mol. Microbiol.* 108, 16–31 (2018).

9 Bryan, S. J. *et al*. Localisation and interactions of the Vipp1 protein in cyanobacteria. *Mol. Microbiol.* 94, 1179–1195 (2014).

10 Zhang, L., Kato, Y., Otters, S., Vothknecht, U. C. & Sakamoto, W. Essential role of VIPP1 in chloroplast envelope maintenance in Arabidopsis. *Plant Cell* 24, 3695–3707 (2012).

11 Kroll, D. *et al*. VIPP1, a nuclear gene of Arabidopsis thaliana essential for thylakoid membrane formation. *Proc. Natl. Acad. Sci. U. S. A.* 98, 4238–4242 (2001).

12 Westphal, S., Heins, L., Soll, J. & Vothknecht, U. C. Vipp1 deletion mutant of synechocystis: A connection between bacterial phage shock and thylakoid biogenesis? *Proc. Natl. Acad. Sci. U. S. A.* 98, 4243–4248 (2001).

13 Fuhrmann, E., Gathmann, S., Rupprecht, E., Golecki, J. & Schneider, D. Thylakoid membrane reduction affects the photosystem stoichiometry in the cyanobacterium Synechocystis sp. PCC 6803. *Plant Physiol.* 149, 735–744 (2009).

14 Lo, S. M. & Theg, S. M. Role of vesicle-inducing protein in plastids 1 in cpTat transport at the thylakoid. *Plant J* 71, 656–668 (2012).

15 Zhang, L. & Sakamoto, W. Possible function of VIPP1 in thylakoids: Protection but not formation? *Plant Signal. Behav*. 8 (2013).

16 McDonald, C., Jovanovic, G., Ces, O. & Buck, M. Membrane stored curvature elastic stress modulates recruitment of maintenance proteins pspa and vipp1. *MBio* 6 (2015).

17 McDonald, C., Jovanovic, G., Wallace, B. A., Ces, O. & Buck, M. Structure and function of PspA and Vipp1 N-terminal peptides: Insights into the membrane stress sensing and mitigation. *Biochim. Biophys. Acta Biomembr* 1859, 28–39 (2017).

18 Thurotte, A., Brüser, T., Mascher, T. & Schneider, D. Membrane chaperoning by members of the PspA/IM30 protein family. *Commun. Integr. Biol* 10, e1264546 (2017).

19 Benning, C., Xu, C. & Awai, K. Non-vesicular and vesicular lipid trafficking involving plastids. *Current Opinion in Plant Biology* 9, 241–247 (2006).

20 Benning, C. A role for lipid trafficking in chloroplast biogenesis. *Progress in Lipid Research* 47, 381–389 (2008).

21 Nordhues, A. *et al*. Evidence for a role of VIPP1 in the structural organization of the photosynthetic apparatus in Chlamydomonas. *Plant Cell* 24, 637–659 (2012).

22 Zhang, S., Shen, G., Li, Z., Golbeck, J. H. & Bryant, D. A. Vipp1 is essential for the biogenesis of Photosystem I but not thylakoid membranes in Synechococcus sp. PCC 7002. *J. Biol. Chem.* 289, 15904–15914 (2014).

23 Hennig, R. *et al*. IM30 triggers membrane fusion in cyanobacteria and chloroplasts. *Nat. Commun.* 6 (2015).

24 Hennig, R. *et al*. The IM30/Vipp1 C-terminus associates with the lipid bilayer and modulates membrane fusion. *Biochim. Biophys. Acta Bioenerg* 1858, 126–136 (2017).

25 Siebenaller, C., Junglas, B. & Schneider, D. Functional Implications of Multiple IM30 Oligomeric States. *Front. Plant Sci.* 10 (2019).

26 Junglas, B. & Schneider, D. What is Vipp1 good for? *Molecular Microbiology* 108, 1–5 (2018).

27 Heidrich, J., Thurotte, A. & Schneider, D. Specific interaction of IM30/Vipp1 with cyanobacterial and chloroplast membranes results in membrane remodeling and eventually in membrane fusion. *Biochimica et Biophysica Acta Biomembranes* 1859, 537–549 (2017).

28 Westphal, S., Soll, J. & Vothknecht, U. C. A vesicle transport system inside chloroplasts. *FEBS Lett* 506, 257–261 (2001).

29 Morré, D. J., Selldén, G., Sundqvist, C. & Sandelius, A. S. Stromal low temperature compartment derived from the inner membrane of the chloroplast envelope. *Plant Physiol.* 97, 1558–1564 (1991).

30 Lindquist, E. & Aronsson, H. Chloroplast vesicle transport. *Photosynth. Res.* 138, 361–371 (2018).

31 Khan, N. Z., Lindquist, E. & Aronsson, H. New Putative Chloroplast Vesicle Transport Components and Cargo Proteins Revealed Using a Bioinformatics Approach: An Arabidopsis Model. *PLoS One* 8, e59898 (2013).

32 Kirchhoff, H. *et al*. Dynamic control of protein diffusion within the granal thylakoid lumen. *Proc. Natl. Acad. Sci. U. S. A.* 108, 20248–53 (2011).

33 Chuartzman, S. G. *et al*. Thylakoid membrane remodeling during state transitions in Arabidopsis. *Plant Cell* 20, 1029–39 (2008).

34 Stingaciu, L. R. *et al*. Revealing the Dynamics of Thylakoid Membranes in Living Cyanobacterial Cells. *Sci. Rep.* 6 (2016).

35 Nagy, G. *et al*. Reversible membrane reorganizations during photosynthesis *in vivo*: Revealed by

small-angle neutron scattering. *Biochem. J.* 436, 225–230 (2011).

36 Jilly, R., Khan, N. Z., Aronsson, H. & Schneider, D. Dynamin-like proteins are potentially involved in membrane dynamics within chloroplasts and cyanobacteria. *Front. Plant Sci.* 9, 206 (2018).

37 Heidrich, J. *et al*. Organization into higher ordered ring structures counteracts membrane binding of IM30, a protein associated with inner membranes in chloroplasts and cyanobacteria. *J. Biol. Chem.* 291, 14954–14962 (2016).

38 Zhang, L., Kondo, H., Kamikubo, H., Kataoka, M. & Sakamoto, W. VIPP1 has a disordered C-terminal tail necessary for protecting photosynthetic membranes against stress. *Plant Physiol.* 171, 1983–1995 (2016).

39 Ohnishi, N., Zhang, L. & Sakamoto, W. VIPP1 Involved in Chloroplast Membrane Integrity Has GTPase Activity *in Vitro*. *Plant Physiol.* 177, 328–338 (2018).

40 Brune, M., Hunter, J. L., Corrie, J. E. T. & Webb, M. R. Direct, Real-Time Measurement of Rapid Inorganic Phosphate Release Using a Novel Fluorescent Probe and Its Application to Actomyosin Subfragment 1 ATPase. *Biochemistry* 33, 8262–8271 (1994).

41 Cao, W. & De La Cruz, E. M. Quantitative full time course analysis of nonlinear enzyme cycling kinetics. *Sci. Rep* 3, 2658 (2013).

42 Zhang, Y.-Z. *et al*. Interaction of malachite green with bovine serum albumin: Determination of the binding mechanism and binding site by spectroscopic methods. *J. Hazard. Mater.* 163, 1345–1352 (2009).

43 Ingerman, E. & Nunnari, J. A continuous, regenerative coupled GTPase assay for dynamin-related proteins. in *Methods in Enzymology* 404, 611–619 (Academic Press Inc., 2005).

44 Song, B. D., Leonard, M. & Schmid, S. L. Dynamin GTPase domain mutants that differentially affect GTP binding, GTP hydrolysis, and clathrin-mediated endocytosis. *J. Biol. Chem.* 279, 40431–40436 (2004).

45 Reubold, T. F. *et al*. Crystal structure of the dynamin tetramer. *Nature* 525, 404–408 (2015).

46 Thurotte, A. & Schneider, D. The fusion activity of IM30 rings involves controlled unmasking of the fusogenic core. *Front. Plant Sci.* 10, 108 (2019).

47 Heidrich, J. *et al*. Mg2 binding triggers rearrangement of the IM30 ring structure, resulting in augmented exposure of hydrophobic surfaces competent for membrane binding. *J. Biol. Chem.* 293, 8230–8241 (2018).

48 Rudack, T., Xia, F., Schlitter, J., Kötting, C. & Gerwert, K. The role of magnesium for geometry and charge in GTP hydrolysis, revealed by quantum mechanics/Molecular mechanics simulations. *Biophys. J.* 103, 293–302 (2012).

49 Song, B. D., Leonard, M. & Schmid, S. L. Dynamin GTPase domain mutants that differentially affect

GTP binding, GTP hydrolysis, and clathrin-mediated endocytosis. *J. Biol. Chem.* 279, 40431–40436 (2004).

50 Shan, S. O., Schmid, S. L. & Zhang, X. Signal recognition particle (SRP) and SRP receptor: A new paradigm for multistate regulatory GTPases. *Biochemistry* 48, 6696–6704 (2009).

51 De Boer, P., Crossley, R. & Rothfield, L. The essential bacterial cell-division protein FtsZ is a GTPase. *Nature* 359, 254–256 (1992).

52 Zhang, B., Zhang, Y., Wang, Z. X. & Zheng, Y. The role of Mg^{2+} cofactor in the guanine nucleotide exchange and GTP hydrolysis reactions of Rho family GTP-binding proteins. *J. Biol. Chem.* 275, 25299–25307 (2000).

53 McNew, J. A., Sondermann, H., Lee, T., Stern, M. & Brandizzi, F. GTP-Dependent Membrane Fusion. *Annu. Rev. Cell Dev. Biol.* 29, 529–550 (2013).

54 Newton, C., Pangborn, W., Nir, S. & Papahadjopoulos, D. Specificity of Ca^{2+} and Mg^{2+} binding to phosphatidylserine vesicles and resultant phase changes of bilayer membrane structure. *BBA Biomembr.* 506, 281–287 (1978).

55 Nir, S., Newton, C. & Papahadjopoulos, D. 201 Binding of Cations to Phosphatidylserine Vesicles. *Bioelectrochemistry Bioenerg* 5, 116–133 (1978).

56 Düzgüne, N. *et al.* Calciumand magnesium-induced fusion of mixed phosphatidylserine/phosphatidylcholine vesicles: Effect of ion binding. *J. Membr. Biol.* 59, 115–125 (1981).

57 Wilschut, J., Düzgüne, N. & Papahadjopoulos, D. Calcium/Magnesium Specificity in Membrane Fusion: Kinetics of Aggregation and Fusion of Phosphatidylserine Vesicles and the Role of Bilayer Curvature. *Biochemistry* 20, 3126–3133 (1981).

58 Ohki, S. A mechanism of divalent ion-induced phosphatidylserine membrane fusion. *BBA Biomembr* 689, 1–11 (1982).

59 Mondal Roy, S. & Sarkar, M. Membrane Fusion Induced by Small Molecules and Ions. *J. Lipids* 2011, 1–14 (2011).

60 Liang, H., Harries, D. & Wong, G. C. L. Polymorphism of DNA-anionic liposome complexes reveals hierarchy of ion-mediated interactions. *Proc. Natl. Acad. Sci. U. S. A.* 102, 11173–11178 (2005).

61 Antipina, A. Y. & Gurtovenko, A. A. Molecular-level insight into the interactions of DNA with phospholipid bilayers: Barriers and triggers. *RSC Adv* 6, 36425–36432 (2016).

62 Wittinghofer, A. & Vetter, I. R. Structure-Function Relationships of the G Domain, a Canonical Switch Motif. *Annu. Rev. Biochem.* 80, 943–971 (2011).

63 Nogales, E., Downing, K. H., Amos, L. A. & Löwe, J. Tubulin and FtsZ form a distinct family of GTPases. *Nat. Struct. Biol* 5, 451–8 (1998).

64 Osadnik, H. *et al*. PspF-binding domain PspA1-144 and the PspA·F complex: New insights into the coiled-coil-dependent regulation of AAA+ proteins. *Mol. Microbiol.* 98, 743–759 (2015).

65 Shenoy, A. R. & Visweswariah, S. S. Site-directed mutagenesis using a single mutagenic oligonucleotide and DpnI digestion of template DNA. *Anal. Biochem.* 319, 335–6 (2003).

66 Xia, Y., Chu, W., Qi, Q. & Xun, L. New insights into the QuikChangeTM process guide the use of Phusion DNA polymerase for site-directed mutagenesis. *Nucleic Acids Res* 43, e12 (2015).

67 Parasassi, T., Krasnowska, E. K., Bagatolli, L. & Gratton, E. Laurdan and Prodan as Polarity-Sensitive Fluorescent Membrane Probes. *J. Fluoresc* 8, 365–373 (1998).

68 Meers, P., Ali, S., Erukulla, R. & Janoff, A. S. Novel inner monolayer fusion assays reveal differential monolayer mixing associated with cation-dependent membrane fusion. *Biochim. Biophys. Acta Biomembr* 1467, 227–243 (2000).

ACKNOWLEDGEMENTS

This work was funded by the Max-Planck Graduate Center at the Max Planck Institutes and the University of Mainz. We thank Dr. Ruven Jilly for preparing a sample of *Syn*DLP and assisting with the PK/LDH-coupled GTPase assay. We thank Renate Genswein for help with the protein purification and for excellent technical support.

AUTHOR CONTRIBUTIONS

D.S., B.J., C.S. and N.H. designed the experiments and analyzed data. B.J., C.S. and L.S. performed the experiments. D.S., B.J., C.S. and N.H. wrote the paper.

COMPETING INTERESTS

The authors declare no competing interests.

ADDITIONAL INFORMATION

Supplementary information is available for this paper at https://doi.org/10.1038/s41598-020-66818-9. Correspondence and requests for materials should be addressed to D.S.

VIII.3. Binding and/or hydrolysis of purine-based nucleotides is not required for IM30 ring formation

Carmen Siebenaller, Lukas Schlösser, Benedikt Junglas, Martina Schmidt-Dengler, Dominik Jacob, Nadja Hellmann, Carsten Sachse, Mark Helm, Dirk Schneider

1 Department of Chemistry, Biochemistry, Johannes Gutenberg University Mainz, Germany
2 Ernst-Ruska Centre for Microscopy and Spectroscopy with Electrons (ER-C-3/Structural Biology), Forschungszentrum Jülich, Germany
3 JuStruct: Jülich Center for Structural Biology, Forschungszentrum Jülich, Germany
4 Institute for Pharmaceutical and Biomedical Sciences, Johannes Gutenberg University Mainz, Germany
5 Institute of Molecular Physiology, Johannes Gutenberg University Mainz, Germany

*__Correspondence__: D. Schneider, Department of Chemistry, Johannes Gutenberg University Mainz, Hanns-Dieter-Hüsch-Weg 17, 55128 Mainz, Germany, Tel: (+49) 6131 39 25833, E-mail: Dirk.Schneider@uni-mainz.de

Received: 17 December 2020; **revised:** 30 April 2021; **accepted**: 20 May 2021; **available online:** 21 June 2021

Reviewed by: Peter Brzezinsky

ABSTRACT

IM30, the inner membrane-associated protein of 30 kDa, is conserved incyanobacteria and chloroplasts. Although its exact physiological function isstill mysterious, IM30 is clearly essential for thylakoid membrane biogenesisand/or dynamics. Recently, a cryptic IM30 GTPase activity has beenreported, albeit thus far no physiological function has been attributed to this.Yet, it is still possible that GTP binding/hydrolysis affects formation of theprototypical large homo-oligomeric IM30 ring and rod structures. Here, weshow that the Synechocystis sp. PCC 6803 IM30 protein in fact is annTPase that hydrolyzes GTP and ATP, but not CTP or UTP, with aboutidentical rates. While IM30 forms large oligomeric ring complexes, nucleo-tide binding and/or hydrolysis are clearly not required for ring formation.

Keywords: cyanobacteria; IM30; PspA; Synechocystis; thylakoid membrane;Vipp1

INTRODUCTION

The inner membrane-associated protein of 30 kDa (IM30), also known as the vesicle-inducing protein in plastids 1 (Vipp1), is a member of the PspA/IM30 protein family. The protein is conserved

and essential in cyanobacteria and chloroplasts [1–3]. Depletion of IM30 in cyanobacteria leads to drastically impaired formation of thylakoid membranes (TMs), accompanied by a reduced photosynthetic activity [1,4–6]. Similar, but not entirely conclusive results have been reported for chloroplasts of Arabidopsis thaliana and Chlamydomonas rheinhardtii [3,7]. All results indicate a role of IM30 in TM dynamics, and IM30 appears to be crucially involved in two physiological processes: (i) membrane protection/repair and (ii) membrane remodeling [8]. The membrane-protective activity of IM30 does not appear to be limited to TM-containing photosynthetic organisms, but is rather conserved in the entire PspA/IM30 family, as e.g. expression of IM30 complements the deficiencies of an E. coli pspA deletion strain [9,10]. In contrast, TM-specific functions of IM30 can likely not be accomplished by PspA [1,2,11,12].

A distinct structural feature of all PspA/IM30 family members is their intrinsic propensity to form large, homo-oligomeric ring/rod structures with masses >1 MDa [8]. In vitro formation of rings and rods has been observed multiple times via electron microscopy [11,13–19] and atomic force microscopy (AFM) [20]. While E. coli PspA appears to form rings with a mainly constant diameter of ~20 nm [13], Synechocystis PspA and IM30 rings/rods were found to have varying diameters and symmetries [19,21]. Recently, the preliminary structures of homo-oligomeric cyanobacterial IM30 (Synechocystis sp., Nostoc punctiforme sp. PCC 73102) and PspA (Synechocystis sp. PCC 6803) have been made available [21–23]. PspA/IM30 monomers are mainly α-helical when organized into high molecular mass oligomers, with flexible linkers connecting individual α-helical regions [21–24]. IM30 monomers are arranged horizontally to the ring axis, forming an interwoven, layer-like structure with 11-18 monomers per layer and 5-7 layers per ring [22–24]. In contrast to the homo-oligomer, the structure of membrane-bound IM30 is currently enigmatic. IM30 binds to thylakoid membranes in vivo [25,26] as well as to negatively charged model membranes in vitro [27–30]. Recently, upon membrane binding, dissociation of IM30 rings into partly unfolded monomers and subsequent formation of a membrane surface-covering carpet structure has been observed [20]. Thus, monomer adhesion to the membrane surface appears to be thermodynamically favored over ring formation. As the IM30 membrane-binding propensity is enhanced at acidic conditions, IM30 potentially binds specifically to stressed TM regions via sensing proton leakage followed by ring dissociation and formation of the membrane-protecting carpet [31]. Yet, IM30 is also able to trigger fusion of TM-mimicking liposomes in vitro when Mg^{2+} is present [27]. In fact, Mg^{2+}-binding leads to a rearrangement of the oligomeric IM30 structure [29], which potentially switches the IM30 function from membrane protection to membrane remodeling.

Recently, GTP-binding and hydrolysis was observed for the IM30 proteins of Arabidopsis thaliana and Synechocystis sp. PCC 6803, although IM30 does not contain any canonical domains or motifs

involved in GTP-binding [32,33]. While GTP-binding and/or hydrolysis do not seem to decisively regulate membrane interactions or the membrane remodeling activity of IM30 [32], it is still possible that GTP-binding and/or hydrolysis might affect formation of IM30 rings. Actually, based on the identification of a stably bound nucleotide in oligomeric IM30, it has been suggested that ATP-binding and/or hydrolysis is crucial for the formation of IM30 rings budding off from membrane surfaces [22].

In the present study, we show that SynIM30 rings self-assemble in complete absence of nucleotides, and thus nucleotide binding or hydrolysis does not trigger ring formation. Yet, SynIM30 rings are able to hydrolyze ATP and GTP at about similar rates, but not CTP or UTP, and thus, IM30 in fact specifically binds and hydrolyzes purine-based nucleotides.

EXPERIMENTAL PROCEDURES

Cloning, expression, and purification of IM30

Construction of the plasmid used for expression of His-tagged wt *Syn*IM30 (pRSET IM30 wt) was described in detail previously [4], and construction of the plasmid used for expression of the IM30 FERM_EE mutant (E83A, E84A, F168A, E169A, R170A, M171A) is described in [32].

IM30 of *Synechocystis* sp. PCC 6803 (*Syn*IM30 wt and FERM_EE) was heterologously expressed in *E. coli* BL21 DE3 and purified as described in detail earlier [16]. In short, after expression, cells were lysed via sonification in 50 mM Na-phosphate buffer (300 mM NaCl, 20 mM imidazole, pH 7.6). Cell debris was removed by centrifugation, and the supernatant was applied to a Ni^{2+}-NTA affinity column. The column was washed with increasing concentrations of imidazole (20/50/100 mM; 50 mM Na-phosphate, 300 mM NaCl, pH 7.6) and finally eluted with 500 mM imidazole (Na-phosphate, 300 mM NaCl, pH 7.6). The buffer was exchanged for 20 mM HEPES (pH 7.6) by gel-filtration (Sephadex G25 or Superose 12). Where necessary, the protein solution was concentrated using an Amicon Ultra Centrifugal filter unit (MWCO 30 kDa, regenerated cellulose membrane). The protein concentration was determined via a Bradford assay using BSA as a standard. For denaturation, 6 M urea was added to the lysis buffer and the cell extract was incubated in 6 M urea for 4 h at 4 °C. Subsequently, upon loading the sample onto the affinity column, the sample was washed multiple times with buffer containing 20 mM imidazole plus 6 M urea. For refolding on the column, the subsequent washing steps (compare above) and the elution were performed using urea-free buffer, as used in case of purification under native conditions. For analysis of the NTPase activity, the

purification was performed in HEPES buffer instead of phosphate buffer as described before [32]. In this case, the protein solutions were stored in 1:1 (v/v) glycerol at -20 °C.

Size exclusion chromatography

The size of *Syn*IM30 oligomers was analyzed using an ÄKTA basic system (GE Healthcare) with a Superose12 10/300 GL column (GE Healthcare) equilibrated with 20 mM HEPES (pH 7.6) at 8 °C. Protein elution was followed via monitoring the absorbance at 280 nm. The column was calibrated using standards of known size (blue dextran > 2000 kDa, ferritin (440 kDa), β-amylase (200 kDa), aldolase (158 kDa), conalbumin (75 kDa), ovalbumin (44 kDa), carbonic anhydrase (29 kDa) and cytochrome c oxidase (16.4 kDa).

Circular dichroism spectroscopy

Circular dichroism (CD) spectra were measured using a JASCO J815 CD spectrometer (JASCO Corporation, Tokyo, Japan). With purified native and the refolded protein, spectra ranging from 200 to 260 nm were recorded at 20 °C with a scan rate of 100 nm/min, 1 nm steps and 1 s data integration time. When urea-denatured protein was analyzed, spectra were measured from 210 to 260 nm. Each sample contained 0.1 mg/mL *Syn*IM30 in 10 mM HEPES buffer (pH 7.6) or 10 mM HEPES buffer and 6 M urea (pH 7.6). For each sample, three spectra were averaged and smoothened by the JASCO software package (Savitzky-Golay filter), if necessary.

Electron microscopy

For negative-staining electron microscopy, 3 µL sample was applied to glow-discharged (PELCO easiGlow Glow Discharger, Ted Pella Inc.) continuous carbon grids (CF-300 Cu, Electron Microscopy Sciences). The sample was incubated on the grid for 1 min. Then the grid was side-blotted on filter paper, washed with 3 µL water and stained with 3 µL 2% uranyl acetate for 30 s and air-dried. The grids were imaged with a 120 kV Talos L120C electron microscope (ThermoFisher Scientific/FEI) equipped with a CETA camera at a pixel size of 4.06 Å/pix at an underfocus of 1.0 to 2.5 µm.

Malachite Green assay

0.1 µM *Syn*IM30 was mixed with 0.5 mM of GTP, ATP, CTP or UTP and Mg^{2+} (2.5 mM) in 20 mM Hepes (pH 7.6) and incubated for 30 min at 37 °C. 200 µL of this sample was transferred to a 96-well plate, mixed with 50 µL of the malachite green reaction mixture ("Gold mix", PiColorLock Gold Phosphate Detection Kit, Innova Biosciences) and incubated for 5 min at RT. Finally, 20 µL of "stabilizer" (PiColorLock Gold Phosphate Detection Kit by Innova Biosciences) was added. Absorbance at 635 nm was measured using an OMEGA FLUOstar Platereader (BMG Labtech). Buffer blank (including the respective GTP concentration) absorbance was subtracted, and the concentration of released phosphate was determined by linear regression from a phosphate standard curve.

LC-MS analysis of extracted nucleoside phosphates in negative ion mode

25 µM *Syn*IM30 was incubated for 30 min in methanol (final concentration 80%) to denature the protein. Protein denaturation was verified via CD spectroscopy. Denaturation dismantles the potential nucleotide-binding site and releases any bound nucleotide. The precipitated protein was removed by centrifugation at 16000 g and 4 °C for 15 min. The supernatant containing any beforehand protein-bound substances was collected, dried in a SpeedVac (Eppendorf vacuum centrifuge) and finally resuspended in water.

For separation and subsequent mass-spectrometric analysis of the nucleotide solutions, a chromatographic approach from Xing *et al.* was adapted [34]. Sample amounts corresponding to 500 pmol initial protein were injected onto a Hypercarb column (5 µm, 100x2.1 mm) (ThermoScientific) and the column oven was set to 35 °C. Mobile phase A (MPA) consisted of 50 mM ammonium acetate and 0.1% diethylamine in water (pH = 9) and mobile phase B (MPB) of pure, LC-MS grade ACN. At a flow rate of 0.5 mL/min, the following gradient was run: 5% MPB from 0 to 2 min, 5-20% MPB from 2 to 8 min, 20-90% MPB from 8 to 14 min, 90% MPB from 14 to 15 min, 90-5% MPB from 15 to 17 min and 5% MPB from 17 to 22 min. Mass spectrometric analyses of the negatively charged ions was conducted using an Agilent 6460 QQQ mass spectrometer in the dynamic multiple reaction monitoring mode (dMRM). This allows monitoring a specific fragmentation reaction at a given retention time. The selected mass transitions and retention time windows are displayed in Table 1. Ion source parameters were set as followed: gas temperature 350 °C, gas flow 8 l/min, nebulizer pressure 50 psi, sheath gas temperature 350 °C, sheath gas flow 2 l/min, capillary voltage -3500V.

Table 1. QQQ parameters for the detection of NTPs.

Compound name	Precursor ion	Product ion	Fragmentor	Collision energy	Cell accelerator voltage	Ret. time (min)	Delta ret. time
ATP	506	159	95	29	5	9.3	4
ADP	426	79	100	40	5	9.1	4
GTP	522.3	424	105	17	5	9	4
GDP	442	79	105	40	5	9	4

RESULTS AND DISCUSSION

IM30 hydrolyzes purine-based, but not pyrimidine-based nucleotides

As shown before, IM30 oligomers of *Synechocystis* and *Arabidopsis* hydrolyze GTP reaching a P_i release rate of about 20 µM at 2 µg/100 µL protein concentration [32,33]. To gain further insights into the specificity and (potential) function of GTP-binding, we at first analyzed the nucleotide-binding/hydrolysis specificity and tested whether IM30 of the cyanobacterium *Synechocystis* sp. PCC 6803 (*Syn*IM30) is also able to hydrolyze other nucleoside triphosphates (NTPs). Therefore, we used a well-established malachite green-based assay to analyze the apparent NTPase activity of *Syn*IM30. As a negative control, we used the IM30 mutant *Syn*IM30 FERM_EE, which does not hydrolyze GTP as shown recently [32]. Based on the now available IM30 structure this is obvious, as this mutant does not form higher-ordered oligomers anymore, and oligomerization is required for nucleotide-binding as further discussed below [22].

When the purity of IM30 wt was analyzed via SDS-PAGE (Fig. 1A), no other proteins were detected (Fig. 1A). While the purified *Syn*IM30 wt protein, but not the mutant, clearly hydrolyzes the purine-based nucleotides GTP and ATP to a similar extent, very little activity was observed when the pyrimidine-based CTP or UTP were added instead (Fig. 1B). This implies that IM30 specifically hydrolyzes purine-based, but not pyrimidine-based nucleotides, and IM30 is in fact not a GTPase but an NTPase, hydrolyzing GTP and ATP with about identical rates (Fig. 1B). This observation is in excellent agreement with the initially observed GTP-hydrolyzing activity of *Syn*IM30 [32] and the now observed binding of ADP to IM30 rings [22,24].

Thus far, solely interaction between defined IM30 side chains with the phosphate groups of the NTP have been suggested to be involved in nucleotide binding [22]. Our results now clearly indicate that also the interactions with the base are decisive for the interaction with IM30, and the putative nucleotide-binding pocket appears to specifically bind the larger purine-heterocycle of NTPs.

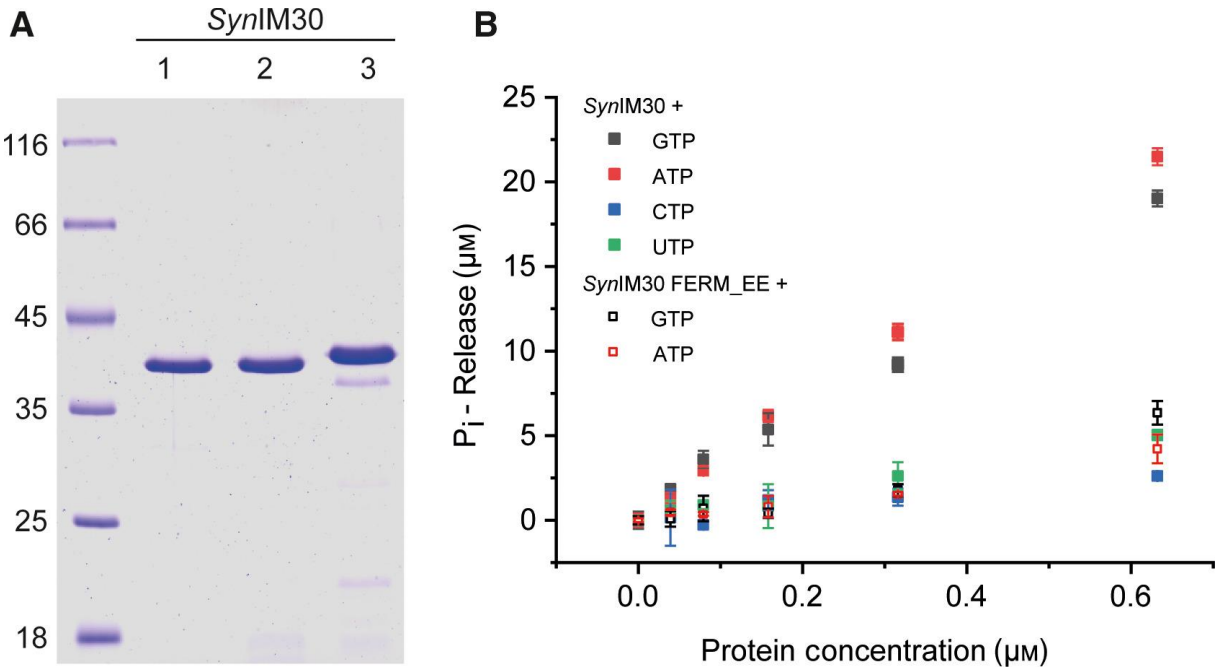

Figure 1: IM30 specifically hydrolyzes purine-based nucleotides

A: SDS-PAGE analysis of heterologously expressed and purified IM30 wt (lane 1), of *in vitro* refolded IM30 wt (lane 2), as well as of purified IM30 FERM_EE (lane 3). The wt protein was electrophoretically pure, whereas we observed some small degradation products in case of IM30 FERM_EE. The molecular masses of the protein standard are given on the left. **B:** The P_i release caused by increasing amounts of IM30 in presence of 0.5 mM GTP (black), ATP (red), CTP (green) or UTP (blue) and 2.5 mM Mg^{2+} after incubation for 30 min at 37 °C was measured using a malachite green-based assay. Only minor release of P_i was detected in the negative control (IM30 FERM_EE) (black squares with holes: GTP, red squares with holes: ATP). When the wt protein was analyzed, exclusively in presence of the purine-based nucleotides GTP or ATP, a significant amount of P_i was released (error bars represent SD, n=3).

Substrate promiscuity is not common but reported for several ATP/GTPases, and *e.g.* the predicted GTP-binding protein HflX exhibits a GTPase as well as an ATPase activity, albeit the activities were not identical [35]. Similarly, the YchF subfamily, a unique subgroup of the Obg family of P-loop GTPases, binds both, GTP and ATP [36]. It has been hypothesized that during the evolution of the GTPase superclass from a primordial GTPase, the activity of some proteins has switched to an ATPase activity on several independent occasions [37,38]. Nevertheless, all these proteins do contain canonical nucleotide-binding motifs in their sequence, in contrast to IM30.

Compared to most other GTP-hydrolyzing enzymes, the activity, as well as the GTP-binding affinity of IM30, is relatively low [32]. In fact, the rates observed previously [32] and here, as well as described for the isolated *Arabidopsis* IM30 [33] are at least 10-fold higher than the putative activity reported very recently for the wt and mutated *Synechocystis* proteins [22]. The rather low NTPase activity of IM30 might be due to a very slow k_{off} rate for ADP and GDP from the putative binding pocket, resulting in a very slow regeneration of the IM30 protein. This assumption is supported by

the observation that after the addition of ATP, a stably bound ADP was detected in the cryo-EM structure of IM30 even after further purification steps [22]. Tight binding of ADP/GDP is rather uncommon for classical GTP/ATPases, but clarifies the negative result of an enzyme-coupled GTPase assay that is based on the detection of free GDP [32].

IM30 nucleotide-binding is not required for IM30 ring formation

The structure of oligomeric IM30 was recently analyzed via cryo-EM single-particle analysis [22]. In the reported structure, a stably bound ADP in a unique nucleotide-binding site has been detected, when the protein was incubated in ATP solutions prior to structural analyses [22].

When we analyzed the presence of nucleotides in our protein sample (500 pmol protein) that was purified without an ATP-including washing step, we did not observe any measurable concentrations of the nucleotides ADP/ATP or GDP/GTP (Fig. 2A, B). The lower limit of quantification was 10 pmol, resulting in a maximum nucleotide-bound protein fraction of not more than 2 %. Thus, we exclude that endogenous nucleotides from the *E. coli* cells were co-purified with the protein.

Next, we analyzed the structure of the nucleotide-free IM30 protein by negative-staining electron microscopy. Here we observed the characteristic IM30 ring structures as well as some rod-like structures (Fig. 2C), as observed multiple times before for purified IM30 [16,19,29,30,39,40]. Thus, nucleotide-binding clearly is not crucial for stabilizing the IM30 ring structures.

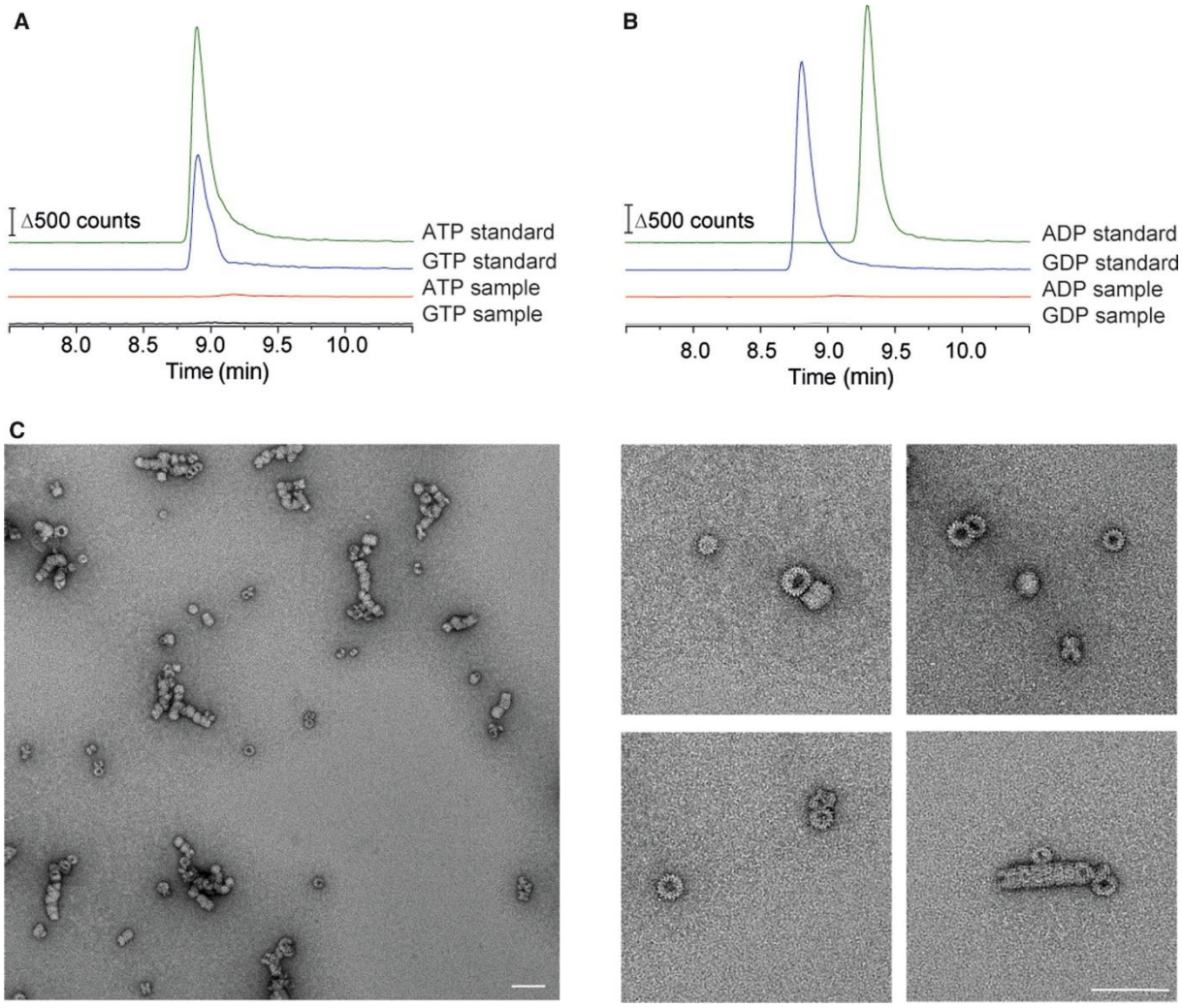

Figure 2: IM30 assembles into rings in complete absence of nucleotides.

A/B: Extracted Ion Chromatograms (EIC) of specific mass transitions for (A) ATP (*m/z* 506→159) and GTP (*m/z* 522,3 → 442) and for (B) ADP (*m/z* 426→79) and GDP (*m/z* 442 → 79) from the wt IM30 sample (500 pmol) and nucleotide standards (200 pmol) as a control. **C:** Electron microscopy of purified IM30 wt in absence of nucleotides. Scale bars represent 100 nm.

Yet, this does not allow to finally exclude that ATP (or GTP)-binding and/or hydrolysis might be a crucial (initial) step in IM30 ring formation, as this might already take place in *E. coli* during protein expression. However, we have shown previously that IM30 elutes as monomers or lower ordered oligomers from the Ni-NTA matrix, which (re)assemble and form rings/rods likely only later on after the purification process in complete absence of nucleotides [19]. Noteworthy, when IM30 is not assembled in higher ordered oligomers, about half of the protein is unfolded [20]. Furthermore, also the recently published structure of *Syn*IM30 [22] was solved using a protein that was purified when its N-terminus was fused to a chitin-binding domain. The mature IM30 protein was released only after protease treatment [22]. As the protein's N-terminus is embedded within the narrow center of

an IM30 ring [22], likely monomers or smaller oligomers were purified, which assembled to the final ring structures only after removal of the fusion domain.

Nevertheless, to further test whether ATP/GTP (or ADP/GDP) is required for IM30 ring assembly, we completely denatured IM30 prior to protein purification via addition of 6 M urea. As shown before, IM30 has no α-helical structure in 6 M urea solutions, resulting in the loss of any potential nucleotide-binding site [29] (Fig. 3A). The Ni^{2+}-NTA-bound denatured protein was washed multiple times with 6 M urea-containing buffer to remove any potentially co-purified substances, such as proteins, lipids, ions or nucleotides. Subsequently, the protein was refolded on the column by washing with urea-free buffer. Note that the overall secondary structure of renatured IM30 did not differ from the secondary structure of IM30 purified under native conditions (Fig. 3A), indicating correct refolding of secondary structure elements of IM30 in absence of nucleotides. As the monomeric protein is partly unfolded [20], this already indicated formation of higher-ordered structures where the IM30 monomer is largely α-helical. Furthermore, when the refolded protein was analyzed via size-exclusion chromatography, solely high molecular weight oligomers were detected, but no smaller oligomers or monomers (Fig 3B), and these high molecular weight species were identified by negative staining EM as the prototypical IM30 ring and rod structures (Fig. 3C). As expected, we did not detect any nucleotides in our urea-treated and refolded protein samples, when analyzed by LC/MS as described (Fig. S1).

Thus, IM30 is unequivocally self-assembling and oligomerizing into ring structures without nucleotide binding and/or hydrolysis.

The ADP molecules observed in the cryo-EM structure most likely are a result of the ATP-including washing step that was applied during purification of *Syn*IM30 [22]. It is well possible that ATP- or GTP-binding slightly distorts the IM30 structure and/or ATP/GTP bind solely to slightly distorted protein regions. In fact, the putative nucleotide-binding site is formed by different regions of three different IM30 monomers, two from layer 1 and one from layer 2. Yet, due to the basket-like structure of IM30 rings, the structure of IM30 monomers is somewhat distorted in the first three layers of a ring [22]. When natively folded *Syn*PspA was compared to *in vitro* refolded *Syn*PspA, formation of the prototypical rod structures was observed, but the refolded rods appeared to exhibit extended lengths and even looked more regular compared to the natively folded protein [21]. Due to these observations, we next tested whether the *in vitro* refolded IM30 rings still have a GTP/ATP-hydrolyzing activity. As can be seen in Figure S2, the prototypical IM30 rings do not show any significant ATP or GTP-hydrolyzing activity anymore after *in vitro* folding. While the here measured values (background) are still higher than reported recently for the *Syn*IM30 wt protein [22], the

refolded protein releases P_i at similar low rates as measured with the negative control. Thus, the nucleotide binding site of IM30 likely might be slightly differently structured after refolding, which does, however, neither lead to overall misfolding of the secondary structure (Fig. 3A), nor to a disturbed oligomerization and ring formation (Fig. 3B, C). This again indicates that nucleotide-binding/hydrolysis is not relevant for formation and/or stabilization of the prototypical IM30 ring structures, despite the localization of the proposed binding site at the interface of three monomers inside the ring [22].

In fact, based on a recent *de novo* protein design study, it has been discussed that some level of ATP-binding and ATPase activity is not unusual in protein sequence space, and an ATP-hydrolyzing activity can be observed for proteins that differ substantially from naturally occurring ATPases [41]. Thus, determining a low ATP/GTP hydrolyzing activity, as e.g. observed with IM30, might not be uncommon. Yet, the apparent lack of structural diversity among naturally occurring ATPases (and GTPases) strongly indicates that, while binding and catalysis can be accomplished by alternative sequences and structures, the energy gained via NTP hydrolysis might not be properly transmitted into a biological activity by non-canonical binding sites.

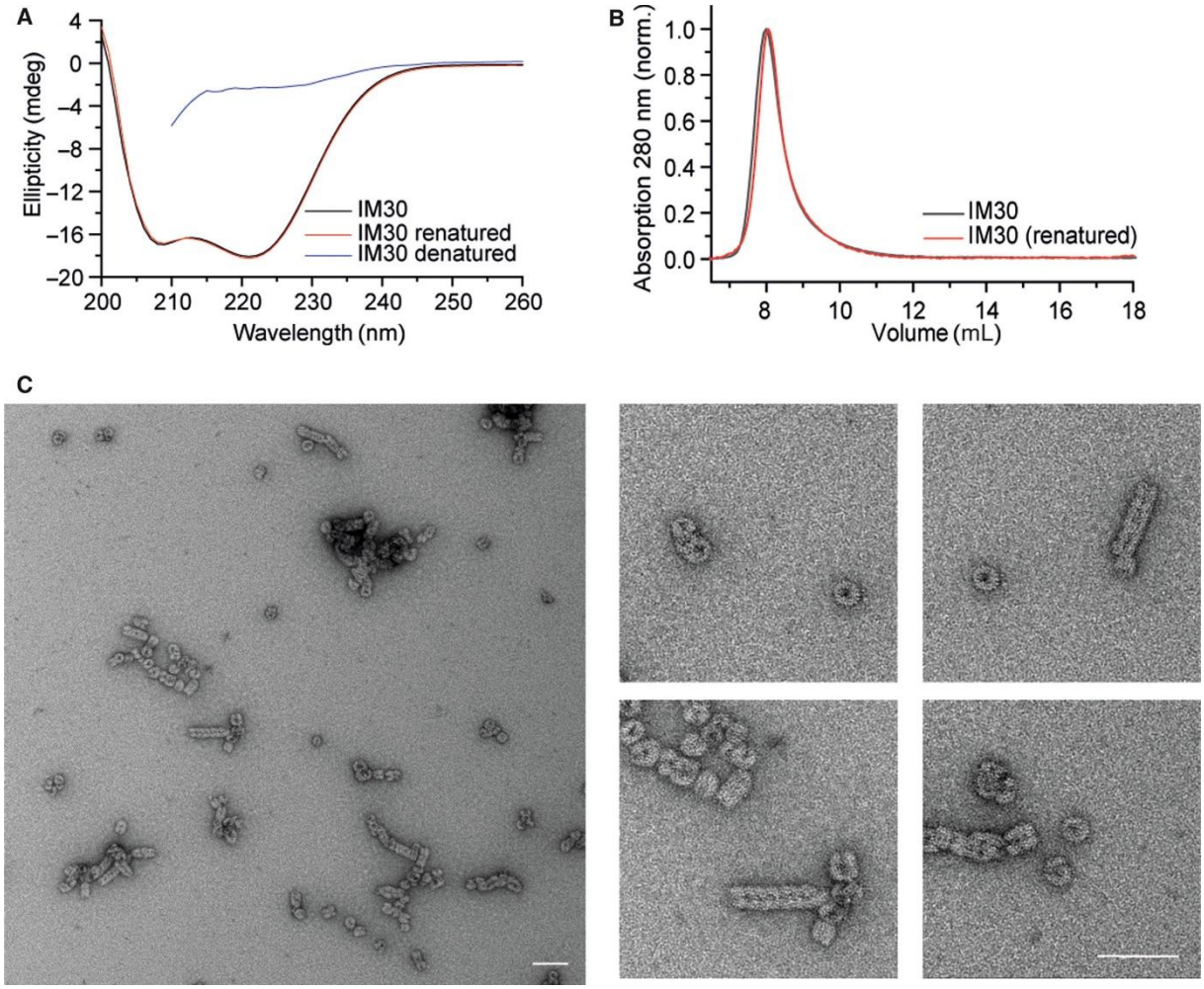

Figure 3: IM30 self-assembles into ring-like structures.

A: CD spectra of IM30 purified under standard conditions or after renaturation were measured from 200-260 nm. The spectra do not differ, indicating proper folding of the secondary structure of the renatured sample. The spectra were smoothened using a Savitzky-Golay filter. n=3, no error bars are shown. When the secondary structure of IM30 was analyzed after urea denaturation, the spectra indicated complete unfolding of the protein. **B:** The oligomeric state of IM30 was monitored by SEC (Superose 12 10/300 GL column). Both, IM30 wt purified under standards conditions (black) and IM30 wt purified under denaturing conditions and refolded (red) eluted in the void volume (>300 kDa). **C:** IM30 purified under denaturing conditions was analyzed by negative staining EM. Ring as well as some rod structures were observed. The scale bar represents 100 nm.

CONCLUSION

We here show that *Syn*IM30 rings can hydrolyze ATP and GTP at about identical rates, but not CTP or UTP. The absence of nucleotides does not influence oligomerization of IM30 monomers into ring structures, and the negative staining EM analyses clearly showed formation of typical ring- and rod structures (Fig. 2C). Furthermore, IM30 prototypical rings do also spontaneously assemble from completely denatured protein in complete absence of nucleotides (Fig. 3C). As a putative ADP-binding pocket has been detected between two layers of an IM30 ring, which involves interactions

of a single nucleotide with three different IM30 monomers [22,24], the oligomeric structure of IM30 clearly is a prerequisite for nucleotide binding. This is perfectly in line with the observation that the oligomerization-inactive IM30 mutant had no GTP hydrolyzing activity [32] (Fig. 1B). This consequently implies that nucleotide binding and (potentially) hydrolysis can physiologically only be relevant (if at all), when the large oligomeric complex has already formed. Clearly, membrane interaction destabilizes IM30 rings resulting in formation of an IM30 carpet structure on the membrane surface [20], and thus, ring dissociation and IM30 monomer-membrane interactions are thermodynamically favored over ring formation at membrane surfaces. Furthermore, the presence of GTP tends to decrease the thermal stability of IM30 rings [32], and thus nucleotide binding does not stabilize, but destabilize an IM30 ring structure. These observations do not support the idea that IM30 ring formation is initiated on membrane surfaces by ATP/GTP binding and/or hydrolysis, but rather suggests a nucleotide-independent mechanism for IM30 oligomerization. Thus, as nucleotide binding to and/or hydrolysis by IM30 neither decisively regulates the IM30 oligomeric structure nor membrane interactions [32], we suggest that IM30 nucleotide hydrolysis may not play a crucial role in the function of membrane repair based on the current knowledge. Nevertheless, the residues identified to be involved in nucleotide binding in the ATP-washed sample appear to establish important contacts within the IM30 oligomer or with other factors, as mutation of these residues results in an impaired *in vivo* activity of IM30 [22]. Future information on the *in vivo* IM30 structure might be of help to unravel a potential *in vivo* function of the cryptic nucleotide-binding/hydrolysis activity.

REFERENCES

1 Westphal S, Heins L, Soll J & Vothknecht UC (2001) Vipp1 deletion mutant of Synechocystis: A connection between bacterial phage shock and thylakoid biogenesis? *Proc Natl Acad Sci* 98, 4243–4248.

2 Vothknecht UC, Otters S, Hennig R & Schneider D (2012) Vipp1: A very important protein in plastids?! *J Exp Bot* 63, 1699–1712.

3 Kroll D, Meierhoff K, Bechtold N, Kinoshita M, Westphal S, Vothknecht UC, Soll J & Westhoff P (2001) VIPP1, a nuclear gene of Arabidopsis thaliana essential for thylakoid membrane formation. *Proc Natl Acad Sci* 98, 4238–4242.

4 Fuhrmann E, Gathmann S, Rupprecht E, Golecki J & Schneider D (2009) Thylakoid membrane

reduction affects the photosystem stoichiometry in the cyanobacterium Synechocystis sp. PCC 6803. *Plant Physiol* 149, 735–744.

5 Gao H & Xu X (2009) Depletion of Vipp1 in Synechocystis sp. PCC 6803 affects photosynthetic activity before the loss of thylakoid membranes. *FEMS Microbiol Lett* 292, 63–70.

6 Zhang S, Shen G, Li Z, Golbeck JH & Bryant DA (2014) Vipp1 is essential for the biogenesis of Photosystem I but not thylakoid membranes in Synechococcus sp. PCC 7002. *J Biol Chem* 289, 15904–15914.

7 Nordhues A, Schottler MA, Unger A-K, Geimer S, Schonfelder S, Schmollinger S, Rutgers M, Finazzi G, Soppa B, Sommer F, Muhlhaus T, Roach T, Krieger-Liszkay A, Lokstein H, Crespo JL & Schroda M (2012) Evidence for a Role of VIPP1 in the Structural Organization of the Photosynthetic Apparatus in Chlamydomonas. *PLANT CELL ONLINE*.

8 Siebenaller C, Junglas B & Schneider D (2019) Functional Implications of Multiple IM30 Oligomeric States. *Front Plant Sci* 10, 1–11.

9 DeLisa MP, Lee P, Palmer T & Georgiou G (2004) Phage Shock Protein PspA of Escherichia coli Relieves Saturation of Protein Export via the Tat Pathway. *J Bacteriol* 186, 366–373.

10 Zhang L, Kato Y, Otters S, Vothknecht UC & Sakamoto W (2012) Essential Role of VIPP1 in Chloroplast Envelope Maintenance in Arabidopsis. *Plant Cell* 24, 3695–3707.

11 Aseeva E, Ossenbühl F, Eichacker LA, Wanner G, Soll J & Vothknecht UC (2004) Complex formation of Vipp1 depends on its alpha-helical PspA-like domain. *J Biol Chem* 279, 35535–41.

12 Bultema JB, Fuhrmann E, Boekema EJ & Schneider D (2010) Vipp1 and PspA. *Commun Integr Biol* 3, 162–165.

13 Hankamer BD, Elderkin SL, Buck M & Nield J (2004) Organization of the AAA+ Adaptor Protein PspA Is an Oligomeric Ring. *J Biol Chem* 279, 8862–8866.

14 Wolf D, Kalamorz F, Wecke T, Juszczak A, Mäder U, Homuth G, Jordan S, Kirstein J, Hoppert M, Voigt B, Hecker M & Mascher T (2010) In-depth profiling of the LiaR response of bacillus subtilis. *J Bacteriol* 192, 4680–4693.

15 Liu C, Willmund F, Golecki JR, Cacace S, Heß B, Markert C & Schroda M (2007) The chloroplast HSP70B-CDJ2-CGE1 chaperones catalyse assembly and disassembly of VIPP1 oligomers in Chlamydomonas. *Plant J* 50, 265–277.

16 Fuhrmann E, Bultema JB, Kahmann U, Rupprecht E, Boekema EJ & Schneider D (2009) The

vesicle-inducing protein 1 from Synechocystis sp. PCC 6803 organizes into diverse higher-ordered ring structures. *Mol Biol Cell* 20, 4620–4628.

17 Gao F, Wang W, Zhang W & Liu C (2015) α-Helical Domains Affecting the Oligomerization of Vipp1 and Its Interaction with Hsp70/DnaK in *Chlamydomonas*. *Biochemistry* 54, 4877–4889.

18 Male AL, Oyston PCF & Tavassoli A (2014) Self-Assembly of Escherichia coli Phage Shock Protein A. *Adv Microbiol* 04, 353–359.

19 Saur M, Hennig R, Young P, Rusitzka K, Hellmann N, Heidrich J, Morgner N, Markl J & Schneider D (2017) A Janus-Faced IM30 Ring Involved in Thylakoid Membrane Fusion Is Assembled from IM30 Tetramers. *Structure* 25, 1380-1390.e5.

20 Junglas B, Orru R, Axt A, Siebenaller C, Steinchen W, Heidrich J, Hellmich UA, Hellmann N, Wolf E, Weber SAL & Schneider D (2020) IM30 IDPs form a membrane-protective carpet upon super-complex disassembly. *Commun Biol* 3, 595.

21 Junglas B, Huber ST, Heidler T, Schlösser L, Mann D, Hennig R, Clarke M, Hellmann N, Schneider D & Sachse C (2021) PspA adopts an ESCRT-III-like fold and remodels bacterial membranes. *bioRxiv*, 2020.09.23.309765.

22 Kumar Gupta T, Klumpe S, Gries K, Heinz S, Wietrzynski W, Ohnishi N, Niemeyer J, Schaffer M, Rast A, Strauss M, Plitzko JM, Baumeister W, Rudack T, Sakamoto W, Nickelsen J, Schuller JM, Schroda M & Engel BD (2020) Structural basis for VIPP1 oligomerization and maintenance of thylakoid membrane integrity. *bioRxiv*, 2020.08.11.243204.

23 Liu J, Tassinari M, Souza DP, Naskar S, Noel JK, Bohuszewicz O, Buck M, Williams TA, Baum B & Low HH (2020) Bacterial Vipp1 and PspA are members of the ancient ESCRT-III membrane-remodelling superfamily. *bioRxiv*, 2020.08.13.249979.

24 McCullough J & Sundquist WI (2020) Membrane Remodeling: ESCRT-III Filaments as Molecular Garrotes. *Curr Biol* 30, R1425–R1428.

25 Bryan SJ, Burroughs NJ, Shevela D, Yu J, Rupprecht E, Liu LN, Mastroianni G, Xue Q, Llorente-Garcia I, Leake MC, Eichacker LA, Schneider D, Nixon PJ & Mullineaux CW (2014) Localisation and interactions of the Vipp1 protein in cyanobacteria. *Mol Microbiol* 94, 1179–1195.

26 Zhang L, Kondo H, Kamikubo H, Kataoka M & Sakamoto W (2016) VIPP1 has a disordered C-terminal tail necessary for protecting photosynthetic membranes against stress. *Plant Physiol* 171, 1983–1995.

27 Hennig R, Heidrich J, Saur M, Schmüser L, Roeters SJ, Hellmann N, Woutersen S, Bonn M, Weidner T, Markl J & Schneider D (2015) IM30 triggers membrane fusion in cyanobacteria and chloroplasts. *Nat Commun* 6, 7018.

28 McDonald C, Jovanovic G, Ces O & Buck M (2015) Membrane stored curvature elastic stress modulates recruitment of maintenance proteins pspa and vipp1. *MBio* 6, e01188-15.

29 Heidrich J, Junglas B, Grytsyk N, Hellmann N, Rusitzka K, Gebauer W, Markl J, Hellwig P & Schneider D (2018) Mg2+ binding triggers rearrangement of the IM30 ring structure, resulting in augmented exposure of hydrophobic surfaces competent for membrane binding. *J Biol Chem* 293, 8230–8241.

30 Thurotte A & Schneider D (2019) The fusion activity of IM30 rings involves controlled unmasking of the fusogenic core. *Front Plant Sci* 10, 108.

31 Siebenaller C, Junglas B, Lehmann A, Hellmann N & Schneider D (2020) Proton Leakage Is Sensed by IM30 and Activates IM30-Triggered Membrane Fusion. *Int J Mol Sci* 21, 4530.

32 Junglas B, Siebenaller C, Schlösser L, Hellmann N & Schneider D (2020) GTP hydrolysis by Synechocystis IM30 does not decisively affect its membrane remodeling activity. *Sci Rep* 10, 1–14.

33 Ohnishi N, Zhang L & Sakamoto W (2018) VIPP1 involved in chloroplast membrane integrity has GTPase activity in vitro. *Plant Physiol* 177, 328–338.

34 Xing J, Apedo A, Tymiak A & Zhao N (2004) Liquid chromatographic analysis of nucleosides and their mono-, di- and triphosphates using porous graphitic carbon stationary phase coupled with electrospray mass spectrometry. *Rapid Commun Mass Spectrom* 18, 1599–1606.

35 Dutta D, Bandyopadhyay K, Datta AB, Sardesai AA & Parrack P (2009) Properties of HflX, an enigmatic protein from escherichia coli. *J Bacteriol* 191, 2307–2314.

36 Cheung MY, Li X, Miao R, Fong YH, Li KP, Yung YL, Yu MH, Wong KB, Chen Z & Lam HM (2016) ATP binding by the P-loop NTPase OsYchF1 (an unconventional G protein) contributes to biotic but not abiotic stress responses. *Proc Natl Acad Sci U S A* 113, 2648–2653.

37 Leipe DD, Koonin E V. & Aravind L (2004) STAND, a class of P-loop NTPases including animal and plant regulators of programmed cell death: Multiple, complex domain architectures, unusual phyletic patterns, and evolution by horizontal gene transfer. *J Mol Biol* 343, 1–28.

38 Leipe DD, Wolf YI, Koonin E V. & Aravind L (2002) Classification and evolution of P-loop GTPases and related ATPases. *J Mol Biol* 317, 41–72.

39 Heidrich J, Wulf V, Hennig R, Saur M, Markl J, Sönnichsen C & Schneider D (2016) Organization into higher ordered ring structures counteracts membrane binding of IM30, a protein associated with inner membranes in chloroplasts and cyanobacteria. *J Biol Chem* 291, 14954–14962.

40 Hennig R, West A, Debus M, Saur M, Markl J, Sachs JN & Schneider D (2017) The IM30/Vipp1 C-terminus associates with the lipid bilayer and modulates membrane fusion. *Biochim Biophys Acta - Bioenerg* 1858, 126–136.

41 Wang MS & Hecht MH (2020) A Completely de Novo ATPase from Combinatorial Protein Design. *J Am Chem Soc* 142, 15230–15234.

ACKNOWLEDGMENTS

This work was funded by the Max-Planck Graduate Center at the Max Planck institutes and the University of Mainz and a DFG Grant HE 3397/13-2 to M.H.

CONFLICT OF INTEREST

The authors declare that they do not have any competing conflict of interest.

AUTHOR CONTRIBUTIONS

M.H., C.Sa. and D.S. conceived and supervised the study. C.Si, L.S.B.J., M.S., and D.J. performed the experiments. C.Si, L.S., B.J., M.S., D.J. and N.H. analyzed the data. All authors wrote the manuscript.

VIII.4. Proton Leakage Is Sensed by IM30 and Activates IM30-Triggered Membrane Fusion

Carmen Siebenaller[†], Benedikt Junglas[†], Annika Lehmann, Nadja Hellmann and Dirk Schneider *

Department of Chemistry, Biochemistry, Johannes Gutenberg University Mainz, 55128 Mainz, Germany; siebenal@uni-mainz.de (C.S.); b.junglas@fz-juelich.de (B.J.); alehma01@students.uni-mainz.de (A.L.); nhellmann@uni-mainz.de (N.H.)

*** Correspondence:** dirk.schneider@uni-mainz.de; Tel: (+49) 6131 39-25833

† These authors contributed equally.

Received: 28 May 2020; Accepted: 23 June 2020; Published: 25 June 2020

ABSTRACT

The inner membrane-associated protein of 30 kDa (IM30) is crucial for the development and maintenance of the thylakoid membrane system in chloroplasts and cyanobacteria. While its exact physiological function still is under debate, it has recently been suggested that IM30 has (at least) a dual function, and the protein is involved in stabilization of the thylakoid membrane as well as in Mg^{2+}-dependent membrane fusion. IM30 binds to negatively charged membrane lipids, preferentially at stressed membrane regions where protons potentially leak out from the thylakoid lumen into the chloroplast stroma or the cyanobacterial cytoplasm, respectively. Here we show in vitro that IM30 membrane binding, as well as membrane fusion, is strongly increased in acidic environments. This enhanced activity involves a rearrangement of the protein structure. We suggest that this acid-induced transition is part of a mechanism that allows IM30 to (i) sense sites of proton leakage at the thylakoid membrane, to (ii) preferentially bind there, and to (iii) seal leaky membrane regions via membrane fusion processes.

KEYWORDS

IM30; Vipp1; membrane fusion; membrane binding; thylakoid membrane; Mg^{2+}; pH; CD spectroscopy; quartz crystal microbalance

INTRODUCTION

IM30, the Inner Membrane-associated protein of 30 kDa, is conserved in almost all oxygenic photosynthetic organisms, involving cyanobacteria as well as algae and higher plants [1]. Likely, IM30 has evolved via gene duplication from its bacterial ancestor PspA (phage shock protein A) [2], which is suggested to be involved in membrane protection/maintenance in bacteria [3]. In fact, while in bacteria solely PspA is encoded and in algae/plants solely IM30, cyanobacterial genomes typically contain two genes coding for PspA and IM30, respectively [2].

Based on computational predictions and secondary structure analyses, IM30 and PspA share a highly similar, mainly α-helical secondary structure [4–7]. The large, N-terminally localized PspA- domain (~220 aa) consists of six α-helices connected via short linker regions. Based on the x-ray structure of a small PspA fragment (aa 1-144), helices 2 and 3 form an extended coiled–coil structure [8]. An extra C-terminal α-helix (helix 7) is exclusively present in IM30 proteins and probably responsible for the IM30-specific functions [1,2,4,6,9]. Members of the IM30/PspA family, including IM30, PspA, and LiaH, the PspA homolog found in *Bacillus* and *Listeria* species, are known to spontaneously assemble into large, homo-oligomeric ring structures with molecular masses of at least 1 MDa [5,9–16]. Such ring structures have a diameter of 20 nm and a height of 8–11 nm in the case of *E. coli* PspA [5], and a diameter of 25 nm in the case of the *B. subtilis* LiaH [16]. In contrast, IM30 proteins appear to form multiple ring structures (from the same building blocks) [11,14]. IM30 of the cyanobacterium *Synechocystis* sp. PCC 6803 (from here on: *Synechocystis*), the currently best-studied IM30 protein, forms rings with diameters of 24–33 nm, which, however, have a constant height of 13–15 nm [14].

The exact physiological function of IM30 is still not finally clarified (reviewed in detail in [17]), albeit two major functions have emerged in recent years: A membrane-stabilizing/protecting function and a membrane remodeling function (recently reviewed in [18]).

IM30 likely shares its membrane protecting function with PspA, its bacterial ancestor. PspA is known to stabilize membranes, which is required to maintain the proton motive force (PMF) in many Gram-negative bacteria [3,19,20]. Both, PspA and IM30 bind to negatively charged lipid membranes in a curvature-dependent manner [13,19,21,22], and IM30 can even replace PspA in organisms where PspA was deleted, but not vice versa [23,24]. In chloroplasts and cyanobacteria, maintaining the membrane integrity and organization is especially crucial for preserving an electrochemical gradient across the thylakoid membrane (TM) system. The TM system is continuously stressed and impaired due to oxidative damage caused by reactive oxygen species generated in the photosynthetic electron-transfer reaction [25]. Especially highly curvature-stressed TM regions could bear the risk of

dissipating the ΔpH across the TM, as lipid packing defects clearly are enhanced with increasing membrane curvature [26,27]. In fact, recent *in vivo* studies show that IM30 particularly localizes to highly curved TM margins under light-stress conditions, where it forms large clusters [28]. These clusters potentially represent protective IM30 assemblies on the membrane [18,26,29]. While the molecular details of its proposed membrane-protecting activity are rather enigmatic, it has been shown that membrane binding of IM30 increases the membrane lipid order, which might be key for membrane protection [13].

Besides membrane protection, IM30 also has a membrane remodeling activity. Photosynthetic organisms continuously rearrange their TM system to dynamically adapt their photosynthetic apparatus to changing light intensities [30–34]. TM membrane rearrangements involve membrane fusion events [35], which are potentially mediated by IM30 [21]. In fact, IM30 can fuse TM-mimicking model membranes *in vitro* when Mg^{2+} is present [21,36]. Direct binding of Mg^{2+} to IM30 induces structural changes, such as increased exposure of hydrophobic surface regions, an overall more compact structure and increased protein stability [37]. The Mg^{2+} concentration in the cyanobacterial cytoplasm and the chloroplast stroma is light-dependent and is related to the photosynthetic activity of chloroplasts and cyanobacteria [38], which directly links IM30-mediated membrane fusion processes to photosynthetic electron-transfer reactions.

As IM30 is predominately found at TM regions that are prone to membrane defects, such as the highly curved TM margins [28], IM30 potentially seals membrane regions where protons leak out of the TM lumen, and thus, IM30 likely encounters conditions with significantly lowered (local) pH. Therefore, in the present study we have analyzed the structural properties and membrane interaction of the *Synechocystis* IM30 under acidic conditions.

We here show that IM30 adopts an altered structure and that membrane binding and membrane fusion of IM30 is enhanced at around pH 5. We propose that the structural rearrangements of IM30 induced by an acidified environment enable the protein to specifically sense and bind to defective TM regions where protons leak out of the TM lumen into the cytoplasm, which increases the membrane fusion capabilities of IM30.

RESULTS

IM30 Has an Unconventional Secondary Structure at pH *5.5*

Based on sequence analyses, IM30's secondary structure is roughly 80% α-helical with seven predicted α-helices that are connected via flexible linkers [6,12,14,37,39]. In line with the prediction, the far-UV CD spectrum of IM30 at physiological pH (pH 7.6) shows pronounced minima at 222 ($n \rightarrow \pi^*$ transition peak) and 208 nm ($\pi \rightarrow \pi^*$ (||) transition peak) (Figure 1a), as typical for α-helices. Yet, when the pH was successively decreased from 7.6 to 5.5, the CD-spectrum of IM30 changed drastically (Figure 1a): the amplitude of both transitions strongly decreased with a minimum at around pH 5.5, but the amplitude of the $\pi \rightarrow \pi^*$ (||) transition peak dropped more dramatically. As a representation for the spectral shape change, the ratio of the peak areas of the two transitions is shown in Figure 1b. The area ratio found at pH 7.6 (~0.3) drops to ~0 at pH 5.5, and thus, the $\pi \rightarrow \pi^*$ (||) transition does barely contribute to the CD spectrum at this pH. When the pH was further decreased below 5.5, the structural changes vanished steadily, again reaching an area ratio of 0.3 at pH 4 and even increasing slightly at pH 3.5 to 2.6, compared to pH 7.6 (Figure 1b).

Additionally, the $n \rightarrow \pi^*$ transition peak shifted from ~222 nm at pH 7.6 to ~226 nm (Figure 1c), and the $\pi \rightarrow \pi^*$ (||) transition peak from ~208 nm at pH 7.6 to ~211 at around pH 5.5 (Figure 1d). Lowering the pH beyond 5.5 reversed the described effect, and below pH 5.0, the center of the $n \rightarrow \pi^*$ transition peak was again located at ~221 nm and the $\pi \rightarrow \pi^*$ (||) transition peak centered at ~207 nm.

Thus, at around pH 5.5, the CD-spectrum of IM30 significantly differs from the spectrum measured at physiological pH, indicating a pronounced change of the secondary structure. Unfortunately, we did not succeed in categorizing the IM30 secondary structure at pH 5.5 based on a superposition of canonical secondary structure elements, *i.e.*, α-helix, β-sheet or random-coil. Thus, the protein may contain a large fraction of atypical secondary structure elements at this pH (such as β-turns, as determined by the BeStSel algorithm [40]). The spectrum to some extent resembles a mainly α-helical spectrum, distorted by absorption flattening due to light scattering [41,42]. However, the photomultiplier voltage did not show any suspicious, pH-dependent increase. Possibly, at least partially atypical β-sheets are formed, as seen in some lectins, where the β-sheet characteristic minimum is shifted from 217 to about 225 nm [43]. Interestingly, below pH ~ 4 and even at pH values as low as pH 2.6, IM30 again shows a CD-spectrum typical for regular α-helices (Figure 1a).

Taken together, the overall structure of IM30 is highly pH-dependent, and IM30 adopts an uncommon secondary structure at a mildly acidic pH of 5.5.

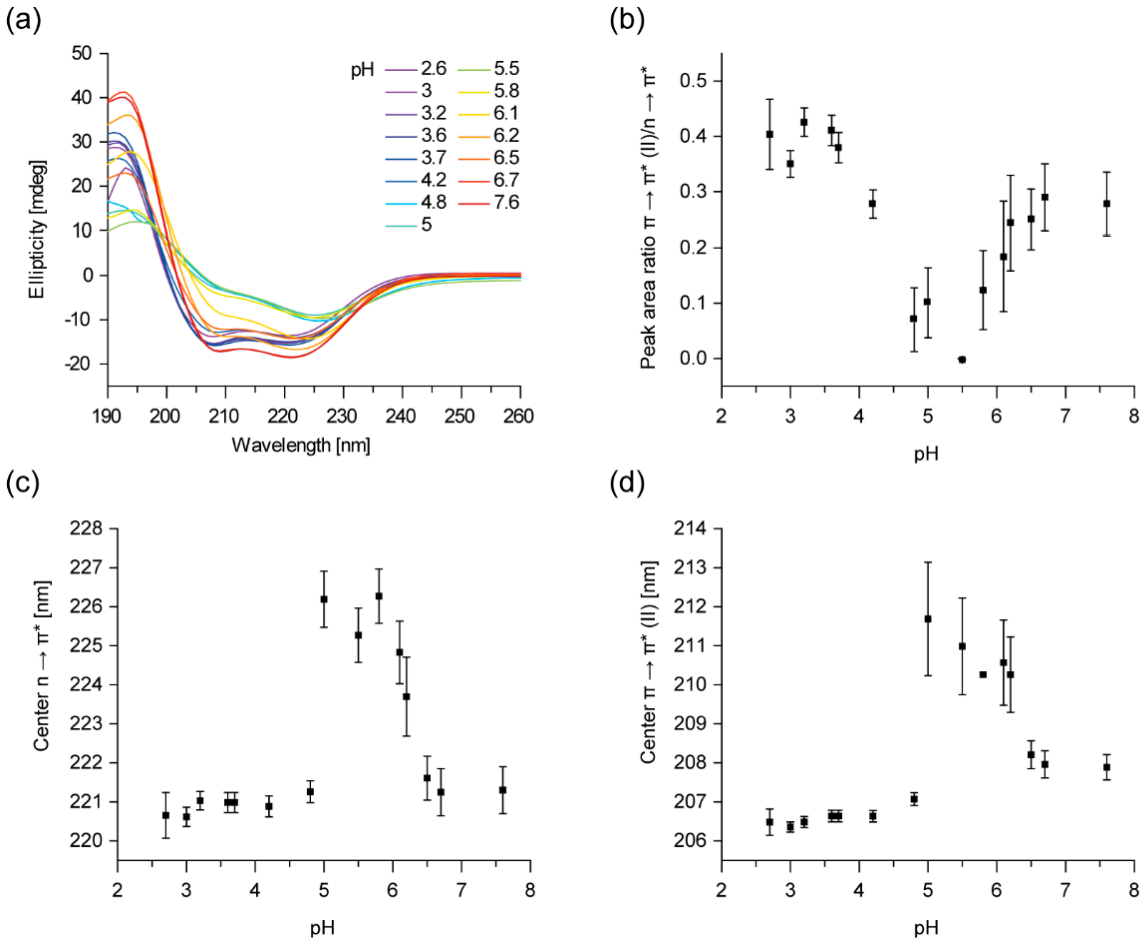

Figure 1. The secondary structure of IM30 (the Inner Membrane-associated protein of 30 kDa changes in an acidic environment.

(a) Far UV CD-spectra of IM30 were measured in a pH range from 7.6 to2 .6. The spectrum changes from a typical α-helix spectrum to an atypical CD-spectrum at around pH 5.5 and back to a "typical" α-helix spectrum below pH 4. The spectra were averaged from three samples, no error bars are shown. **(b)** The ratio of the $n \rightarrow \pi^*$ transition peak area and of the parallel polarized $\pi \rightarrow \pi^*$ (||) transition peak is shown in dependence on the pH. A minimal peak area ratio can be observed at ~pH 5.5 (n = 3, error bars=SD). **(c)** The dependence of the $n \rightarrow \pi^*$ transition peak center on pH reveals a maximum of the peak shift at ~pH 5.5 (n = 3, error bars=SD). **(d)** The dependence of the peak center of the parallel polarized $\pi \rightarrow \pi^*$ (||) transition reveals a maximum of the peak shift at ~pH 5.5 (n = 3, error bars=SD).

The Tertiary Structure of IM30 Changes upon Acidification

The changes in the secondary structure described above are accompanied by a clear increase of the exposed hydrophobic area, as monitored by the spectral changes of the 8-anilinonaphthalene-1-sulfonic acid (ANS) fluorescence (Figure 2a). ANS is a fluorescent dye that changes its spectral properties upon binding to hydrophobic protein surfaces via its anilino-naphthalene group. Free ANS has an emission maximum at 525 nm, which blue shifts in a more hydrophobic environment. This spectral shift is accompanied by a pronounced intensity increase [44]. The fluorescence intensity of

ANS in the presence of IM30 steadily increased with decreasing pH, reaching a maximum at pH ~4.5, followed by a shallow decrease (Figure 2b), accompanied by the characteristic blue shift of the emission maximum. In contrast, the fluorescent properties of ANS in absence of IM30 were not affected by the pH (Suppl. Figure S1).

Thus, also the tertiary structure of IM30 clearly changes upon acidification, resulting in an increased exposure of hydrophobic surfaces. Next, we probed whether the environment of the single Trp of *Synechocystis* IM30, located within the extended coiled-coil formed by helices 2 and 3 [14], is also altered. While no dramatic effect on the Trp's fluorescence emission spectrum was observed (Suppl. Figure S2, Figure 2c), analysis of the spectral shape based on the spectral center of mass revealed also a biphasic trend, with a minimum at around pH 6 and a maximum at about pH 4 (Figure 2d). Note that the Trp fluorescence intensity is in general not pH-dependent upon acidification to a pH as low as 3, whereas further lowering the pH leads to quenching of the Trp fluorescence [45].

Thus, the coiled–coil region appears to rearrange to some extent, leading to a slightly more hydrophobic environment at mildly acidic pH, followed by a slight increase in polarity at further lowered pH values.

In conclusion, the Trp71 solvent exposure appears to be a biphasic process when the pH decreases. A similar effect, with a maximum at around pH 4.5, has been observed for the surface hydrophobicity of IM30 when IM30 was transferred from pH 7.6 to 2.6. These results, combined with the observed changes of the IM30 secondary structure (Figure 1), clearly suggest a rearrangement of the IM30 protein structure upon acidification.

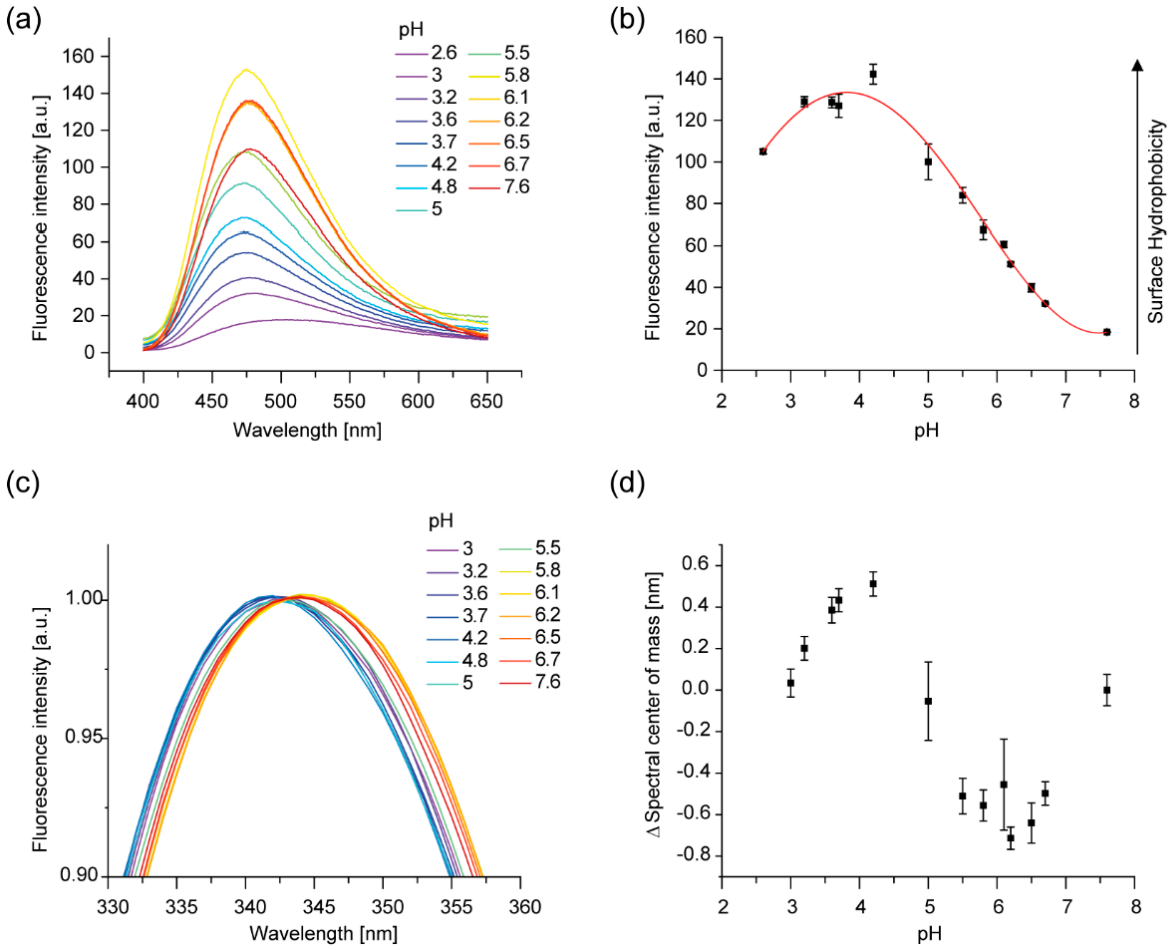

Figure 2. The tertiary structure and surface properties of IM30 change in an acidic environment.

(a) 8-anilinonaphthalene-1-sulfonic acid (ANS) fluorescence spectra of IM30 were measured at decreasing pH. At lowered pH, an increase of the fluorescence intensity and a blue shift was observed. The spectra shown are the average of three samples; no error bars are shown. **(b)** The ANS fluorescence intensity at 490 nm changes with pH, exhibiting a maximum at ~pH 4.5 (n = 3, error bars=SD). **(c)** Intrinsic Trp fluorescence spectra suggest an altered environment of the single IM30 Trp residue upon decreasing the pH from pH 7.6 to 3. The spectra are normalized at 343 nm and smoothed using a Savitzky–Golay-filter (n = 3, no error bars shown). **(d)** To quantify the differences between the measured Trp spectra, the spectral center of mass was calculated. A biphasic transition upon acidification, with a minimum at ~pH 6 and a maximum at ~pH 4.5, is observed (n = 3, error bars=SD).

Acidic pH *and* Mg^{2+} *Have Similar Effects on the IM30 Structure*

Mg^{2+} binds directly to IM30, which causes several secondary structure rearrangements, an increased surface hydrophobicity as well as an overall more compact protein structure [37]. Indeed, the Mg^{2+}-induced changes in IM30's CD spectrum are similar to the pH-induced changes observed here. In particular, in presence of Mg^{2+} the amplitude of the $\pi \rightarrow \pi^*$ (||) transition is also decreased compared to the $n \rightarrow \pi^*$ transition. Yet, the effects observed upon Mg^{2+}-binding were not as

pronounced as observed here upon lowering the pH. Furthermore, a shift of the $n \rightarrow \pi^*$ transition peak was not observed at constant pH in absence vs. presence of Mg^{2+}.

Thus, we next tested whether Mg^{2+} still binds to IM30 at pH 5.5 and whether the effect on the protein structure observed upon addition of Mg^{2+} is additive at pH 5.5, *i.e.*, would cause a more intense decrease in the amplitude of the $n \rightarrow \pi^*$ transition peak. Yet, under these conditions we observed a slight increase of the amplitude (Figure 3). However, Mg^{2+} clearly binds to IM30 also at more acidic pH and induces a change in the IM30 structure. Interestingly, the CD-spectra of IM30 measured at pH 7.6 and 5.5 are very similar when Mg^{2+} is present (Figure 3), indicating that Mg^{2+}- binding potentially stabilizes a particular IM30 structure.

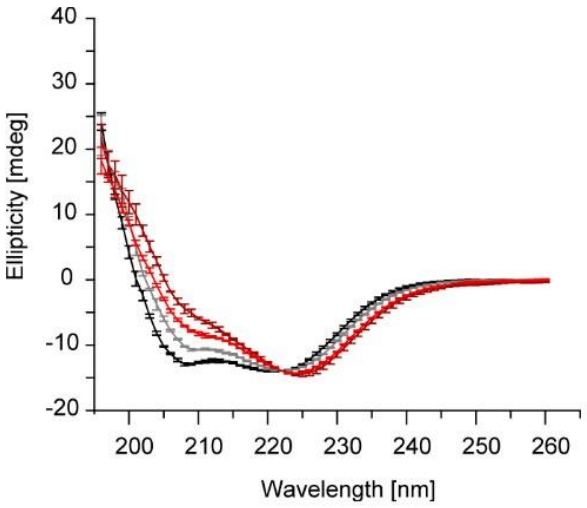

Figure 3. Acidic pH and Mg^{2+} increase the 222/208 nm ratio.

Far UV CD-spectra of IM30 measured in absence (black), in presence of Mg^{2+} (gray) at pH 7.6, and of IM30 in absence (dark red) and in presence of Mg^{2+} (light red) at pH 5.5. Spectra were normalized at 222 nm (n = 3, error bars=SD).

The Membrane-Binding Affinity of IM30 is Increased at Low pH

Interaction of IM30 with membrane surfaces is essential for its proposed *in vivo* functions, involving membrane protection and membrane remodeling [18,21,23,26,28,46–48]. To assess the impact of a decreased pH on the membrane-binding propensity of IM30, we used two different quantitative experimental setups.

We first monitored changes in the Laurdan fluorescence spectra upon addition of protein, as described previously [13,21]. As a mimic of a TM-membrane we used liposomes containing 40% of the negatively charged lipid DOPG and 60% of the most abundant TM lipid MGDG [49], and compared the changes in Laurdan's GP value induced by IM30 binding at pH 7.6 and pH 5.5, where

the secondary structure changes were maximal. While the Laurdan fluorescence spectra monitored in absence of IM30 did not change when the pH was decreased from 7.6 to 5.5 (Suppl. Figure S3), binding of IM30 to DOPG/MGDG membranes clearly differed at pH 5.5 compared to pH 7.6, as quantified by comparing the GP values (Figure 4a). Compared to pH 7.6, the amplitude of the change in GP is substantially larger at pH 5.5, accompanied by a steeper increase at low protein concentrations, indicating a higher membrane-binding affinity or an increased extent of polarity changes per bound IM30. The K_d extracted from these curves was calculated to be ~ 9.8 ± 5.8 µM at pH 7.6. A substantially lower K_d of ~ 1.8 ± 0.4 µM was determined at pH 5.5. Thus, the IM30 membrane binding affinity clearly is increased at lowered pH.

To further support the observations and interpretations of the Laurdan spectral changes and to further analyze membrane-binding of IM30 at acidic pH, we next analyzed binding of IM30 to a solid supported lipid bilayer (SLB) employing a quartz-crystal microbalance (QCM) (Figure 4b). Due to difficulties in formation of SLBs with a high content of anionic lipids, we were limited to SLBs containing 80% DOPC and 20% DOPG in our QCM measurements. In QCM measurements, mass deposition on a quartz-chip is followed by monitoring the decrease in resonance frequency of the chip. If the adsorbed layer is rigid, the observed frequency shift is directly proportional to the mass adsorbed on the chip, and thus the mass can be calculated [50,51]. However, if the layer is viscoelastic, as indicated by a visible change in damping of the oscillation, the frequency shift is reduced, and the calculation of the mass based on a rigid layer leads to an underestimation of the adsorbed mass ("missing mass effect") [52].

Binding of IM30 to the SLB at pH 7.6 was observed as a decrease of the resonance frequency over a time course of 3500 s (Figure 4b), accompanied by an increase in the damping signal. Interestingly, the changes in the frequency and damping were substantially larger at pH 5.5, reaching a final level of ~ $\Delta f = -150$ Hz and $\Delta\Gamma = 12$ Hz after 1000 s, compared to −75 Hz and 7 Hz at pH 7.6. Since both frequency and damping differ by about the same factor, we conclude that at pH 5.5 more IM30 binds to the SLB, in excellent agreement with the increased membrane-binding affinity observed with Laurdan-labeled MGDG/DOPG liposomes (Figure 4a).

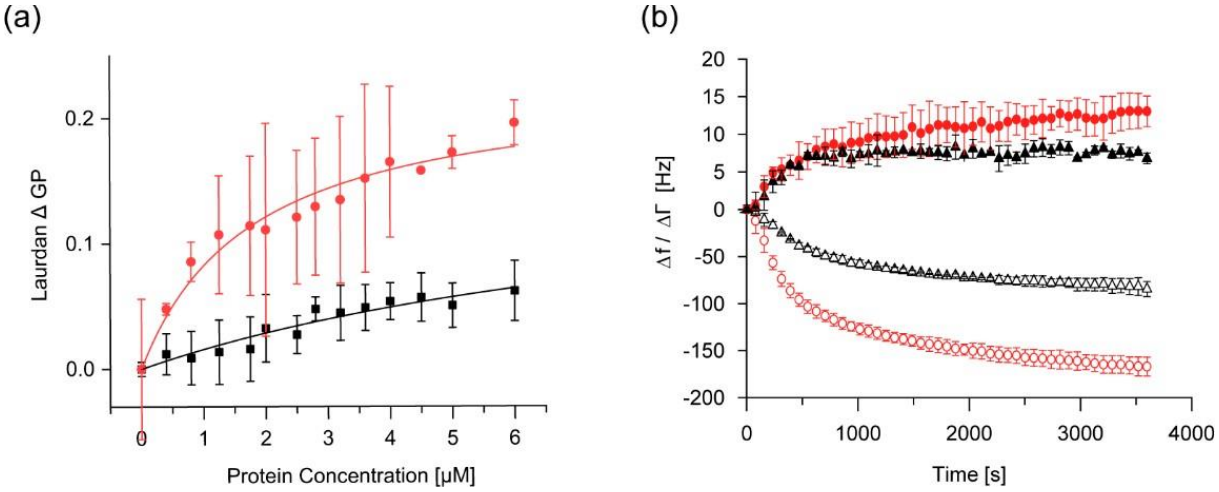

Figure 4. IM30 membrane binding is enhanced at low pH.

(a) Steady-state membrane binding of IM30 was measured using Laurdan fluorescence spectroscopy at pH 5.5 (red) and pH 7.6 (black). The Laurdan ΔGP at 100 μM lipid (40% DOPG/60% MGDG) with 0–6 μM IM30 was strongly increased at pH 5.5. The membrane-binding affinity of IM30 at pH 7.6 is characterized by a K_d = 9.8 ± 5.8, and at pH 5.5 by a K_d = 1.8 ± 0.4 (*n* = 3, error bars=SD). **(b)** Kinetics of IM30 binding (4.5 μM) to a solid-supported bilayer (20% DOPG/80% DOPC) was monitored using QCM-D at pH 5.5 (red) and pH 7.6 (black), respectively. Empty symbols represent the change in frequency (Δf), filled symbols represent the change in damping (ΔΓ). At pH 5.5, faster binding kinetics reflected by the change in frequency Δf was observed (*n* = 3, error bars=SD).

IM30-mediated Membrane Fusion is Enhanced at Low pH

IM30 triggers the fusion of TM-mimicking model membranes, which is strictly Mg^{2+} dependent [21,36,53]. As we observed changes of the IM30 structure at acidic pH that appear to be related to the structural changes caused by Mg^{2+} binding [37], we wondered whether the membrane fusion activity of IM30 is also pH-dependent.

Since sufficiently high concentrations of Mg^{2+} alone result in fusion of liposomes containing anionic lipids [21], we first analyzed the IM30-independent fusion propensities of the DOPG/MGDG (40/60) liposomes at different pH values in presence of 15 mM Mg^{2+}. Here, we observed a decreased fusion when the pH was lowered from 7.6 to 5.5 when 15 mM Mg^{2+} was present (Suppl. Figure S4), and no fusion was observed at 7.5 mM Mg^{2+}. In stark contrast, the IM30-induced membrane fusion activity in presence of 7.5 mM Mg^{2+} was substantially higher at pH 5.5 than at pH 7.6 (Figure 5a). Interestingly, IM30 was able to induce membrane fusion even in the absence of Mg^{2+} at pH 5.5 (Figure 5a, b). However, addition of 7.5 mM Mg^{2+} to 2.5 μM IM30 further increased its membrane fusion activity, outperforming the activity of 5 μM IM30 in absence of Mg^{2+}. Thus, Mg^{2+} clearly supports, but is not mandatory for, IM30-mediated membrane fusion at pH 5.5.

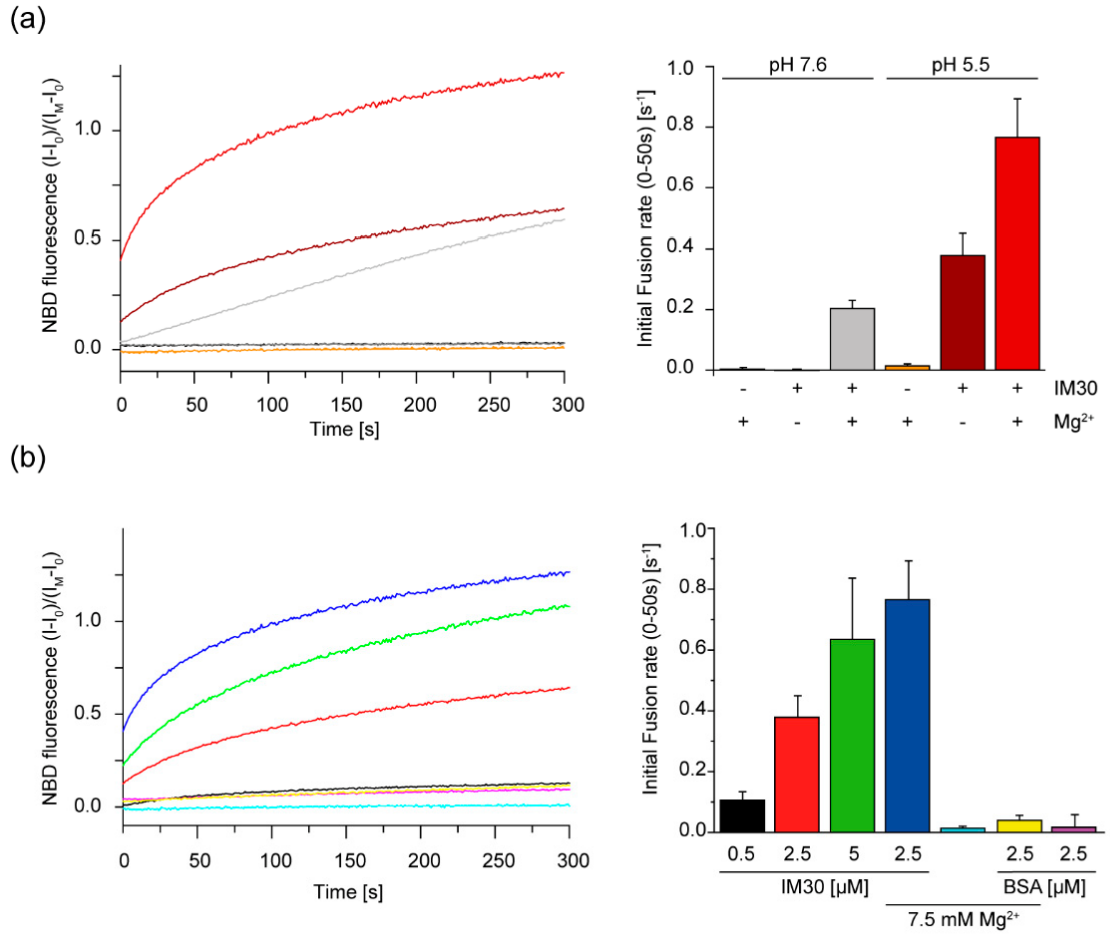

Figure 5. IM30-mediated membrane fusion is enhanced under acidic conditions.

(a) Liposome fusion was measured in presence of 2.5 μM IM30 and/or 7.5 mM Mg^{2+} by a FRET-based fusion assay. No membrane fusion was observed in presence of solely 7.5 mM Mg^{2+} at pH 5.5 or pH 7.6, respectively. At pH 5.5 and in presence of 7.5 mM Mg^{2+}, addition of 2.5 μM IM30 triggered increased membrane fusion compared to pH 7.6. Notably, at pH 5.5, membrane fusion was observed even in absence of Mg^{2+}. The initial fusion rates were calculated from the first 50 s. The curves represent the average of three independent measurements (n = 3, error bars=SD). The colors of the fusion curves (left) are defined in the bar diagram (right). **(b)** Increased liposome fusion was measured at pH 5.5 when the IM30 content was increased from 0.5 - 5 μM. Addition of 7.5 mM Mg^{2+} further enhanced the membrane fusion rate. Controls containing BSA instead of IM30 did not show any membrane fusion activity. The curves represent the average of three independent measurements. The initial fusion rate in the first 50 s was calculated for membrane fusion at pH 5.5 in presence of 0.5–5 μM μM IM30, for 2.5 μM IM30 + 7.5 mM Mg^{2+} and for the corresponding controls using BSA instead of IM30 (n = 3, error bars=SD). The colors of the fusion curves (left) correspond to the bar diagram (right).

DISCUSSION

The Structure and Membrane Interaction of IM30 is Modulated by a More Acidic pH

We here show that a more acidic environment induces changes in the IM30 secondary and tertiary structure (Figure 1, 2). While all observed changes were at least biphasic, not all followed the exact

same pattern in the pH range between 7.6 and 2.6. The surface hydrophobicity changed almost linearly between pH 6.7 and pH 4.2, as indicated by the increase in ANS fluorescence, whereas the changes in the CD-spectrum are most pronounced at pH 5.5, and have regained basically the original shape at pH 4.0. Thus, the protein structure observed at around pH 5.5 further alters at pH values below 5.5, most likely due to further protonation of particular amino acid side chains. While it remains unclear what structure is actually acquired at pH 5.5, the protein potentially contains some unconventional β-sheet structures, as, for example, described in McCubbin et al. [54]. Similar CD-spectra with a shifted β-sheet minimum were, for example, observed when the structure of small peptides was monitored upon pH changes or TFE treatment [55]. The intimate environment of Trp71 also changed in a biphasic manner when the pH was lowered, indicating a structural modification involving the region containing the coiled-coil forming helices 2 and 3 (Figure 2). Nevertheless, the observed rather minor changes of the Trp fluorescence indicate no drastic changes of the protein's tertiary (and potentially quaternary) structure, such as protein denaturation.

The observed changes of the secondary structure (Figure 1, 3) and the increase in the surface hydrophobicity (Figure 2) observed at low pH values, resemble structural changes observed previously in presence of Mg^{2+} [37]. Since presence of Mg^{2+} is mandatory for IM30's fusion activity (at physiological pH), we investigated to what extent an acidic pH influences the IM30 fusion activity. Indeed, when lowering the pH from pH 7.6 to 5.5, IM30-mediated membrane fusion was dramatically enhanced (Figure 5), which was not observed for Mg^{2+}-induced membrane fusion (Suppl. Figure S4). Furthermore, at pH 5.5, membrane fusion was triggered by IM30 even in the absence of Mg^{2+}, showing that IM30 is already fusion-competent under these conditions (Figure 5). This implies that the alterations in the CD spectrum observed at this pH are not only similar to the ones observed in presence of Mg^{2+}, but also that possibly the underlying structural changes and thus the functional consequences are similar. Thus, apparently both, protons and Mg^{2+}, induce and/or stabilize a fusion-competent conformation of IM30. As the divalent cation Mg^{2+} binds to IM30, potentially via negatively charged amino acid side-chains, protonation of negatively charged amino acids of IM30 is not unexpected and appears to have similar effects as Mg^{2+}-binding. However, protons appear to be much more effective in this aspect, since the structural changes are considerably more pronounced upon lowering the pH than upon addition of Mg^{2+}.

The enhanced fusion activity observed at acidic pH might be related to some extent to the increased IM30 membrane-binding propensity, as observed via Laurdan fluorescence spectroscopy as well as via QCM measurements. While membrane binding of IM30 is usually attributed to electrostatic interactions with negatively charged lipids [21], our results here indicate a partial contribution of

hydrophobic interactions to membrane binding. The increased proton concentration at lowered pH induces increased exposure of hydrophobic patches (Figure 2), thereby promoting hydrophobic interactions, leading to a higher membrane-binding affinity. On the other hand, increased proton concentrations will lead to a reduction of the membrane surface charge density, due to protonation of the lipid PG. Thus, it seems that the exposure of hydrophobic surface area accompanying proton binding outweighs the weakened electrostatic interactions between IM30 and the negatively charged membrane.

Physiological Implications of a pH-responsive IM30 Structure and Function

Proteins of the PspA/IM30/LiaH family are involved in membrane stabilization in bacteria and chloroplasts [29]. At least in *E. coli* and *Yersinia enterocolitica,* membrane defects and secretin mislocalization are sensed by the membrane proteins PspB and C, which induce the *phage shock protein (psp)* stress response via binding the effector protein PspA at the damaged membrane site, where it can stabilize the membrane [56]. Yet, not all bacteria expressing *pspA* encode the full *psp* response system: *e.g.*, in *Streptomyces lividans* the *psp* system only consists of a PspA homolog, which is also crucial under stress conditions [57], giving rise to the assumption that not all PspA homologs require PspB and PspC for being guided to membrane defects. The same appears to be true for IM30, as no IM30-related PspB or PspC homologs have been identified in cyanobacteria or chloroplasts yet. However, it still is enigmatic how PspA and IM30 ultimately stabilize membranes.

While PspA is suggested to maintain the proton motive force across the cytoplasmic membrane in a large number of Gram-negative bacteria [1,3,19,56], IM30 is thought to be of special importance for stabilizing TMs in chloroplasts and cyanobacteria [1,46,48]. Maintaining a ΔpH across the TM network in cyanobacteria as well as in chloroplasts is vital for energy production. In cyanobacteria, the TM system is a completely separated compartment [58], and due to proton translocation driven by electron transfer reactions, the pH of the thylakoid lumen is much more acidic than the pH of the cytoplasm. In the dark and at an external pH of about 7, the pH of the cyanobacterial cytoplasm is between 7 and 8, whereas the pH of the thylakoid lumen is between 4.5 and 5.5 [59–64]. In the light, the pH increases by at least 0.5 pH units in the cytoplasm, while the pH in the thylakoid lumen also roughly decreases by 0.5 pH units, due to the uptake of protons into the thylakoid lumen and extrusion of protons into the surrounding medium [65,66].

Cyanobacteria and chloroplasts need to constantly maintain a stable proton gradient across the TM, which involves preserving the integrity of a TM system. However, due to curvature stress and light-induced oxidative stress the TM system is prone to get destabilized or even damaged. In fact, IM30

appears to be of special importance for stabilizing the TM system in chloroplasts and cyanobacteria [1,46,48]. We here show that the structure of IM30 is pH sensitive, with a maximum effect on the IM30 structure observed in the range of pH 4 to 5 (Figure 1 and 2). Yet, IM30 is localized in the chloroplast stroma and cyanobacterial cytoplasm, respectively, with a fraction bound to the cytoplasmic face of the TM and the cytoplasmic membrane or inner envelope membrane in cyanobacteria or chloroplasts, respectively [28,67]. Thus, IM30 typically experiences pH values between 7 to 8.

However, defects in the TM system will result in protons leaking out of the TM lumen into the cytoplasmic space, leading to a spatio-temporal accumulation of protons in close proximity to the leak. We here suggest that IM30 "senses" and "repairs" such TM defects by changing its structure if located nearby areas of the TM where the proton concentration is locally increased. Although we cannot yet provide a detailed molecular mechanism, we show here that a decreased pH results in rearrangements of the IM30 structure (Figure 1 and 2). Most likely, acidification leads to protonation of ionizable amino acid side chains, which likely affects intra- and intermolecular electrostatic interactions as well as the protein's net surface charge [68]. The responsible pH-sensitive amino acids are hard to predict without a crystal structure of the protein, especially considering potential large pKa shifts of (buried) amino acids in proteins [68]. Nevertheless, the observed structural alterations clearly enhance the IM30 membrane binding affinity (Figure 4), which could result in preferential binding of IM30 to defect TM regions. How exactly IM30 stabilizes the defect membrane regions upon binding is currently unclear. Accumulation of IM30 at defined membrane regions has been observed *in vivo*, and it has been hypothesized that IM30 (as well as PspA) rings disassemble on membrane surfaces to form membrane-protective clusters [18,26,29]. However, experimental evidence supporting (or challenging) this hypothesis is missing thus far.

We here additionally show that the membrane fusion activity of IM30 is strongly enhanced at pH 5.5, even in the absence of Mg^{2+} (Figure 5). While it is reasonable to expect that an increased membrane-binding affinity results in an increased membrane fusion activity of IM30, membrane fusion and membrane protection would actually contradict each other at first glance, as membrane fusion requires partial membrane destabilization.

Then why should the IM30 membrane fusion activity get "activated" at defective membrane regions? We suggest that membrane sealing/repair at these defective regions involves membrane fusion. At pre-destabilized membrane regions, the energy cost for lipid reorientation is significantly lowered. Thus, it is reasonable to expect an increased fusion activity of IM30 especially at these sites, where IM30 is crucially involved in sealing the membrane leak. Membrane fusion might function as

an active membrane repair mechanism: IM30 binds to defective and/or stressed membrane regions and fuses an intact membrane patch to this area to seal the defect. Nevertheless, the general mechanism of TM repair *in vivo* still is largely unknown. Yet, a similar physiological role has *e.g.*, been suggested for the fusion activity of the dynamin-like protein DynA in *B. subtilis*, when cells are stressed by pore-forming agents, such as nisin or phages [69,70]. Similar to PspA and IM30, DynA aggregates to punctated foci *in vivo*, which are regions where membranes are supposed to be sealed. Spatio-temporal TM defects result in locally increased proton concentrations at defined TM regions. Due to a locally decreased pH, the IM30 structure rearranges, resulting in an increased membrane-binding affinity. Thus, the spatio-temporal drop in the pH enhances preferential binding of IM30 to leaky membrane regions. The lowered pH also renders IM30 more fusion competent, and IM30 seals defect membrane regions, which involves membrane fusion processes.

MATERIALS AND METHODS

Cloning, Expression, and Purification of IM30

IM30 of *Synechocystis* sp. PCC 6803 was heterologously expressed in *Escherichia coli* BL21 DE3 and purified as described [11,13,21,37]. In short, after expression, cells were lysed via sonification in lysis buffer (50 mM Na-Phosphate, 20 mM imidazole, 300 mM NaCl pH 7.6). The lysate was cleared by centrifugation and the supernatant was applied to a Ni^{2+}-NTA affinity column. The column was washed with increasing concentrations of imidazole and the protein was eluted with 500 mM imidazole. The elution fractions were pooled and the buffer was exchanged to 20 mM HEPES pH 7.6 by dialysis or gel-filtration (Sephadex G25).

Circular Dichroism Spectroscopy

Circular dichroism (CD) spectra were measured using a JASCO J815 CD spectrometer (JASCO Corporation, Tokyo, Japan). Spectra ranging from 190 to 260 nm were recorded at 20 °C with a scan rate of 100 nm/min, 1 nm steps and 1 s data integration time. Each sample contained 0.1 mg/mL IM30 and 10 mM HEPES buffer pH 7.6 or a mixture of HEPES buffer and phosphate buffer (pH 2.2) for each tested pH value in the range of pH 7.6 to 2.6. The samples were incubated for at least 15 min at room temperature. For each sample, three spectra were averaged and smoothed by the JASCO software package (Savitzky-Golay filter), if necessary. For quantification of the spectral change, the

spectra were fitted with three gaussian peaks, using the Multi-PeakFit function of Origin2019 (OriginLabs), which rendered values for the center of the peak and the peak areas.

ANS Fluorescence Measurements

If not mentioned otherwise, all fluorescence measurements were performed using a FluoroMax- 4 fluorimeter (Horiba Scientific, Kyoto, Japan) with an integration time of 0.1 s at 25 °C. For the ANS fluorescence measurements, 1 µM IM30 was mixed with 7.5 µM 8-anilinonaphthalene-1-sulfonic acid (ANS) (Sigma-Aldrich, Munich, Germany) in a mixture of 20 mM HEPES buffer (pH 7.6) and phosphate buffer (pH 2.2), resulting in samples with pH values ranging from pH 7.6 to 2.6. The samples were incubated in the dark for at least 15 min at room temperature. The excitation wavelength was 370 nm (slit widths 4 nm), the emission wavelength ranged from 400 to 650 nm (slit widths 4 nm). Fluorescence intensities of at least three independent measurements were averaged and spectra of ANS in the respective buffer in absence of the protein were subtracted.

Trp Fluorescence Measurements

1 µM IM30 were incubated in buffer (pH 2.6 – pH 7.6) for 2 h at 25 °C. Trp fluorescence was measured at 25 °C from 300 to 450 nm (slit width 3 nm) upon excitation at 280 nm (slit width 3 nm). The measurements were performed using a Fluoromax-4 spectrometer (Horiba Scientific, Kyoto, Japan).

Liposome Preparation

The lipids DOPG (1,2-dioleoyl-*sn*-glycero-3-phosphoglycerol), DOPC (1,2-dioleoyl-*sn*-glycero- 3-phosphocholine), MGDG (monogalactosyldiacylglycerol) and the fluorescently labeled lipids NBD-PE (1,2-distearoyl-*sn*-glycero-3-phosphoethanolamine-N-(7-nitro-2-1,3-benzoxadiazol-4-yl) and LissRhod-PE (Lissamine Rhodamine PE; 1,2-Dioleoyl-*sn*-glycero-3-phosphoethanolamine-N-(Lissamine Rhodamine B sulfonyl) (ammonium salt)) were purchased from Avanti Polar Lipids, Inc. (Birmingham, AL, USA). For liposome preparation, lipids were dissolved in chloroform/methanol (2:1, v/v). The organic solvent was evaporated under a gentle stream of nitrogen gas followed by overnight vacuum desiccation to remove any traces of solvent. Unilamellar liposomes were prepared by rehydration of the dried lipid film with the corresponding buffer and five cycles of freeze-thawing. For use in QCM measurements, the rehydrated lipid film was subsequently sonified with a tip-sonicator in an ice bath followed by centrifugation (10 min 16,500 g) to produce smaller liposomes.

For the liposome fusion assay, the liposomes were instead extruded 15 times through a 100 nm filter, using an extruder from Avanti Polar Lipids, Inc. (Alabaster, AL, USA).

Laurdan Fluorescence Measurements

Laurdan (6-dodecanoyl-*N*,*N*-dimethyl-2-naphthylamine) is a fluorescent dye that incorporates into lipid bilayers. Its fluorescence is sensitive to changes in the polarity of the environment and is therefore used to report changes of the membrane fluidity. In order to quantify the spectral changes, the Generalized Polarization (GP) value defined by [71] is calculated for each spectrum.

$$GP = \frac{I_{440} - I_{490}}{I_{440} + I_{490}} \quad (1)$$

Here, I_{440} and I_{490} are the fluorescence emission intensities at 440 and 490 nm, respectively.

Laurdan (Sigma, Taufkirchen, Germany) was added to the dissolved lipids MGDG/DOPG (40:60, w/w) in a molar ratio of 1:500. Unilamellar liposomes were prepared as described before. To analyze the effect of acidic pH on binding of IM30 to the liposomes, 0 - 6 µM IM30 and 0.1 mM liposomes in the corresponding buffer were mixed and incubated for 30 min in the dark at 25 °C. Buffers with different pH were prepared by mixing appropriate portions of 20 mM HEPES (pH 7.6) and 50 mM sodium acetate buffer (pH 4.8).

The fluorescence emission spectra were recorded at 25 °C on an FP8500 (JASCO Corporation, Tokyo, Japan) from 400 to 600 nm with excitation at 350 nm. The slit width was set at 2.5 nm for excitation and emission of Laurdan.

Membrane Fusion Assay

The influence of acidic pH on IM30-triggered liposome fusion was measured using a FRET- based assay, as described earlier [21,72]. Unlabeled liposomes were mixed in 10-fold excess with labeled liposomes containing two fluorescent dyes that form a FRET pair. Upon fusion of labeled with unlabeled liposomes, the FRET dyes redistribute over the membrane and consequently FRET decreases, resulting in increasing donor emission intensity. To simulate complete membrane fusion, liposomes containing only 1/10 of the fluorescently labeled lipids were used as a positive control.

To analyze the spontaneous fusion of MGDG/DOPG (40:60, w/w) membranes in absence of IM30, membrane fusion was induced via addition of 15 mM Mg^{2+}. For the IM30-dependent membrane

fusion assay, 2.5 µM IM30, 0.1 mM liposomes (MGDG/DOPG, 40:60, w/w) and 7.5 mM Mg^{2+} were used. All components were dissolved in an appropriate mixture of 20 mM Hepes (pH 7.6) and 50 mM sodium acetate buffer (pH 4.8).

The measurements were performed using a Fluoromax-4 spectrometer (Horiba Scientific, Kyoto, Japan). The IM30-containing solutions were preincubated with Mg^{2+} for about 5 min. After fast mixing of all compounds, the measurement was started immediately. Upon excitation of the FRET-donor NBD-PE at 460 nm, the donor emission was monitored at 525 nm over 300 s at 25 °C. The slit widths for excitation and emission were set at 5 nm.

The raw fluorescence data was converted to a fusion rate by equation 2, using the intensities of the negative control (I_0), positive control (I_M) and the measured sample (I) at every point in time t.

The initial fusion rate was determined by the slope of the fusion curve over the first 50 s.

$$\mathrm{NBD}\,(t) = \frac{I - I_0}{I_M - I_0} \tag{2}$$

Quartz Crystal Microbalance

For QCM measurements, only degassed buffers were used. QCM chips were cleaned with 30 mM EDTA, 2% SDS followed by 1 M NaOH. Then the chip was rinsed with water and dried with nitrogen. Prior to the measurement, the chip was treated with an ozone plasma cleaner for 20 s to remove any organic contaminations. Fifty microliters of a liposome suspension (1 mM lipid, 80% DOPC 20% DOPG (w/w)) was mixed with 450 µL 20 mM HEPES + 5 mM $CaCl_2$. A SiO_2-coated QCM chip (3T Analytik, Tuttlingen, Germany) was calibrated with the QCM device (3T Analytik, Tuttlingen, Germany). To produce an SLB on the SiO_2 surface, the chip was washed with HEPES buffer. Next, 150 µL of the liposome suspension was pumped on the chip (60 µL/min). After completion of liposome spreading (*i.e.*, when the frequency shift reached a constant level with a damping signal close to zero), the chip was washed again with HEPES buffer (pH 7.6) or HEPES/acetate buffer (pH 5.5) (150+300 µL; 60 µL/min). To start the measurement, 150 µL IM30 wt (4.5 µM in HEPES buffer or HEPES/acetate buffer was pumped on the SLB (60 µL/min). The pump was stopped and binding of the protein was monitored over ~3500 s.

REFERENCES

Vothknecht, U.C.; Otters, S.; Hennig, R.; Schneider, D. Vipp1: A very important protein in plastids *J. Exp. Bot.* 2012, *63*, 1699–1712, doi:10.1093/jxb/err357.

Westphal, S.; Heins, L.; Soll, J.; Vothknecht, U.C. Vipp1 deletion mutant of synechocystis: A connection between bacterial phage shock and thylakoid biogenesis? *Proc. Natl. Acad. Sci. U. S. A.* 2001, *98*, 4243–4248, doi:10.1073/pnas.061501198.

Joly, N.; Engl, C.; Jovanovic, G.; Huvet, M.; Toni, T.; Sheng, X.; Stumpf, M.P.H.; Buck, M. Managing membrane stress: The phage shock protein (Psp) response, from molecular mechanisms to physiology. *FEMS Microbiol. Rev.* 2010, *34*, 797–827, doi:10.1111/j.1574-6976.2010.00240.x.

Bultema, J.B.; Fuhrmann, E.; Boekema, E.J.; Schneider, D. Vipp1 and PspA. *Commun. Integr. Biol.* 2010, *3*, 162–165, doi:10.4161/cib.3.2.10529.

Hankamer, B.D.; Elderkin, S.L.; Buck, M.; Nield, J. Organization of the AAA+ Adaptor Protein PspA Is an Oligomeric Ring. *J. Biol. Chem.* 2004, *279*, 8862–8866, doi:10.1074/jbc.M307889200.

Otters, S.; Braun, P.; Hubner, J.; Wanner, G.; Vothknecht, U.C.; Chigri, F. The first α-helical domain of the vesicle-inducing protein in plastids 1 promotes oligomerization and lipid binding. *Planta* 2013, *237*, 529– 540, doi: 10.1007/s00425-012-1772-1.

Brissette, J.L.; Russel, M.; Weiner, L.; Model, P. Phage shock protein, a stress protein of Escherichia coli.

Proc. Natl. Acad. Sci. U. S. A. 1990, *87*, 862–866, doi:10.1073/pnas.87.3.862.

Osadnik, H.; Schöpfel, M.; Heidrich, E.; Mehner, D.; Lilie, H.; Parthier, C.; Risselada, H.J.; Grubmüller, H.; Stubbs, M.T.; Brüser, T. PspF-binding domain PspA1-144and the PspA·F complex: New insights into the coiled-coil-dependent regulation of AAA+ proteins. *Mol. Microbiol.* 2015, *98*, 743–759, doi:10.1111/mmi.13154.

Aseeva, E.; Ossenbühl, F.; Eichacker, L.A.; Wanner, G.; Soll, J.; Vothknecht, U.C. Complex formation of Vipp1 depends on its α-helical PspA-like domain. *J. Biol. Chem.* 2004, *279*, 35535–35541, doi:10.1074/jbc.M401750200.

Liu, C.; Willmund, F.; Whitelegge, J.P.; Hawat, S.; Knapp, B.; Lodha, M.; Schroda, M. J-domain protein CDJ2 and HSP70B are a plastidic chaperone pair that interacts with vesicle-inducing protein in plastids 1. *Mol. Biol. Cell* 2005, *16*, 1165–1177, doi:10.1091/mbc.E04-08-0736.

Fuhrmann, E.; Bultema, J.B.; Kahmann, U.; Rupprecht, E.; Boekema, E.J.; Schneider, D. The vesicle-inducing protein 1 from Synechocystis sp. PCC 6803 organizes into diverse higher-ordered ring structures. *Mol. Biol. Cell* 2009, *20*, 4620–4628, doi:10.1091/mbc.E09-04-0319.

Gao, F.; Wang, W.; Zhang, W.; Liu, C. α-Helical Domains Affecting the Oligomerization of Vipp1 and Its Interaction with Hsp70/DnaK in Chlamydomonas. *Biochemistry* 2015, *54*, 4877–4889, doi:10.1021/acs.biochem.5b00050.

Heidrich, J.; Wulf, V.; Hennig, R.; Saur, M.; Markl, J.; Sönnichsen, C.; Schneider, D. Organization into higher ordered ring structures counteracts membrane binding of IM30, a protein associated with inner membranes in chloroplasts and cyanobacteria. *J. Biol. Chem.* 2016, *291*, 14954–14962, doi:10.1074/jbc.M116.722686.

Saur, M.; Hennig, R.; Young, P.; Rusitzka, K.; Hellmann, N.; Heidrich, J.; Morgner, N.; Markl, J.; Schneider,

D. A Janus-Faced IM30 Ring Involved in Thylakoid Membrane Fusion Is Assembled from IM30 Tetramers.

Structure 2017, *25*, 1380–1390.e5, doi:10.1016/j.str.2017.07.001.

Liu, C.; Willmund, F.; Golecki, J.R.; Cacace, S.; Heß, B.; Markert, C.; Schroda, M. The chloroplast HSP70B- CDJ2-CGE1 chaperones catalyse assembly and disassembly of VIPP1 oligomers in Chlamydomonas. *Plant. J.* 2007, *50*, 265–277, doi:10.1111/j.1365-313X.2007.03047.x.

Wolf, D.; Kalamorz, F.; Wecke, T.; Juszczak, A.; Mäder, U.; Homuth, G.; Jordan, S.; Kirstein, J.; Hoppert, M.; Voigt, B.; et al. In-depth profiling of the LiaR response of bacillus subtilis. *J. Bacteriol.* 2010, *192*, 4680–4693, doi:10.1128/JB.00543-10.

Heidrich, J.; Thurotte, A.; Schneider, D. Specific interaction of IM30/Vipp1 with cyanobacterial and chloroplast membranes results in membrane remodeling and eventually in membrane fusion. *Biochim. Biophys. Acta - Biomembr.* 2017, *1859*, 537–549, doi:10.1016/j.bbamem.2016.09.025.

Siebenaller, C.; Junglas, B.; Schneider, D. Functional Implications of Multiple IM30 Oligomeric States. *Front. Plant. Sci.* 2019, *10*, 1–11, doi:10.3389/fpls.2019.01500.

Kobayashi, R.; Suzuki, T.; Yoshida, M. Escherichia coli phage-shock protein A (PspA) binds to membrane phospholipids and repairs proton leakage of the damaged membranes. *Mol. Microbiol.* 2007, *66*, 100–109, doi:10.1111/j.1365-2958.2007.05893.x.

Kleerebezem, M.; Crielaard, W.; Tommassen, J. Involvement of stress protein PspA (phage shock protein A) of Escherichia coli in maintenance of the protonmotive force under stress conditions. *Embo J.* 1996, *15*, 162–171, doi:10.1128/JCM.43.1.19.

Hennig, R.; Heidrich, J.; Saur, M.; Schmüser, L.; Roeters, S.J.; Hellmann, N.; Woutersen, S.; Bonn, M.; Weidner, T.; Markl, J.; et al. IM30 triggers membrane fusion in cyanobacteria and chloroplasts. *Nat. Commun.* 2015, *6*, doi: 10.1038/ncomms8018.

McDonald, C.; Jovanovic, G.; Ces, O.; Buck, M. Membrane stored curvature elastic stress modulates recruitment of maintenance proteins pspa and vipp1. *MBio* 2015, *6*, e01188-15, doi:10.1128/mBio.01188-15.

Zhang, L.; Kato, Y.; Otters, S.; Vothknecht, U.C.; Sakamoto, W. Essential role of VIPP1 in chloroplast envelope maintenance in Arabidopsis. *Plant. Cell* 2012, *24*, 3695–3707, doi:10.1105/tpc.112.103606.

DeLisa, M.P.; Lee, P.; Palmer, T.; Georgiou, G. Phage Shock Protein PspA of Escherichia coli Relieves Saturation of Protein Export via the Tat Pathway. *J. Bacteriol.* 2004, *186*, 366–373, doi:10.1128/JB.186.2.366-373.2004.

Foyer, C.H. Reactive oxygen species, oxidative signaling and the regulation of photosynthesis. *Environ. Exp. Bot.* 2018, *154*, 134–142.

Junglas, B.; Schneider, D. What is Vipp1 good for? *Mol. Microbiol.* 2018, *108*, 1–5, doi:10.1111/mmi.13924.

Cui, H.; Lyman, E.; Voth, G.A. Mechanism of membrane curvature sensing by amphipathic helix containing proteins. *Biophys. J.* 2011, *100*, 1271–1279, doi:10.1016/j.bpj.2011.01.036.

Gutu, A.; Chang, F.; O'Shea, E.K. Dynamical localization of a thylakoid membrane binding protein is required for acquisition of photosynthetic competency. *Mol. Microbiol.* 2018, *108*, 16–31, doi:10.1111/mmi.13912.

Thurotte, A.; Brüser, T.; Mascher, T.; Schneider, D. Membrane chaperoning by members of the PspA/IM30 protein family. *Commun. Integr. Biol.* 2017, *10*, e1264546, doi:10.1080/19420889.2016.1264546.

Chuartzman, S.G.; Nevo, R.; Shimoni, E.; Charuvi, D.; Kiss, V.; Ohad, I.; Brumfeld, V.; Reicha, Z. Thylakoid membrane remodeling during state transitions in Arabidopsis. *Plant. Cell* 2008, *20*, 1029–1039, doi:10.1105/tpc.107.055830.

Nagy, G.; Posselt, D.; Kovács, L.; Holm, J.K.; Szabó, M.; Ughy, B.; Rosta, L.; Peters, J.; Timmins, P.; Garab,

G. Reversible membrane reorganizations during photosynthesis in vivo: Revealed by small-angle neutron scattering. *Biochem. J.* 2011, *436*, 225–230, doi: 10.1042/BJ20110180.

Liberton, M.; Collins, A.M.; Page, L.E.; O'Dell, W.B.; O'Neill, H.; Urban, V.S.; Timlin, J.A.; Pakrasi, H.B. Probing the consequences of antenna modification in cyanobacteria. *Photosynth. Res.* 2013, *118*, 17–24, doi: 10.1007/s11120-013-9940-0.

Nestler, H.; Groh, K.J.; Schönenberger, R.; Eggen, R.I.L.; Suter, M.J.F. Linking proteome responses with physiological and biochemical effects in herbicide-exposed Chlamydomonas reinhardtii. *J. Proteomics* 2012, *75*, 5370–5385, doi:10.1016/j.jprot.2012.06.017.

Herbstová, M.; Tietz, S.; Kinzel, C.; Turkina, M.V.; Kirchhoff, H. Architectural switch in plant photosynthetic membranes induced by light stress. *Proc. Natl. Acad. Sci. U. S. A.* 2012, *109*, 20130–20135, doi:10.1073/pnas.1214265109.

Findinier, J.; Delevoye, C.; Cohen, M.M. The dynamin-like protein Fzl promotes thylakoid fusion and resistance to light stress in Chlamydomonas reinhardtii. *PLOS Genet.* 2019, *15*, e1008047, doi:10.1371/journal.pgen.1008047.

Thurotte, A.; Schneider, D. The fusion activity of IM30 rings involves controlled unmasking of the fusogenic core. *Front. Plant. Sci.* 2019, *10*, 108, doi:10.3389/fpls.2019.00108.

Heidrich, J.; Junglas, B.; Grytsyk, N.; Hellmann, N.; Rusitzka, K.; Gebauer, W.; Markl, J.; Hellwig, P.; Schneider, D. Mg2+ binding triggers rearrangement of the IM30 ring structure, resulting in augmented exposure of hydrophobic surfaces competent for membrane binding. *J. Biol. Chem.* 2018, *293*, 8230–8241, doi:10.1074/jbc.RA117.000991.

Pohland, A.C.; Schneider, D. Mg2+ homeostasis and transport in cyanobacteria - at the crossroads of bacterial and chloroplast Mg2+ import. *Biol. Chem.* 2019, *400*, 1289–1301.

Fuhrmann, E.; Gathmann, S.; Rupprecht, E.; Golecki, J.; Schneider, D. Thylakoid membrane reduction affects the photosystem stoichiometry in the cyanobacterium Synechocystis sp. PCC 6803. *Plant. Physiol.* 2009, *149*, 735–744, doi:10.1104/pp.108.132373.

Micsonai, A.; Wien, F.; Kernya, L.; Lee, Y.-H.; Goto, Y.; Réfrégiers, M.; Kardos, J. Accurate secondary structure prediction and fold recognition for circular dichroism spectroscopy. *Proc. Natl. Acad. Sci. U. S. A.* 2015, *112*, E3095–103, doi:10.1073/pnas.1500851112.

Urry, D.W.; Ji, T.H. Distortions in circular dichroism patterns of particulate (or membranous) systems. *Arch. Biochem. Biophys.* 1968, *128*, 802–807, doi: 10.1016/0003-9861(68)90088-X.

Duysens, L.N. The flattening of the absorption spectrum of suspensions, as compared to that of solutions.

Biochim. Biophys. Acta 1956, *19*, 1–12, doi: 10.1016/0006-3002(56)90380-8.

Biswas, S.; Kayastha, A. Spectroscopic Characterization Of Phaseolus Vulgaris Leucoagglutinin. *Protein Pept. Lett.* 2005, *11*, 1–7, doi: 10.2174/0929866043478392.

LaPorte, D.C.; Wierman, B.M.; Storm, D.R. Calcium-induced exposure of a hydrophobic surface on calmodulin. *Biochemistry* 1980, *19*, 3814–3819, doi: 10.1021/bi00557a025.

White, A. Effect of *pH* on fluorescence of tryosine, tryptophan and related compounds. *Biochem. J.* 1959, *71*, 217–220, doi: 10.1042/bj0710217.

Zhang, L.; Sakamoto, W. Possible function of VIPP1 in thylakoids: Protection but not formation? *Plant. Signal. Behav.* 2013, *8*, doi:10.4161/psb.22860.

Zhang, S.; Shen, G.; Li, Z.; Golbeck, J.H.; Bryant, D.A. Vipp1 is essential for the biogenesis of Photosystem I but not thylakoid membranes in Synechococcus sp. PCC 7002. *J. Biol. Chem.* 2014, *289*, 15904–15914, doi:10.1074/jbc.M114.555631.

Zhang, L.; Sakamoto, W. Possible function of VIPP1 in maintaining chloroplast membranes. *Biochim. Biophys. Acta - Bioenerg.* 2015, *1847*, 831–837, doi:10.1016/j.bbabio.2015.02.013.

Wada, H.; Murata', N. *Synechocystis PCC6803 Mutants Defective in Desaturation of Fatty Acids*; 1989, 30.

Sauerbrey, G. Verwendung von Schwingquarzen zur Wägung dünner Schichten und zur Mikrowägung.

Zeitschrift für Phys. 1959, *155*, 206–222, doi: 10.1007/BF01337937.

Reviakine, I.; Johannsmann, D.; Richter, R.P. Hearing What You Cannot See and Visualizing What You Hear: Interpreting Quartz Crystal Microbalance Data from Solvated Interfaces. *Anal. Chem.* 2011, *83*, 8838– 8848, doi: 10.1021/ac201778h.

Voinova, M.V.; Jonson, M.; Kasemo, B. "Missing mass" effect in biosensor's QCM applications. *Biosens. Bioelectron.* 2002, *17*, 835–841, doi: 10.1016/S0956-5663(02)00050-7.

Hennig, R.; West, A.; Debus, M.; Saur, M.; Markl, J.; Sachs, J.N.; Schneider, D. The IM30/Vipp1 C-terminus associates with the lipid bilayer and modulates membrane fusion. *Biochim. Biophys. Acta - Bioenerg.* 2017, *1858*, 126–136, doi:10.1016/j.bbabio.2016.11.004.

McCubbin, W.D.; Oikawa, K.; Kay, C.M. Circular dichroism studies on concanavalin A. *Biochem. Biophys. Res. Commun.* 1971, *43*, 666–674, doi: 10.1016/0006-291X(71)90666-8.

Bañares-Hidalgo, A.; Pérez-Gil, J.; Estrada, P. Acidic *pH* triggers conformational changes at the NH2-terminal propeptide of the precursor of pulmonary surfactant protein B to form a coiled coil structure. *Biochim. Biophys. Acta - Biomembr.* 2014, *1838*, 1738–1751, doi:10.1016/j.bbamem.2014.03.016.

Darwin, A.J. The phage-shock-protein response. *Mol. Microbiol.* 2005, *57*, 621–628, doi:10.1111/j.1365- 2958.2005.04694.x.

Vrancken, K.; Van Mellaert, L.; Anné, J. Characterization of the Streptomyces lividans PspA response. *J. Bacteriol.* 2008, *190*, 3475–3481, doi:10.1128/JB.01966-07.

Schneider, D.; Fuhrmann, E.; Scholz, I.; Hess, W.R.; Graumann, P.L. Fluorescence staining of live cyanobacterial cells suggest non-stringent chromosome segregation and absence of a connection between cytoplasmic and thylakoid membranes. *BMC Cell Biol.* 2007, *8*, doi: 10.1186/1471–2121–8–39.

Belkin, S.; Mehlhorn, R.J.; Packer, L. Proton gradients in intact cyanobacteria. *Plant. Physiol.* 1987, *84*, 25–30, doi:10.1104/pp.84.1.25.

Falkner, G.; Horner, F.; Werdan, K.; Heldt, H.W. *pH* Changes in the Cytoplasm of the Blue-Green Alga Anacystis nidulans Caused by Light-dependent Proton Flux into the Thylakoid Space . *Plant. Physiol.* 1976, *58*, 717–718, doi:10.1104/pp.58.6.717.

Gibson, J. Movement of acetate across the cytoplasmic membrane of the unicellular cyanobacteria Synechococcus and Aphanocapsa. *Arch. Microbiol.* 1981, *130*, 175–179, doi: 10.1007/BF00411073.

Kallas, T.; Dahlquist, F.W. Phosphorus-31 Nuclear Magnetic Resonance Analysis of Internal *pH* during Photosynthesis in the Cyanobacterium Synechococcus. *Biochemistry* 1981, *20*, 5900–5907, doi: 10.1021/bi00523a038.

Masamoto, K.; Nishimura, M. Estimation of internal *pH* in cells of blue-green algae in the dark and under illumination. *J. Biochem.* 1977, *82*, 483–487.

Padan, E.; Schuldiner, S. Energy transduction in the photosynthetic membranes of the cyanobacterium (blue-green alga) Plectonema boryanum. *J. Biol. Chem.* 1978, *253*, 3281–3286.

Nitschmann, W.H.; Peschek, G.A. Modes of proton translocation across the cell membrane of respiring cyanobacteria. *Arch. Microbiol.* 1985, *141*, 330–336, doi: 10.1007/BF00428845.

Scherer, S.; Stürzl, E.; Böger, P. Oxygen-dependent proton efflux in cyanobacteria (blue-green algae). *J. Bacteriol.* 1984, *158*, 609–614.

Bryan, S.J.; Burroughs, N.J.; Shevela, D.; Yu, J.; Rupprecht, E.; Liu, L.N.; Mastroianni, G.; Xue, Q.; Llorente- Garcia, I.; Leake, M.C.; et al. Localisation and interactions of the Vipp1 protein in cyanobacteria. *Mol. Microbiol.* 2014, *94*, 1179–1195, doi:10.1111/mmi.12826.

Pace, C.N.; Grimsley, G.R.; Scholtz, J.M. Protein Ionizable Groups: pK Values and Their Contribution to Protein Stability and Solubility. *J. Biol Chem.* 2009, *284(20),* 13285–13289, doi:10.1074/jbc.R800080200.

Sawant, P.; Eissenberger, K.; Karier, L.; Mascher, T.; Bramkamp, M. A dynamin-like protein involved in bacterial cell membrane surveillance under environmental stress. *Environ. Microbiol.* 2016, *18*, 2705–2720, doi:10.1111/1462-2920.13110.

Guo, L.; Bramkamp, M. Bacterial dynamin-like protein DynA mediates lipid and content mixing. *FASEB J.* 2019, *33*, 11746–11757, doi:10.1096/fj.201900844RR.

Parasassi, T.; Gratton, E. Membrane lipid domains and dynamics as detected by Laurdan fluorescence. *J. Fluoresc.* 1995, *5*, 59–69, doi: 10.1007/BF00718783.

Meers, P.; Ali, S.; Erukulla, R.; Janoff, A.S. Novel inner monolayer fusion assays reveal differential monolayer mixing associated with cation-dependent membrane fusion. *Biochim. Biophys. Acta - Biomembr.* 2000, *1467*, 227–243, doi: 10.1016/S0005-2736(00)00224-8.

Author Contributions: Conceptualization, C.S, B.J., N.H. and D.S.; methodology, C.S. and B.J.; validation, C.S, B.J., N.H. and D.S.; formal analysis, C.S. and B.J.; investigation, C.S., B.J. and A.L.; resources, D.S.; writing— original draft preparation, C.S, B.J., N.H. and D.S.; writing—review and editing, C.S, B.J., N.H. and D.S.; visualization, C.S. and B.J.; supervision, D.S; project administration, D.S.; funding acquisition, D.S. All authors have read and agreed to the published version of the manuscript.

Supplementary Materials: Supplementary materials can be found at www.mdpi.com/1422-0067/21/12/4530/s1.

Funding: This work was funded by the Max-Planck graduate center at the Max Planck institutes and the University of Mainz.

Acknowledgments: We thank Hildegard Pearson for carefully reading the manuscript.

Conflicts of Interest: The authors declare no conflict of interest.

ABBREVIATIONS

IM30	Inner-membrane associated protein of 30 kDa
PspA	Phage shock protein A
PMF	Proton motive force
TM	Thylakoid Membrane
CD	Circular Dichroism
SD	Standard Deviation
QCM	Quartz Crystal Microbalance

VIII.5. IM30 IDPs form a membrane protective carpet upon supercomplex disassembly

Benedikt Junglas[1], Roberto Orru[2], Amelie Axt[3,4], Carmen Siebenaller[1], Wieland Steinchen[5], Jennifer Heidrich[1], Ute A. Hellmich[1,6], Nadja Hellmann[1], Eva Wolf[2,7], Stefan A. L. Weber[3,4] and Dirk Schneider[1]

1 Department of Chemistry, Biochemistry, Johannes Gutenberg University Mainz, 55128 Mainz, Germany.
2 Institute of Molecular Physiology, Johannes Gutenberg University Mainz, 55128 Mainz, Germany.
3 Max Planck-Institute for Polymer Research, 55128 Mainz, Germany.
4 Institute of Physics, Johannes Gutenberg University Mainz, 55099 Mainz, Germany.
5 Philipps-University Marburg, Center for Synthetic Microbiology (SYNMIKRO) and Department of Chemistry, 35032 Marburg, Germany.
6 Centre for Biomolecular Magnetic Resonance (BMRZ), Goethe-University Frankfurt, 60438 Frankfurt, Germany.
7 Institute of Molecular Biology (IMB), 55128 Mainz, Germany. email: Dirk.Schneider@uni-mainz.de

ABSTRACT

Members of the phage shock protein A (PspA) family, including the inner membrane-associated protein of 30 kDa (IM30), are suggested to stabilize stressed cellular membranes. Furthermore, IM30 is essential in thylakoid membrane-containing chloroplasts and cyanobacteria, where it is involved in membrane biogenesis and/or remodeling. While it is well known that PspA and IM30 bind to membranes, the mechanism of membrane stabilization is still enigmatic. Here we report that ring-shaped IM30 super-complexes disassemble on membranes, resulting in formation of a membrane-protecting protein carpet. Upon ring dissociation, the C-terminal domain of IM30 unfolds, and the protomers self-assemble on membranes. IM30 assemblies at membranes have been observed before in vivo and were associated to stress response in cyanobacteria and chloroplasts. These assemblies likely correspond to the here identified carpet structures. Our study defines the thus far enigmatic structural basis for the physiological function of IM30 and related proteins, including PspA, and highlights a hitherto unrecognized concept of membrane stabilization by intrinsically disordered proteins.

INTRODUCTION

The *inner membrane-associated protein of 30 kDa* (IM30), also known as *vesicle inducing protein in plastids* (VIPP1), is a protein conserved in chloroplasts and cyanobacteria, where it is involved in thylakoid membrane (TM) biogenesis and/or maintenance[1–15]. A striking feature of IM30 protein family members is the ability to form large homo-oligomeric super-complexes with masses

exceeding 1 MDa[16–18]. With transmission electron microscopy (TEM), a ring-like organization with a distinct spike architecture has been observed for these complexes[19]. Besides ring structures, rod-like particles have also been observed that might form via ring stacking[17,19–24]. Although no high-resolution structure of IM30 is currently available, the IM30 structure appears to resemble the structure of its supposed ancestor, the bacterial *phage shock protein A* (PspA)[1,16,20]. For both protein monomers, six α-helical segments have been predicted. In addition, IM30 contains an extra helix at its C-terminus. A coiled-coil hairpin structure of two extended helices (helices 2 and 3) likely represents the structural core of both, PspA and IM30[25]. The structure of this fragment has recently been solved and was used as a template for the prediction of the IM30 full-length tertiary structure[19]. IM30 binds to membranes, where it forms assemblies, as it has been observed in *in vivo* studies with GFP-labeled IM30. In cyanobacteria and chloroplasts, such assemblies form dynamically at TM margins[3,9,11]. It has been proposed that these assemblies are involved in membrane protection/stabilization[4,26], due to the membrane protective effects of IM30 observed in *Arabidopsis thaliana* chloroplasts[9,10,13,14]. Importantly, the IM30 rings can adsorb to negatively charged membranes[12], albeit the formation of large ring structures is clearly not crucial for membrane binding *in vitro*, as small IM30 oligomers bind to negatively charged membranes with even higher affinity than IM30 rings[27]. Therefore, the interaction of IM30 with membranes may thermodynamically drive ring disassembly on membrane surfaces and thus entail disassembly of IM30 rings on the membrane surface. However, the question whether and how IM30 rings may disassemble during membrane interaction is completely unsolved so far.

Here we show that IM30 rings disassemble on membrane surfaces upon binding, and disassembly of IM30 rings involves unfolding of the predicted helices 3-7 located in the C-terminal half of the protein. Intrinsically disordered IM30 can bind with high affinity to membrane surfaces where protomers assemble to form a surface-covering carpet structure that stabilizes membranes.

RESULTS

IM30 super-complexes disassemble upon membrane binding and rearrange into carpet-like structures

Supporting the hypothesis that IM30 rings undergo a structural rearrangement upon membrane binding, we observed differences in the trypsin-digestion pattern of IM30 in absence *vs.* presence of phosphatidylglycerol (PG)-containing liposomes (Supplementary Fig. 1). Yet, these observations do not allow to clearly discriminate between rearrangements of the IM30 structure, shielding of IM30 regions due to membrane binding, or a combination of both. To probe potential ring disassembly upon membrane binding more directly, we next employed the FRET signal established between CFP

and Venus-labeled IM30 monomers incorporated in IM30 rings. While we observed decreasing FRET in the presence of PG liposomes (Fig. 1a), indicating a change in the relative distance between individual monomers upon membrane binding, these FRET changes remained minor and leveled off at high lipid concentrations. Thus, some structural changes potentially occur, possibly limited disassembly; yet, on average the monomers appear to stay in close contact on the membrane surface.

To visualize IM30 bound to PG supported lipid bilayers (SLBs), we next used Atomic Force Microscopy (AFM). While the expected ring structures were apparent when IM30 WT was bound to a mica surface (Supplementary Fig. 3a/b), flat carpet-like structures became visible on the membrane surfaces after incubating a PG bilayer with IM30 WT (Fig. 1a). These structures cover an area of several hundred nm^2, have a rough and uneven surface, and a height of 0.7-1.9 nm (average height: ~0.9 nm). As IM30 rings have a height of 13-15 nm [19], these carpets do clearly not form simply via lateral association of multiple IM30 rings on a membrane surface, again suggesting disassembly of membrane-bound IM30 rings into smaller oligomers and their rearrangement on the membrane surface. To investigate whether the formation of the observed carpet structures requires the preceding formation of IM30 rings, we made use of an oligomerization-impaired mutant (IM30*). At suitable NaCl concentrations, IM30* exclusively forms dimers (Supplementary Fig. 2). Since the IM30* carpets are alike those formed by the WT protein, we conclude that carpet formation by IM30 does not *per se* require ring formation (and subsequent dissociation) (Fig. 1.b). Noteworthy, carpet formation was not observed when IM30 WT or IM30* were incubated on mica surfaces, *i.e.,* in absence of a membrane (Supplementary Fig. 4). As cyanobacterial and chloroplast membranes typically contain about 40% negatively charged membrane lipids [15], we additionally analyzed the formation of carpet structures on PC: PG (60:40) membrane surfaces (Supplementary Fig. 5). Yet, IM30 WT, as well as IM30*, disassemble and form carpet structures, also on this membrane surface, excluding the possibility that the observed carpet-formation was induced by the highly charged membrane surface.

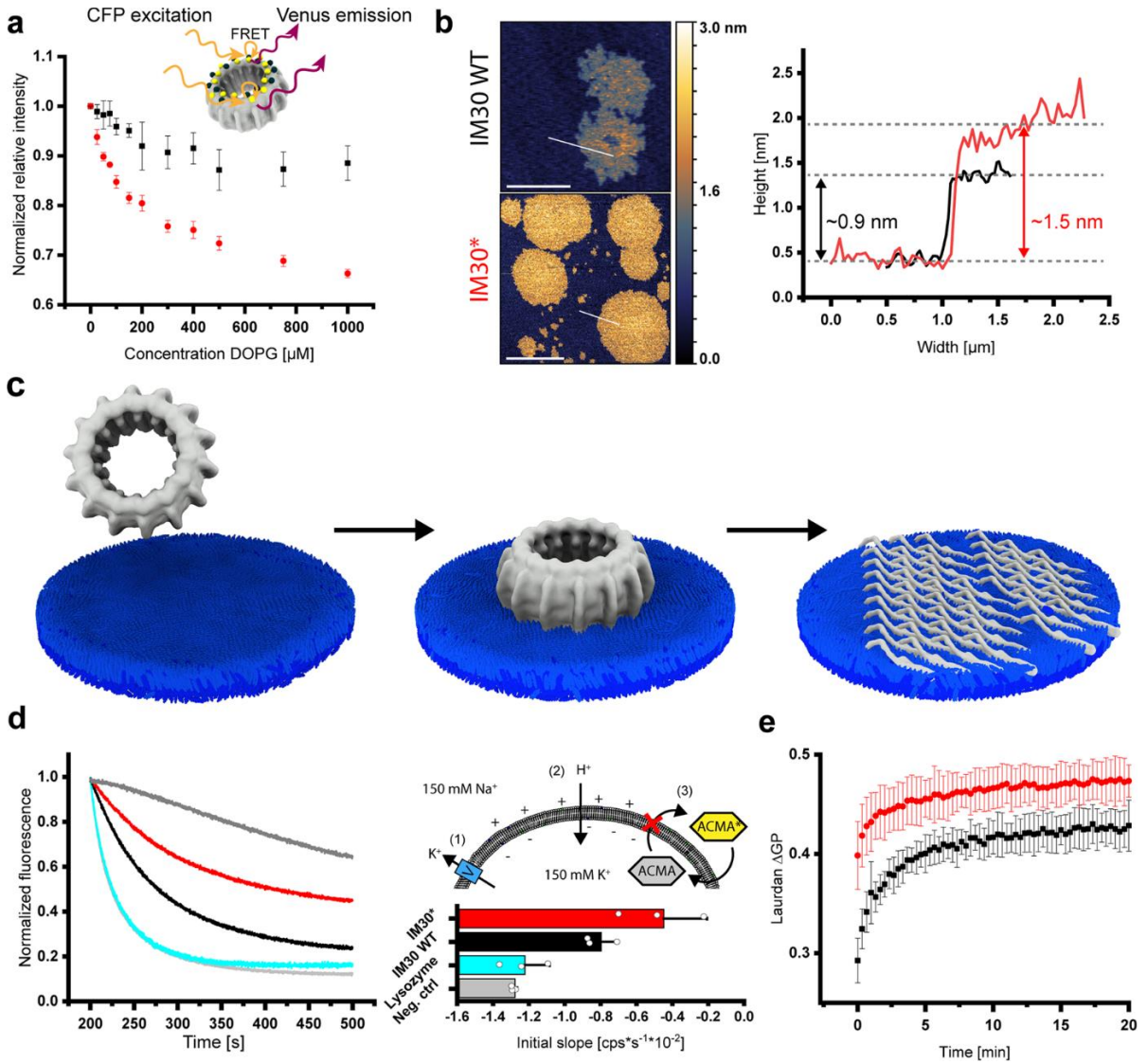

FIGURE 1

a FRET was measured using IM30 rings containing both, IM30-CFP and IM30-Venus monomers (red). The normalized relative fluorescence intensity (see "Methods") is plotted against the DOPG concentration. The intensity decreases with increasing DOPG concentrations, indicating an increasing average distance between the monomers upon interaction with membranes. Noteworthy, the fluorescence characteristics of the fluorophores alone change only slightly upon membrane binding, resulting in an apparently altered FRET (black). The error bars represent SD, $n = 5$. **b** The structure of IM30 WT and IM30* bound on a PG bilayer was imaged via AFM (the false-color ruler indicates the heights in the images). Both IM30 variants form carpet-like structures. The height-profiles (white section lines in the images) of the carpet-like structures indicate similar heights of IM30 WT (black line) and IM30* (red line) carpets. Determined heights are in the range of 0.7–1.9 nm). Single coherent IM30* carpets have increased dimensions, which leads to edges appearing rounder than the fractal-like shape of IM30 WT carpets. Scale bar: 1 µm (upper panel) and 3 µm (lower panel). **c** IM30 appears to initially bind to the membrane as a ring, followed by disassembly into small oligomers/monomers and rearrangement to a carpet-like structure. The ring structure was taken from EMD:3740(19). **d** ACMA fluorescence was used to monitor proton flux across DOPG membranes. Untreated liposomes were slightly permeable for protons (positive control, dark gray), whereas DOPG liposomes have high proton permeability in presence of 6% isopropanol (negative control, light gray). Lysozyme, which was used as a control (cyan), had no effect on the proton permeability. In presence of IM30 WT (black), the proton permeability of isopropanol-treated DOPG liposomes was reduced. This effect was much stronger in presence of IM30* (red). For quantitative analysis, the initial slope of the fluorescence changes was evaluated. Error bars represent SD ($n = 3$). **e** Lipid-binding of IM30 WT (black) and IM30* (red) to PG liposomes was determined via monitoring Laurdan fluorescence changes. IM30* affects the Laurdan fluorescence emission characteristics (ΔGP) much faster than the WT protein. Error bars represent SD ($n = 3$).

IM30 carpets protect destabilized liposomal membranes

Due to the importance of IM30 for TM maintenance, we wondered whether formation of the carpet structures might have functional consequences, *e.g.,* for the membrane integrity. We therefore compared the ability of IM30 WT super-oligomeric rings *vs.* IM30* dimers to maintain a proton gradient across a membrane, using a fluorescence-based proton leakage assay. Here, proton flux into the liposomes was measured as a decrease in ACMA fluorescence[28,29]. Only a small proton flux was measured with untreated PG liposomes (control, Fig. 1d), whereas addition of 6% (v/v) isopropanol weakened the membrane integrity considerably and increased the proton permeability of the liposomal membranes (negative control, Fig. 1d). Addition of IM30 WT and IM30* led to a reduced proton permeability of the liposomes, with IM30* showing enhanced reduction, possibly because the energetic cost of disassembly did not have to be paid. When we compared membrane binding of IM30* with IM30 WT rings over 20 min, the binding kinetics between the two proteins differed (Fig. 1e). Binding of the dimeric IM30* reached equilibrium earlier than the WT protein. This indicates that membrane binding of IM30 WT rings is slower than binding of smaller IM30* oligomers. The faster binding of IM30* could just be due to a larger number of particles adsorbing to the membranes compared to the rings, at identical monomer concentration. Only upon ring disassembly, full membrane adsorption of IM30 WT monomers is accomplished. Taken together, the interaction of IM30 with negatively charged membranes involves an initial membrane-binding step (potentially involving minor structural changes and ring destabilization), subsequent ring disassembly and rearrangement to carpet structures that form a protective layer on the membrane.

IM30 is highly flexible when not organized in super-complexes

As the dimeric IM30* protein appears to be hyper-functional in the proton leakage assay (Fig. 1d), we next elucidated the structure and shape of small IM30 oligomers using SAXS (small-angle X-ray scattering) coupled to size exclusion chromatography (SEC-SAXS). The SEC elution profile and the averaged scattering intensity confirmed a high sample homogeneity (Fig. 2a/b and Supplementary Fig. 10a). Analysis of the SAXS data resulted in a molecular mass of 63.2±5.2 kDa, expected for an IM30* dimer (Supplementary Fig. 10a). We obtained a radius of gyration of 6.13±0.05 nm and the pair distance distribution yielded a D_{max} of 26 nm (Fig. 2c and Supplementary Fig. 10b), indicating that IM30* adopts an elongated shape. When we compared our SAXS data with the structures of other proteins in a dimensionless Kratky-plot, it became apparent that IM30* does not have a well-defined, compact and spherical shape, but an extended and somewhat flexible structure with a high content of unstructured regions (Fig. 2d). Indeed, CD analyses showed that ~40% of IM30* is

unstructured. In contrast, the IM30 WT protein has an α-helix content of ~80% (Fig. 2e/f), in line with the IM30 structural model proposed by Saur *et al.*[19].

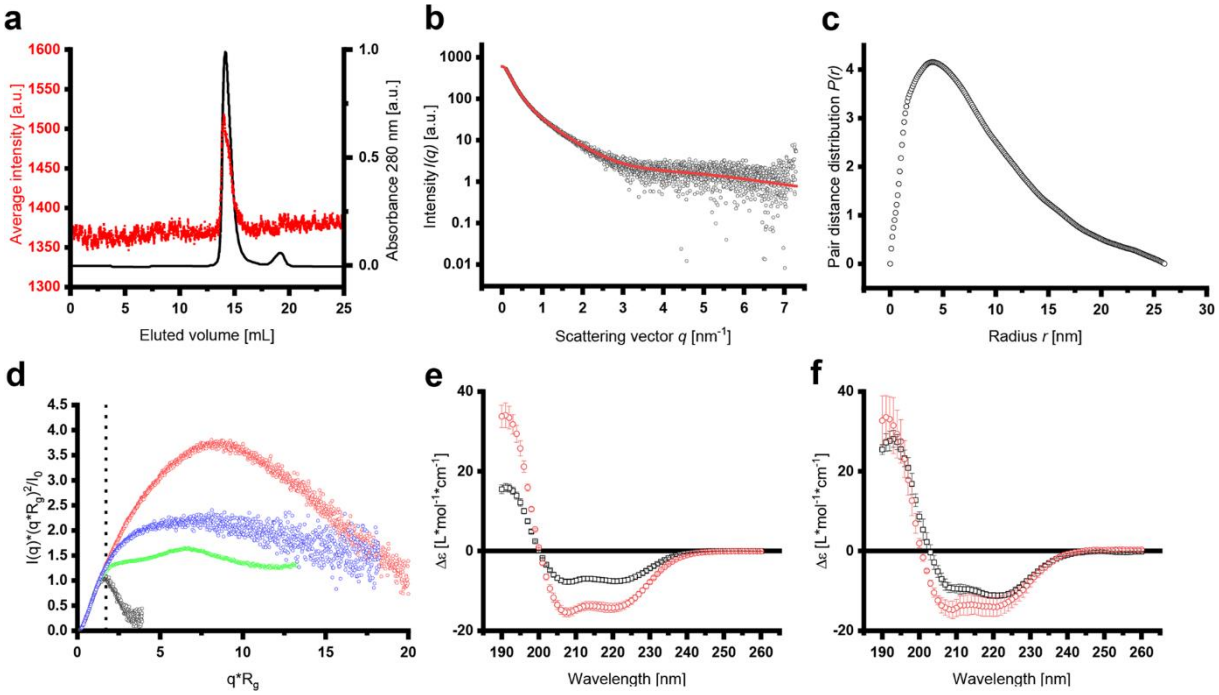

FIGURE 2

a The average SAXS intensity (red dots) is compared to the normalized absorbance at 280 nm (black line) over the whole elution volume. **b** The scattering intensity after buffer subtraction was plotted against the scattering angle q. The red line represents the fit of the data for the pair distance distribution analysis by GNOM (χ^2 = 1.0392). **c** The pair distance distribution analysis in the range of q = 0.0929–7.2965 nm^{-1} and forcing to 0 at D_{max} = 26 nm gave I_0 = 601.3 ± 4.5 cm^{-1} and R_g = 6.86 ± 0.07 nm (total quality estimate from GNOM 0.59). **d** A dimensionless Kratky-plot was used to compare the scattering data obtained with IM30* and other proteins. Apparently, the Kratky curve of IM30 dimers lies in between the curves of the unfolded lysine riboswitch protein and the Plakin domain of Human plectin, which has an extended protein shape, clearly implying an extended and somewhat flexible structure of IM30* dimers. The dashed line indicates q∗Rg=3–√q∗Rg=3. Black dots: Lysozyme (SASDA96)[72]. Red dots: Plakin domain of human plectin (SASDBC4)[73]. Green dots: Unfolded lysine riboswitch (BIOISIS ID:2LYSRR)[74]. Blue dots: IM30*. **e** The CD spectrum of IM30* (black squares) showed the typical characteristics of a mainly α-helical protein, i.e., pronounced minima at 222 and 208 nm. Yet, the amplitudes of the minima at 222 nm and 208 nearly doubled upon addition of 8 M TFE (red circles), which is known to induce α-helical structures in proteins/peptides. This implies that IM30* is highly unstructured. Error bars represent SD (n = 3). **f** The amplitudes of the minima at 222 nm and 208 nm of IM30 WT (black squares) only slightly increase upon addition of TFE (red circles), confirming the expected high content of α-helical structures. Error bars represent SD (n = 3). Based on the CD-spectra, the α-helix content of IM30* (e) was calculated to be ~57%, which is considerably lower than the reported and predicted α-helix content of IM30 WT of ~80%[16,17,18]. In presence of TFE, both proteins reach about 100% α-helix content.

IM30 dimers have a disordered N-terminus and C-terminal domain

To assess the inherent structural flexibility of IM30* dimers in greater detail, we carried out limited proteolysis and observed a single stable IM30 fragment of ~17 kDa, which contained parts of helix 1 to approximately half of helix 4 (Fig. 3a). In conclusion, helix 1 and helix 4-7 appear to be flexible in

the IM30 monomer, whereas helices 2 and 3 form a stable structure. To more clearly define the disordered regions, we next used hydrogen-deuterium exchange (HDX) measurements coupled to LC-MS on the IM30* and IM30 WT proteins. The results were mapped on the structural model of the monomer suggested by Saur *et al.*[19] (Fig. 3b). The HDX data confirmed that helices 2 and 3a in the suspected stable core region indeed exhibited only weak H/D exchange in both IM30 WT and IM30*. As expected, the flexible linker between helix 6 and 7 showed high H/D exchange in both variants, as did helix 7 (Supplementary Fig. 8a/b). The major structural difference between IM30* and IM30 WT lies in the region of the predicted helices 1, 3b, 4, and 5/6, where the WT protein showed less H/D exchange than the mutant (Fig. 3b and Supplementary Fig. 8). Likely, IM30* has an unstructured N-terminal domain (helix 1) and a mostly unstructured C-terminal domain (helices 3b-7), in excellent agreement with the limited proteolysis data (Fig. 3a). Indeed, using CD and 1D-^{1}H-NMR spectroscopy of the isolated IM30_H3b-7 fragment, we could confirm that this region is completely unstructured (Supplementary Fig. 9). Hence, IM30* dimers have an unstructured C-terminal domain, while IM30 is highly structured when organized in higher-ordered (ring) structures (Fig. 2e/f and Supplementary Fig. 8b). Thus, as IM30 WT forms nearly exclusively large super-complexes in solution[17,19], the formation of such higher-ordered structures appears to induce folding of otherwise intrinsically disordered IM30 regions.

To generate a structural model of IM30 monomers that includes the highly flexible nature of the IM30* C-terminus, we used a fragmentation-based modeling approach based on SAXS envelopes, starting from the structural model described in Saur *et al.*[19]. The SAXS envelopes were calculated as described in detail in Supplementary Fig. 10. We used the available X-ray structure of the PspA helix 2/3 fragment[25] as a rigid structural core and rendered the remaining parts of the structure as highly flexible and/or unstructured (as identified above). The resulting models and their respective SAXS envelopes are shown in Supplementary Fig. 12. All envelopes used are compatible with the experimental scattering pattern, fitting to a similar degree, and thus all calculated conformations likely represent actual IM30* dimer structures. Each envelope can be considered as a snapshot of one possible conformer, indicating enormous flexibility in the dimer interface region. In Fig. 4d, the intrinsic flexibility is visualized by superimposing individual monomers from each SAXS-model, aligned at the structured core (helices 2+3) of the respective monomers.

To define the IM30 regions that mediate dimer formation, we next used SEC coupled multi-angle laser light scattering (SEC-MALS) and determined the oligomeric state of two truncated IM30 versions, representing the stable structural core (helices 2+3; IM30_H2-3a) and the intrinsically disordered C-terminus (helices 3b-7; IM30_H3b-7) (Supplementary Fig. 13). While IM30_H3b-7 likely formed dimers, IM30_H2-3a exclusively formed monomers under our experimental

conditions. Thus, IM30* dimerizes via residues located in the C-terminal domains, in line with our dimer models (Supplementary Fig. 12), whereas the N-terminal region could mediate membrane interaction.In fact, stable membrane interaction of the isolated helix 2/3 fragment has been demonstrated recently[30]. Based on our dimer models (Supplementary Fig. 12), the flexible linker between the regions assigned as helix 6 and 7 in the model predicted by Saur *et al.*[19], appears to be crucially involved in mediating contacts between two adjacent monomers. To validate the predicted role of this region in IM30* dimerization, we created an IM30* variant where Ala227, located in the extended linker between helix 6 and 7 (compare Supplementary Fig. 2a), was mutated to Cys. This mutant ran as a dimer on SDS gels after purification (Fig. 3c), which indicates that the regions between helix 6 and 7 of two adjacent monomers are indeed in close contact in IM30* dimers. Noteworthy, also the IM30 WT protein formed covalently linked dimers, when we introduced the A227C mutation into the IM30 WT sequence (Fig. 3c). Thus, when not arranged in super-complexes, (at least) IM30 dimers have an intrinsically disordered C-terminal domain that clearly is involved in protein dimerization (as shown here). Furthermore, at reduced salt concentrations, this domain can also form higher-ordered oligomers (Supplementary Fig. 13c), and thus the isolated disordered region likely has multiple positions for binding other IM30 proteins, which facilitates self-assembly on membranes.

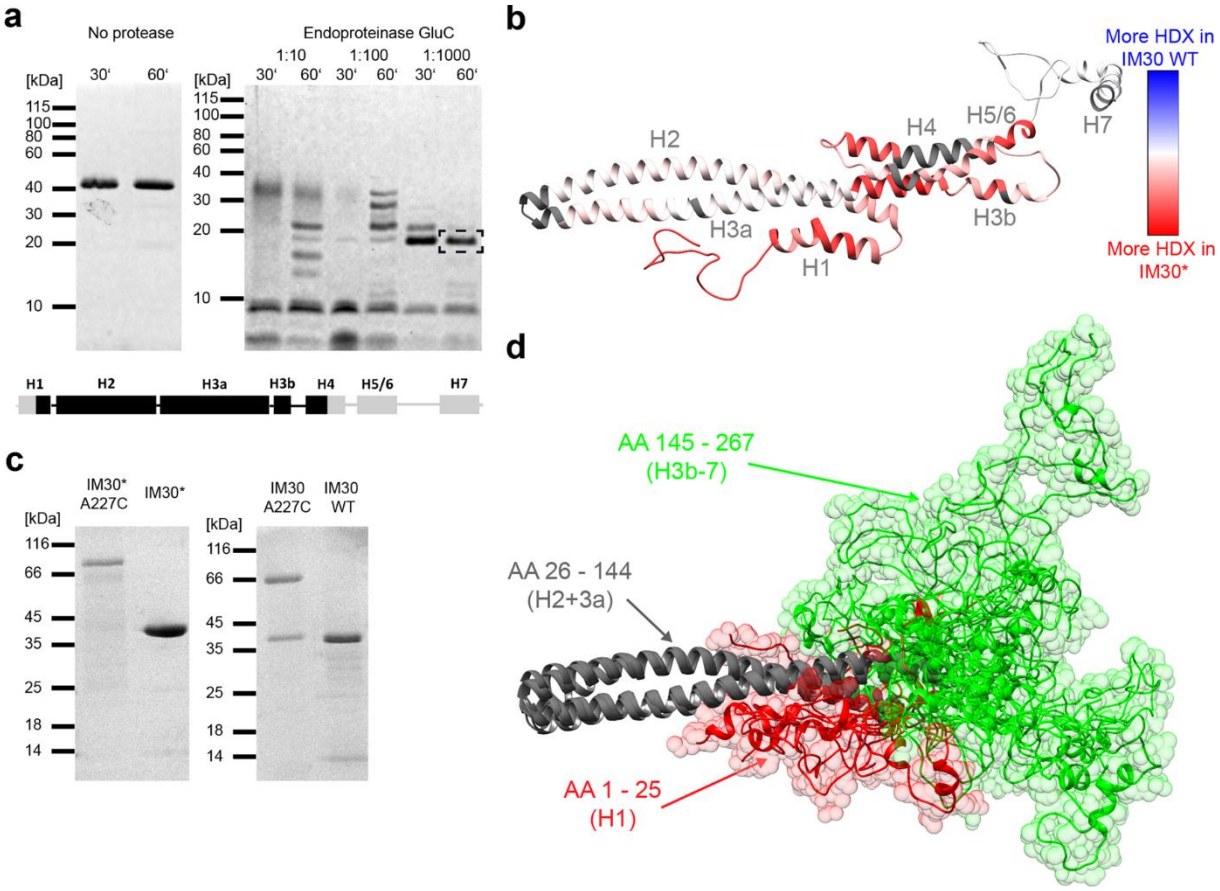

FIGURE 3

a Limited proteolysis of IM30*: IM30* was incubated with the endoproteinase GluC at different enzyme-to-substrate ratios for 30 or 60 min, respectively. The peptide patterns were analyzed via SDS-PAGE. The band highlighted with a black box was analyzed by mass spectrometry. Below, the predicted secondary structure of IM30 is shown, whereby each box represents an α-helical segment. After treatment with endoproteinase GluC, a stable helix 2/3 fragment was identified (with a sequence coverage of ~60%). For more details, see Supplementary Fig. 7 **b** The difference of relative HDX between IM30* and IM30 WT after 10 s mapped on the predicted IM30 monomer structure revealed an increased flexibility of helix 1 and helices 3a-5/6 of IM30* compared to the WT. A large part of helix 7 and the linker region between helix 7 and 6 is highly flexible in both variants. Dark gray regions mark sites where no peptides were detected in the HDX experiment, and thus no data is available. (For more details see Supplementary Fig. 8). **c** SDS-PAGE analysis of A227C mutants of IM30 WT and IM30* in absence of reducing agents. d IM30 monomer models generated based on the SAXS data were aligned at helix 2 and 3a to visualize the flexibility of the C-terminal region. Helices 2 and 3a (amino acids 26–144) are depicted in gray, the C-terminal amino acids 145–267 (H3b-7) are colored in green, and amino acids 1–25 (H1) in red. The N-terminal region (red) fills a small volume, starting from the rim between helix 2 and 3 with an only small overlap between the N-terminal and the C-terminal regions. However, the C-terminal region (green) nearly fills the entire conformational space at the end of the structural core, with higher accumulation at the very end of helix 3a.

DISCUSSION

The core structure of IM30 proteins is the coiled-coil formed by the helices 2 and 3[15,19,30,31]. This structure is stable even in the isolated, monomeric helix 2-3a fragment[30]; thus, no additional interactions with other parts of the protein are required for secondary and tertiary structure

formation of this fragment. In contrast, the isolated C-terminal region comprising helix 3b-7 is largely unstructured, albeit capable of forming stable dimers. If combined in the full-length WT protein, large oligomeric rings form, in which also the helix 3b-7 region appears to be mostly α-helical (Supplementary Fig. 8b). Thus, folding and homo-oligomerization of the h3b-7 region are interconnected, and inter-molecular interactions within the oligomer appear to induce the formation of α-helices. This interconnection is supported by the observation that the C-terminal region of the oligomerization-incompetent mutant IM30* remains unstructured even in the full-length protein, most likely because stabilizing interactions with neighboring protomers are largely reduced. Actually, the structure of the full-length IM30* protein resembles the sum of the two WT fragments. Thus, it is reasonable to assume that also in the full-length WT protein the C-terminal region is largely unstructured when the protein is not part of IM30 super-complexes.

While the isolated C-terminal region of IM30 oligomerizes, assembly of IM30 ring super-complexes involves additional interactions between other IM30 regions. In fact, we recently observed that the isolated helix 2/3 coiled-coil does have an intrinsic propensity to dimerize[30] but does not form higher-ordered super-complexes. Thus, interactions involving both, the helix 2-3 coiled-coil as well as (at least) the region containing helices 4-6, are required for ring formation[30].

Likely, the residues of the conserved FERM cluster located in helix 4 are crucially involved in mediating and/or stabilizing contacts between adjacent IM30 protomers in the ring. Weakening (or abolishing) these contacts via mutation of these residues has now enabled us to analyze the structure and activity of small IM30 oligomer, *i.e.*, IM30* dimers. While the structure of the helix 2-3 core is mostly unaffected when the dimers are compared with the super-complexes (see Fig. 3b), the structure of the C-terminal helices 4-7 dramatically differs when IM30$^{(*)}$ monomers are not part of ring super-complexes. While the introduced Ala residues were expected to further promote α-helix formation[32], the C-terminal part of the here analyzed variant remains completely unstructured (Fig. 3).

Yet, the dimeric IM30* protein shows faster membrane binding and more efficient membrane protection than the WT protein (Fig. 1d/e). This observation is perfectly in line with the recent notion that the isolated helix 2-3 coiled-coil effectively binds to membrane surfaces[30]. As this coiled-coil is buried and involved in protomer-protomer interactions when IM30 monomers are part of higher-ordered ring structures[19,30], the WT protein can efficiently bind to membrane surfaces only upon ring disassembly. This crucial step in carpet formation is not required anymore in case of the dimeric IM30* protein, where the helix 2/3 coiled-coil is readily exposed to facilitate membrane binding. However, membrane binding of the helix 2-3 coiled-coil alone does not result in membrane

protection, but rather in membrane destabilization[30]. This strongly suggests that the C-terminus is mainly responsible for the membrane protecting activity of IM30, in line with the observation that the isolated C-terminus oligomerizes (Supplementary Fig. 13a). As shown here, IM30-mediated membrane protection is associated with the formation of carpet-like structures on the membrane surface (Fig. 1). These carpets form via association of IM30 protomers on the membrane surface, but not in solution, and involve interactions between the disordered C-terminal regions.

Disordered protein domains exhibit an increased surface area for interaction, which can be beneficial for interaction with multiple binding partners. Self-assembling IDPs (intrinsically disordered proteins) can form higher-ordered protein complexes, where disordered protomers undergo binding-induced folding during super-complex formation[33,34,35], which also appears to be the case when IM30 rings form in solution. *Vice versa*, IM30 rings appear to disassemble upon membrane binding and condensate into extended carpets on the membrane, which again requires interactions between the disordered C-termini. Noteworthy, while not observed here, carpet formation could also involve partial structuring of this region.

Protein self-assembly on membrane surfaces, resulting in membrane-covering protein structures, has been observed before, *e.g.* in case of Alzheimer's or Parkinson's disease[36,37]. Yet, here formation of protein assemblies on membrane surfaces results in membrane destabilization and rupture. In contrast, IM30 carpets suppress proton leakage in liposomes and thereby maintain the integrity of membranes, as previously suggested for its ancestor PspA, which is thought to form scaffold-like structures to cover large membrane areas and prevent leakage[38,39]. The idea of IM30 and PspA having similar membrane stabilizing functions is in agreement with the observation that IM30 can functionally complement *E. coli pspA* null mutants[40]. This finding is also in line with the observation that IM30-overexpressing *Arabidopsis thaliana* strains display improved heat stress recovery[14] and that IM30 forms large assemblies at TMs in cyanobacteria under stress conditions[11,14]. These assemblies, which likely correspond to the IM30 carpet structures observed in the present study, have been identified *in vivo* to dynamically localize, preferably at stressed TM regions[3]. In fact, dynamic self-assembly is typically observed with IDPs, often involving liquid-liquid phase separation[33,41,42]. In contrast to the formation of membrane-less organelles in cells, induced by liquid-liquid phase separation of IDPs, demixing into a condensed and a protein-light fraction (*i.e.* carpets and unassociated but membrane-attached protomers) appears to take place on the membrane surface in case of IM30. Restricting protein-protein interaction to the membrane surface limits the degrees of freedom to a 2D surface, which likely increased the efficiency of carpet formation.

METHODS

Expression and purification of IM30

N-terminally His-tagged *Synechocystis* IM30 (IM30 WT; from *Synechocystis sp.* PCC 6803) was expressed in *E. coli* BL21 (DE3) using a pRSET6 based plasmid. Cells were resuspended in 50 mM NaPhosphate, 300 mM NaCl, 20 mM imidazole (pH 7.6) and lysed by sonification. IM30 was purified from the cleared lysate using Ni-Affinity chromatography[12]. IM30* (E83A, E84A, F168A, E169A, R170A, M171A), IM30_A227C (A272C) and IM30*_A227C (E83A, E84A, F168A, E169A, R170A, M171A, A227C) were generated via site-directed mutagenesis. The WT-fragments IM30_H2-3a (amino acids 22-145) and IM30_H3b-7 (amino acids 147-267) were generated by PCR cloning[30]. IM30-CFP and IM30-Venus were generated by restriction digestion and T4 ligation of the CFP/Venus fragments into pRSET *Syn*IM30 plasmids[43]. All IM30 variants were expressed and purified as described for the WT[12]. After isolation, the proteins were further purified by size exclusion chromatography (Superdex 200 16/60 HL, GE Healthcare) and eluted in 20 mM HEPES pH 7.6 at 8 °C. Peak fractions were pooled and concentrated by a centrifugal filter unit (PES membrane (PALL), 5000 g, 4 °C). Protein concentration was estimated by absorbance at 280 nm or 230 nm for the IM30_H3b-7, respectively.

Size Exclusion Chromatography (SEC)

The oligomeric state of IM30* and IM30 fragments was analyzed using an ÄKTA basic system (GE Healthcare) with a Superose12 10/300 GL column (GE Healthcare) equilibrated with 20 mM HEPES pH 7.6 and 0, 50, 100, 150 or 300 mM NaCl at 8 °C. Protein elution was monitored at 280 nm. The column was calibrated using proteins of known molecular mass.

SEC coupled multi-angle laser light scattering

The oligomeric states of IM30_H2-3a and IM30_H3b-7 were analyzed by SEC coupled multi-angle laser light scattering (SEC-MALS). Protein solutions of IM30_H2-3a or IM30_H3b-7 in 25 mM HEPES, 125 mM NaCl, 5% glycerol (w/w) were analyzed at RT, using a Superdex 200 Increase 10/300 GL column (GE Healthcare) equilibrated with 25 mM HEPES (pH 7.5), 125 mM NaCl, 5% glycerol (w/w) connected to an UV-Vis detector (BioRad UV 1806) and a MALS detector (Wyatt DAWN DSP) using an Agilent 1100 series pump. Protein elution was monitored by absorbance at 280 nm for IM30_H2-3a (ε_{280}=0.417 cm^2*mg^{-1}) or 230 nm for IM30_H3b-7 (ε_{230}=2.747 cm^2*mg^{-1}), respectively.

Trypsin digestion of IM30

2.5 µM IM30 WT was incubated in absence or presence of 0.1 mM DOPG (dioleoylphosphatidylglycerol; Avanti Polar lipids) unsized unilamellar liposomes[12] for 30 min at RT. Trypsin (bovine pancreas, 5000 USP/mg, Sigma-Aldrich) was added to a final concentration of 0.01 mg/mL and the mixture was incubated for 60 min at 4 °C. The mixture was sampled periodically and the reaction in each sample was stopped by adding 5x SDS loading buffer (containing 250 mM Tris, 10% SDS (w/v), 0.2% bromophenol blue (w/v), 50% glycerol (w/v), 500 mM DTT) and immediate heating to 95 °C. The samples were analyzed via SDS-PAGE on a 12% acrylamide gel.

Limited proteolysis

IM30* in 20 mM HEPES pH 7.6 was incubated with the endoproteinase GluC on ice at protease:protein ratios of 1:10, 1:100 and 1:1000 for 30 or 60 min. The reaction was stopped by addition of 5xSDS-sample buffer and subsequent heating to 95 °C. Samples were analyzed by SDS-PAGE on a 12% acrylamide gel. A suitable band was cut and analyzed by in-gel digestion followed by MALDI mass fingerprinting[44].

FRET measurements

For FRET (Förster resonance energy transfer) measurements, IM30-CFP and IM30-Venus were expressed as described[43] and copurified after mixing cell pellets prior to cell lysis in a ratio of 27% CFP and 63% Venus (w/w). A solution with 0.2 µM of the purified CFP/Venus labeled IM30 rings was incubated with increasing DOPG concentrations (0 – 1000 µM lipid, unilamellar liposomes) for ~2 h at RT. Fluorescence was measured using a FluoroMax 4 fluorimeter (Horiba Scientific). For FRET measurements, an excitation wavelength of 420 nm (slit width 3 nm) was chosen and spectra were recorded from 440 - 700 nm (slit width 3 nm). In order to correct for the contribution of liposome light scattering and to detect a change in the relative contribution of CFP and Venus fluorescence due to decreased FRET, a superposition of spectra measured for the individual components in absence of the others was fitted to each spectrum (equation 1) yielding the fractional contribution *f* for each spectrum, relative to the corresponding reference spectrum.

$$S_{meas} = f_{lip}S_{lip} + f_{cfp}S_{cfp} + f_{ven}S_{ven} \quad (1)$$

The buffer spectrum was subtracted beforehand. In presence of liposomes f_{cfp} tends to increase, while f_{ven} tends to increase, indicating reduced FRET. Since the overall change is not very large, the trend

in the values for f is overlaid by the slight change in the individual apparent quantum yields, as determined by measuring the CFP and Venus fluorescence in absence of the FRET partner, but presence of lipids. Furthermore, variations in the IM30 concentration leads to scattering of the f values. In order to correct for the variations of IM30 concentration, the data are presented as ratio of f_{ven}/f_{cfp} and finally normalized to the value in absence of liposomes. By comparing the resulting curve with the one observed for the controls (f_{ven}/f_{cfp} obtained individually in absence of the FRET partner) the effect of FRET can be distinguished from the effect of changes in quantum yield due to presence of liposomes. This procedure was performed for three sets of data (each including control and FRET measurements), and the average and standard error calculated for the resulting normalized f-ratio.

CD spectroscopy

CD spectra of IM30*, IM30_H3b-7 and IM30 WT (0.1 mg/mL) were measured in absence and presence of 2,2,2-trifluoroethanol (TFE, 8 M) using a JASCO-815 CD spectrometer with an MPTC-490S temperature-controlled cell holder. Spectra were measured from 260 to 190 nm (cell length 0.1 cm, 1 nm data pitch, 5 nm bandwidth, 100 nm/min, 1 s data integration time, averaged over 6 accumulations of the same sample). Spectra were smoothed with a Savitzky-Golay filter and the spectra of three samples were averaged. The secondary structure composition was analyzed with BeStSel[45].

The stability of the secondary structure of IM30 WT in 10 mM HEPES or Tris was measured by urea denaturation. The protein was incubated with 0 to 5 M urea overnight. CD spectra were measured from 200 nm to 260 nm (2 nm bandwidth, 1 s data integration time, 100 nm/min, 9 accumulations per sample). The ellipticity at 222 nm was plotted against the urea concentration and the resulting denaturation curve was normalized between 0 and 1, assuming full denaturation at 5 M urea. Then the data were fitted with a two-state unfolding model:

$$f_D = \frac{F - U}{1 + e^{(c - T_m)/dc}} + U \qquad (2)$$

Where f_D is the fraction of denatured protein, F is the folded state, U is the unfolded state, c is the concentration of urea and T_m is the transition midpoint.

The thermal stability of IM30* at increasing NaCl concentrations and of IM30 WT at increasing isopropanol concentrations was determined via CD spectroscopy. During the temperature ramp, CD spectra were measured from 200 to 250 nm (cell length 0.1 cm, 1 nm data pitch, 5 nm bandwidth,

200 nm/min, 1 s data integration time, averaged over 3 accumulations of the same sample). The temperature gradient was set to 15 - 95 °C (2 °C steps, overall heating rate 0.27 °C/min). Spectra were smoothed with a Savitzky-Golay filter. The denaturation curves (ellipticity at 222 nm *vs.* temperature) from three independent measurements were averaged. The first derivative of the averaged denaturation curves was used to determine the phase transition temperature as the center of the transition peak.

Hydrogen-deuterium exchange

For comparison of soluble IM30 with membrane-bound IM30, IM30 (37 µM) was preincubated in 20 mM HEPES buffer or 20 mM HEPES buffer with 2.5 mM DOPG (unilamellar liposomes). Prior to the measurement the samples were diluted 10-fold in D_2O-containing buffer (20 mM HEPES-Na pH 7.6).

For comparison of IM30 with IM30*, a 50 50 µM solution of each protein was diluted 10-fold in D_2O-containing buffer (20 mM HEPES-Na pH 7.6). Sample preparation for hydrogen-deuterium exchange mass spectrometry (HDX-MS) was aided by a two-arm robotic autosampler (LEAP Technologies).

After incubating for 10/95/1000/10000 s at 25 °C, the reaction of all samples was stopped at 1 °C by mixing with an equal volume of pre-dispensed quench buffer (400 mM potassium phosphate + 2 M guanidine-HCl pH 2.2) and 100 µl of the resulting mixture injected into the LC-MS system. Peptide generation, chromatography, mass spectrometry, and data analysis were carried out as described before[46,47].

Nuclear magnetic resonance (NMR) spectroscopy

The ^{1}H NMR spectrum of a 110 µM sample of IM30_H3b-7 in 20 mM HEPES pH 7.6, 100 mM NaCl supplemented with 10% D_2O was recorded on an 800 MHz Bruker Avance III HD NMR spectrometer equipped with a triple resonance HCN-cryogenic probe head at 298 K. Suppression of the water signal was achieved by excitation sculpting, using a Bruker standard pulse sequence. The spectrum was processed with Topspin (Bruker, Karlsruhe, Germany).

SEC coupled small-angle X-ray scattering (SEC-SAXS)

SAXS experiments were performed at beamline P12 operated by EMBL Hamburg at the PETRA III storage ring (DESY, Hamburg, Germany). SAXS data, *I(q) versus* q, where $q=4\pi\sin\theta/\lambda$ is the

momentum transfer and 2θ is the scattering angle and λ the X-ray wavelength (λ =1.24 Å; 10 keV), were collected using online size exclusion chromatography with a splitter, directing half of the eluted sample to MALS light detectors as described in[48] and the remaining half to the beamline for SAXS data collection. The protein was heated to 50 °C and subsequently cooled down to room temperature slowly followed by buffer exchange via SEC to 25 mM HEPES (pH 7.5), 125 mM NaCl, 5% glycerol (w/w) and 2 mM TCEP. This treatment appeared to be necessary, as especially lipids, which tend to stick to IM30 proteins even after purification by usual SEC[16], were removed. The structure of the protein was verified by comparing CD-spectra before and after the procedure (Supplementary Fig. 2g). 75 µL of 14.4 mg/mL IM30* were loaded on a Superdex 200 10/300 GL column (GE Healthcare) equilibrated with 25 mM HEPES (pH 7.5), 125 mM NaCl, 5% glycerol (w/w) and 2 mM TCEP at RT. Each run consisted of 50 minutes of data-collection, with 3000 frames being collected at an exposure time of 1 s. Data were analyzed using the ATSAS software package[49]. The primary 2D-data underwent standard automated processing (radial averaging), and background subtraction was performed using CHROMIXS[50], combined with additional manual and statistical evaluation (*e.g.*, for radiation damage) to produce the final 1D-SAXS profiles presented here. The molecular mass of the particles across the analyzed peak was calculated based on the methods implemented in CHROMIXS. The values presented in this report are averages of both the consensus Bayesian assessment[51] and the SAXSMoW volume correlation[52] approach for calculating the masses. Estimation of the radius of gyration (R_g) by Guinier-plot analysis was performed using the *autorg* function of PRIMUS[53]. The first 19 data points at low angles in the Guinier region were excluded from further analysis. GNOM was used for pair distance distribution analysis of the data within a range of q=0.0929-7.2965 nm^{-1}, choosing a D_{max} of 26 nm and forcing the *P(r)* function to 0 at D_{max}[54]. *Ab initio* modeling via the generation of dummy residue models was performed with GASBOR based on the *P(r)* function in reciprocal space[55]. The number of dummy residues was set to 290 for a p2 particle symmetry. A p2 symmetry was assumed, as choosing higher degrees of freedom did result in bead models with higher χ^2 values. 115 GASBOR bead models were generated in total. The bead models were clustered by running DAMCLUST and setting a p2 symmetry and considering only backbone atoms to ignore water molecules in the GASBOR models[56].

Model building

IM30 dimer models were generated according to the scheme presented in Supplementary Fig. 11b. From the clusters generated by DAMCLUST, one isolated cluster (cluster 14) was excluded from further analysis. For each of the other clusters, the most typical bead model according to DAMCLUST

was chosen. Water molecules in the bead model were removed. Then the model was transformed into a density map with a resolution of 4 Å by the Molmap command implemented in CHIMERA[57]. A resolution of 4 Å was chosen because the beads were treated as hard spheres and have a diameter of 3.8 Å. The resulting dimer maps were split along the symmetry axes to create maps of the monomer using SEGGER[58]. To fit IM30 into the map, a predicted structure of the monomer (IM30_Saur2017[19]) was used as an initial template. The predicted structure was fragmented by removing the loops and keeping the helices intact, yielding six helix fragments (Supplementary Fig. 11a). The fragments were placed manually into the map to roughly fit the density. MODELLER was used to recreate the missing loop regions between the fragments and to remodel the parts of the structure, which are considered to be flexible according to the results of the HDX measurements of IM30*[59]. A threshold of 45% relative HDX (after 10 s) was set as the limit to define a part of the structure as flexible. We refined the models by a simulated annealing molecular dynamics (MD) approach guided by the density map using FLEX-EM[60,61]. At least 50 runs of subsequent MD refinement were performed, using a cap shift of 0.15 to restrain secondary structure elements and keeping helix 2 and 3a as rigid bodies. Two of each refined monomer structures were then placed into the dimer maps by exhaustive One-At-A-Time 6D search (colores) and simultaneous multi-fragment refinement (collage), using the SITUS package[62]. Where necessary, clashes in the dimer interfaces were removed by running a short minimization procedure implemented in CHIMERA (100 steepest descent steps, step size 0.02 Å, 10 conjugate gradient steps, step size 0.02 Å)[63,64].

ACMA proton leakage assay

An aliquot of unsized unilamellar DOPG liposomes (400 µM lipid concentration, in 20 mM HEPES pH 7.6 + 150 mM KCl) was incubated with 2.4 µM protein for 5 min at RT. Thereafter, the mixture was diluted with 20 mM HEPES pH 7.5 + 150 mM NaCl and isopropanol to a final concentration of 6% isopropanol (v/v), 100 µM lipid and, 0.6 µM protein (Noteworthy, the secondary structure and overall stability of IM30 were preserved at 6% isopropanol (Supplementary Fig. 6)). 1 µL ACMA (*9-Amino-6-chloro-2-methoxyacridine*) was added to a final concentration of 2 µM. The sample was then incubated for another 200 s at RT in a 3 mL glass cuvette with continuous stirring. The fluorescence intensity was measured with a FluoroMax 4 fluorimeter (Horiba Scientific), using an excitation wavelength of 410 nm (slit width 2 nm), an emission wavelength of 490 nm (slit width 2 nm) and a measurement interval of 0.1 s. The measurement was started by addition of 1 µL valinomycin (final concentration 0.02 µM), to render the liposomes permeable for K^+, which results in formation of a proton gradient across the membrane. The fluorescence intensity was monitored

for 300 s with continuous stirring. Thereafter, the proton gradient was quenched by the addition of CCCP ([(3-chlorophenyl)hydrazono]malononitrile) to a final concentration of 2 µM, and the fluorescence intensity was monitored for another 100 s.

The fluorescence intensity was normalized by setting the intensity to 100% prior to the addition of valinomycin and the intensity 100 s after addition of CCCP to 0%. The initial slopes were estimated by a linear fit over 10 to 30 s after addition of valinomycin.

Laurdan fluorescence measurement

Unsized unilamellar DOPG liposomes containing Laurdan (6-Dodecanoyl-N, N-dimethyl-2-naphthylamine, from Sigma, Taufkirchen, Germany) (molar ratio lipid:Laurdan=1:500) were produced as described elsewhere[12]. To analyze the kinetics of IM30 membrane binding, liposomes and protein were mixed to a final concentration of 2.5 µM IM30 and 100 µM lipid. Fluorescence emission spectra were recorded at 25 °C over 20 minutes every 20 s using a FluoroMax-4 spectrometer (Horiba Scientific) from 425 to 505 nm upon excitation at 350 nm The excitation and emission slit width was set at 1 nm and 10 nm, respectively. The Generalized Polarization (GP) defined by Parasassi *et al.*[65] was calculated according to equation 3. ΔGP values were calculated via subtraction of the linear fit function of the DOPG control from the measurements in presence of protein.

$$GP = \frac{I_{440} - I_{490}}{I_{440} + I_{490}} \quad (3)$$

Atomic force microscopy (AFM)

To visualize IM30-binding to mica surfaces, 50 µL adsorption buffer (10 mM TRIS, 150 mM KCl, 25 mM $MgCl_2$, pH 7.6 or 10 mM HEPES, 150 mM KCl, 25 mM $MgCl_2$, pH 7.6) was incubated on freshly cleaved muscovite mica (12 mm diameter; Ted Pella Inc. grade V1) for 5 min at RT. All buffers and solutions were freshly prepared and filter sterilized (0.2 µm filter) before use. The mica substrate was washed two times with 50 µL of adsorption buffer. Then, 5 µL IM30 WT was added to a final concentration of ~ 0.5 µM. The protein was incubated on the substrate for 10 min at RT. Thereafter, the substrate was washed with ~ 1 mL imaging buffer (10 mM TRIS, 150 mM KCl, pH 7.6 or 10 mM HEPES, 150 mM KCl, pH 7.6).

To visualize IM30 binding on membranes, a solid-supported lipid bilayer (SLB) was prepared as follows: A freshly cleaved muscovite mica disc (12 mm diameter; Ted Pella Inc. grade V1) was washed with adsorption buffer (20 mM $MgCl_2$, 20 mM HEPS, pH 7.6) two times (50 µL). All buffers and

solutions were freshly prepared and filter sterilized (0.2 µm filter) before use. 50 µL of the adsorption buffer was left on the mica, and 50 µL liposome suspension (100% DOPG or 40% DOPG 60% DOPC, 5 mg/mL unilamellar liposomes[12]) was added. The solution on the mica disc was gently mixed by pipetting a volume of 50 µL up and down two to three times. Then, the mixture was incubated on the mica disc for 20 to 30 min at RT. Afterwards, the mica was washed with 1 mL imaging buffer (20 mM HEPES pH 7.6), and a drop of 100 µL buffer was left on the mica disc.

The samples were imaged with a Nanowizard IV AFM (JPK) using uncoated silicon cantilevers (OMCL AC240; Olympus, tip radius 7 nm, resonance frequency ~70 kHz and ~2 N/m spring constant). Measurements were carried out in QI mode or tapping mode in imaging buffer at approximately 30 °C. The force setpoint was set as low as possible, typically around 5 nN for measurements on SLBs, and <1 nN for measurements on mica. Formation of an intact lipid bilayer was confirmed by analysis of force-distance curves with high setpoint[66] and by imaging the bilayer before protein addition. The protein was added to the sample in small volumes (30 -50 µL) to achieve a final solution of roughly 1.5 µM. Images were scanned with 512x512 px or 256x256 px and 4.8 ms (or 6 ms) pixel time. The resulting images were analyzed with GWYDDION[67]. The measured height- images were leveled by removing a polynomial background, and scan rows were aligned by fitting a second-degree polynomial and aligning the offsets of the substrate or the lipid surface. The images were cropped to the area of interest. Full images are shown in Supplementary Fig. 5a/b.

Data availability statement

The authors declare that the data supporting the findings of this study are available within the paper and its supplementary information files. The data used to generate graphs and charts shown in Figs. 1a, 1b, 1d, 1e, 2a-f are provided in the Supplementary Data 1. The HDX-MS data used to generate Fig. 3b are provided in the Supplementary Data 2. All other relevant data are available from the corresponding author upon reasonable request.

EXCERPT OF SUPPLEMENTARY DATA AND FIGURES

IM30 binding to membranes involves structural rearrangement

We analyzed possible structural alterations upon membrane binding of IM30 via tryptic digestion of IM30 in absence and presence of DOPG liposomes. The protein (2.5 µM with or without liposomes (0.1 mM DOPG)) was incubated for 30 min at 4 °C, and then the protease was added (0.01 mg/mL)

(Supplementary Fig. 1). Samples were taken at the indicated time points and analyzed via SDS-PAGE. As shown previously, helix 7 of IM30 is rapidly cleaved1,2. The remaining fragment H1-6, i.e. the PspA-domain, is more protease-resistant, and thus the corresponding band is detectable until about 10 min after addition of trypsin. Strikingly, in contrast to soluble IM30, this band remained visible for about 60 min after trypsin addition when DOPG liposomes were present (Supplementary Fig. 1, red box). Thus, membrane binding appears to protect the PspA-domain from tryptic digestion. The altered protease resistance in presence of DOPG membranes indicates a structural change of IM30 upon membrane binding, which involves shielding of protein regions.

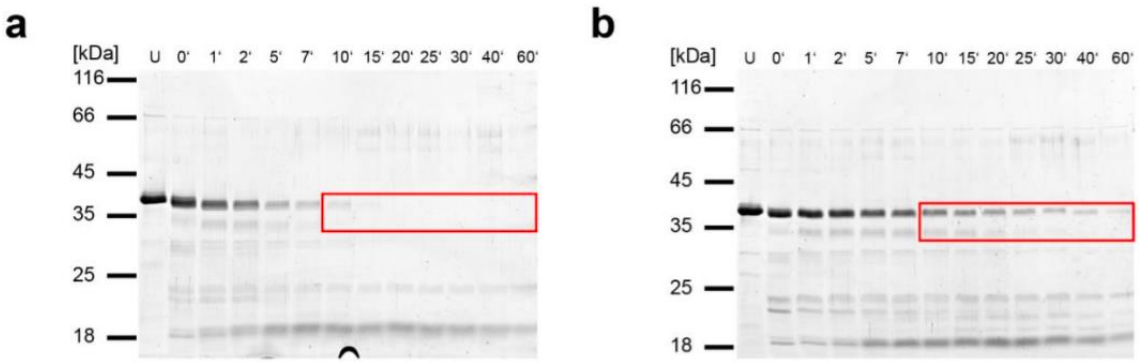

Supplementary Figure 1: The structure of IM30 changes upon membrane binding. (a/b) Limited trypsin digestion of IM30 in absence (a) and presence (b) of DOPG liposomes shows that the protease accessibility of IM30 is altered upon binding to PG liposomes. U = untreated sample. Time points indicate the time of incubating the sample with trypsin. The boxed area highlights the bands showing the major difference between trypsin digestion in absence vs. presence of DOPG

SUPPLEMENTARY DATA AND FIGURES

https://www.nature.com/articles/s42003-020-01314-4#Sec24

REPORTING SUMMARY

Further information on research design is available in the Nature Research Reporting Summary linked to this article.

DATA AVAILABILITY

The authors declare that the data supporting the findings of this study are available within the paper and its Supplementary information files. The data used to generate graphs and charts shown in Figs. 1a, b, d, e, 2a–f are provided in the Supplementary Data 1. The HDX-MS data used to generate Fig.

3b are provided in the Supplementary Data 2. All other relevant data are available from the corresponding author upon reasonable request.

Received: 3 February 2020; Accepted: 22 September 2020; Published online: 21 October 2020

REFERENCES

1 Westphal, S., Heins, L., Soll, J. & Vothknecht, U. C. Vipp1 deletion mutant of synechocystis: A connection between bacterial phage shock and thylakoid biogenesis? *Proc. Natl Acad. Sci. USA* 98, 4243–4248 (2001).

2 Fuhrmann, E., Gathmann, S., Rupprecht, E., Golecki, J. & Schneider, D. Thylakoid membrane reduction affects the photosystem stoichiometry in the cyanobacterium *Synechocystis* sp. PCC 6803. *Plant Physiol.* 149, 735–744 (2009).

3 Gutu, A., Chang, F. & O'Shea, E. K. Dynamical localization of a thylakoid membrane binding protein is required for acquisition of photosynthetic competency. *Mol. Microbiol.* 108, 16–31 (2018).

4 Junglas, B. & Schneider, D. What is Vipp1 good for? *Mol. Microbiol.* 108, 1–5 (2018).

5 Siebenaller, C., Junglas, B. & Schneider, D. Functional implication of multiple IM30 oligomeric states. *Front. Plant Sci.* https://doi.org/10.3389/ fpls.2019.01500 (2019).

6 Kroll, D. et al. VIPP1, a nuclear gene of *Arabidopsis thaliana* essential for thylakoid membrane formation. *Proc. Natl Acad. Sci. USA* 98, 4238–4242 (2001).

7 Aseeva, E. et al. Vipp1 is required for basic thylakoid membrane formation but not for the assembly of thylakoid protein complexes. *Plant Physiol. Biochem.* 45, 119–128 (2007).

8 Vothknecht, U. C., Otters, S., Hennig, R. & Schneider, D. Vipp1: A very important protein in plastids?! *J. Exp. Bot.* 63, 1699–1712 (2012).

9 Zhang, L., Kato, Y., Otters, S., Vothknecht, U. C. & Sakamoto, W. Essential role of VIPP1 in chloroplast envelope maintenance in Arabidopsis. *Plant Cell* 24, 3695–3707 (2012).

10 Zhang, L. & Sakamoto, W. Possible function of VIPP1 in thylakoids: protection but not formation? *Plant Signal. Behav.* 8, e22860 (2013).

11 Bryan, S. J. et al. Localisation and interactions of the Vipp1 protein in cyanobacteria. *Mol. Microbiol.* 94, 1179–1195 (2014).

12 Hennig, R. et al. IM30 triggers membrane fusion in cyanobacteria and chloroplasts. *Nat. Commun.* 6, 7018 (2015).

13 Zhang, L. & Sakamoto, W. Possible function of VIPP1 in maintaining chloroplast membranes. *Biochim. Biophys. Acta - Bioenerg.* 1847, 831–837 (2015).

14 Zhang, L., Kondo, H., Kamikubo, H., Kataoka, M. & Sakamoto, W. VIPP1 has a disordered C-terminal tail necessary for protecting photosynthetic membranes against stress. *Plant Physiol.* 171, 1983–1995 (2016).

15 Heidrich, J., Thurotte, A. & Schneider, D. Specific interaction of IM30/Vipp1 with cyanobacterial and chloroplast membranes results in membrane remodeling and eventually in membrane fusion. *Biochim. Biophys. Acta Biomembr.* 1859, 537–549 (2017).

16 Otters, S. et al. The first α-helical domain of the vesicle-inducing protein in plastids 1 promotes oligomerization and lipid binding. *Planta* 237, 529–540 (2013).

17 Fuhrmann, E. et al. The vesicle-inducing protein 1 from *Synechocystis* sp. PCC 6803 organizes into diverse higher-ordered ring structures. *Mol. Biol. Cell* 20, 4620–4628 (2009).

18 Gao, F., Wang, W., Zhang, W. & Liu, C. α-Helical domains affecting the oligomerization of Vipp1 and Its Interaction with Hsp70/DnaK in Chlamydomonas. *Biochemistry* 54, 4877–4889 (2015).

19 Saur, M. et al. A Janus-faced IM30 Ring Involved in Thylakoid membrane fusion is assembled from IM30 tetramers. *Structure* 25, 1380–1390.e5 (2017).

20 Bultema, J. B., Fuhrmann, E., Boekema, E. J. & Schneider, D. Vipp1 and PspA. *Commun. Integr. Biol.* 3, 162–165 (2010).

21 Hennig, R. et al. The IM30/Vipp1 C-terminus associates with the lipid bilayer and modulates membrane fusion. *Biochim. Biophys. Acta Bioenerg.* 1858, 126–136 (2017).

22 Theis, J. et al. VIPP1 rods engulf membranes containing phosphatidylinositol phosphates. *Sci. Rep.* 9, 8725 (2019).

23 Liu, C. et al. J-domain protein CDJ2 and HSP70B are a plastidic chaperone pair that interacts with vesicle-inducing protein in plastids 1. *Mol. Biol. Cell* 16, 1165–1177 (2005).

24 Liu, C. et al. The chloroplast HSP70B-CDJ2-CGE1 chaperones catalyse assembly and disassembly of VIPP1 oligomers in Chlamydomonas. *Plant J.* 50, 265–277 (2007).

25 Osadnik, H. et al. PspF-binding domain PspA1-144and the PspA·F complex: New insights into the coiled-coil-dependent regulation of AAA+ proteins. *Mol. Microbiol.* 98, 743–759 (2015).

26 Thurotte, A., Brüser, T., Mascher, T. & Schneider, D. Membrane chaperoning by members of the PspA/IM30 protein family. *Commun. Integr. Biol.* 10, e1264546 (2017).

27 Heidrich, J. et al. Organization into higher ordered ring structures counteracts membrane binding of IM30, a protein associated with inner membranes in chloroplasts and cyanobacteria. *J. Biol. Chem.* 291, 14954–14962 (2016).

28 Lee, S. Y., Letts, J. A. & MacKinnon, R. Functional Reconstitution of Purified Human Hv1 H+Channels. *J. Mol. Biol.* 387, 1055–1060 (2009).

29 Zhang, J., Feng, Y. & Forgac, M. Proton conduction and bafilomycin binding by the V0 domain of the coated vesicle V-ATPase. *J. Biol. Chem.* 269, 23518–23523 (1994).

30 Thurotte, A. & Schneider, D. The fusion activity of IM30 rings involves controlled unmasking of the fusogenic core. *Front. Plant Sci.* 10, 108 (2019).

31 Siebenaller, C., Junglas, B. & Schneider, D. Functional implications of multiple IM30 oligomeric states. *Front. Plant Sci.* https://doi.org/10.3389/ fpls.2019.01500 (2019).

32 Pace, C. N. & Scholtz, J. M. A helix propensity scale based on experimental studies of peptides and proteins. *Biophys J.* 75, 422–427 (1998).

33 Uversky, V. N. Paradoxes and wonders of intrinsic disorder: Stability of instability. *Intrinsically Disord. Proteins* 5, e1327757 (2017).

34 Rauscher, S. & Pomès, R. The liquid structure of elastin. *Elife* 6, e26526 (2017).

35 Muiznieks, L. D., Weiss, A. S. & Keeley, F. W. in *Biochemistry and Cell Biology* Vol. 88, 239–250 (National Research Council of Canada, 2010).

36 Fabiani, C. & Antollini, S. S. Alzheimer's disease as a membrane disorder: spatial cross-talk among beta-amyloid peptides, nicotinic acetylcholine receptors and lipid rafts. *Front. Cell. Neurosci.* 13, 309 (2019).

37 Uversky, V. & Eliezer, D. Biophysics of Parkinsons disease: structure and aggregation of alpha-synuclein. *Curr. Protein Pept. Sci.* 10, 483–499 (2009).

38 Kobayashi, R., Suzuki, T. & Yoshida, M. Escherichia coli phage-shock protein A (PspA) binds to membrane phospholipids and repairs proton leakage of the damaged membranes. *Mol. Microbiol.* 66, 100–109 (2007).

39 Standar, K. et al. PspA can form large scaffolds in Escherichia coli. *FEBS Lett.* 582, 3585–3589 (2008).

40 DeLisa, M. P., Lee, P., Palmer, T. & Georgiou, G. Phage shock protein PspA of *Escherichia coli* relieves saturation of protein export via the Tat pathway. *J. Bacteriol.* 186, 366–373 (2004).

41 Majumdar, A., Dogra, P., Maity, S. & Mukhopadhyay, S. Liquid–Liquid phase separation is driven by large-scale conformational unwinding and fluctuations of intrinsically disordered protein molecules. *J. Phys. Chem. Lett.* 10, 3929–3936 (2019).

42 Schuster, B. S. et al. Controllable protein phase separation and modular recruitment to form responsive membraneless organelles. *Nat. Commun.* 9, 2985 (2018).

43 Heidrich, J. et al. Mg^{2+} binding triggers rearrangement of the IM30 ring structure, resulting in augmented exposure of hydrophobic surfaces competent for membrane binding. *J. Biol. Chem.* 293, 8230–8241 (2018).

44 Shevchenko, A., Tomas, H., Havli, J., Olsen, J. V. & Mann, M. In-gel digestion for mass spectrometric characterization of proteins and proteomes. *Nat. Protoc.* 1, 2856–2860 (2006).

45 Micsonai, A. et al. Accurate secondary structure prediction and fold recognition for circular dichroism spectroscopy. *Proc. Natl Acad. Sci. USA* 112, E3095–E3103 (2015).

46 Pausch, P. et al. Structural basis for (p)ppGpp-mediated inhibition of the GTPase RbgA. *J. Biol. Chem.* 293, 19699–19709 (2018).

47 Han, X. et al. A kiwellin disarms the metabolic activity of a secreted fungal virulence factor. *Nature* 565, 650–653 (2019).

48 Wales, T. E., Fadgen, K. E., Gerhardt, G. C. & Engen, J. R. High-speed and high-resolution UPLC separation at zero degrees Celsius. *Anal. Chem.* 80, 6815–6820 (2008).

49 Geromanos, S. J. et al. The detection, correlation, and comparison of peptide precursor and product ions from data independent LC-MS with data dependant LC-MS/MS. *Proteomics* 9, 1683–1695 (2009).

50 Li, G. Z. et al. Database searching and accounting of multiplexed precursor and product ion spectra from the data independent analysis of simple and complex peptide mixtures. *Proteomics* 9, 1696–1719 (2009).

51 Masson, G. R. et al. Recommendations for performing, interpreting and reporting hydrogen deuterium exchange mass spectrometry (HDX-MS) experiments. *Nature* 16, 595–602 (2019).

52 Graewert, M. A. et al. Automated pipeline for purification, biophysical and X- ray analysis of biomacromolecular solutions. *Sci. Rep.* 5, 10734 (2015).

53 Franke, D. et al. ATSAS 2.8: a comprehensive data analysis suite for small - angle scattering from macromolecular solutions. *J. Appl. Cryst.* 50, 1212–1225 (2017).

54 Panjkovich, A. & Svergun, D. I. CHROMIXS: automatic and interactive analysis of chromatography-coupled small-angle X-ray scattering data. *Bioinformatics* 34, 1944–1946 (2018).

55 Hajizadeh, N. R., Franke, D., Jeffries, C. M. & Svergun, D. I. Consensus Bayesian assessment of protein molecular mass from solution X-ray scattering data. Sci. Rep. 8, 7204 (2018).

56 Fischer, H., de Oliveira Neto, M., Napolitano, H. B., Polikarpov, I. & Craievich, A. F. Determination of the molecular weight of proteins in solution from a single small-angle X-ray scattering measurement on a relative scale. *J. Appl. Crystallogr.* 43, 101–109 (2010).

57 Konarev, P. V. et al. PRIMUS: a Windows PC-based system for small-angle scattering data analysis. *J. Appl. Crystallogr.* 36, 1277–1282 (2003).

58 Svergun, D. I.IUCr. Determination of the regularization parameter in indirect- transform methods using perceptual criteria. *J. Appl. Cryst.* 25, 495–503 (1992).

59 Svergun, D. I., Petoukhov, M. V. & Koch, M. H. Determination of domain structure of proteins from X-ray solution scattering. *Biophys. J.* 80, 2946–2953 (2001).

60 Petoukhov, M. V. et al. New developments in the ATSAS program package for small-angle scattering data analysis. *J. Appl. Cryst.* 45, 342–350 (2012).

61 Pettersen, E. F. et al. UCSF Chimera?A visualization system for exploratory research and analysis. *J. Comput. Chem.* 25, 1605–1612 (2004).

62 Pintilie, G. D., Zhang, J., Goddard, T. D., Chiu, W. & Gossard, D. C. Quantitative analysis of cryo-EM density map segmentation by watershed and scale-space filtering, and fitting of structures by alignment to regions. *J. Struct. Biol.* 170, 427–438 (2010).

63 Šali, A. & Blundell, T. L. Comparative protein modelling by satisfaction of spatial restraints. *J. Mol. Biol.* 234, 779–815 (1993).

64 Joseph, A. P. et al. Refinement of atomic models in high resolution EM reconstructions using Flex-EM and local assessment. *Methods* 100, 42–49 (2016).

65 Topf, M. et al. Protein structure fitting and refinement guided by Cryo-EM density. *Structure* 16, 295–307 (2008).

66 Wriggers, W. Conventions and workflows for using Situs. *Acta Crystallogr. Sect. D. Biol. Crystallogr.* 68, 344–351 (2012).

67 Wang, J., Wolf, R. M., Caldwell, J. W., Kollman, P. A. & Case, D. A. Development and testing of a general amber force field. *J. Comput. Chem.* 25, 1157–1174 (2004).

68 Wang, J., Wang, W., Kollman, P. A. & Case, D. A. Automatic atom type and bond type perception in molecular mechanical calculations. *J. Mol. Graph. Model.* 25, 247–260 (2006).

69 Parasassi, T., De Stasio, G., d'Ubaldo, A. & Gratton, E. Phase fluctuation in phospholipid membranes revealed by Laurdan fluorescence. *Biophys. J.* 57, 1179–1186 (1990).

70 Loi, S., Sun, G., Franz, V. & Butt, H. J. Rupture of molecular thin films observed in atomic force microscopy. II. Experiment. *Phys. Rev. E Stat. Nonlin. Soft Matter Phys.* 66, 31602 (2002).

71 Nečas, D. & Klapetek, P. Gwyddion: an open-source software for SPM data analysis. *Open Phys.* 10, 181–188 (2012).

72 Franke, D., Jeffries, C. M. & Svergun, D. I. Correlation Map, a goodness-of-fit test for one-dimensional X-ray scattering spectra. *Nat. Methods* 12, 419–422 (2015).

73 Ortega, E. et al. The structure of the plakin domain of plectin reveals an extended rod-like shape. *J. Biol. Chem.* 291, 18643–18662 (2016).

74 Garst, A. D., Héroux, A., Rambo, R. P. & Batey, R. T. Crystal structure of the lysine riboswitch regulatory mRNA element. *J. Biol. Chem.* 283, 22347–22351 (2008).

ACKNOWLEDGEMENTS

This work was funded by the Max-Planck graduate center at the Max-Planck institutes and the University of Mainz. We thank Prof. Dr. Elmar Jaenicke (Institute for Molecular Physiology, Johannes Gutenberg University Mainz) assistance with MALS measure- ments, Mario Dejung (Institute of

Molecular Biology, Johannes Gutenberg University) for assistance with MS analysis and Sabine Wecklein (Department of Chemistry - Bio- chemistry, Johannes Gutenberg University Mainz) for support with the data acquisition of ACMA proton leakage measurements. The synchrotron SAXS data were collected at beamline P12 operated by EMBL Hamburg at the PETRA III storage ring (DESY, Hamburg, Germany). We would like to thank the beamline staff (especially Dr. Nelly Hajizadeh) for assistance in using the beamline. We thank the Deutsche For- schungsgemeinschaft for co-financing the HDX-system and support through the "DFG core facility for interactions, dynamics and macromolecular assembly structure" at the Philipps-University Marburg. Molecular graphics and analyses were performed with UCSF Chimera, developed by the Resource for Biocomputing, Visualization, and Informatics at the University of California, San Francisco, with support from NIH P41- GM103311. We thank Prof. Dr. Luning Liu and Dr. Longsheng Zhao (University of Liverpool, Institute of Integrative Biology) helping us find the necessary imaging para- meters and conditions for atomic force microscopy of IM30 rings on mica.

AUTHOR CONTRIBUTIONS

B.J., C.S., J.H., U.H., W.S., N.H., and D.S. were responsible for the general protein characterization study conception. The AFM studies were conceptualized by B.J., A.A., and S.W. The SAXS studies were conceptualized by B.J., R.O., and E.W. B.J., C.S., and J.H. prepared the protein and liposome samples. B.J., C.S., J.H., and N.H. collected and analyzed the general protein characterization data (fluorescence spectroscopy, CD spectroscopy, SEC, SEC-MALS, gel electrophoresis). B.J. and A.A. collected and analyzed the AFM data. R.O. collected the SAXS data. B.J. and R.O. analyzed the SAXS data. U.H. collected and analyzed the NMR data. W.S. collected and analyzed the HDX data. B.J. built and analyzed the structural models. B.J., A.A., C.S., and W.S. visualized the data. W.S., U.H., E.W., S.W., and D.S. were responsible for supervision, project administration, funding acquisition, and resources.

FUNDING

Open Access funding enabled and organized by Projekt DEAL.

COMPETING INTERESTS

The authors declare no competing interests.

ADDITIONAL INFORMATION

Supplementary information: is available for this paper at https://doi.org/10.1038/s42003-020-01314-4. Correspondence and requests for materials should be addressed to D.S.

Danksagung

Curriculum vitae